NOTICE

The quality of this microform is heavily dependent upon the quality of the original thesis submitted for microfilming. Every effort has been made to ensure the highest quality of reproduction possible.

If pages are missing, contact the university which granted the degree.

Some pages may have indistinct print especially if the original pages were typed with a poor typewriter ribbon or if the university sent us an inferior photocopy.

Reproduction in full or in part of this microform is governed by the Canadian Copyright Act, R.S.C. 1970, c. C-30, and subsequent amendments.

AVIS

La qualité de cette microforme dépend grandement de la qualité de la thèse soumise au microfilmage. Nous avons tout fait pour assurer une qualité supérieure de reproduction.

S'il manque des pages, veuillez communiquer avec l'université qui a conféré le grade.

La qualité d'impression de certaines pages peut laisser à désirer, surtout si les pages originales ont été dactylographiées à l'aide d'un ruban usé ou si l'université nous a fait parvenir une photocopie de qualité inférieure.

La reproduction, même partielle, de cette microforme est soumise à la Loi canadienne sur le droit d'auteur, SRC 1970, c. C-30, et ses amendements subséquents.

Canada

The Universal Multifractal Nature of Radar Echo Fluctuations

Mike R. Duncan

In Partial Fulfillment of the
Requirements for the Degree
of
Doctor of Philosophy

Department of Natural Resource Sciences
McGill University, Montréal

November 1993

ISBN 0-315-94614-8

Canada

Abstract.

The intensity returns obtained by a radar from precipitation are well known to fluctuate violently in space and time. We present a systematic study of the resolution dependence time series with overlapping time resolutions spanning 10 orders of magnitude (0.77 ms to 4 months), of the fluctuating radar echo from precipitation. The results undermine the current assumptions of homogeneity of rainfield at scales smaller than the radar resolution, due to Marshall and Hitschfeld (1953), by showing that the only length scales identifiable in the time series are those of the radar pulse volume, the wavelength, and a very small inner scale of the order of millimeters. An analysis of the multiscaling nature of the time series of echo fluctuations reveals multiscaling behaviour at scales down to the resolution or pulse volume scale. Since there are no *a priori* scales in the rainfield we proceed to model the fluctuating radar echo by assuming a multiscaling model of rainfield variability which extends to sub-resolution scales. A systematic analysis of the statistical behaviour of computed reflectivities from this variability gives a full statistical description of reflectivity originating from multiscaling variability, and solves the scalar multifractal radar observer's problem. Computation of time series of reflectivities from a time-space representation of this variability reveals quantitative and qualitative behaviours consistent with those of observed echo fluctuation time series. We conclude that a multiscaling model of the rainfield which extends to the smallest scales of the rainfield is consistent with observation.

Résumé.

On sait que les échos radar provenant de la précipitation fluctuent énormément dans le temps et l'espace. Nous présentons une étude systématique de la dépendance sur la résolution d'une longue série chronologique de mesures d'échos radar de la précipitation. Ces mesure s'étendent sur 10 ordres de magnitude dans le temps, de 0.77 ms jusqu'à 4 mois. Les résultats ne supportent pas les hypothéses formulées par Marshall et Hitschfeld (1953) et couramment acceptées concernant l'homogénité des champs de pluie à la sous-échelle. Nos résultats indiquent que les seules échelles identifiable dans notre longue serie de mesures sont le volume unitaire du radar, la longueur d'onde et une très petite échelle de l'ordre de millimètres. L'analyse de ces données révèle aussi un comportement "multiscaling" pour toutes les échelle jusqu'à la plus petite résolution possible. Puisque il n'y a *a priori* aucune échelle préférentielle dans les champs de pluie, nous avons effectué une modélisation des échos radar en utilisant un modèle "multiscaling" qui s'étend jusqu'aux échelles plus petites que la résolution de base du radar. Une analyse systématique du comportement statistique des réflectivités dérivée de cette variabilité donne une description statistique complète d'une réflectivité provenant d'une variabilité "multiscaling". Ceci résout aussi le problème de l'observateur radar dans un scalaire "multifractal". La simulation de la variabilité temporelle des réflectivités à partir d'une représentation spatio-temporelle démontre des comportements quantitatifs et qualitatifs qui sont compatibles avec ceux qui sont observés en réalité dans une longue série chronologique. Nous concluons donc qu'un modèle "multiscaling" qui s'étend jusqu'aux plus petites échelles est compatible avec les observations.

Statement of Originality.

This thesis presents a new model for the sub-radar-resolution scale variability responsible for the fluctuating radar echo.

The data analysis sections represent a systematic study, using spectral and multifractal techniques, of the resolution dependance of radar echo statistics of very long, very high resolution time series of the fluctuating echo. The analyses allow the following contributions to knowledge: 1) the time series reveal scaling behaviour ($E(k) \propto k^{-\beta}$) to a scale consistent with the pulse volume scale of the radar, 2) the only length scales that could be identified in time series of the fluctuating echo are those of the radar pulse volume and radar wavelength, there is no evidence of a homogeneity scale except at millisecond timescales, 3) the spectral characteristics of the fluctuating echo time series between these two scales is close to that of white noise, 4) there is another scaling range from a scale consistent with the radar wavelength to the smallest scales of the rainfield where evidence of homogeneity can be found.

A new multifractal parameter estimation technique was created by combining the trace moments estimation technique with a genetic algorithm. Multifractal analysis of the time series of the fluctuating echo allows the following contributions to knowledge: 1) the echo fluctuation statistics are multiscaling to a scale consistent with the radar pulse volume scale, 2) the statistics are fit very well by the forms provided by universal multifractals, 3) the presence of zeros in data sets used to estimate multifractal parameters will lead to spurious estimates of the parameters.

The modelling section of this thesis makes the original assumption that the multiscaling behaviour noted at scales greater than the radar resolution or pulse volume scale continues to the smallest scales of the rainfield. Modelling the fluctuating echo as a Fourier component of a multiscaling field yields a complete statistical description of $Z_{\epsilon\lambda}$ from a scaling rainfield and solves the scalar multifractal radar observer's problem. The general implications are that rain statistics can be inferred from radar measurements of effective reflectivity. The following results were found: 1) the Fourier component of multiscaling variability exhibits multiscaling behaviour, 2) the inner scale of the rainfield variability, in time series of $Z_{\epsilon\lambda}$, is replaced by the wavelength scale of the radar, 3) the dressing operation of the Fourier component results in a linear bias, $K_{A,R}(1)$, in the exponents characterizing the statistics of $Z_{\epsilon\lambda}$, 4) the magnitude of the bias is a linear function of the variability of the rainfield characterized by C_1.

The first space-time multifractal model of the fluctuating echo is introduced. The implications of this model are that 1) the statistical behaviours of Z_λ and $Z_{\epsilon\lambda}$ are identical at scales greater than

the pulse volume scale with $C_1 = 2^{\alpha}$ that of the rainfield variability, 2) the spectral plateau is a direct result of the Fourier component operating on a scaling rainfield, 3) the bias in distributions of Z_λ results from the influence of $K_{\lambda,R}(1)$.

Acknowledgements.

I want to thank my wife Simone for her patience and understanding during the seemingly endless process that resulted in this thesis. It is often forgotten how the stress and selfishness of singlemindedly pursuing an academic goal can affect those close to you. I wish to dedicate this work to my wife thank her for the help, support, and understanding that made it all possible.

I wish to thank my fellow graduate student, Mr. Frederic Fabry, for his help. The exercise of trying to convince him increased my own understanding and belief in the concepts expressed in this work.

I have had the good fortune to work with a wide variety of personalities, a process which cannot help but to increase one's understanding of not just the science, but the scientific process. Foremost, I wish to thank my thesis supervisor Prof. S. Lovejoy whose generosity and awesome abilities in the field of multifractals pushed me past the point of reservation and produced a true understanding of and appreciation for a relatively new field. I thank my supervisor, Prof. P.H. Schuepp for his constant enthusiasm and encouragement as well as the many discussions we have had over the years. I thank Geoff Austin, for his humour and guidance and I wish him luck in his new endeavours in New Zealand. I would also like to thank Prof. I. Zawadzki for his support and growing enthusiasm for the ideas contained herein.

Last, but certainly not least, I would like to thank Abnash, Alamelu, Aldo, Brian and Jill, the people of the McGill Radar Weather Observatory for providing a singularly spontaneous working environment. They also provided stimulating discussions and expert help, giving more of themselves than anyone has a right to ask or hope for.

Table of Contents.

Glossary of Symbols.

α	Index into the Lévy-Stable distributions ($0 < \alpha < 2.0$). α is an indicator of the singular nature of a universal multifracta field.
β	Spectral exponent ($E(k) \propto k^{-\beta}$, where E(k) is spectral energy).
B_λ	This variable is taken to represent the pulse volume scale of the radar.
C_1	The codimension of the ensemble mean of a process or field. A measure of the variability of a field.
$c(\gamma)$	Codimension function describing the scaling of probabilities of singularities γ.
D_s	The sampling dimension. A measure of the size of a data set. D_s defines the maximum singularity γ_s as well as the maximum moment q_s that can be observed with a data set.
η	An exponent used in the description of universal multifractals.
γ	The singularity strength (intensity) which is a function of the scale of measurement ($\gamma = K'(q)$).
γ_s	The maximum order of singularity observable within a data set of sampling dimension D_s.
γ_D	The order of singularity corresponding to divergence of moments.
H	Exponent for filtering a conservative multifractal field to produce a non-conservative multifractal field.
$\vec{k}$	The radar wavevector ($\mid k \mid = 2\pi/\lambda_w$).
K(q)	Scaling moment function for multifractals.
λ	Scale ratio between the outer scale of a process and an averaging scale or 'box' scale l. $\lambda = L/l$.
λ_w	The wavelength scale of a radar. Defines the wavenumber k as $k = 2\Pi/\lambda_w$
L	The outer scale of a field.
PRF	Pulse Repetition Frequency. The rate (in Hz) at which a radar sends out pulses of energy. The PRF determines the temporal resolution of radar data.
q	The order of scaling moment ($q = c'(\gamma)$).
q_s	The highest order of scaling moment that can be observed given a data set whose sampling dimension (size) is D_s.
q_D	The critical order of moment above which statistics diverge.
$\sigma(x,t)$	The radar cross section field in time and space.

UMCG	Universal Multifractal Cascade Generator. The technique used to generate multifractals as inputs to the RCS model. The shorthand terminology employed to specify the input fields for discussion is UMCG(C_1,H).
Z or Z_λ	Reflectivity factor. The mean of which current radar data processing strategies attempt to estimate by averaging measures of effective reflectivity.
Ze or $Z_{e\lambda}$	Effective reflectivity factor. The quantity measured by a radar.

List of Tables.

List of Figures.

1.0 Introduction.

The tropical rain fell in drenching sheets...

Michael Crichton
Jurassic Park

Radar.

The technology known as radar went from its infancy to maturity during the years of the second world war. The history of weather radar begins at the end of WW2 and was centered at M.I.T. and at McGill University in Montreal. The earliest work on the statistics and interpretation of echoes received by radars from rain are those of Ryde (see the review by Atlas and Ulbrich, 1990, and references therein). The actual development of the results necessary to convert radar echoes from precipitation into estimates of precipitation rate involved a number of steps that were taken during the years 1947 to 1951 (see Atlas and Ulbrich, 1990). The Stormy Weather Group, led by the late J.S. Marshall, was one of the most active centers of the development of the theory of weather radar after the war (see Douglas, 1990). The issue related to this early work that is of concern to this thesis is that of the interpretation of the fluctuating echo from precipitation. Early research on the statistics of the fluctuating echo was conducted at M.I.T. (Lawson and Uhlenbeck, 1950; Austin, 1952). The work published by Marshall and Hitschfeld (1953) and Wallace (1953), and referred to hereafter as the 'standard theory', presented a set of assumptions which are now routinely used to convert the fluctuations to an estimate of mean reflectivity.

Radar presented awesome potential as a hydrological and meteorological tool since it is able to measure, almost instantly over great distances and over a great range of scales, reflectivity from precipitation. The use of relationships between the quantity of reflected energy and drop sizes as well as drop fall speeds allowed for the measured energy backscattered by drops to be converted into estimates of rainrate through a "Z-R" (or reflectivity factor Z to rainrate R) relationship (Marshall and Palmer, 1948). The potential of radar as a hydrological tool was immediately recognized and attempts made to exploit the information provided by radar. However, as the use of weather radar became more widespread it was increasingly noticed that the rainfield displays extreme variability

in time and space. The various communities using radar slowly became aware of the extreme variability of the rain process and of the corresponding limits of predictability. Although the operational use of radar is widespread it never achieved the respect that the early researchers felt sure it would achieve. Undoubtedly the major reason is the extraordinary space-time variability for which no theoretical frameworks existed at the time. This lead to the continual disagreement of raingauge and radar estimates of rainfall amount.

The issues concerning the disparity of radar and raingauge estimates of rainfall have always centered on the following areas, the drop size distribution (DSD), drop fall speed relations, scattering relations, and the electronic considerations relating to radars (see, for example, Zawadzki (1984) or Austin (1987)). The ensuing debate has therefore always centered on the Z-R relation (see Battan (1973) for a variety of Z-R relations). To date, little attention has been payed to the possibility that the estimates of rainfall from radars and gauges are different primarily because the scales of the devices used are different. Such an argument requires the fundamental recognition that measures acquired from the rainfield are non-trivially dependent upon the scale of measurement. This notion is fundamentally incompatible with the accepted belief that rainfall is homogeneous at radar measurement scales. However, in the review by Katz and Harney (1990) the argument is presented, based on the work of Kerr (1951), that drop motions are dictated by turbulent air motions. Turbulence has long been known for its scaling statistics, especially the Komolgorov (1941) $k^{-5/3}$ power-law spectrum ($E(k) \propto k^{-5/3}$). In the last ten years major advances in scaling theories of turbulence have been the recognition that scaling generally leads to multifractals, and further that the scaling can be far more general than simple self-similarity. A multifractal rainfield would explain a great deal of the difficulty in comparing statistical quantities such as 'mean' rainrate. Applying this argument to the Z-R relation argument, both radars and raingauges have inherent measurement scales which, in a multifractal rainfield, would result in estimates of precipitation that depend in a systematic power-law way on the scale of the measurement.

Weather radars have provided much of the meteorological and hydrological communities' understanding of rainfield variability. Particularly influential radar rainfield studies were those conducted by Austin and Houze (1972) and Zawadzki (1973) which inspired a host of mathematical models of rainfall. However, modern radars, equipped with digital acquisition and recording systems are far more informative as to the fine structure of rainfall than were the early analog displays that showed up to only seven levels of intensity and recording was accomplished using photographic

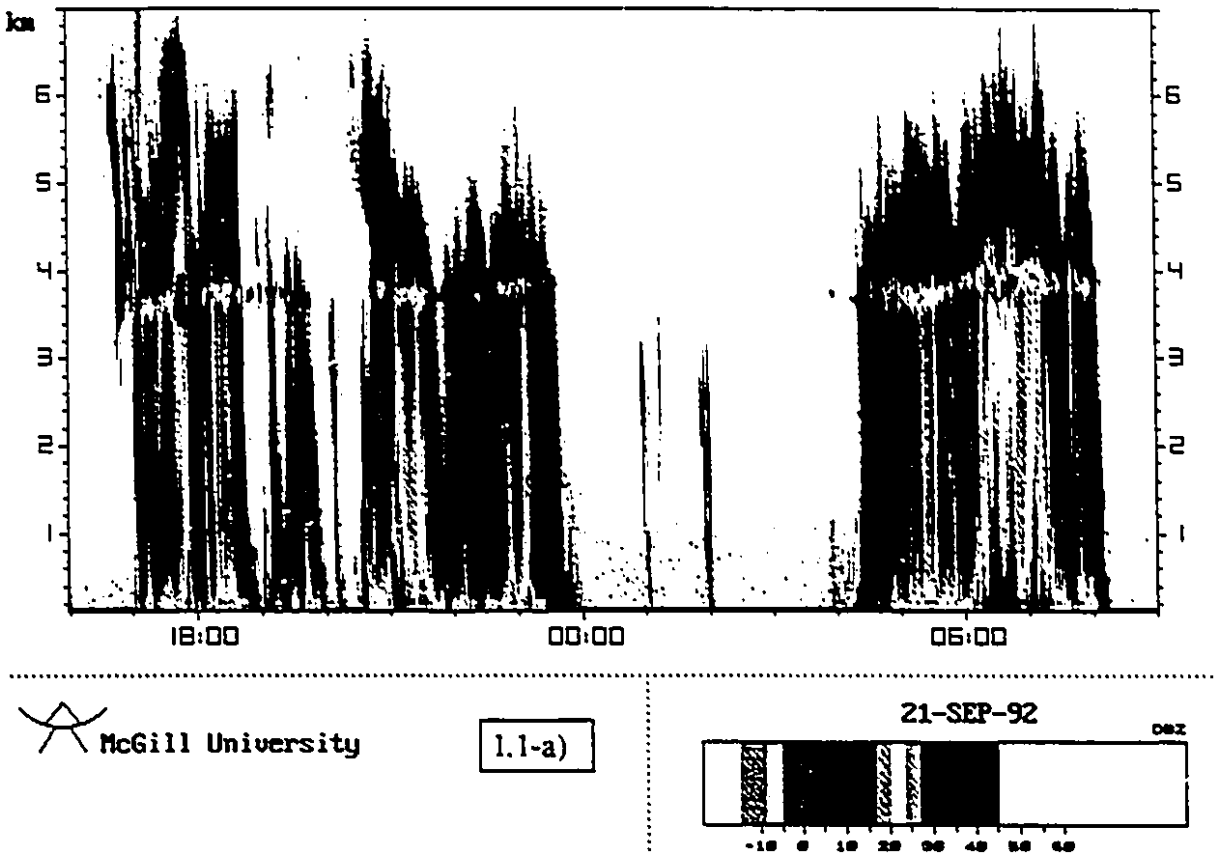

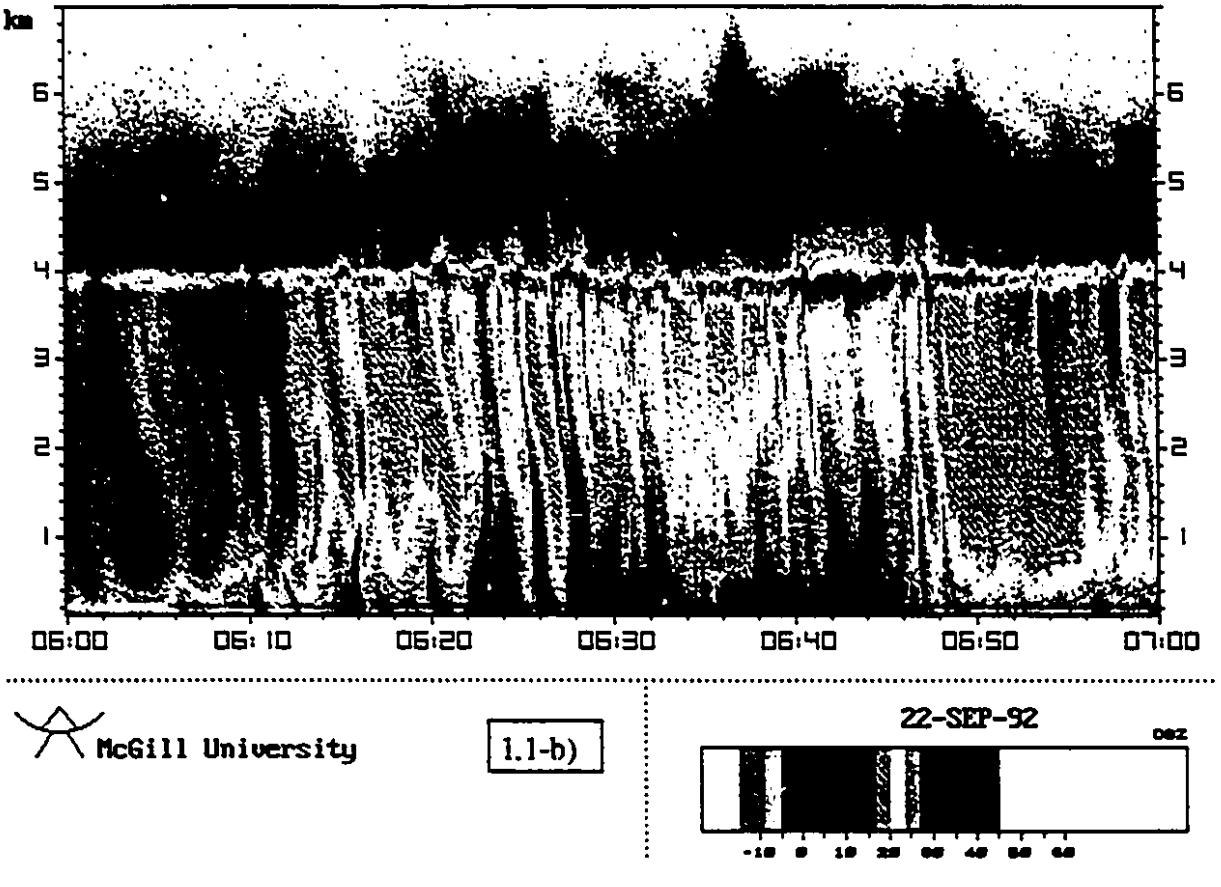

Figure 1.1: HTI time series of the vertical structure of rainfall over the VPR located at the McGill Radar Weather Observatory.

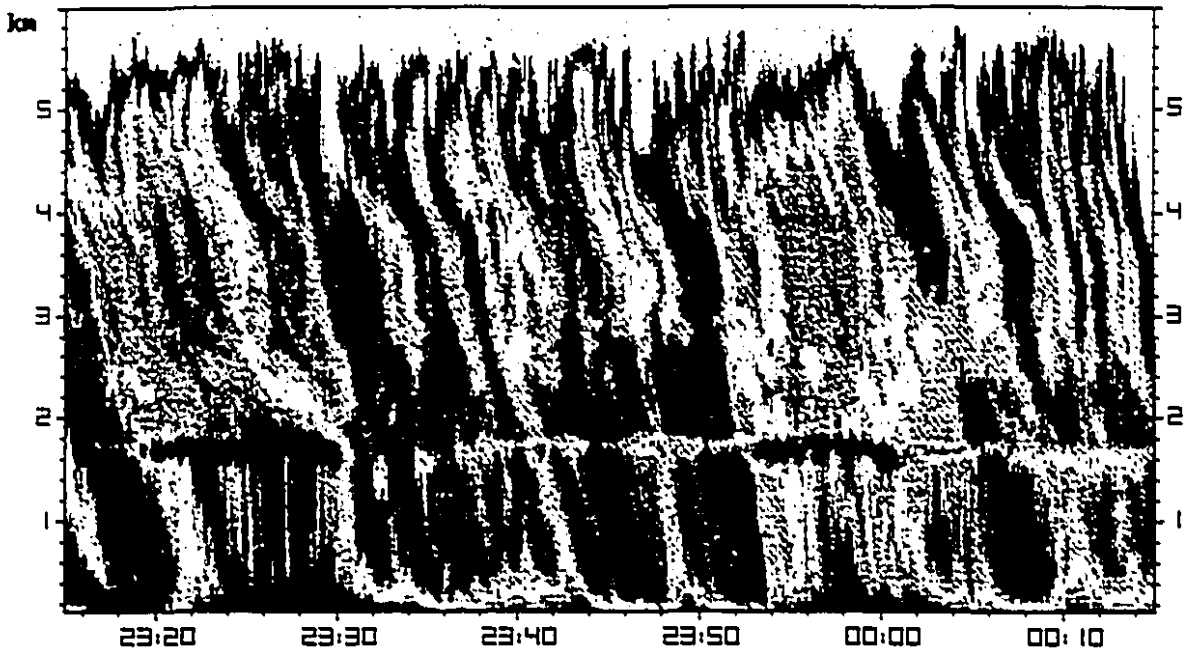

McGill University

1.1-c)

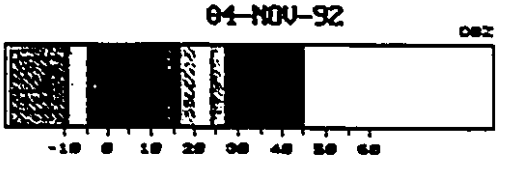

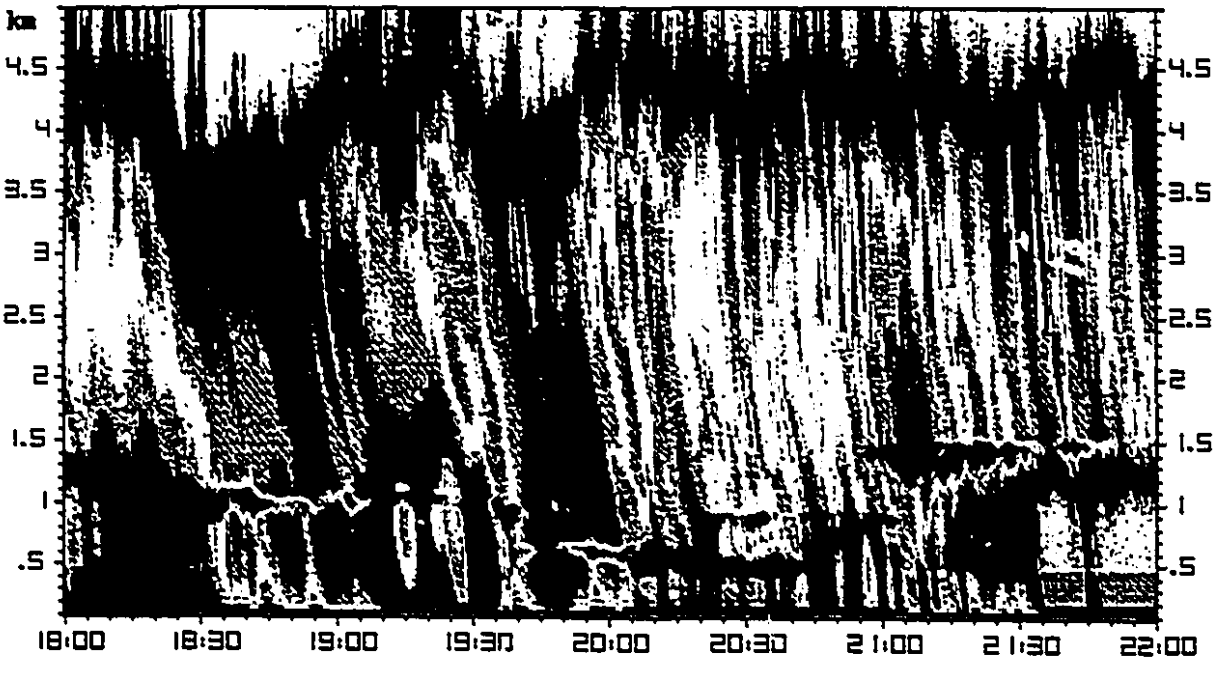

McGill University

1.1-d)

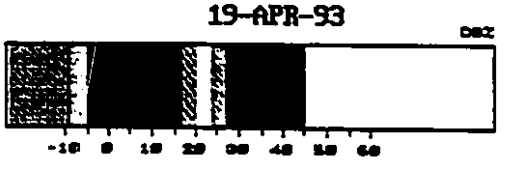

techniques. In recording the extreme variability of rainfall, modern radar systems have pushed our knowledge of the rainfield to the limit. Early models of rainfall, based on radar observations of rain patterns (Kessler, 1966; Armijo, 1966), have fallen by the wayside as it was realized that the extremely variable nature of the rainfall process, revealed by more sophisticated radar apparatus, far exceeded the ability of the models to represent it. The general problem was that most models could account for the observations at a single scale but not over a significant range of scales. What was required was a new class of models with the objective of representing how the rainfield operates from the smallest to the largest scales. Within such a framework the interpretation of measures of the rainfield, such as those provided by radars, can be interpreted properly.

Physical Models of Rainfall.

The lack of knowledge of the non-linear partial differential equations which govern the development of rain, coupled with the extreme variability of rainfall has led to the development of stochastic models of rainfall. Early stochastic models include those by Cole (1964), Armijo (1966) and Bras and Rodriguez-Iturbe (1976). The growing recognition of scaling symmetries in rainfall during the 1980's, largely due to the analysis of radar data, led to the incorporation of scaling symmetries in stochastic models of rainfall (Lovejoy, 1981; Lovejoy and Mandelbrot, 1985; Lovejoy and Schertzer, 1985). The early scaling models were totally ad hoc and were designed to respect a purely statistical scaling symmetry referred to now as 'simple scaling'. Simple scaling, also called 'scaling of the increments', was the first scaling behaviour thought to be associated with rainfall and can be represented as

$$\Delta R(\lambda^{-1}\Delta x) \overset{d}{=} \lambda^{-H}\Delta R(\Delta x) \qquad (1.1)$$

where R is rainrate. The small scale difference is $\Delta R(\lambda^{-1}\Delta x) = R(x_1 + \lambda^{-1}\Delta x) - R(x_1)$ and the large scale difference is $\Delta R(\Delta x) = R(x_2 + \Delta x) - R(x_2)$ where x_1 and x_2 are arbitrary, λ is a reduction ratio, and H is the (unique) scaling parameter. The equality '$\overset{d}{=}$' means equality in probability distributions viz. $a \overset{d}{=} b$ if $Pr(a>q) = Pr(b>q)$ for all q, where Pr indicates probability. This formula states that differences in rainrate observed at different interval lengths are identical except for the scale factor λ^{-H}. This type of scaling was introduced by Lamperti (1962) and later by Mandelbrot and Van Ness (1968) and called 'self-similarity'. However, since graphs of R(x) are in fact not self-similar but self-affine, and self-similarity is a much wider concept, this is a misnomer. The parameter H is

known as the Hurst exponent and was introduced by Hurst (1951) to describe the long range dependence in streamflow for the Nile river. The special case where the probability distributions are Gaussian is Brownian motion where H = 1/2. Mandelbrot and Wallis (1969) proposed a streamflow model with fractional Brownian motions (characterized by $H \neq 1/2$).

The ideas of simple scaling can go a long way to suggesting methods of interpreting the extremely variable measures that are acquired with radars and raingauges. Lovejoy (1981) hypothesized that simple scaling holds for rain but noticed that the extreme variability of rain results in algebraic or 'fat' tails of the probability distribution (see Waymire (1985) or Schertzer and Lovejoy (1985a)). Probability distributions with fat tails have the form $Pr(\Delta R > \Delta r) \approx \Delta r^{-q_D}$ $(\Delta r \gg 1)$ for the probability of a random rainfall fluctuation ΔR exceeding a fixed value Δr. The subscript D is necessary since the value of the exponent is expected to depend on the dimension of space over which the averages are produced. While the ideas concerning scaling have evolved beyond the notion of simple scaling the algebraic tails of probability measures of rainfall recorded by gauge and radar continue to be observed. Estimates of q_D from radar data and raingauge data reveal q_D to be in the range of 1 to 3 (Segal, 1979; Ladoy et al., 1991; Ladoy et al., 1993). The combination of scaling with algebraic tails is an indicator of self-organized systems (Bak et al., 1987) and can now be understood in terms of multifractal phase transitions (Schertzer et al. 1993).

The incorporation of scaling behaviour into stochastic models of rainfall yielded a considerable simplification of the modelling process as well as increasing the ability of these models to represent the extreme spatial variability of rainfall over wide ranges of scale. Scaling models can offer a single description for the behaviour of rain flux from small scales to meso-scales. The 'Fractal Sums of Pulses' model of Lovejoy and Mandelbrot (1985) had features in common with other stochastic rain models of the time (e.g. Waymire and Gupta (1981a,b,c), Rodriguez-Iturbe et al. (1984)) in that they were additive, but its philosophy and properties were different. The FSP model used a construction process to combine structures of various scales and frequency of occurrence to produce a field which respected simple scaling with $q_D = H^{-1}$ (with $1<q_D<2$, $1/2<H<1$). Lovejoy and Schertzer (1985b) introduced the Scaling Sums of Pulses (SCP) model which allowed q_D and H to be varied separately. In contrast, rainfall models such as those reviewed in Rodriguez-Iturbe et al. (1987) and Eagleston et al. (1987) are based on an ad hoc division of the atmosphere into regimes where different parameterizations were postulated. The difficulty with

these models is that realistic statistics were realized over only the very narrow ranges of scale over which they were calibrated. The model of Bell (1987) was another model which involved a large number of parameters and produced statistics that were intended to be realistic (i.e lognormal distributions of intensity were produced). The modelling process of Bell was an attempt to produce noises which resembled those of radar data, but unfortunately scaling behaviour was not respected. Detailed observations of the statistical structure of the rainfield over various scale ranges using radar have revealed no distinct scale breaks separating regimes where different parameterizations might be required.

In parallel to the development of the simple scaling models, work in cascade processes and strange attractors showed that real dynamical systems were much more likely to be multifractal and hence will respect multiple-scaling (e.g. a different fractal dimension for each intensity) (Hentchel and Procaccia, 1983; Grassberger, 1983; Schertzer and Lovejoy, 1983, 1984, 1985a,b; Parisi and Frisch, 1985; Halsey et al., 1986). Indeed, Meneveau and Sreenivasan (1987) introduced a simple 2 state α-model whose statistical properties they claimed were indistinguishable from those of turbulence. It was realized by Schertzer and Lovejoy (1987) and Gupta and Waymire (1993) that mathematical cascade processes posses the same scaling structure as recorded rainfall rates and involve a relatively simple construction process. Thus, the possibility of modelling the extreme variability of rainfall statistics from very large scales to very small scales with a single physically based description became a possibility. Multifractals arise when cascade processes concentrate energy, water or other flux quantities into smaller and smaller regions of space, and generally require an infinite number of exponents to specify their statistics, but these are fixed by the construction process. Cascade models are designed to respect several of the basic symmetries of the governing non-linear dynamical (Navier-Stokes) equation. There are three properties associated with a cascade phenomenology: 1) a scaling symmetry (invariance of statistics under dilation ("zooms")), 2) a quantity conserved by the cascade (i.e. in turbulence the conserved quantity is energy flux from large to small scale), and 3) localness in Fourier space (the dynamics are most effective between neighbouring scales).

The cascade model is predicated on the idea that fluxes, such as rain flux μ (normalized such that $\langle\mu\rangle = 1$, where $\langle\rangle$ denote the ensemble average), are concentrated into progressively smaller volumes. The number of volumes over which the flux is progressively concentrated increases while the volume, identified by its characteristic scale l, decreases. This concept can be represented as a

multiplicative process (see Appendix A). The end result of this process is that a small number of the volumes will contain a great deal of flux while the rest are close to zero. The range of scales over which this process can be defined is limited only by the outer and inner scale of the rain process. The outer scale is the largest scale of the process. The inner scale of the rainfield is a statistical quantity, but would presumably be limited to scales above the turbulent viscosity scale (which is measured in millimeters). The highest resolution element of a cascade (i.e. the smallest scale of the cascade) is usually defined by the dimensionless ratio Λ of the outer cascade scale L to the inner scale l (i.e. $\Lambda = L/l$), thus the highest resolution element is given by Λ^{-1}. The distribution of intensities γ of a rain flux μ at scale ratio λ ($\Lambda \geq \lambda \geq 1$) is given by

$$Pr(\mu_\lambda \geq \lambda^\gamma) \quad = \quad \rho(\gamma)\lambda^{-c(\gamma)} \tag{1.2}$$

where μ_λ is the flux averaged over scale λ^{-1} (the subscript λ is added to show that the flux estimate is dependent upon the scale over which it was averaged), γ is the singularity (or intensity), $\rho(\gamma)$ is a slowly varying (sub exponential) intensity dependent prefactor (which is generally ignored in most developments), and $c(\gamma)$ is a codimension function which depends on the intensity. When $c(\gamma) < D$, the codimension has a simple geometric interpretation as the difference between the space dimension D (the embedded space) and the fractal dimension $D(\gamma)$. Codimensions are useful in stochastic processes as they characterize the process independently of the dimension of the observing space. The codimension function $c(\gamma)$ defines a continuous spectrum of exponents governing the probabilities of various flux intensities γ of flux μ_λ integrated to some scale ratio λ. $c(\gamma)$ is constrained to be a convex function.

Considering the cascade construction process, each stage of construction is independent of the history of the earlier stages of construction. However, due to the hierarchical nature of the construction process the result has long range statistical correlations. This is a basic property of cascades and hence multifractals and is a concept embodied by exponents such as the Hurst exponent H (Hurst, 1951). Thus, moments of a multifractal are also power-law functions of scale. The multiscaling relation for moments is given by

$$\langle \mu_\lambda^q \rangle \quad \propto \quad \lambda^{K(q)} \tag{1.3}$$

where q is a moment and λ defines the box scale over which μ was averaged. This relation was first tested in radar rain data by Schertzer and Lovejoy (1985b). The function K(q) defines a continuum of exponents which characterize the scaling behaviour of μ_λ. The scaling behaviour of moments of μ_λ, characterized by the exponents K(q), can be estimated by plotting the averages as a function of scale for different values of q on a log-log graph.

There are fairly general conditions under which knowledge of probability distributions is equivalent to knowledge of the moment structure of a field. The relationship between $c(\gamma)$ and K(q) for multifractals was shown by Parisi and Frisch (1985). K(q) and $c(\gamma)$ are a Legendre transform pair,

$$K(q) = \max_{\gamma} (q\gamma - c(\gamma)) \; ; \; c(\gamma) = \max_{q} (q\gamma - K(q)) \tag{1.4}$$

which defines a one-to-one correspondence between singularity $\gamma = K'(q)$ and moments $q = c'(\gamma)$. Thus, knowledge of the moment structure is equivalent to knowledge of the probability distributions (see section 3).

The obvious implication of the above scaling relations is that measures from cascade fields are dependent upon the scale of observation. The scaling of the cascade may be exploited, simply by examining moments computed over different scales, to produce functions which are independent of scale and characterize the measures precisely. The functions K(q) and $c(\gamma)$ are scale invariant descriptors of the underlying cascade process and hence characterize the flux μ_λ independent of what scales were used to estimate μ_λ. Such descriptions allow the cross comparison of data sets (e.g. as in calibration) acquired with different resolutions from the same multifractal field. Indeed, if a field exhibits scaling behaviour the only way to compare measures acquired with different resolution sensors is through the scale invariant functions.

Schertzer and Lovejoy (1987) present an argument relevant to atmospheric processes that gives K(q) and $c(\gamma)$ specific forms. The argument they present suggests that the turbulent interaction ("mixing") of cascades yields cascades of the same type. Thus, there are stable and attractive "universality" classes. A useful result of the universality assumption, for conservative multifractals, is that K(q) and $c(\gamma)$, which define an infinite hierarchy of scaling exponents, are dependent upon

two parameters, α and C_1. α is an index to the Levy-Stable distributions characterizing the generator. C_1 is the codimension of the ensemble mean of the cascade field and is a measure of the sparsity of the field. The forms for $c(\gamma)$ and K(q) are

$$c(\gamma)=\left\{\begin{array}{ll} C_1\left(\frac{\gamma}{C_1\alpha'}+\frac{1}{\alpha}\right)^{\alpha'} & with \quad \frac{1}{\alpha'}+\frac{1}{\alpha}=1,(\alpha\neq 1, 0\leq\alpha\leq 2) \\ C_1\exp\left(\frac{\gamma}{C_1}-1\right) & if \quad \alpha=1 \end{array}\right\} \tag{1.5}$$

$$K(q)=\left\{\begin{array}{ll} \frac{C_1}{\alpha-1}(q^{\alpha}-q), & if \quad \alpha\neq 1 \\ C_1 q\ln(q), & \alpha=1 \end{array}\right\} \tag{1.6}$$

The various tests of these relations over the last six years using radar data have been surprisingly successful. Direct verification of relation 1.5 was accomplished by Seed (1989) using a very large database of radar CAPPI maps (Constant Altitude Plan Position Indicators or CAPPIs are constant altitude cuts through volumetric radar data recorded by volume scanning weather radars). Schertzer and Lovejoy (1985a,1987) and Lovejoy and Schertzer (1990a) have tested the universal forms. Gabriel et al. (1988) made a test of universality using radar data. Gupta and Waymire (1990) have shown that multiscaling holds using GATE radar data. Duncan et al. (1992a), and Tessier et al. (1993) present further evidence that radar data conforms to the predictions of universality. Ladoy et al. (1993) and Hubert et al. (1993) show that universality holds using raingauge data. The analyses of Duncan et al. (1992a,b) and Tessier et al. (1993) involve radar data sets of very high spatial and temporal resolution. Both analyses indicate that multifractal behaviour is observed to space scales of 40 meters (which is the resolution scale of the radar data) and timescales of less than seconds in radar data. The data sets used will be described in section 2, but comprise time series of echo fluctuations from a single range gate. The time series analyzed by Tessier et al. (1993) have a temporal resolution of 2 s and the total time series length was one month. The time series analyzed by Duncan et al. (1992a,b) were more varied in their resolutions but support the observation of scaling behaviour, if not the actual parameters extracted from these scaling ranges (see section 5.2), to the pulse volume scale of the radar (see sections 4 and 5).

Radars and Rainfall.

The most outstanding characteristic of radar echoes from precipitation is the fact that they fluctuate violently in space and time. We will argue that the fluctuation is due to the extreme variability of the rain flux μ in space and time. The violent changes in μ at all scales are represented in time series of the fluctuating echo. There are a large number of factors which can affect the space-time behaviour of μ, included are turbulent advection, sedimentation due to gravity, and natural variations due to the inhomogeneous nature of the rain generating regions (see figure 1.1). While large raindrops cannot be considered as passive admixtures, the effect of turbulence will be to concentrate water onto progressively smaller volumes creating an inhomogeneous rain flux μ. The "homogenization" of turbulence is largely a misconception since viscosity is the agent that homogenizes. Turbulence merely concentrates quantities onto smaller volumes in order to generate the large gradients necessary for efficient dissipation. Irrespective of the mechanism, the observation of scaling behaviour in radar data is consistent with cascades which systematically concentrate rain flux to progressively smaller scales. Figure 2.2 is an idealization of a radar operating in a typical rainfield, the inhomogeneity of the rainfield appears organized and highly variable. This picture of the rainfield is completely incompatible with the picture currently used in the interpretation of radar signal fluctuations.

The current theory of the statistical behaviour of radar echoes from rainfall, introduced above as standard theory, is due to Marshall and Hitschfeld (1953), Wallace (1953) and Rogers (1971), but is based on work conducted at the M.I.T. radiation labs and reported by Lawson and Uhlenbeck (1950). The critical assumption of the standard theory is that the drop phases (relative to the radar) are independent random variables. A Poisson model is used to model the drop phases, or positions relative to the radar, in time and space. Wallace (1953) computes the Fourier component of the distribution of drops and examines the statistical behaviour of the resulting amplitude. Ignoring geometrical and dimensional constants the signal amplitude received by a radar from a volume[1] B_λ of scatterers (volume V_j) is given by

1 B_λ serves a double purpose, it defines both the set of drops found within the illuminated volume and the scale of the illuminated volume λ^{-1}.

$$A_k(\vec{x}) = \frac{1}{Vol(B_\lambda)} \sum_{j \in B_\lambda} V_j e^{i\vec{k}\cdot\vec{x}_j} \tag{1.7}$$

where $\vec{k}$ is the radar wavevector and $\vec{x}_j$ is the position vector of the j^{th} drop of volume V_j. We anticipate that this Fourier component of the drop positions will be dependent on the scales of observation λ and wavelength scale $\lambda_w = \frac{2\pi}{|\vec{k}|}$. However, if the drop positions obey Poisson statistics the probability of finding a drop is homogeneous in space and the phases will be independent random variables. If, in addition, the volume variance is finite, then the standard result follows. The "effective reflectivity[2] factor" $Z_{e\lambda}$ measured by a radar is related to the amplitude of the scattered wave by

$$Z_{e\lambda} = \frac{1}{Vol(B_\lambda)} \left| \sum_{j \in B_\lambda} V_j e^{\vec{ik}\cdot\vec{x}_j} \right|^2 = |A_k(\vec{x})|^2 Vol(B_\lambda) \tag{1.8}$$

The corresponding "reflectivity factor" Z_λ is defined by

$$Z_\lambda = \frac{1}{Vol(B_\lambda)} \sum_{j \in B_\lambda} V_j^2 \tag{1.9}$$

These relations define Z_λ and $Z_{e\lambda}$, and initially, assume that only Rayleigh scattering is important. Given that the drop phases are random variables with Poisson statistics the classical result for the conditional probability distribution of $Z_{e\lambda}$ given Z_λ can be established by considering eq. 1.7 as a random walk in phase space:

$$Pr(Z_e \mid Z) = \frac{1}{Z} e^{-Z_e/Z} \tag{1.10}$$

Following the belief that different scale regimes of the rainfield exhibit different statistical behaviours, Rogers (1971) applied the standard theory to the problem of gradients of rainfall intensity affecting estimates of $Z_{e\lambda}$. The scale separation that Rogers (1971) implicitly employed was the

2 The subscript λ is appended to indicate the fact that in a scaling rainfield the measured value of intensity Z_e is dependent upon the radar measurement scales.

assumption that gradients are unimportant below the pulse volume scale B so that the standard theory would apply there. This assumption avoids the need to model the sub-resolution gradients. The concept was predicated on then current data processing strategies which involved cross range or downrange averaging to form estimates of Z from many neighbouring measurements of Z_e. Thus, estimates of Z involved averaging volumes larger than B and within these volumes it was possible that gradients in rainfall rate could affect the average that produced Z_e. Rogers (1971) expressed this possibility as a conditional probability and used an ad hoc rainrate gradient model to show how the statistics of $Z_{e\lambda}$ are affected.

Lovejoy and Schertzer (1990a,b) have discussed various corrections to the standard theory for multifractal rainfields. Lovejoy and Schertzer (1990a) calculated corrections to mean Z_λ and $Z_{e\lambda}$assuming fractal distributions of drops. Lovejoy and Schertzer (1990b) calculated correction factors assuming sub-resolution homogeneity of drop statistics but that larger scale fluctuations were multifractal. Neither study addresses the problem of sub-resolution inhomogeneity. While the blotting paper experiment of Lovejoy and Schertzer (1990a) could certainly be taken for evidence of rainfield gradients to very small scales no effort was made on their part to compute the Fourier components of such a rainfield.

Objectives and Organization of the Thesis.

The main objective of this thesis is the qualitative and quantitative exploration of the effect of multifractal sub pulse volume variability on the statistics of radar echo fluctuations from precipitation. Evidence of the existence of multifractal behaviour of echo fluctuations down to the resolution scale B of the radar will be provided by specially collected time series of the fluctuating echo. Several original observations of the statistical nature of the echo fluctuations are made. The multifractal behaviour of the fluctuating echo will be parameterized by α and C_1. Another special data set provides evidence that the rainfield exhibits scaling behaviour below the resolution scale B, but since there is no *a priori* scale dependence in the rainfield that resulted in the data sets collected it will be argued that the rainfield is multifractal to its smallest scales which we find to be typically of the order of mm. Modelling of the fluctuating echo is accomplished by first examining the statistical behaviour of Fourier components of multifractal variability to determine the statistical properties of $Z_{\epsilon\lambda}$. This corresponds to the assumption that the sub-resolution variability has the same scaling behaviour as the super-resolution variability in the rainfield. A simple assumption concerning the relation between temporal and spatial scaling exponents will then be introduced to explore the effect of temporal as well as spatial scaling on the statistical behaviour of $Z_{\epsilon\lambda}$. The results of this study will strongly suggest that a more appropriate model for the interpretation of echo fluctuations is given by multifractal models of rainfall $\times$ μ. A large concluding section will outline the implications of scaling rainfield to radar measurement strategies and will point out that this information can be used to measure the dynamical properties of the rainfield.

Since the ability to produce multifractals with prescribed properties is a relatively recent capability, the behaviour of a Fourier component of these models has not been known until now. The results developed in this thesis will be presented in the language of universal multifractals, although every effort will be made to incorporate the language of the standard theory for comparison. The recent development of complex valued Lie cascades (Schertzer and Lovejoy, 1993a) allow the results of the Fourier component of multifractals to be expressed quantitatively in simple terms. Examination of the fluctuating echo resulting from a multifractal rainfield will serve to answer the question as to the statistical behaviour of the fluctuating echo, which is a Fourier component, from a multifractal rainfield. It will also serve to show that there is a great deal of information available in the fluctuating echo that is ignored by current processing strategies.

Chapter 2: Data Collection and Processing.

Some unique time series of the fluctuating echo were collected with a vertically pointing radar that provided spatial resolution of 40 m and temporal resolution to millisecond time scales. Time series of the fluctuating echo with lower temporal resolution were also collected. These data sets are supported by a number of corroborating data sets. Data collection procedures, quality control, and details of the devices used to collect the data are provided.

Chapter 3: Universal Multifractals.

This chapter summarizes relevant results of the universal multifractal formalism. Results necessary for the analysis and modelling of multifractals are presented. Emphasis in this chapter is placed on the details pertaining to accurate estimation of universal multifractal parameters. The results for spectral behaviour are also provided.

Chapter 4: Spectral Analysis of Rainfield Intensity Time Series.

This chapter examines the spectral nature of the various data sets collected for this thesis. The objective is to determine the ranges of scales over which scaling behaviours may be observed in time series of the fluctuating echo. The spectral behaviour of time series of rainfall intensities is examined and discussed. A new feature of the spectral behaviour of time series of the fluctuating echo is examined and discussed. This chapter also examines the scaling behaviour of distributions of the fluctuating echo. Estimates of spectral and intensity distribution parameters are presented in tabular format.

Chapter 5: Estimation of Multifractal Parameters.

In this chapter the universal multifractal nature of the echo fluctuation time series is examined and discussed. A general objective is to determine the range of scales over which universal multifractal behaviours can be expected in time series of the fluctuating echo. The specific objective of this chapter is to examine whether universal multifractals are an appropriate model for the sub-resolution variability in radar measurements of precipitation. A new multifractal parameter estimation technique is introduced. The new technique is applied to the data sets along with parameters estimation techniques presented in chapter 3. Estimates of universal multifractal parameters are presented in tabular format and a discussion of issues relevant to the accuracy of the estimates is provided.

Chapter 6: The Statistics of $Z_{\epsilon\lambda}$ from a Spatially Scaling Rainfield.

In this chapter the results of the data analysis sections justify the assumption that radar sub-resolution variability can be modelled as a universal multifractal. The scaling behaviour of a Fourier component is found to lead to general statistical forms which relate the statistics of reflectivity to that of rainfield variability. The statistical forms in this chapter represent the solution to the scalar multifractal radar observer's problem.

Chapter 7: Radar Measures from a Temporally and Spatially Scaling Rainfield.

A space-time multifractal model of the radar echo fluctuation problem is presented. This chapter examines the influence of radar measurement scales on the statistical behaviour of artificial time series of $Z_{\epsilon\lambda}$ and Z_{λ}. The scaling behaviours examined in this chapter are qualitatively and quantitatively similar to the behaviours isolated in the observed intensity time series.

Chapter 8: Conclusions, Implications and Possible Extensions.

In this chapter the results of the data analysis sections and the modelling section are summarized. This chapter also considers the implications of radar measures acquired from a multiscaling rainfield and speculates on possible data processing strategies that preserve and exploit this information.

2.0 Data Collection and Processing.

Radar Measurement Scales and Terminology.

Most meteorological radars operate by sending out a finite length pulse of microwaves. Figure 2.1 is an idealization of the microwave pulse travelling away from the radar. The pulse has a volume, henceforth referred to as the pulse volume (B_λ), that is given by $v = l \cdot r\theta_v \cdot r\theta_h$, where l is the pulse length (for the VPR $l \sim 37$ m, the actual signal is returned from a volume half this length), r is the distance of the pulse from the radar, and θ_v and θ_h are the vertical and horizontal beamwidths. In what follows the radar is assumed to average over a volume $lr^2\theta^2$ ($\theta_v = \theta_h$) and defines a scale ratio λ of the outer scale of the rain process L over the pulse volume scale l (l is taken to symbolize the characteristic scale of the pulse volume in 3D). Thus, B_λ is the set of drops in a 3D volume of scale ratio λ. Figure 2.2 shows an idealization of the VPR operating in a typical rainfield. The pulse length l is selectable on some systems, but remains fixed during measurement. The pulse volume is a function of range due to the beamwidths. Therefore as the pulse travels further away from the radar its lateral dimensions increase and the signal returned averages more of the structure of the rainfield. The wavelength used by a given radar is generally fixed. Meteorological radar systems are traditionally X-band (~3 cm), C-band (~5 cm), or S-band (~10 cm). For a given radar system the number of wavelengths within a pulse volume is a function of the pulse length. Within each wavelength, planes of constant phase (relative to the radar) can be defined.

The rate at which pulses are sent out by a given radar is known as the pulse repetition frequency (PRF) which has units of Hz. The primary data sets collected for this thesis (table 2.1) were collected with a PRF of 1300 Hz[3]. The time between successive pulses is 0.77 ms. In a 0.77 ms interval a drop moving at a velocity of 5 m/s could move 3.85 mm.

The reason that weather radars work is that water is a dielectric molecule and hence when a drop is hit by an electromagnetic wave it produces a backscatter wave which can be measured. The quantity of backscattered energy is a function of a number of parameters including drop size and wavelength. The various relationships between scattering variables is well known and can be found in many references including Gunn and East (1954) and Battan (1973). Acknowledging the various difficulties the naive assumption that the backscattering is limited to the Rayleigh regime is often

3 Exceptions as noted in Table 2.1.

Radar Measurement Scales

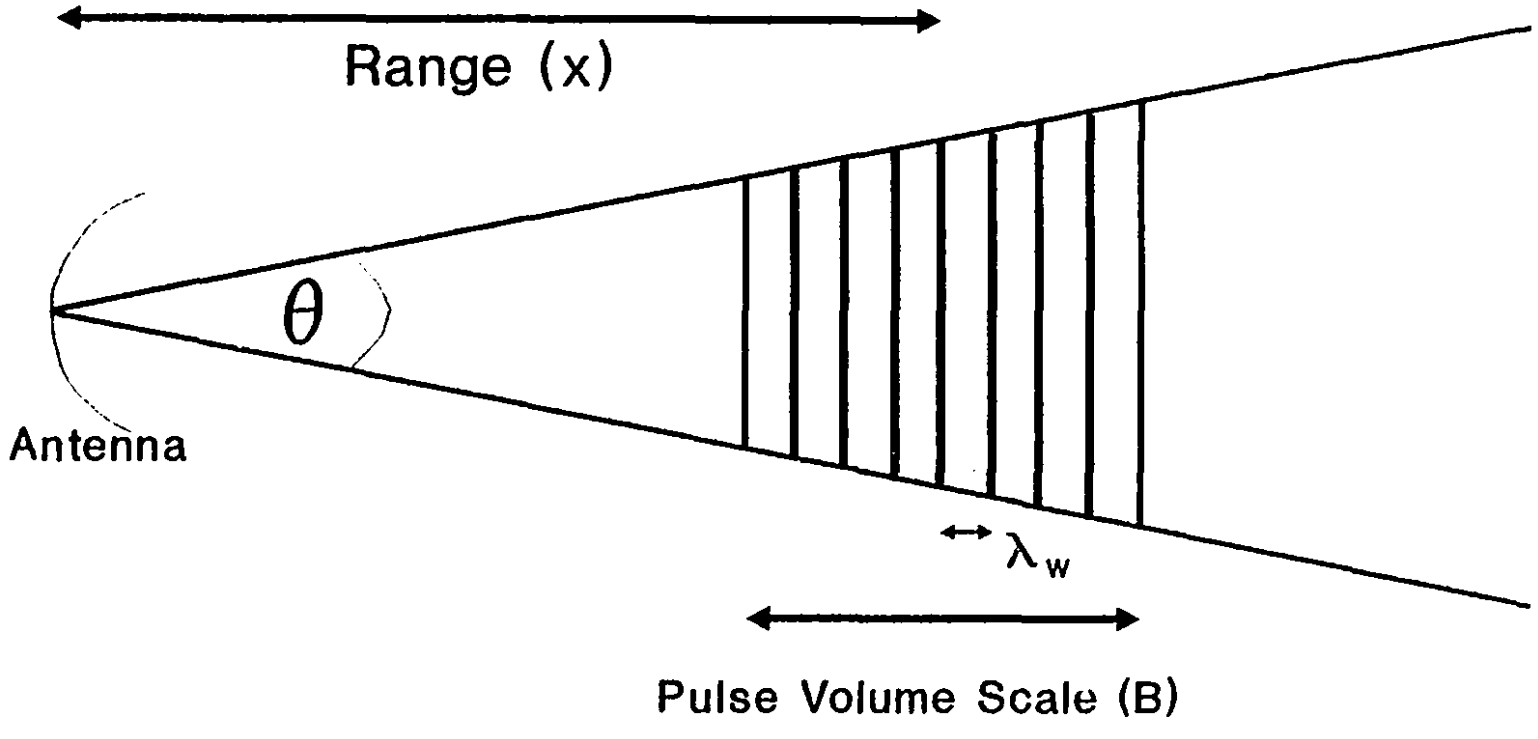

Figure 2.1: Radar measurement scales. As the microwave pulse travels downrange its lateral dimensions change due to the beamwidth. The wavelength λ_w and the pulse volume scale B remain constant.

made. Rayleigh scattering means that the reflectivity factor Z of a drop is proportional to the square of its volume. The Rayleigh scattering condition is that the size factor of the drop $\alpha = \frac{2\pi r}{\lambda}$ is much less than 1 (in fact it is valid up to around $\alpha = 0.1$, Gunn and East (1954)).

The Data Sets.

A vertically pointing X-band radar (VPR) was used to collect a number of unique data sets. The only unique feature of the VPR is that the dish is fixed and faces upward. The VPR is normally used to collect time series of the vertical structure of precipitation. The height-time indicator (HTI) diagrams (see figure 1.1) represent very high spatial and temporal resolution records of the development of precipitation over the radar. For the purposes of studying the fluctuating echo some special data collection routines were written. The special data sets collected with the VPR consist of time series of echo fluctuations from a single volume at fixed range (i.e. fixed pulse volume scale) at the highest pulse repetition frequency (PRF) of the VPR (see figure 2.2). The bulk of these special data sets consist of time series of intensities at two or four heights. These data sets, labelled A through I, are detailed in tables 2.1 and 2.2. However, echo time series A through I are of limited duration (the duration of sampling was limited by available resources). In order to examine a larger range of scales a longer time series was constructed from the HTI data archives of the VPR (the VPR has been in nearly continuous operation since 1989, see Fabry, 1990; Fabry et al, 1993). In its normal mode of operation the VPR collects a vertical reflectivity profile up to 8 km in altitude using oversampling to 7.5 m resolution of a 37.5 m pulse length. The estimates of the profile are collected at 2 s intervals and represent averages of values of $Z_{e\lambda}$. Two time series were composed from this record representing the variability at 1 and 1.41 km altitudes. Table 2.3 contains the two time series, labelled VPR1 and VPR2, of four months duration. Thus, the total range of scales collected to examine the fluctuating echo spans timescales from 0.77 ms to 4 months, or 10 orders of magnitude.

Secondary data sets were employed to verify the observations made with the time series of the fluctuating echo. Of course, it was not possible for one device to overlap the timescales observable with the radar, so a number of devices were used. These secondary data sets include two series of rainfall intensities collected by electronic raingauges presented in table 2.4, and two series of 'sonic' gauge data collected with a device of unique construction presented in table 2.5. The sonic raingauge was constructed by Mr. F. Fabry of the McGill Radar Weather Observatory to provide time series of rainfall intensity that could overlap the time resolution of the hi-res radar

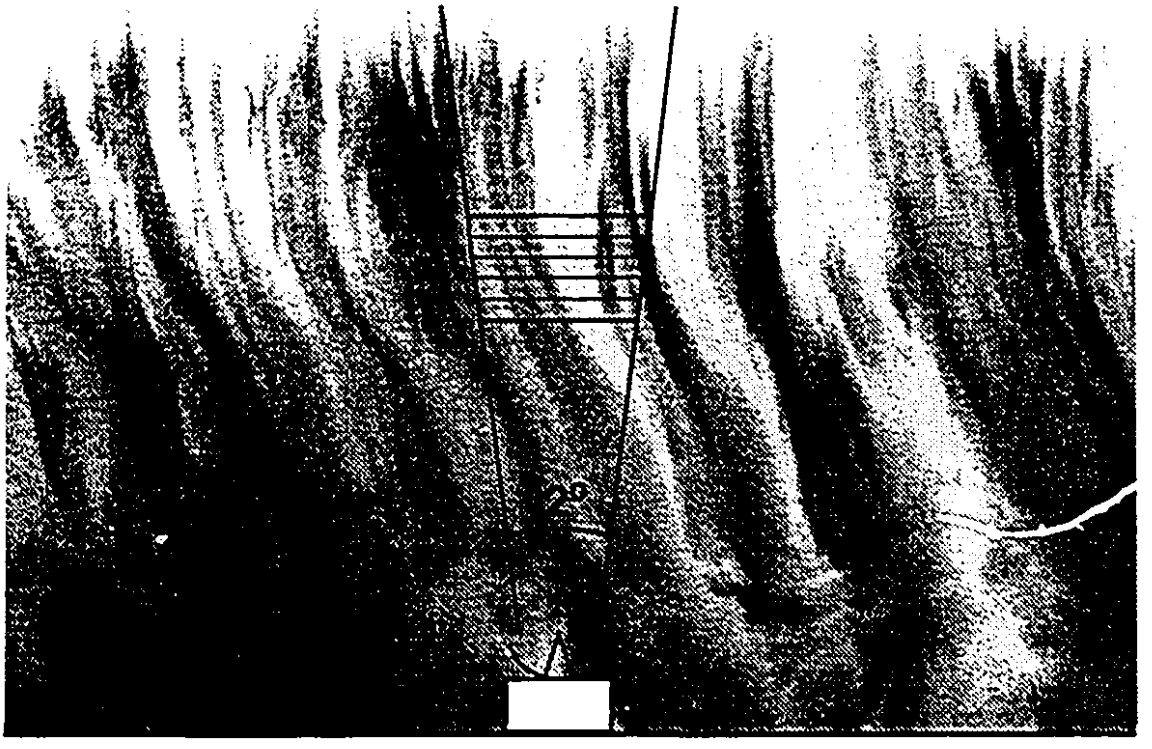

Figure 2.2: An idealized schematic of the VPR operating in a rainfield. The device can be used to collect a continuous vertical profile. The device can also be used to collect a time series of echoes at a fixed altitude. The resulting time series for a collection at a fixed altitude would have a temporal resolution given by the PRF of the VPR. The spatial resolution for a given time series is fixed.

data below 2 s. The timeframe for data collection extends from fall 1990, when series A was collected, to the fall of 1992. The most intensive collection periods were fall 1991 and the spring, summer and fall of 1992. Instrumentation involved four different radar systems, two electronic raingauges and one 'sonic' raingauge.

Table 2.1 outlines the ultra-high space and time resolution intensity time series acquired with the VPR. Series A was collected with a 1700 Hz PRF X-band marine transmitter which has a 10 dB noise figure. Series B through G were collected with the VPR using a new (installed 1990) 1300 Hz PRF marine transmitter which has a very linear response with a 4 dB noise figure (see figure 2.3). The ability of the newer radar to represent even the smallest rainrates is remarkable,

its low intensity resolution limit is estimated at -10 dB or roughly 0.01 mm/hr. Both radars are based on magnetrons which are incoherent devices. An incoherent device is one whose phase is random from pulse to pulse[4]. The time series are direct digital recordings of the output of the logarithmic amplifier of the radar set. Pre-processing was avoided. The precipitation events were selected such that the entire time series was collected inside the duration of a rain event. Thus, all time series of echoes were collected from "continuous" precipitation. This collection scheme represents a bias towards stratiform rain events. However, in Montreal, frontal convection is generally associated with large extents of stratiform precipitation which follow. Further, close examination of the vertical records of stratiform precipitation reveal a great deal of embedded convection.

4 The incoherence of the collection device is important since it will be shown in the spectral analysis section that the echo fluctuations are coherent.

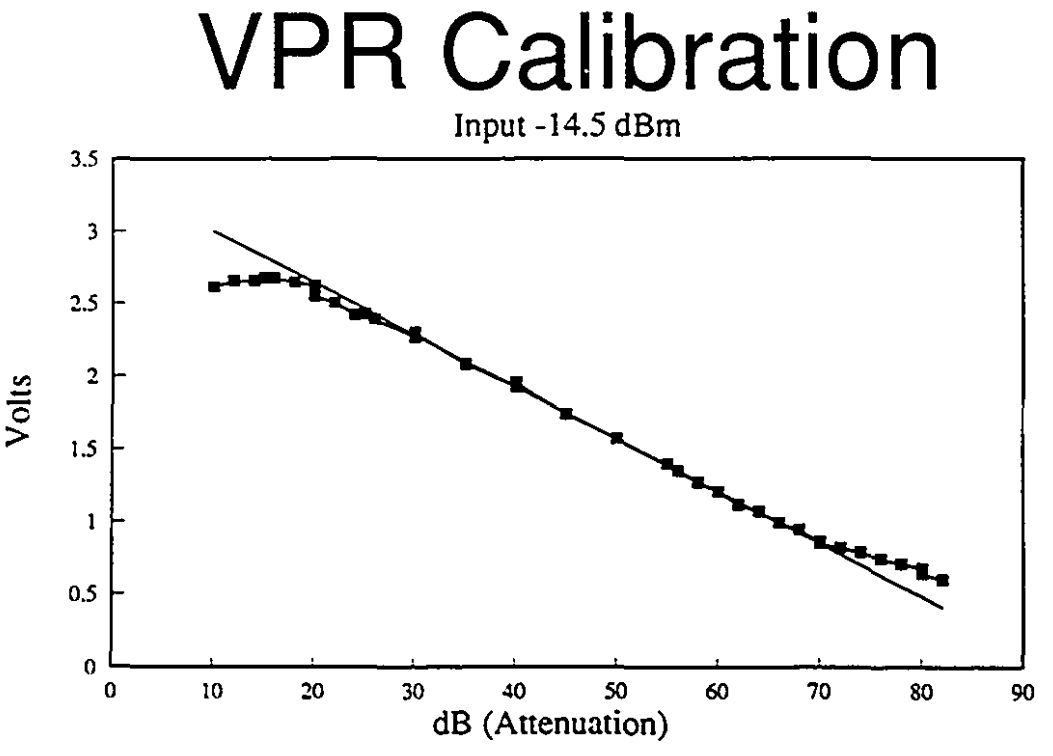

Figure 2.3: Calibration curve for the 1300 PRF transmitter. The linearity of response of the receiver covers nearly 60 dB.

Table 2.1: Radar Echo Fluctuation Time Series Collected with the VPR.						
Series	Precip.	Date	PRF (Hz)	Height (km)	Pulse Volume 1000 m^3	# of Points (× 1024)
A	Convective Rain	19/09/90	1700	1	45	7168
B_1	Convective Rain	26/09/91	1300	1	45	3584
B_2	Convective Rain	26/09/91	1300	1.4	90	3584
C_1	Strat. Rain	23/09/91	1300	1	45	3584
C_2	Strat. Rain	23/09/91	1300	1.4	90	3584
D_1	Strat. Rain	15/10/91	1300	1	45	1792
D_2	Strat. Rain	15/10/91	1300	1.4	90	1792
E_1	Strat. Rain	15/11/91	1300	2.0	183	1792
F_1	Strat. Rain	15/09/91	1300	1.0	45	3584
F_2	Strat. Rain	15/09/91	1300	1.4	90	3584
G	Strat. Rain	20/10/91	1300	1.7	150	1792

The intensity time series detailed in table 2.2 were collected using the X-band and S-band operational radars at MRWO to observe the effect of horizontal incidence (as opposed to vertical incidence). Three collection periods were attempted and the resulting time series are detailed in table 2.2. As with the VPR time series, the collection was from fixed volumes of space in continuous precipitation. Echo time series H was collected with the McGill FPS-18 S-band radar system. The 10 m antenna was used with an elevation angle of 1°. The beamwidth for S-band is 0.86° and for X-band operation the beamwidth is < 0.3°. Ranges and azimuth angles were selected to minimize

ground clutter signals. The noise figure of the S-band radar is very high and is estimated at 17 dB. Echo time series I was collected with the McGill X-band radar through the same antenna and with the same collection strategy using 16 range gates. The noise figure of the X-band system is estimated at 8 dB. Results from series I will be presented as an average of these 16 bins.

Table 2.2: Radar Echo Fluctuation Time Series Collected with Horizontal Pointing Radars

Series	Precip.	Date	PRF (Hz)	Height (km)	Pulse Volume 1000 m^3	# of Points (× 1024)
H_1	Convective Rain	13/03/92	300	< 1.0	6800	1024
H_2	Convective Rain	13/03/92	300	< 1.0	9700	1024
I	Strat. Rain	17/09/91	300	< 1.0	N/A	16 × 256

The VPR system is normally used to make continuous records of vertical rainfield variability. During the summer months of 1992 the VPR was operated continuously. The resulting HTI data set has two second temporal resolution with vertical spatial resolution of 7.5 m (see figure 1.1). Horizontal spatial resolution is a function of height (follows the beamwidth). From these long HTI series it was possible to extract time series of reflectivity at fixed altitude. Table 2.3 details two dependent series, VPR1 and VPR2, extracted from the summer HTI data set. These series contain a continuous record of rainfield variability over the MRWO site for the indicated four month period. The VPR1 and VPR2 time series comprise averages of 512 $Z_{e\lambda}$ values taken every 2 s. Thus, the outer timescale resolvable with VPR1 and VPR2 is several orders of magnitude larger than that of series A through I.

Table 2.3: Time Series of Z_e collected with the VPR.

Series	Dates	Temporal Resolution	PRF	Spatial Resolution
VPR1	July 15, 1992 -> October 11, 1992	2 s	1300	45,000 m^3
VPR2	July 15, 1992 -> October 11, 1992	2 s	1300	90,000 m^3

Supporting Data Sets.

In order to support and aid in quality control of the radar observations, electronic recording raingauges were used to simultaneously sample the rainfield variability. The gauges are known as HYDRAs and are a product of Prof. D. Stow of the University of Auckland in New Zealand. Table 2.4 details the data sets collected by the two HYDRA raingauges located at the radar site (MRWO) and on the McGill campus in downtown Montreal some 40 km away. A limitation of the HYDRAs is that they sample only every 15 s. A further limitation common to all rain measurements is their lack of sensitivity to extremely low rainfall rates. The VPR is sensitive to ~0.01 mm/hr (based on noise figures), the HYDRAs are much less sensitive ~0.5 mm/hr.

Table 2.4: Electronic Gauge Data

Series	Dates/Location	Resolution	Description
HYDRA 1	June, 1992 -> November, 1992 At MRWO	15 s	Counts of fixed size Drops.
HYDRA 2	June, 1992 -> November, 1992 McGill Campus	15 s	Counts of fixed size Drops.

The drop counts produced by the HYDRAs were converted to rainfall rates. Integration of the rainfall rates over storms and over the extended collection period yielded rainfall accumulation estimates in good agreement with local accumulation gauges and radar estimates of rainfall.

Initial spectral plots of the echo time series data revealed a plateau at frequencies higher than 0.2 Hz. A method was conceived to record the variations of intensities of rain to very high frequencies. An analog recording device (a Walkman) was placed beneath a metal plate at the MRWO site and two rainfall events were recorded. The device was termed a 'sonic' gauge. No attempt has, as yet, been made to calibrate the sonic gauge in terms of rain rates. The sound recordings were digitized using the video digitizer employed to collect the radar data. The two time series detailed in Table 3.5 represent simple temporal variations of the sound of rain. The sonic gauge data was introduced in order to overlap the ultra-high time resolution of the VPR data of

table 2.1. The sonic gauge recordings were digitally processed to have 0.1 s time resolution and a total timespan of 45 minutes. The time series can be used to verify the scaling behaviour observed with the radars.

Table 2.5: Sonic Gauge Data		
Series	Date	Sequence length
S_1	August 29, 1992	45 min
S_2	September 3, 1992	45 min

The data sets outlined in this section should be adequate for an initial exploration of the spectral characteristics of the rainfield at the highest resolutions offered by radars and raingauges. The overlapping data collection strategies employed and cross checking of data series limit the possibility of gross data errors.

3.0 Universal Multifractals.

The progression of understanding of the statistical properties of fully developed turbulence has led to a stochastic modelling process known as the multiplicative cascade. Cascades reveal intermittency, extreme variability and scale invariance properties entirely like those found in turbulence. Indeed, the scale invariance found in turbulence, and modelled by cascades, can be found in a large number of other geophysical fields ranging from the rainfield to land surface topography. The justification for cascades is more than skin deep. Cascades embody both the scale invariance permitted by the Navier-Stokes equations as well as the phenomenological 'eddies within eddies' description of turbulence that is currently accepted. The existence of scale invariant or scaling behaviour represents a symmetry of geophysical systems that can be exploited in order to fully characterize the extreme variability of measures acquired from geophysical fields.

Measurement of scale invariant fields leads to measures which are scale dependent. The introduction by most remote sensing devices of one or more scales into the measurement process affects the nature of the measures. This effect can be understood in terms of the averaging ('dressing') of a cascade field. Measures resulting from cascade fields are multifractal. Multifractal formalisms provide a framework within which the scale invariant nature of a measured field can be exploited in order to fully characterize the measured field. It also provides a framework for understanding the extreme inhomogeneity and variability found in most geophysical fields. The study of multifractals is therefore the study of measures resulting from scale invariant fields.

This section constitutes a summary of the concepts of universal multifractals that are used to characterize and model the time series of echo fluctuations. The development will follow that of Schertzer and Lovejoy (1983, 1985, 1987, 1989, 1993a) and Lovejoy and Schertzer (1990a,b, 1991) and will cover results pertinent to the statistical characterization and modelling of time series of radar echo fluctuations. A comprehensive review of multifractal concepts and their application to rain in general can be found in Lovejoy and Schertzer (1993b). The development will also include details of the measurement techniques introduced by Lavallee (1991).

Turbulence Theory: The Roots of Scaling Theories and Cascade Phenomenologies.

Multifractal formalisms are used to describe the behaviours of fluxes of quantities such as turbulent energy in the atmosphere. Fluxes of turbulent energy are increasingly understood in terms of the statistical behaviours of cascade processes. The development of the cascade phenomenology extends at least back to Richardson (1922) and his little poem,

Big whorls have little whorls,
Which feed on their velocity;
And little whorls have lesser whorls,
And so on to viscosity
(in the molecular sense)

which describes a cascade process which carries kinetic energy, as well as passive admixtures, to progressively smaller scales. The work of Kolmogorov (1941) used this conceptual model and showed how a homogeneous cascade of turbulent energy carried by space filling eddies might appear on a spectral representation of velocity fluctuations. Komolgorov (1941) used the term 'universal' to describe the cascade behaviour within the inertial range. This use of the term universal refers to the fact that inertial range cascades are sufficiently far from either the dissipation scale or the scale of introduction of energy that they are free of any influence and always develop according to the symmetries of the governing equations. (The use of the term universal in the description of universal multifractals is in a different sense and the two should not be confused). Kolmogorov (1941) first proposed forms for the distributions of fluctuations based on the assumptions. Namely, the velocity structure functions obey the relation

$$<|\Delta v(L)|^h> \;=\; F_h\left(\frac{\eta_0}{L}\right)(\varepsilon_0 L)^{\frac{h}{3}}, \quad L \ll L_0. \tag{3.1}$$

where L_0 is the outer scale of the turbulent process and F_h is some unknown function whose argument goes to zero for scales significantly larger than the dissipation scale η_0. This assumptions leads directly to the following form of the energy spectrum

$$E(k) \;=\; C\varepsilon_0^{2/3}k^{-5/3} \tag{3.2}$$

for scales sufficiently far from the dissipation scale and outer macroscale L_0. What this prediction suggests is that in the inertial range the transfer of energy is most efficient to adjacent scales. This represents the localness of transfer from one scale to another and embodies the whorls within whorls description of turbulence that has come to be accepted. As work on, and measurements of, turbulent energy dissipation progressed it was realized that the statistics of the homogeneous cascade model were neither extreme enough nor intermittent enough to fully describe the field. Progressive modifications to the theory, Obhukhov (1962) and Kolmogorov (1962) attempted to account for the highly variable nature of the distributions of velocity fluctuations. However, the statistical dependence of the structure functions remained unchanged. It was shown by Anselmet et al. (1984) that the prediction for the velocity fluctuation structure functions breaks down for h > 4. This breakdown suggests a new form for the structure functions,

$$<| \Delta v(L) |^h> \quad \propto \quad L^{\zeta(h)} \tag{3.3}$$

where $\zeta(h)$ is a non-linear function such that $\zeta(h) = h/3$ for $h < 4$ and $\zeta(h) < h/3$ for $h > 4$. It should be noted that the structure functions retain their scaling structure, but not with the exponents predicted by Komolgorov (1941,1962). As the theory of turbulence developed, the spatial information carried by turbulence, namely the intermittency and spatial inhomogeneity of turbulence, became more of a concern. It was realized that turbulence was not homogeneous, but rather, was inhomogeneous. The β-model, introduced by Novikov and Stewart (1964), attempted to provide a conceptual model for the intermittency of turbulence. Frisch et al. (1978) showed how the Kolmogorov (1941, 1962) description could also be applied to the intermittent β-model. Thus began the coupling of spatial description of turbulent intermittency with the statistical nature of the extreme variability of velocity fluctuations. The proposed cascade models have always obeyed the scale invariance suggested by the form of the power spectrum. The governing equations of fluid motions, the Navier-Stokes equations, certainly permit scale invariance and therefore the scale invariant models can be said to respect a symmetry of the governing equations.

Multiplicative Cascades.

The cascade model is predicated on the idea that fluxes, such as turbulent energy or rainfall μ_λ, are concentrated onto progressively smaller volumes without any *a priori* scales. While this does not rule out the possibility that limited samples of a cascade will contain structure (there are structures in figure 3.1) it says that the scales of these structures are not important in an ensemble sense (i.e. the next realization will likely show other scales). It is assumed in a cascade construction that energy is introduced to a system at some large scale L. The energy is then multiplicatively cascaded to progressively smaller scales l. Mathematical details of the α-model construction process can be found in appendix A. The scale ratio $\lambda = L/l$ (we also make use of λ^{-1} to indicate the box scale l) can be used to index the scale of boxes in the current construction step. The range of scales over which this process can be defined is limited only by the outer scale of the field and the 'inner' or dissipation scale. The number of volumes over which the flux is progressively concentrated increases while the volume, identified by its characteristic scale l, decreases. The highest resolution element of a cascade construction is therefore given by Λ^{-1}. At progressive construction stages, indexed by scale ratio λ, the flux density μ_λ becomes more singular. The general measure of singularity of the flux field μ_λ at scale ratio λ is defined by

$$\lambda^{\gamma} = \frac{\int_{\lambda^{-1}} \mu(x)_\lambda d^D x}{\lambda^{-D}} \tag{3.4}$$

where D is the dimension of the space. The singularity γtherefore represents an average or 'dressing' of the flux density over boxes of scale λ^{-1}. The term singularity is used instead of the term intensity to emphasize the fact that for scaling fields intensity is a scale dependent quantity. Thus, intensity can be thought of as singularities integrated over a fixed scale ratio λ. The result of the cascade construction process is that a small number of the volumes will contain a great deal of flux while the rest are close to zero. Thus, the measures of flux μ_λ in the limit $\lambda \rightarrow \infty$ is very singular. The range of singularities available to the system depend on whether a micro-canonical or canonical cascade is being examined. In the case of the micro-canonical cascade the singularities are bounded (i.e. $\gamma_{max} < \infty$). In the case of the canonical cascade the singularities are unbounded (i.e. $\gamma_{max} \rightarrow \infty$ as $\lambda \rightarrow \infty$).

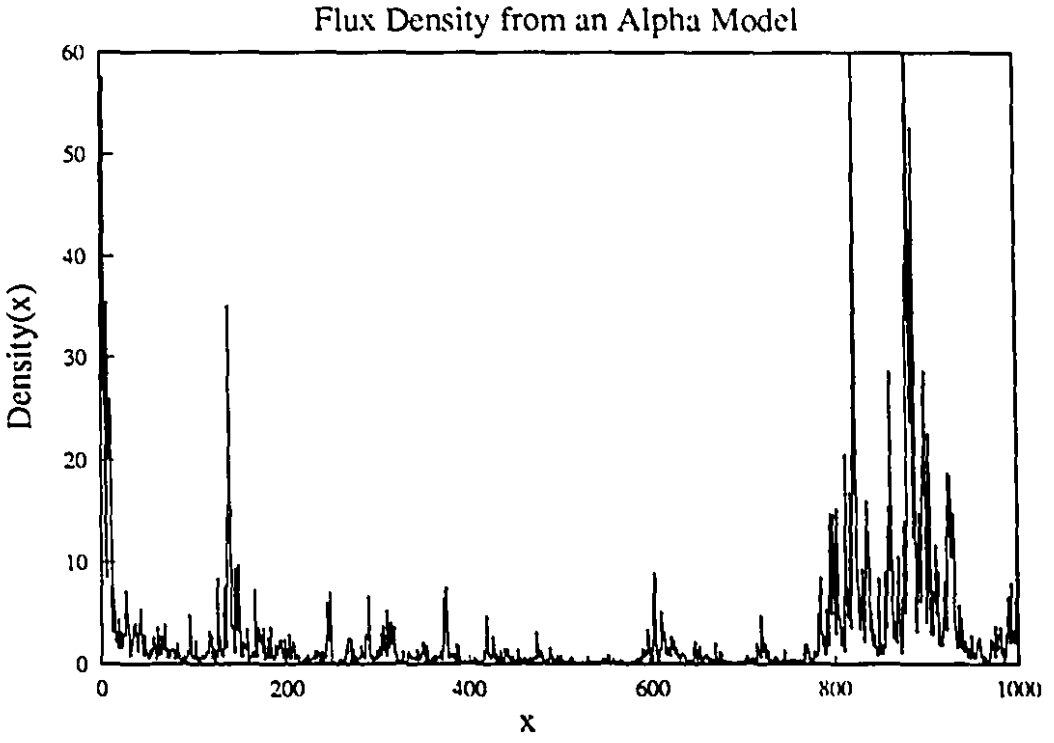

Figure 3.1: Flux density $\mu(x)$ resulting from a cascade model. The scale ratio of this cascade is $\lambda = 1000$, since the inner scale is 1 pixel and the outer scale is 1000 pixels. The singular nature of $\mu(x)$ is intended to reflect the singular nature of atmospheric fields. Measurement of a field such as that depicted here will generally involve averaging over a scale larger than the inner scale and will therefore involve 'dressing' (averaging). If, for instance, we measure this field with a resolution of 4 pixels then our measurement volume B_λ has scale ratio 256 and each of our measures will contain an average of 4 pixels.

The difference between micro-canonical and canonical cascades is non-trivial. A micro-canonical cascade is very restrictive in the sense that flux conservation is guaranteed for each construction step. Thus, each member of an ensemble of micro-canonical cascades obeys strict conservation (i.e. the total density remains constant at every step). The maximum order of singularity that can be achieved with a micro-canonical cascade constructed in a space of dimension D is

$\gamma_{max} = D$. Thus, the singularities are bounded. The micro-canonical α-model is sometimes referred to as the p-model since the probabilities of increase and decreasing are fixed at the outset. The more interesting canonical cascades, or n-state random cascades, have a less stringent flux conservation condition: flux is conserved only in the ensemble. Thus, each member of the ensemble of canonical cascades does not strictly conserve flux. The maximum order of singularity achievable with canonical cascades leads to $\gamma_{max} > D$, which is interpreted to mean that there are extreme singularities that are not seen on all realizations. Thus, there is a distinction between 'calm' micro-canonical multifractals where $\gamma_{max} = D$, and 'wild' canonical multifractals where $\gamma_{max} > D$. Canonical multifractals therefore, necessarily involve the concept of divergence of moments since the singularities γ are unbounded. The remainder of the discussion will deal with canonical cascades since these are better able to represent the extreme variability of rainfall intensity.

Dressing Operations and Bare Cascades.

A 'bare' cascade is defined as a cascade construction terminated at some scale ratio λ. The cascade density field in figure 3.1 is a bare cascade constructed to scale ratio $\lambda = 1000$. Any of the fields generated by the processes described in appendix A will result in bare cascades. As indicated previously a dressed cascade could be constructed from the bare cascade in figure 3.1 simply by averaging (dressing) over boxes of some scale ratio λ. If we consider the small scale limit of the cascade construction process $\lambda \rightarrow \infty$, we find it to be very singular. If we consider $\mu_\lambda \sim \lambda^\gamma$ for all $\gamma > 0$, $\mu_\lambda \rightarrow \infty$ and $< \mu_\lambda^q > = \lambda^{K(q)} \rightarrow \infty$ for all $q > 1$. Therefore, if a limit exists it is not in the sense of functions. Indeed, well defined limits exist only for the fluxes $\Pi_\lambda(B_\lambda) \rightarrow \Pi_\infty(B)$ which are integrals over the flux densities μ: Dressing operations are defined as integrals over the density of flux found in a bare cascade

$$\Pi_\infty(B) = \lim_{\lambda \rightarrow \infty} \Pi_\lambda(B) = \lim_{\lambda \rightarrow \infty} \int_B \mu d^D\vec{x} \qquad (3.5)$$

In order to see why the integration leads to such a drastic calming effect it is necessary to consider the integration of the flux density μ over a ball B_λ embedded in a space of dimension D. Considering a singularity of order γ at the origin yields:

$$\int_{B_\lambda} \frac{1}{|\vec{x}|^\gamma} \sim \int_0^{\lambda^{-1}} \frac{dr r^{D-1}}{r^\gamma} = r^{D-\gamma}\Big|_0^{\lambda^{-1}} = \lambda^{-\alpha_D} \text{ with } \alpha_D = \gamma - D \qquad (3.6)$$

In microcanonical cascades $\gamma < D$ by construction so all singularities can be smoothed out by averaging: $\lambda^{-\alpha_D} \to 0$. However, in canonical cascades singularities $\gamma > D$ are present which cannot be averaged out, so the canonical forms retain their divergent behaviour even under averaging. The singular nature of the limit $\lambda \to \infty$ and the possibility of smoothing out some of the singularities by integration lead Schertzer and Lovejoy (1987) to distinguish between bare and dressed cascades.

The integrating effect of most remote sensing devices over the scales they use for measurement makes the distinction between bare and dressed cascades necessary. Since atmospheric processes will generally carry out a cascade to only a finite scale ratio λ, it is necessary to have a reasonable explanation why statistics compiled from remote sensing devices indicate divergence of moments.

Multifractals: Measures from Scale Invariant Fields.

Multifractals arise when cascade processes concentrate fluxes into progressively smaller and smaller regions. The term multifractal was coined to represent the fact that different intensities or singularities of the flux resulting from a cascade have different fractal dimensions. The measures of cascade fields produced by remote sensing devices are also multifractal. Multifractal formalisms provide a framework within which the scale invariant nature of cascade fields can be exploited to yield a statistical characterization of the field which is independent of scale.

A number of notations for the description of multifractals exist in the literature. The basic elements of multifractal descriptions are embodied in the $(\alpha_D, f_D(\alpha_D), \tau_D(q))$ notation[5] (see e.g. Hentschel and Procaccia, 1983, Parisi and Frisch 1985, Halsey et al, 1986, Meneveau and Sreenivasan, 1989) or the $(\gamma, c(\gamma), K(q))$ notation of Schertzer and Lovejoy (1987). However, the two notations were developed to explore different questions. The $(\alpha_D, f_D(\alpha_D), \tau_D(q))$ notation was intended for low dimensional work in strange attractors. The Schertzer and Lovejoy notation is specifically suited to analysis of geophysical fields where stochastic processes can involve dimensions approaching infinity. The two notations share concepts, but little terminology. For

5 The D subscript is added to show that these measures of dimension depend on the dimension D of space in which the field is embedded.

example, averages over scale l of measures are characterized by exponents α_D in the $(\alpha_D, f_D(\alpha_D))$ notation and by γ in the $(\gamma, c(\gamma))$ notation, where $\alpha_D = D - \gamma$ (D is the dimension of the space). γ is a singularity as is α_D, but $c(\gamma)$ is a codimension function whereas $f_D(\alpha_D)$ is a dimension function. Codimensions are simply defined by $c(\gamma) = D - D(\gamma)$, where $c(\gamma)$ is the codimension, D is the dimension of the embedded space (i.e. for time series D = 1, for CAPPIs D = 2, etc...), and $D(\gamma)$ is the fractal dimension of the space D occupied by singularities exceeding γ. Codimensions are more practical for describing stochastic processes since they remain invariant as the number of dimensions of the systems tends to infinity. $c(\gamma)$ is preferred for the simple reason that as $D \rightarrow \infty$ $c(\gamma)$ is defined while $f_D(\alpha_D)$ is not.

The distribution of intensities γ of the flux μ_λ from a cascade at scale ratio λ for a cascade field is given by (see Schertzer and Lovejoy, 1987),

$$Pr(\mu_\lambda \geq \lambda^\gamma) = \rho(\gamma)\lambda^{-c(\gamma)} \tag{3.7}$$

where μ_λ is the flux averaged over scale λ^{-1}, γ is the singularity (or intensity), $\rho(\gamma)$ is a slowly varying intensity dependent prefactor (which is generally ignored in most developments), and $c(\gamma)$ is a codimension function which depends on the intensity. The codimension function $c(\gamma)$ defines a continuous spectrum of exponents governing the probabilities of various intensities γ of flux μ_λ integrated to some scale ratio λ. $c(\gamma)$ is constrained to be a convex function.

At a fixed scale ratio λ, the probabilities can be estimated as the ratios of the number of structures with singularities $\geq \gamma$ to the total number of structures N_λ. (Recall that a scale ratio λ means that a data set is being dressed over 'boxes' of scale λ^{-1} and therefore the singularity γ represents the average intensity over the box). Thus, the probabilities can be approximated as

$$Pr(\mu_\lambda \geq \lambda^\gamma) \approx N_\lambda(\gamma)/N_\lambda \tag{3.8}$$

Whenever $D \geq c(\gamma)$, $c(\gamma)$ also has a geometrical interpretation. In this case, on almost all realizations $N_\lambda(\gamma) = \lambda^{D(\gamma)}$, where $D(\gamma) = D - c(\gamma)$ and $c(\gamma)$ is the fractal dimension of singularities exceeding some threshold (This relation is central to the 'functional box counting' technique of Lovejoy et al. (1987) to estimate $c(\gamma)$). Thus, different singularities (or intensities) have different fractal dimensions and

the field is multifractal. The case where $c(\gamma) > D$ represents the "hard" singularities that are almost never observed in finite samples but lead to divergence of moments and first order multifractal phase transitions (see below).

The moments of a multifractal are also dependent upon scale. By moments we refer to averages of the quantity of flux within boxes of scale λ^{-1} exponentiated to some power q. The relation for moments is given by

$$< \mu_\lambda^q > \quad \propto \quad \lambda^{K(q)} \tag{3.9}$$

where q is a real valued moment and λ defines the box scale over which μ_λ was averaged. The function K(q) defines a continuum of exponents which characterize the scaling behaviour of μ_λ. The scaling behaviour of moments of μ_λ, or more precisely estimates of K(q), are examined by plotting the averages as a function of scale for different values of q on a log-log graph (see figure 3.3).

There are fairly general conditions under which knowledge of probability distributions is equivalent to knowledge of the moment structure of a field. The relationship between $c(\gamma)$ and K(q) for multifractals was shown by Parisi and Frisch (1985). K(q) and $c(\gamma)$ are a Legendre transform pair,

$$K(q) = \max_{\gamma} (q\gamma - c(\gamma)) \;\; ; \;\; c(\gamma) = \max_{q} (q\gamma - K(q)) \tag{3.10}$$

These equations establish a one-to-one correspondence $q = c'(\gamma)$ and $\gamma = K'(q)$, where prime (') indicates differentiation. Thus, knowledge of the moment structure is equivalent to knowledge of the probability distributions.

The obvious implication of the relations for moments and probabilities presented above are that measures from cascade fields are dependent upon the scale of observation. The scale inavariance or self-similarity of the cascade may be exploited in measurements simply by examining moments computed over different scales to produce functions which are independent of scale and characterize the measures precisely. The functions K(q) and $c(\gamma)$ are scale invariant descriptors of the underlying cascade process and hence characterize the flux μ_λ independent of what scales were used to collect estimates of μ_λ. Such descriptions allow the cross comparison of data sets acquired with different

resolutions from the same cascade field. Indeed, if a field exhibits cascade behaviour the only way to compare measures acquired with different resolution sensors is through the scale invariant functions.

Universal Multifractals and the Generator Γ_λ.

Schertzer and Lovejoy (1987) present an argument relevant to atmospheric mixing processes that gives K(q) and $c(\gamma)$ specific forms. The argument they present suggests that the turbulent mixing of cascades yields other cascades of the same type. Thus, there are stable and attractive classes to which multifractals can belong. The most useful result of this universality assumption is that K(q) and $c(\gamma)$ are dependent upon only two parameters, α and C_1. α is an index to the Levy-Stable distributions used to generate the multiplicative terms in the cascade construction process. C_1 is the codimension of the ensemble mean of the cascade field and is a measure of its sparsity. The forms for K(q) and $c(\gamma)$ are

$$c(\gamma)=\begin{cases} C_1\left(\dfrac{\gamma}{C_1\alpha'}+\dfrac{1}{\alpha}\right)^{\alpha'} & with \quad \dfrac{1}{\alpha'}+\dfrac{1}{\alpha}=1,(\alpha\neq 1,0\le\alpha\le 2) \\ C_1\exp\left(\dfrac{\gamma}{C_1}-1\right) & if \quad \alpha=1 \end{cases} \tag{3.11}$$

$$K(q)=\begin{cases} \dfrac{C_1}{\alpha-1}(q^\alpha-q), & if \quad \alpha\neq 1 \\ C_1 q\ln(q), & \alpha=1 \end{cases} \tag{3.12}$$

(Sometimes, C_1 is mistaken as the support (geometry or dimension of the non-zero densities) of a cascade field).

The 'universal' multifractal formalism is cast in terms of the codimension functions $c(\gamma)$ and K(q) (which has led to the new name 'codimension multifractal formalism', Lovejoy, personal communication, 1993). The parameter α, in relations 3.11 and 3.12, is an index to the class of Levy-Stable distributions to which a given multifractal belongs. The range of possible α values is $0 \le \alpha \le 2$. The special case of $\alpha = 2$ produces a nearly log-normal distribution, which is nearly the same as the log-normal multiscaling models of turbulence proposed by Kolmogorov (1962) and Obhukhov (1962). The $\alpha = 2$ case uses a Gaussian sub-generator (see Appendix A) and will be used for the bulk of the modelling performed in chapters 6 and 7. However, analysis of the fluctuating

echo will reveal that estimates of α can cover the range $1.4 \leq \alpha \leq 2$. Multifractal processes with $1 < \alpha < 2$ have Levy-Stable generators, the case $\alpha = 1$ has multifractal processes with Cauchy generators. These three cases involve "unconditionally hard" multifractals, which means that for some moment q, given by q_D, the moments will diverge. The case $0 < \alpha < 1$ yields multifractal processes with Levy-Stable generators, but these processes have bounded singularities as long as sufficient averaging of the process is involved, which give rise to the term "conditionally hard" multifractal processes. The case $\alpha = 0$ (actually it should be considered as α approaching zero from above) produces a β-model after the turbulence model by Novikov and Stewart (1964).

Universal multifractals have found application in a wide range of fields. Gabriel et al. (1988) provides the first test of universality with empirical data (measurement techniques will be discussed below). Seed (1989) measured α and C_1 using radar data. Universality in turbulent temperature and wind data was found by Schertzer et al. (1991), Schmitt et al. (1991), Kida (1991). Universality has also been found in high energy physics by Brax and Pechanski (1991), Ratti (1991), Ratti et al. (1991), oceanography by Lavallee et al. (1991), land topography by Lavallee et al. (1991), and the low frequency component of the human voice by Lardner et al. (1993). The work by Tessier et al. (1993) reveals universality in cloud radiances measured by satellite, but most important is the documentation of universality in time series of radar echoes down to time scales of seconds (which corresponds to a space scale consistent with the radar resolution volume B_λ with the application of an appropriate velocity).

Universality is embodied in the definition of the multifractal generator Γ_λ. The generator Γ_λ is defined by $\Gamma_\lambda = \ln \mu_\lambda$ and represents a cascade completed to scale ratio λ. Γ_λ is further defined by

$$< \mu_\lambda^q > = < e^{q\Gamma_\lambda} > = e^{K_\lambda(q)} = e^{\ln(\lambda)K(q)} = \lambda^{K(q)} \tag{3.13}$$

Some details of the generator, which is used to produce multifractal noises with specific α and C_1, can be found in Appendix A. The basic result is that generators are additive. Thus, addition of two or more generators results in a generator of the same type

$$\Gamma_{\lambda\lambda'} = T_\lambda \Gamma_{\lambda'} + \Gamma_\lambda \tag{3.14}$$

where $\Gamma_{\lambda'}$ is a cascade developed to scale ratio λ', and T_λ is a scale change operator. The scaling noises defined this way belong to a stable and attractive or 'universal' class.

Sample Size and the Sampling Dimension D_s.

A major feature of multifractal characterizations of variability is the Legendre transform between moments and probability distributions of singularities. Due to this relation, limitations in dynamic range of remote sensing devices, which limits the range of singularities observable, may be described in terms of limitations of accessibility to moments. Sampling strategies play a large role in the estimation of multifractal parameters. Due to the convexity of $c(\gamma)$ larger samples of the same variability invariably hold a wider range of intensities allowing a greater range of statistical moments to be defined. Such relations are defined in terms of the sampling dimension D_s (Schertzer and Lovejoy, 1989). The sampling dimension D_s quantifies the extent to which the probability space is explored. D_s allows us to define the highest singularity γ_s observed on N_s independent realizations of a field.

The maximum singularity γ observed at least once in N_s samples of volume D is defined as γ_s and is approximated by

$$N_s \lambda^D \lambda^{-c(\gamma_s)} \tag{3.15}$$

A sampling dimension D_s can be defined by the number of samples N_s of dimension D by

$$D_s = \frac{\log(N_s)}{\log(\lambda)} \tag{3.16}$$

this allows for the following relation for γ_s

$$c(\gamma_s) \approx D + D_s \tag{3.17}$$

Using the Legendre transform between probabilities and moments ($q_s = c'(\gamma_s)$) defined by relation 3.4 the largest moment that can be reliably estimated from a sample size N_s is

$$q_s = \left(\frac{D + D_s}{C_1}\right)^{\frac{1}{\alpha}} \tag{3.18}$$

q_s represents a sampling limitation to the moments that can be reliably analyzed.

Second Order Multifractal Phase Transitions.

The upper bound of observable singularities γ_s and moments q_s leads to a second order multifractal phase transition (Schertzer et al., 1993). The Legendre transform of $c(\gamma)$ with $\gamma \geq \gamma_s$ leads to a spurious linear form for the exponents K(q) for moments $q > q_s$. $q_s = c'(\gamma_s)$ is the maximum moment that can accurately be estimated given a sample of dimension D_s. The form of $K_s(q)$ is

$$K_s(q) = \gamma_s(q - q_s) + K(q_s), \quad q \geq q_s; K_s(q) = K(q), \quad q \leq q_s \tag{3.19}$$

If we consider that the probability description $(\gamma, c(\gamma))$ is the multifractal analogue of the (energy, entropy) description of standard thermodynamics, then the moment description (q,K(q)) is the analogue of the (inverse temperature, Massieu potential) description. An analogue of the free energy is C(q) = K(q)/(q-1). (Entropy,Massieu potential) and $(c(\gamma),K(q))$ are Lengendre transform pairs. In this analogy the change in $K_s(q)$ from the familiar non-linear behaviour for $q \leq q_s$ to linear behaviour for $q > q_s$ represents a change in the free energy of the system. The corresponding $C_s(q)$ becomes frozen at the value γ_s:

$$\Delta C''(q_s) \equiv C''_s(q_s) - C''(q_s) = \frac{-K''(q_s)}{q_s^{-1}} \tag{3.20}$$

This phase transition causes a spurious saturation in the statistics of measures of a scaling field. The major implication is that if the data set is not large enough then the statistics saturate and no more information can be extracted from the data. This effect makes the measurement of multifractal parameters a delicate matter. Depending on the convexity of $c(\gamma)$ and on the sampling dimension D_s q_s can take on values close to zero.

An important result is that for moments q smaller than q_s the bare and dressed statistical properties of cascades are exactly the same. From a measurement standpoint it is important to keep the phase transition in mind, but below q_s the behaviour of bare and dressed moments are indistinguishable.

The scaling limit of very small moments q is also very important. A high signal-to-noise ratio is required to detect small moments. The moment q can be considered as a microscope which examines the statistical properties of different singularities γ (using the Legendre relation to

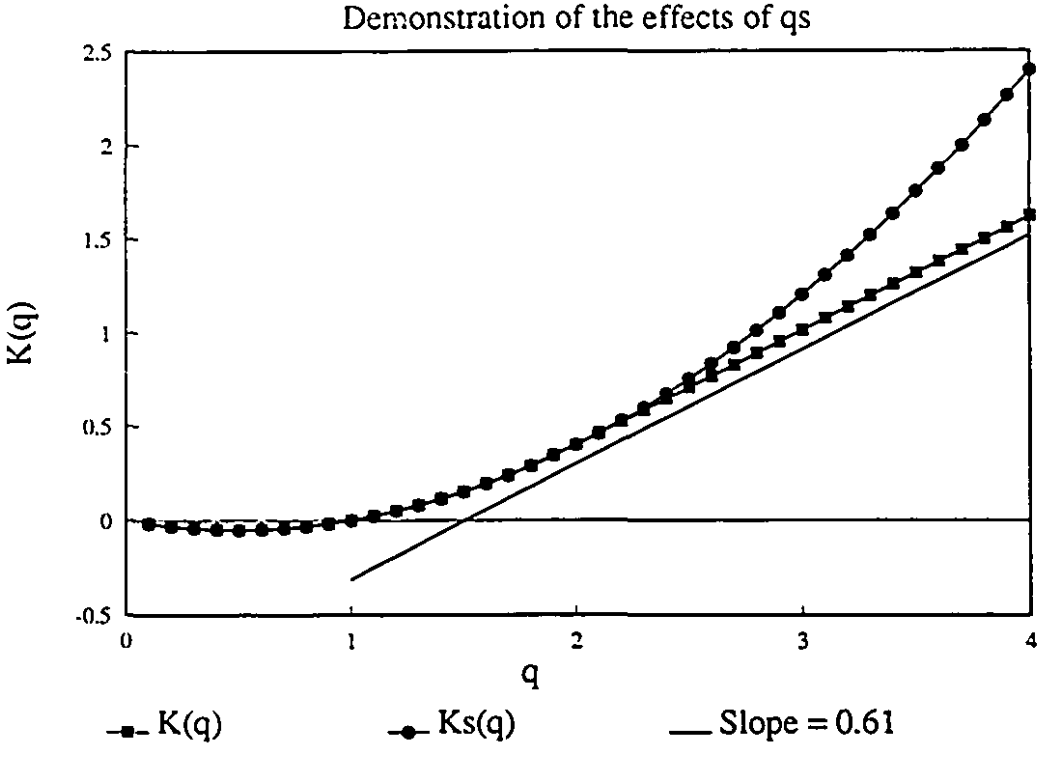

Figure 3.2: Demonstration of the effect of q_s. q_s is 2 for this example. The graph shows how $K_s(q)$ exhibits straight line behaviour beyond q_s and deviates from K(q) near q = 2. The slope of $K_s(q)$ at q values beyond q_s is $\gamma_s = 0.61$ (but this value depends on the α and C_1 of the cascade field). A line of slope 0.61 is plotted for reference.

transform between moments and singularities). Smaller moments examine the behaviour of lower singularities. At some small q the scaling behaviour will be broken because taking low powers kills the extreme singularities and allows the measurement noise (which is space filling C_1=0.0) to dominate. The noise figure of the VPR is very low (sensitivity to 0.01 mm/hr rainrates), as such, it permits very small moments to be defined. Lesser devices affect the range of moments over which the scale invariant function may be investigated.

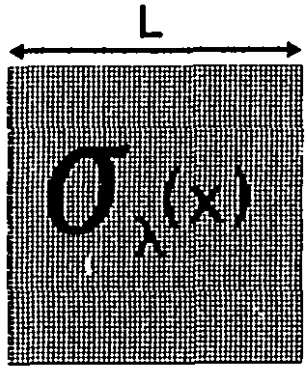

Boxes = 1

$\lambda = (L/l) = 1$

Trace Moments Calculation on Cascade Field $\sigma_\lambda(x)$

$$Tr = \sum_{Boxes} \sum_{Box_i} \sigma_\lambda^q(x) = \lambda^{K(q) - (q-1)D}$$

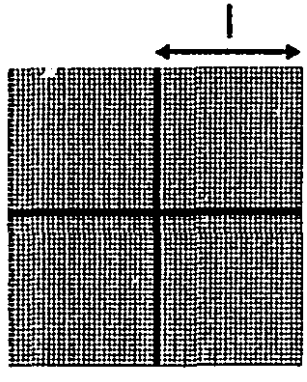

Boxes = 4

$\lambda = 2$

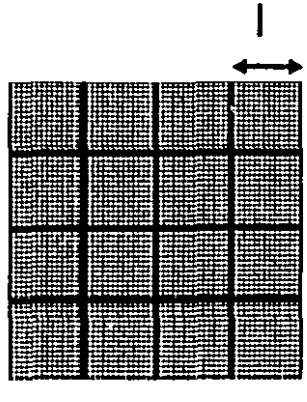

Boxes = 16

$\lambda = 4$

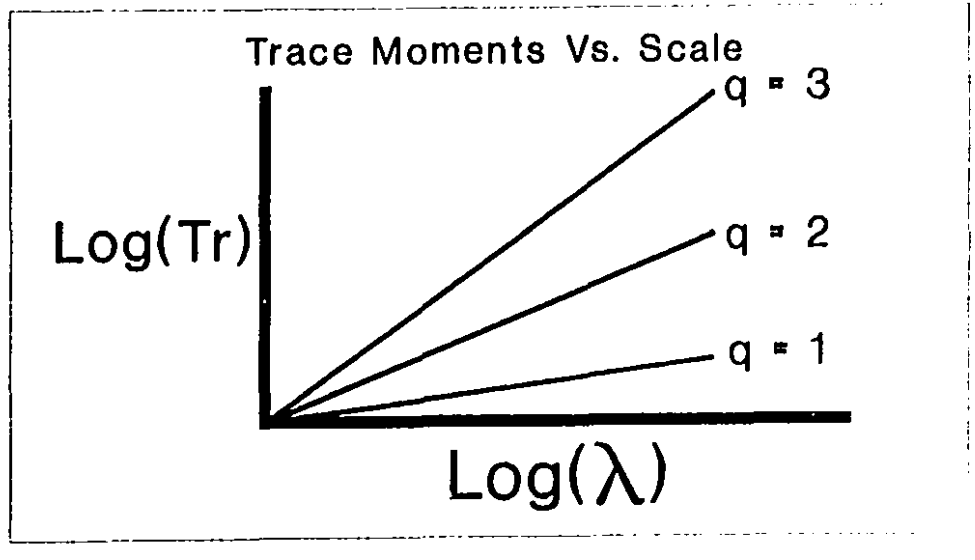

Figure 3.3: The mechanics of the determination of scaling moments and hence the scale invariant function K(q). The notation used here involves sums rather than integrals. The outer scale L remains constant while the inner or averaging scale *l* decreases by factors of 2. Estimates of the slopes of Log(Trace Moments) vs Log(λ) for moment q gives K(q).

A more critical transition in the statistics occurs when q is increased beyond a critical value q_D. The moment q_D corresponds to the divergence of statistical moments beyond which the statistics are no longer defined in terms of smooth functions. In this case the more serious first order multifractal phase transition is encountered. However, if q_s is smaller that q_D then divergence of moments will not be observed. Further, small q_s can lead to erroneous estimates of q_D from histograms. The divergence of statistics is a real phenomenon and necessarily implies fat algebraic tails on distributions of intensity. However, for small samples the singularities responsible for this divergence may not be sampled. The behaviour of the tails of histograms of intensities for small samples may exhibit fat behaviour that is not due to divergence of moments q_D.

Trace Moments: Measurement of α *and* C_1.

The standard techniques used to estimate the moment functions are the partition functions which give $\tau(q)$ (see for example Halsey et al., 1986; Meneveau and Sreenivasan, 1987, 1989; Gupta and Waymire, 1990; Sreenivasan, 1991). The trace moments are used to estimate the function K(q) at points q, and combine the partition function with ensemble averaging (Schertzer and Lovejoy, 1987). Given a cascade developed to scale ratio Λ of the flux μ_Λ, estimates of K(q) can be achieved by examining the log-log behaviour of powers q of the total flux over successive scales λ of averaging. The integrated or total rain flux Π over a box of scale B_λ is given by

$$\Pi_\Lambda(B_\lambda) = \int_{B_\lambda} \mu_\Lambda d^D x \tag{3.21}$$

where D is the dimension over which the integral is computed (i.e. D = 1 for time series data, D = 2 for 2-D data, etc...). The definition of the flux integral only differs from that defining singularity (relation 3.4) by the normalization. $\Pi_\Lambda(B_\lambda)$ simply represents the total flux over some box of scale ratio λ of a cascade developed to scale ratio Λ. The trace moments are then defined as

$$Tr_\lambda(\mu^q) = < \sum_i (\Pi_\Lambda(B_{\lambda,i}))^q > \approx \lambda^{K(q)-(q-1)D} \tag{3.22}$$

where the subscript i indexes the boxes of size B_λ for the sum. Figure 3.3 shows an idealization of the trace moments computation for a scaling field. Estimates of α and C_1 from trace moments are

nearly impossible due to the ill-conditioned non-linear regression required to fit the estimated K(q) to the universal form. Conventional fitting techniques are quickly bogged down by the functional correlation between α and C_1 as well as the difficulties associated with second order phase transitions.

Demonstration of scaling moments and the resulting K(q) function for a multifractal produced by the universal multifractal cascade generator (UMCG) (see appendix A) is presented in figures 3.4 and 3.5. The multifractal field was created with $\alpha = 2$ and $C_1 = 0.1$. Figure 3.4 shows the scaling of the various moments. The intensities were summed over box sizes ranging from 2x2 to 256x256 pixels by integer orders of 2 in scale. Plotting the scaling exponent for each moment q in figure 3.5 gives a realization of the K(q) function (only the first 60 moments are shown). The K(q) function is expected to exhibit straight line behaviour for moments greater than q_D, which for this realization $q_D \sim 4.4$.

The trace moments, and hence the techniques to estimate $\tau(q)$, is actually a very limited estimation technique. The trace moments are adversely affected by either low q_s or q_D. Trace moments are therefore only applicable to data sets large enough (large D_s) or calm enough that convergence of moments is not a problem. The trace moments for $q > \max(q_s, q_D)$ results in a linear dependence of K(q) on q. Consequently, K(q) can be used to estimate q_s and hence γ_s. This considerable limitation to the applicability of trace moments led to the creation of the double trace moments (DTM) by Lavalleé (1991) (see next section).

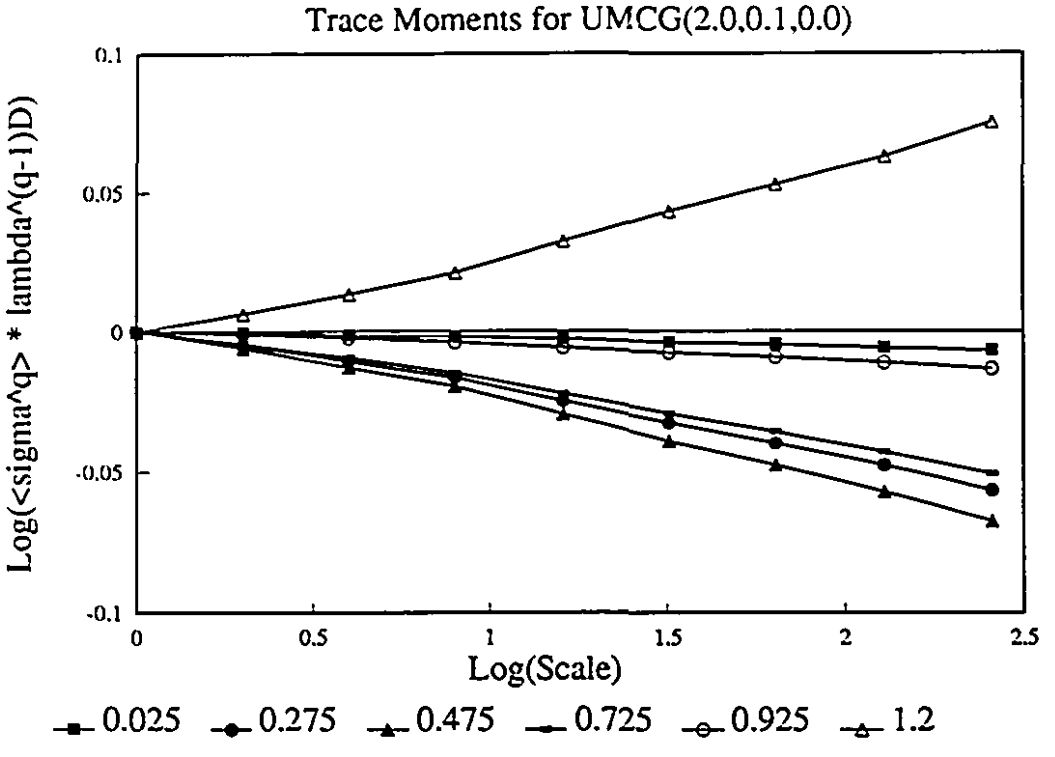

Figure 3.4: Demonstration of scaling moments for a realization of the Universal Multifractal Cascade Generator (UMCG) (see appendix A). The UMCG field was created to produce a multifractal with $\alpha = 2.0$ and $C_1 = 0.1$, the H parameter is set to zero for convenience since it has no effect on the moments. Moments are expected to scale and do so in a convincing manner for this 'artificial' data set. Only six of the 80 scaling moments calculated are shown. The moments q used to compute these curves ranged between 0 and 2 with an interval of 0.025.

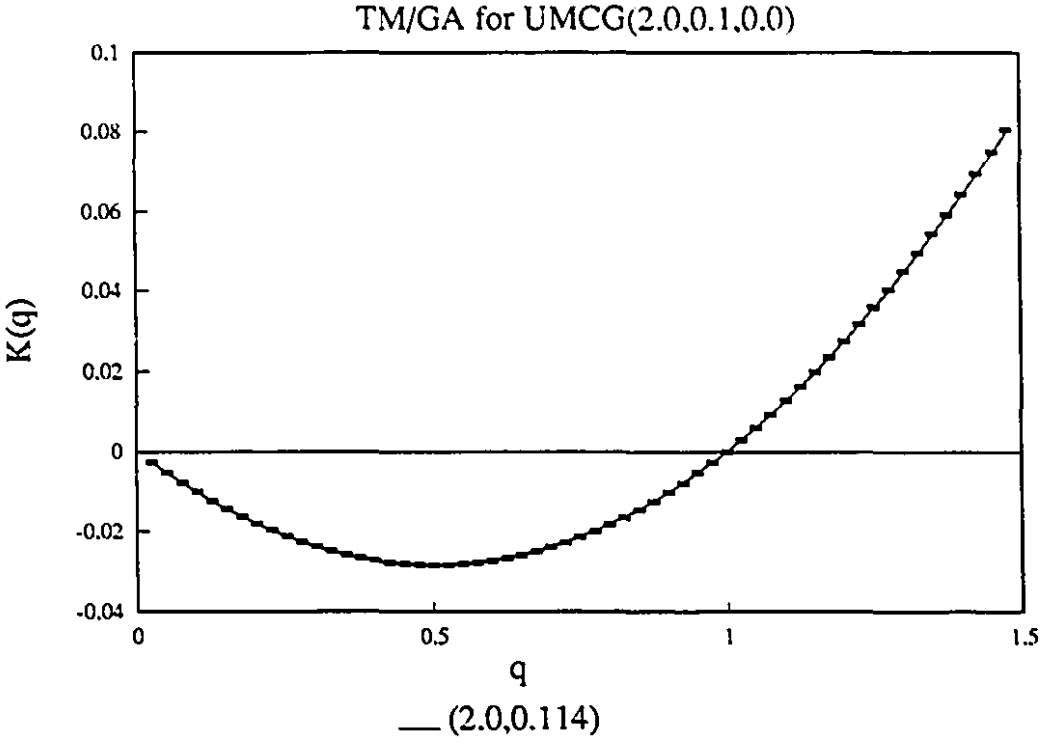

Figure 3.5: Estimate of the function K(q) resulting from the scaling moments in figure 3.4. The points on the curve correspond to estimates of the slopes of the 80 moment curves computed for figure 3.4. The legend gives the α and C_1 parameters estimated from the points using the TM/GA technique (see section 4.1.2).

Double Trace Moments and $K(q,\eta)$.

The double trace moments (DTM) technique was introduced by Lavallee (1991) to directly estimate α and C_1 for universal multifractals. The technique is interesting since it introduces a new exponent into the description of multifractals which is germane to the analysis and discussion of radar echo fluctuation time series. The DTM introduces a second exponent (in addition to q) η by transforming μ into μ^η. This transforms the flux Π into an "η flux" Π^η. The total or integrated flux Π^η is given by

$$\Pi_\lambda^\eta(B_\lambda) = \int_{B_\lambda} \mu_\lambda^\eta d^D x \tag{3.23}$$

The double trace moments are then defined as

$$Tr_\lambda((\mu^\eta)^q) = < \sum_i (\Pi_\lambda^\eta(B_{\lambda,i}))^q > \approx \lambda^{K(q,\eta)-(q-1)D} \tag{3.24}$$

where the double exponent K(q,η) is introduced. K(q,η) reduces to the usual exponent K(q) when η = 1 (i.e. intuitively K(q,1) = K(q)). An example of the utility of K(q,η) is provided by the following example. If the statistics of concentration of water ($= \sum_j V_j$) is known and can be described via K(q) then the statistics of Z ($= \sum_j V_j^2$) can be intuited as being described by K(q,2). The relation between K(q) or K(q,1) and K(q,η) is given by

$$K(q,\eta) = \eta^\alpha K(q,1) = \begin{Bmatrix} \frac{C_1}{\alpha - 1}\eta^\alpha(q^\alpha - q), & \alpha \neq 1 \\ C_1 \eta q \ln(q), & \alpha = 1 \end{Bmatrix} \tag{3.25}$$

Thus, K(q,η) has a simple dependence upon η. This simple dependence on α allows it to be estimated by plotting $|K(q,\eta)|$ Vs η on log-log graph paper and performing a regression on the linear part of the curve. If the $|K(q,\eta)|$ Vs η plotted on log-log graph paper reveals no linear region then the cascade cannot be approximated by a universal multifractal.

The range of η values where universality is expected to hold is dependent upon q_s and/or q_D. K(q,η) will become independent of η whenever max(qη,q) > min(q_s,q_D) (Lavallee, 1991). Since q_D is the exponent above which divergence of moments is expected it is natural to expect the statistical structure to break down beyond this point. q_s is related to the sampling dimension and reveals that samples must be large enough for at least some moments to converge.

The effect of q_s on the DTM is graphically illustrated in figure 3.6. The field being examined in figure 3.6 is the same as that in figure 3.4 and 3.5. The linear behaviour of K(q,η) for q = 1.5

terminates near $\eta = 3$, which is consistent with the estimate of a q_s of 4.4. The estimates of α and C_1 made from the linear region are very close to the input values of $\alpha = 2.0$ and $C_1 = 0.1$ (the difference is due to the stochastic nature of the UMCG generator).

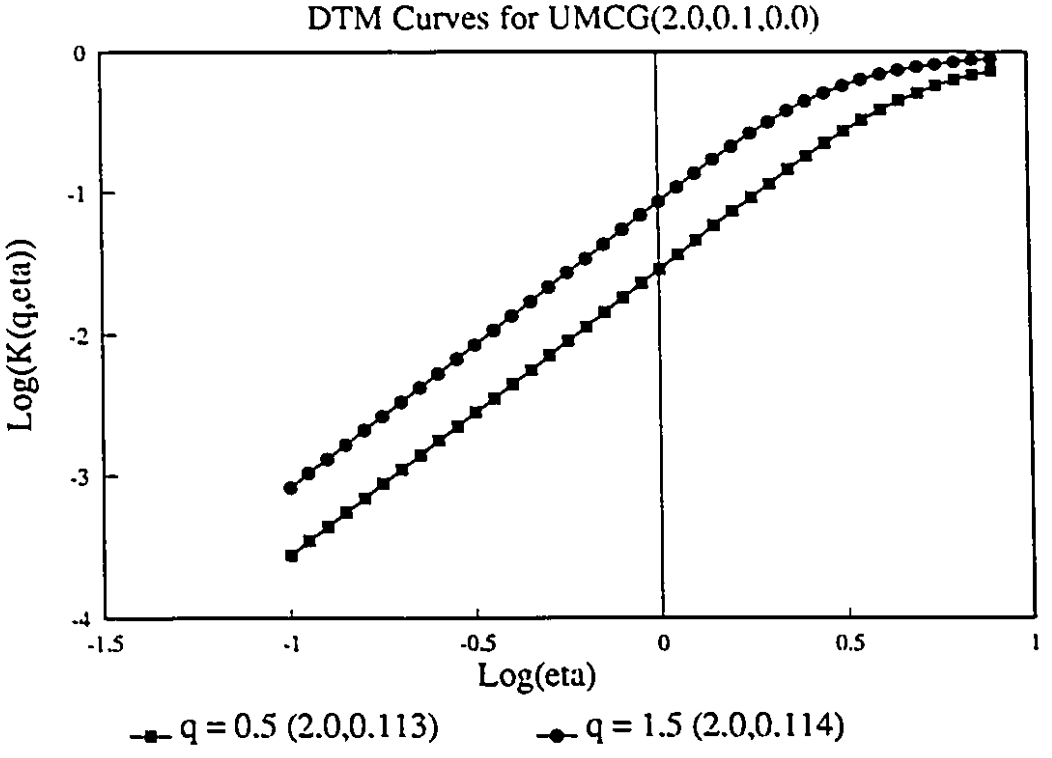

Figure 3.6: Plots of Log(K(q,η)) Vs. Log(η) for the same UMCG field presented in the last section. The two curves represent the two moments q = 0.5 and q = 1.5. Regression of the lines gives estimates of α. The estimates of α and C_1 are given in the legend for the two moments q. The value of q_D is ~2.0 which gives log(η) = 0.5.

Spectral Behaviour of Universal Multifractals.

The power spectrum E(k) can be used to examine the scaling behaviour of universal multifractals. The scaling nature of the cascade construction process guarantees the power law behaviour of the spectrum of the flux and hence localness of transfer of flux in Fourier space. For statistically isotropic scaling fields E(k) will be of the form $k^{-\beta}$ where k is a wavevector modulus and β is the spectral exponent. The relationship between the spectral exponent β and the universal parameters α and C_1 is given by (Lavallee, 1991),

$$\beta = 1 - K(2,\eta) \tag{3.26}$$

The non-conservative nature of a multifractal can be natural, as it is in the case of turbulence or rainfall measures, or it can be the result of signal processing by some remote sensing device. Given a measured multifractal field ρ_λ measured with some remote sensing device, ρ_λ can be considered in the following way (Schertzer and Lovejoy, 1987):

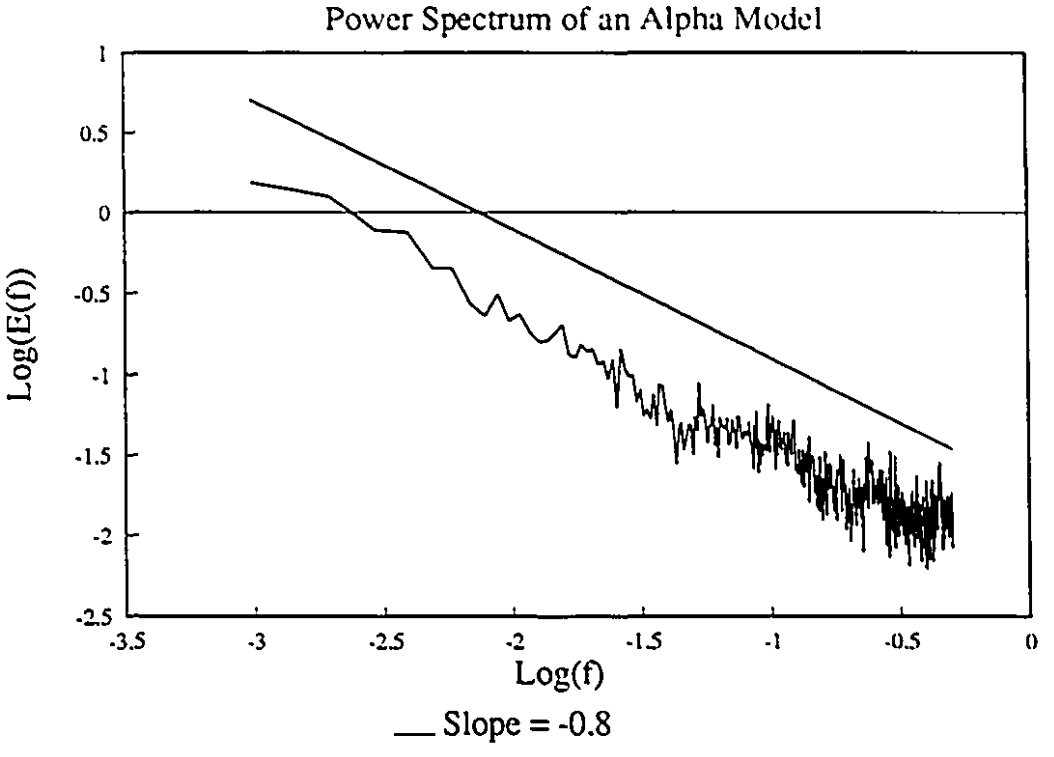

Figure 3.7: Power Spectrum of an α-model created with the UMCG. A straight line of slope 0.8 is plotted for reference. The α-model has $\alpha = 2.0$ and $C_1 = 0.1$ (see figure 3.2). The spectrum is an average of 64 spectra, each of length 1024. The spectral slope can be seen to match closely the expected $\beta = 1 - K(2,1)$, which for $\alpha = 2$ is $\beta = 1 - 2C_1 = 0.8$.

$$\rho_\lambda = \sigma_\lambda \lambda^{-H} \tag{3.27}$$

(with $< \rho_\lambda >= 1$) where σ_λ is a conservative multifractal field characterized by α and C_1, and H is a filtering exponent. In turbulence this relation gives

$$\Delta v(l) \approx \varepsilon_l^{\frac{1}{3}} l^{\frac{1}{3}} \tag{3.28}$$

where ε_l is the density of the energy flux. $\Delta v(l)$ is the characteristics fluctuation in velocity at scale l. The scaling $l^{\frac{1}{3}}$ can be understood as a power law filter. The effect of this filter should be removed to analyze the energy density ε directly. A multifractal field with spectral exponent $\beta > 1$ can be interpreted as the product of some conservative universal multifractal and a filter. Once estimates of α and C_1 have been achieved for a measured field (observing the necessity to fractionally integrate the field), the relation between the various variables is given by (Schertzer and Lovejoy, 1987)

$$H = \frac{\beta - 1}{2} + \frac{C_1(2^{\alpha} - 2)}{2(\alpha - 1)} \tag{3.29}$$

A subtle point concerning the measurement of universal parameters arises due to the non-conservative aspect of most geophysical multifractals. The trace moments and DTM analysis techniques require that the multifractal being measured be conservative. In order to properly measure α and C_1 from, for instance, turbulence data, the data must be fractionally integrated such that $\beta < 1$. This can be accomplished using spectral techniques but under most circumstances a simple differencing operation (i.e. replacing a time series by the differences between adjacent intensities) will serve (see Tessier et al. 1993 for applications in 1D and 2D radar data).

Non-conservative fields such as rainfall intensity which have spectral exponents in excess of 1 can be modelled by employing a spectral filter to the multifractal construction process. The spectral exponent for a filtered, or non-conservative, multifractal is given by (Lavallee, 1991),

$$\beta = 1 + 2H - K(2, \eta) \tag{3.30}$$

where H is the value of the exponent of a power law spectral filter. H can be considered as a third universal multifractal parameter. Figure A.2 which shows the UMCG algorithm shows that the spectral filter is applied after the creation of the universal multifractal. Thus, the statistical characterization of the multifractal is retained (i.e. α and C_1 do not change) but the spectral slope is altered and the field is made non-conservative.

Dressed Cascades, Divergence of Moments and the First Order Multifractal Phase Transition.

The existence of divergence of moments leads to a first order multifractal phase transition (Schertzer et al. 1993). There exists a moment q_D beyond which the statistics will no longer be describable in terms of smooth functions. By definition bare cascades have all of their moments q defined since they are only constructed to finite λ. A dressed cascade (i.e. a cascade produced by dressing a bare canonical cascade) will generally have divergent moments for $q > q_D$ (for a complete argument see Schertzer and Lovejoy, 1987). In terms of the C(q) (= K(q)/(q-1)) function defined above, the behaviour of C(q) will display a jump in slope or a first order phase transition. Multifractal analysis techniques such as DTM will break down for moments greater than q_D. The result that is relevant here is that if q_D is greater than q_s then the analysis will break down for moments greater than q_D otherwise it will break down for moments greater than q_s.

4.0 Spectral Analysis of Rainfield Intensity Time Series.

This chapter is devoted to the examination of the spectral behaviour of time series of the fluctuating echo as well as of the HYDRA data and the sonic gauge data. The objective is to determine the range of scaling. A scaling regime on a power spectrum is indicated by a power-law dependence of the spectral energy on frequency $E(k) \propto k^{-\beta}$, where k is a wavenumber. This chapter also shows the behaviour of distributions of the fluctuating echo. The standard theory predicts that the distribution of intensities from independent scatterers is Rayleigh. Contrary to this expectation the echo fluctuation time series yield distributions of intensity with algebraic tails.

The power spectrum of the return intensity can be expressed as:

$$E_k(\omega) = \frac{1}{2T} \int_{-T}^{T} e^{i\omega\tau} < I(k,0) I(k,\tau) > d\tau \qquad (4.1)$$

The dependence upon wavelength is left as an index since it is anticipated that the statistical behaviour of the intensity time series from a radar will depend upon this measurement scale and hence so will the spectral behaviour. The power spectrum is the Fourier transform of the correlation function of intensities. This follows from the Wiener-Khintchin theorem (using the assumption that I(k,t) is stationary in time). The implementation of fast Fourier transforms (FFTs) makes computation of spectra and examination of spectral behaviour a simple matter (See Press et al. 1992).

4.1 Scaling Spectral Behaviour in the Rainfield.

Before analyzing the high resolution echo fluctuation time series of tables 2.1 and 2.2, the lower resolution time series of VPR1 and the HYDRA data are analyzed to provide a framework into which the analysis of the higher resolution data may be introduced. The spectral characteristics of the rainfield revealed by the HYDRA gauges and the VPR1 time series are shown in figures 4.1, 4.2 and 4.3. Figures 4.1 and 4.2 are spectra formed from the rainfall intensity series collected by the HYDRA gauges. The spectra were formed by averaging several hundred 1024 point spectra (timescales range from 4.3 hours to 15 seconds). The spectral slopes estimated from figures 4.1 and 4.2 are $\beta = -1.5 \pm 0.1$. As mentioned previously, the scaling regime in figure 4.3, that of VPR1,

extends to longer timescales than those of figures 4.1 and 4.2. The scaling range shown by the HYDRA time series have a scaling break at a timescale below 1000 seconds. The spectrum of VPR1 has a scaling range that extends to well beyond 3000 s (or 50 minutes).

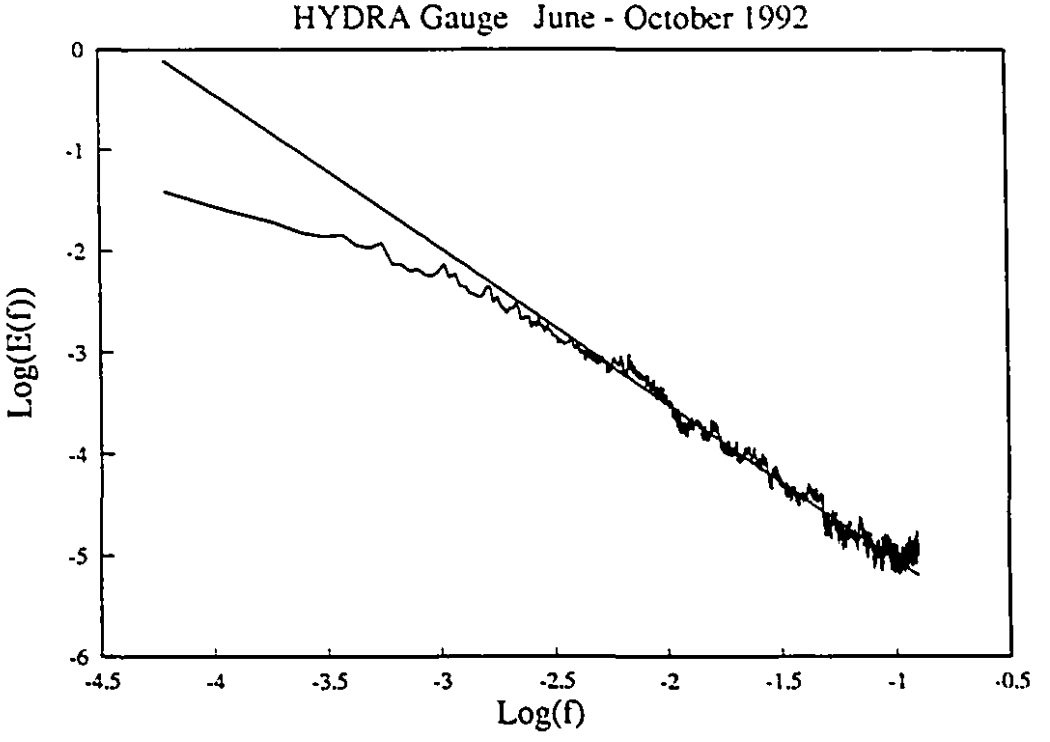

Figure 4.1: Power spectrum of rainfall intensities recorded by HYDRA1. Data resolution is 15 s. The spectrum is an average of 228 4096 point spectra. The spectral slope is estimated at $\beta = -1.5 \pm 0.1$.

Characteristics to be noted in figures 4.1, 4.2 and 4.3 are an obvious break in the scaling behaviour at low frequencies. The reason for this break could be related to the temporal duration of rainfall during the sampling period, but it could also be related to limits of sensitivity in the recording devices. Indeed, comparison of figures 4.1 and 4.2 with figure 4.3 reveals that the low frequency scaling break occurs at different frequencies. Recent work by Lardner et al. (1993) has

shown that the extent of the scaling regime present on a power spectrum is dependent upon the dynamic range of intensities resolved by a data acquisition system. Narrower dynamic ranges will result in smaller scaling ranges. Generally, the loss will be observed as a scaling break at the low frequency end of the spectrum which moves to higher frequencies as the dynamic range is reduced. This result is of interest since the devices, specifically the HYDRAs and the VPR, used to collect rainfall time series for this thesis have very different dynamic ranges. The VPR has a very high signal to noise ratio (SNR) which allows it to resolve rainrates down to ~0.01 mm/hr. The HYDRA gauges have significantly less intensity resolution. The result of these differences is the low frequency scaling break in figures 4.1 and 4.2 for the HYDRA occurs at a timescale of ~700 seconds while that for the VPR in figure 4.3 occurs at a timescale of ~3000 seconds.

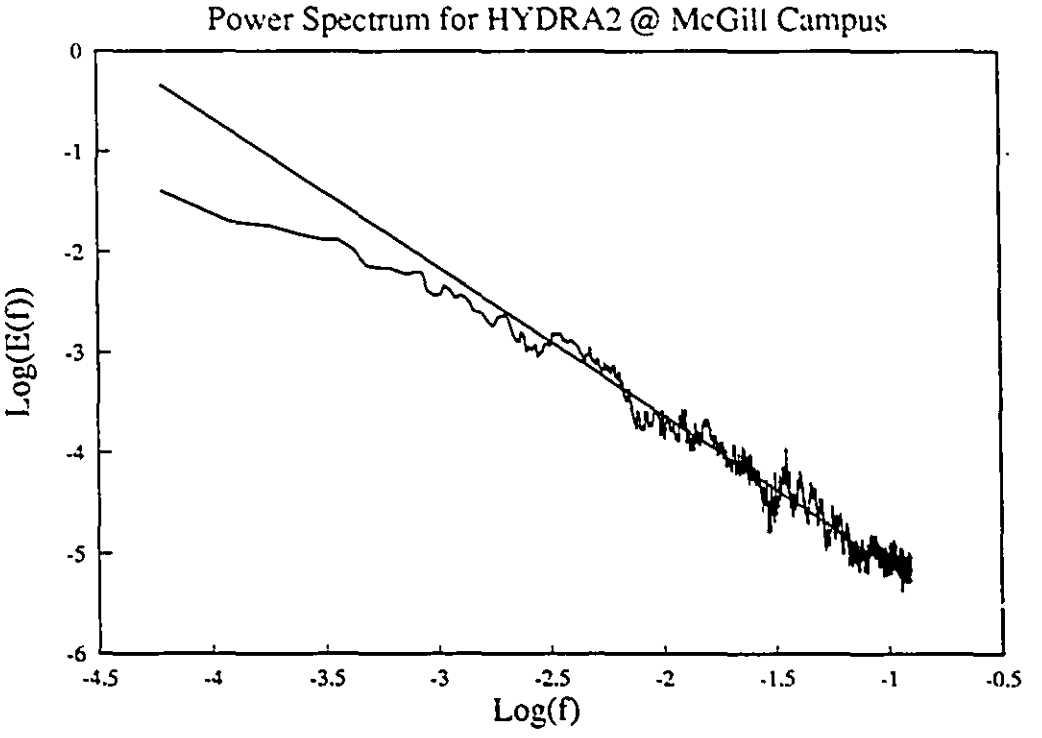

Figure 4.2: Power spectrum of rainfall intensities recorded by HYDRA2. Data resolution is 15 s. The spectrum is an average of 276 4096 point spectra. The spectral slope is estimated at $\beta = 1.5$.

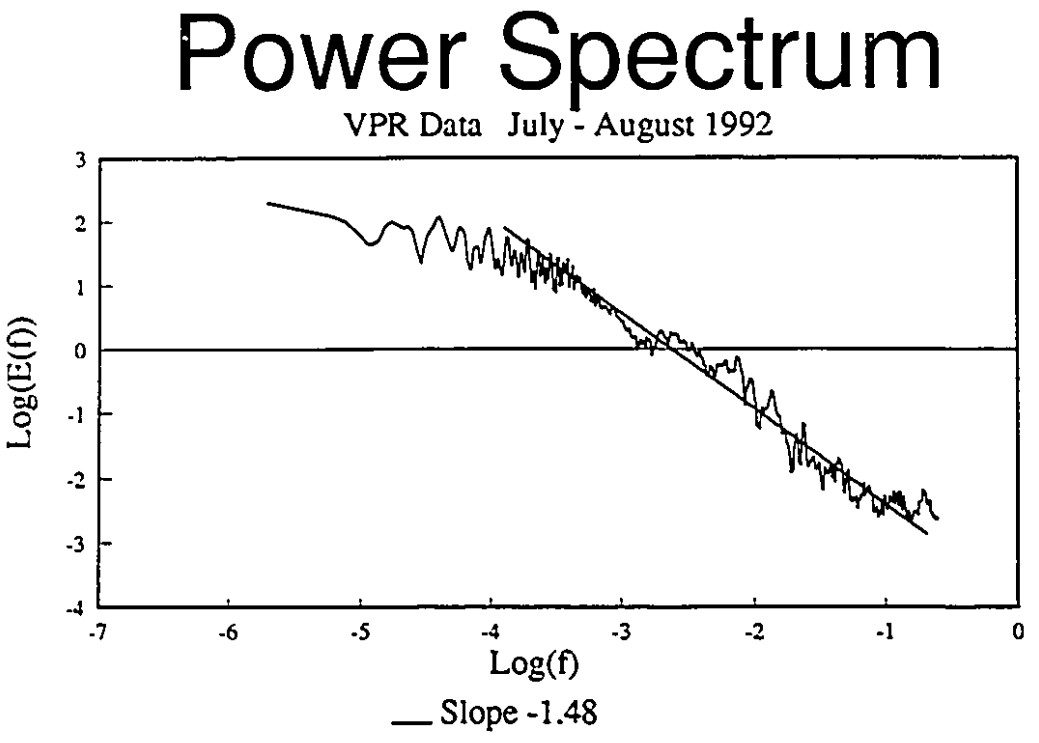

Figure 4.3: Power spectrum of a time series of radar reflectivity intensities from a 2 month sequence of HTI data collected by the vertical pointing radar (Series VPR1). The spectral slope is estimated at $\beta = 1.5$.

Figure 4.3 reveals a plateau at frequencies beyond Log(f) = -0.3 (2 s time resolution). This feature, which extends from second time scales to millisecond timescales, will be examined in detail in the next sub-section. We wish to show here evidence that the plateau is an artifact due to the radar measurement process in the statistics of the fluctuating echo. Series S2 is a sound recording of the intensity of rainfall, however, no attempt has been made to relate the intensity of the sound to rainrate. The scaling behaviour of the spectrum (figure 4.4) extends from 45 minutes to 0.2 seconds, which overlaps the spectral plateau found with the radar data. What the sonic gauge data tells us is that the intensities of sound support scaling behaviour over the entire range

of temporal measurement scales. The lower limit for scaling behaviour in the rainfield is an important issue. Tessier et al. (1993) and figure 4.3 show scaling behaviour to second time resolutions. The sonic gauge is able to show that the scaling extends to time scales smaller than seconds, and therefore to space scales smaller than the resolution scale of the VPR. Scaling power spectra in dynamic fields will occur if there is no preferred scale in the system. There is, therefore, no *a priori* reason why the scaling behaviour shown by the gauge data and the radar data should not extend to very small scales. The fact that the scaling spectrum of S2 is not broken below the scale of the plateau in figure 4.3 strongly suggests that the spectral plateau found in the echo fluctuation time series is a radar measurement artifact.

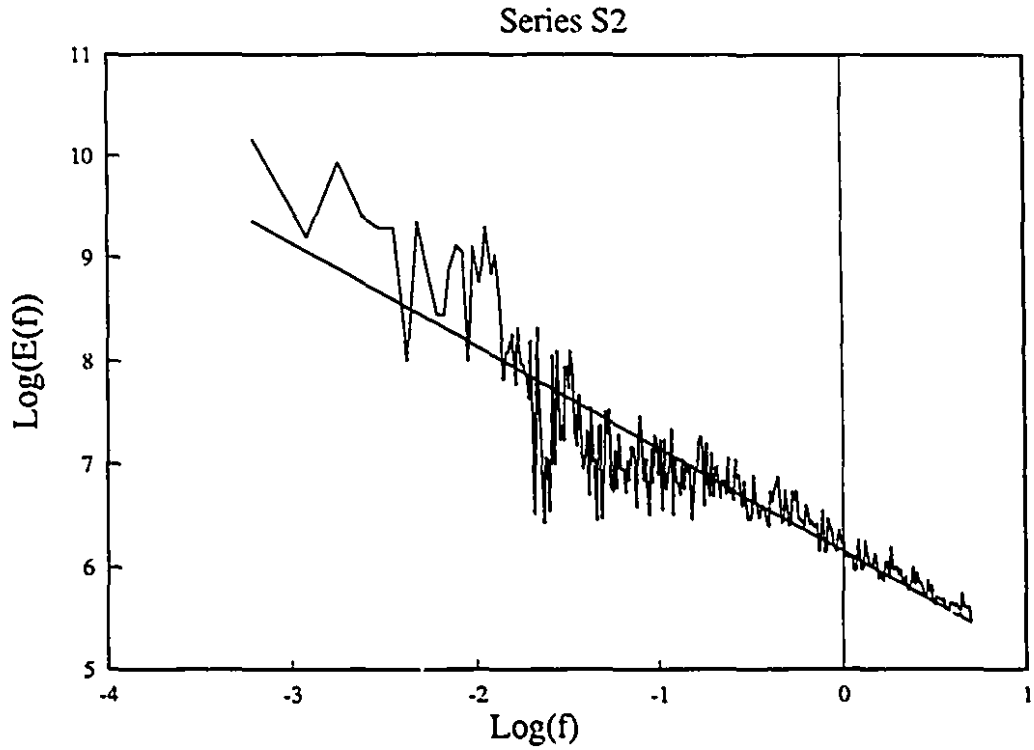

Figure 4.4: Power spectrum of series S2. The spectral slope is estimated at $\beta = 1.3 \pm 0.1$.

Spectral analysis of the various time series of rainfall intensities agree that the rainfield exhibits scaling spectral behaviour to the smallest observable scales with β in the neighborhood of 1.5. The small scale limit of the scaling behaviour present in the VPR1 time series is the same as that shown by Tessier et al. (1993). The spectrum of the rainfield as revealed by VPR1 extends down to timescales of 2 s, which corresponds to a space scale of around 40 m. The spectrum of the sonic gauge time series S2 reveals no plateau at these timescales, but, rather shows a nearly smooth scaling regime from 45 minute time scales to the 0.4 s nyquist resolution limit.

The sonic gauge data supports the notion that rainfield variability exhibits scaling behaviour to very small time/space scales in the rainfield. This is the first indication that sub radar resolution variability has a form which is easily related to the variability at super resolution scales by a simple scale changing operation. Thus, rainfield gradients at large scale are plausibly related in a simple scaling way to gradients at sub-resolution (for the radar) scales.

4.2 Pulse Volume Effect.

The most striking feature common to all power spectra of the ultra-high time resolution intensity time series, figures 4.6a-j, is that there are three distinct regions clearly evident on each spectrum. The longest of the high time resolution time series extends for only 40 minutes (limited by computer resources), as such, it would not be expected to show the 50 minute scale break noticed on the spectrum of VPR1. The immediate implication of the spectra is that there are three distinct statistical regions in the time series, each relating to a specific scale range. The three regions, idealized in figure 4.6, are referred to as (from left to right) the low frequency scaling regime, the plateau and the high frequency scaling regime.

The spectra presented in figures 4.5 represent averages 262144 point spectra. Figure 4.5-a, the spectrum for series A, is an average of 28 262144 point spectra. The number of spectra averaged to produce each figure is directly related to the size of the time series sample.

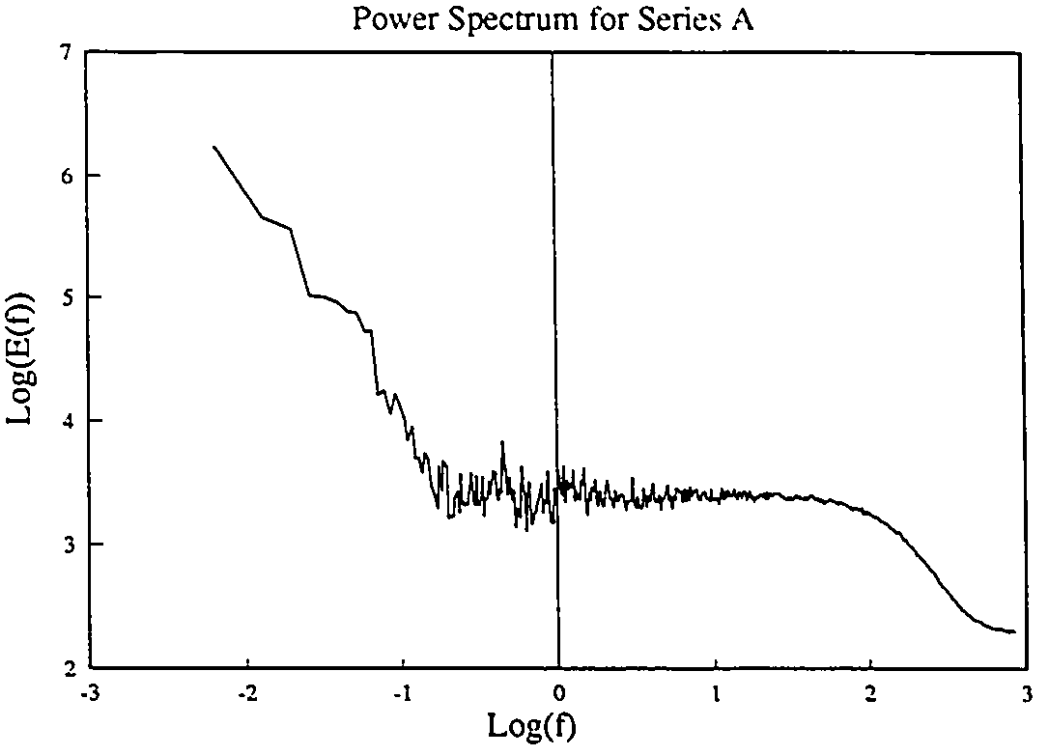

Figure 4.5-a: Power spectrum of series A revealing the characteristic shape of the low frequency scaling regime, the plateau and the high frequency scaling regime.

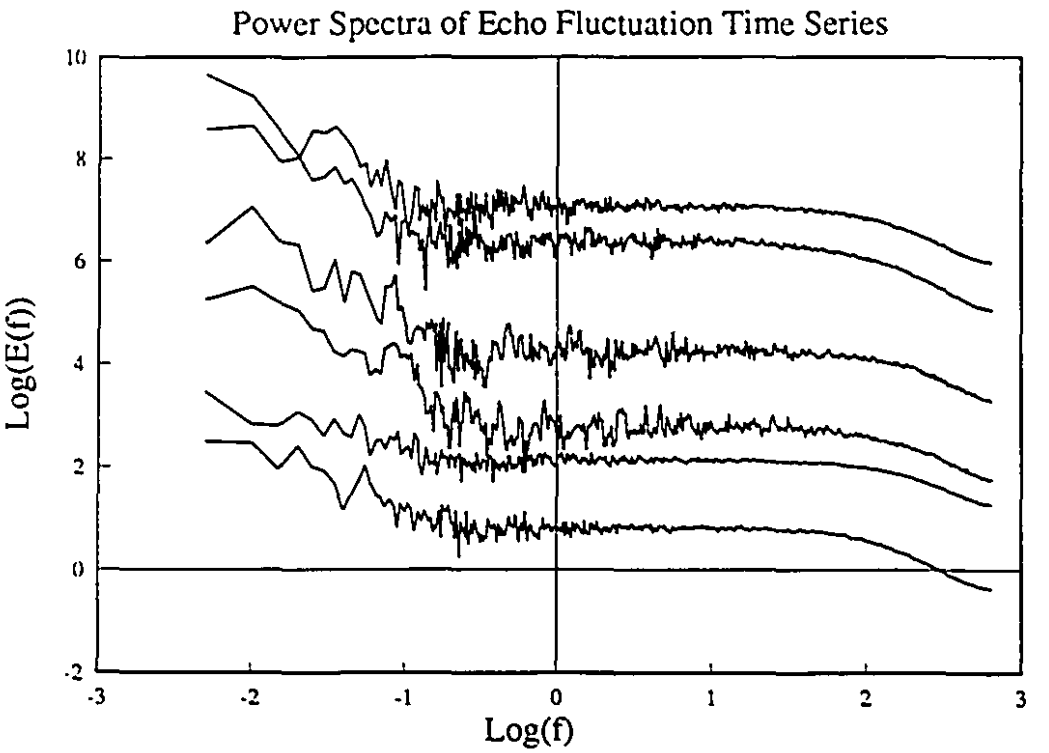

Figure 4.5-b: Power spectrum of series B_1 (Top) through D2 (bottom). A constant is added to each spectrum to space them for comparison purposes. Comparison of the scale breaks shows that the low frequency break separating the plateau from the low frequency scaling regime is consistent from sample to sample. The same is true of the high frequency scaling break.

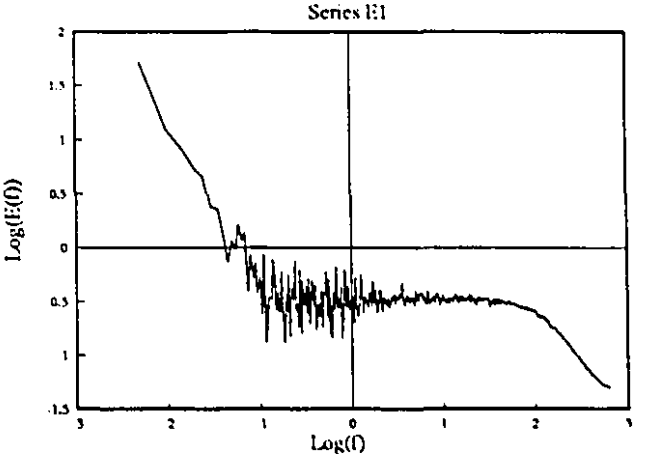

Figure 4.5-c: Power spectrum of series E.

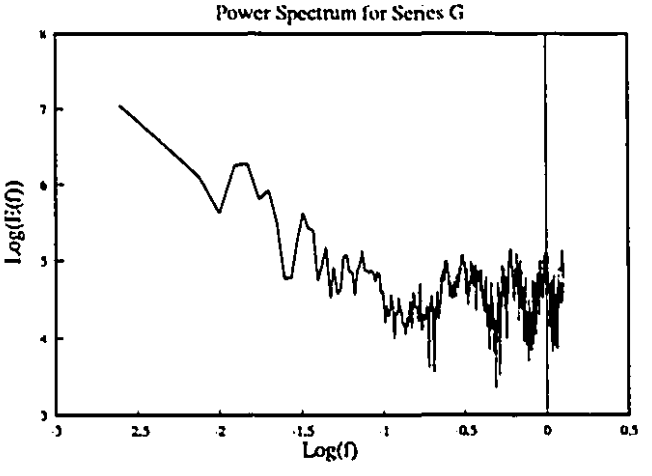

Figure 4.5-d: Power spectrum of series G. Only the low frequency scaling regime and low frequency portion of the plateau are shown.

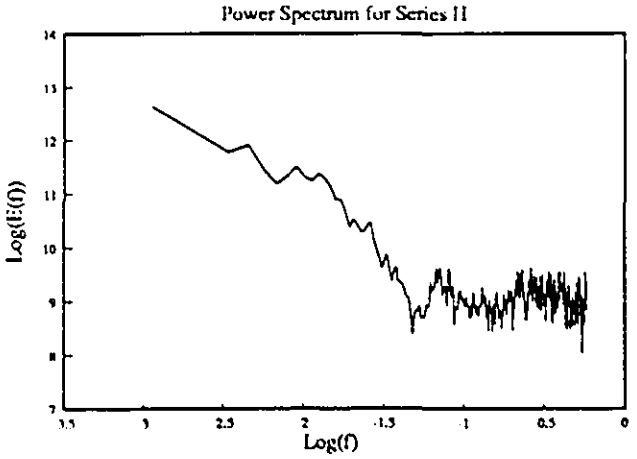

Figure 4.5-e: Power spectrum of series H_1. Only the low frequency scaling regime and low frequency portion of the plateau are shown.

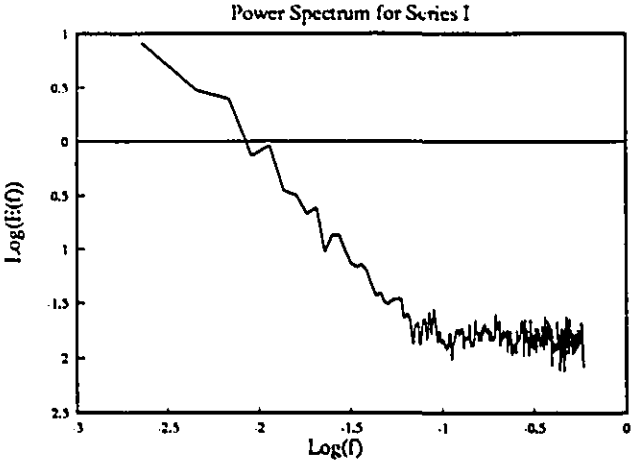

Figure 4.5-f: Power spectrum of series I. Only the low frequency scaling regime and low frequency portion of the plateau are shown.

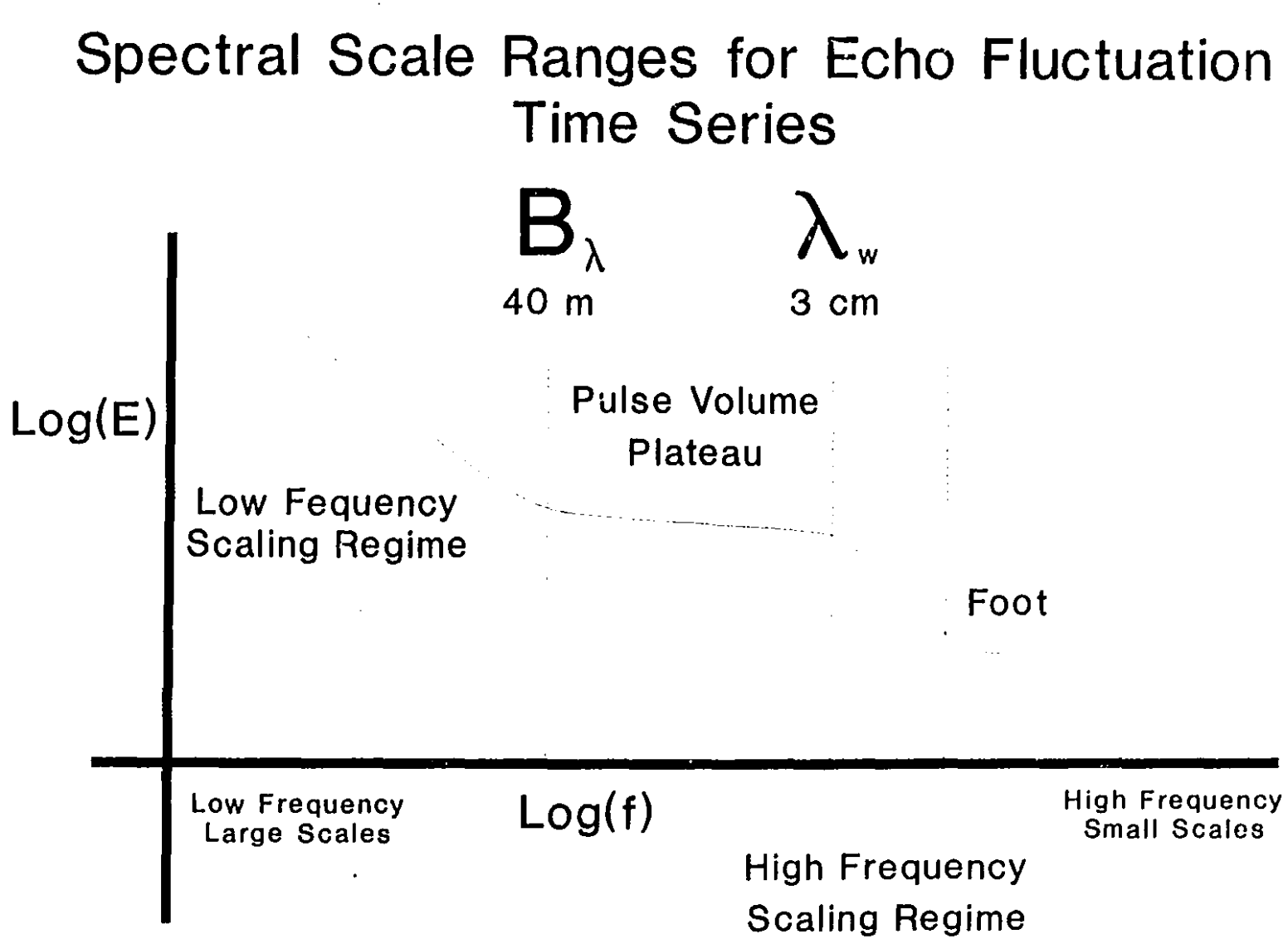

Figure 4.6: An idealization of the power spectrum of time series of echo fluctuations. The low frequency scaling regime, high frequency scaling regime, pulse volume plateau, and the 'foot' are shown.

Crude estimates of the two scales which separate the low frequency scaling regime from the plateau and the plateau from the high frequency scaling regime can be achieved by fitting straight lines to the three spectral regimes. Figures 4.7 and 4.8 show the crude scale estimation procedure applied to the spectrum of series A. Observing the scale at the intersection of the two regression lines and applying a suitable velocity yields an estimate of scale. An advection velocity during the collection of time series A was determined to be 9.0 m/s (velocities were determined by the PPS system located at MRWO, for a description see Duncan et al., 1992). Estimates of the corresponding scales are ~36 m and ~1.0 cm which are very close to the pulse volume and wavelength scales respectively. Table 4.1 contains a complete summary of the application of this procedure to the time series. The column titled **L.F. Scale** is an estimate of the time scale of the low frequency end of the plateau, as the column titled **H.F. Scale** is an estimate of the time scale of the high frequency end of the plateau.

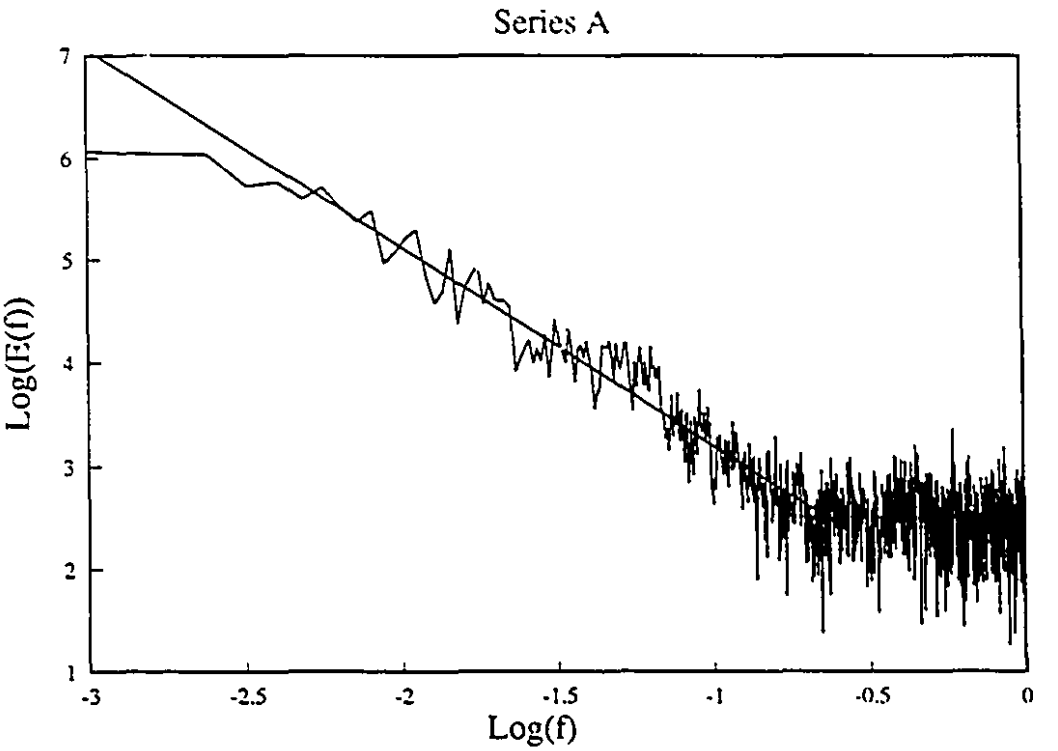

Figure 4.7: Low frequency end of the power spectrum for series A showing the line fitting technique used to estimate the scale separating the plateau from the low frequency scaling regime. The line has slope $\beta = 2$. The figure shows the noise of the spectrum that results in uncertainty of the scale estimates.

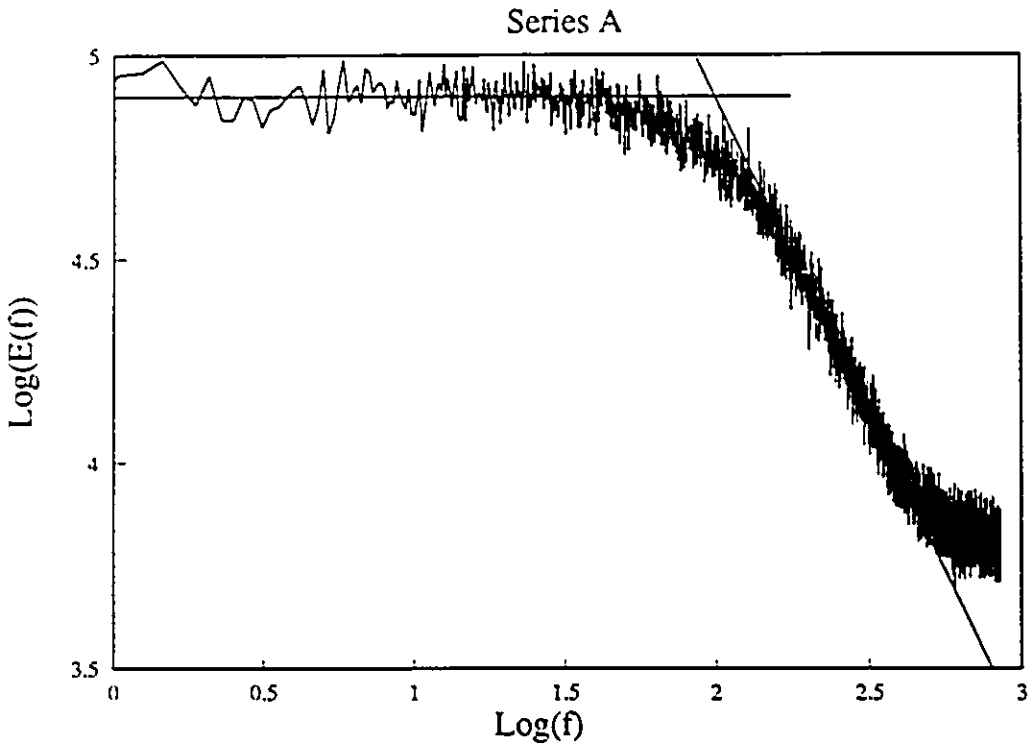

Figure 4.8: High frequency end of the power spectrum for series A. The line has slope β = -1.9. The intersection point of the two fitted lines, one for the plateau and one for the scaling regime, is taken as an estimate for the wavelength scale.

Examination of table 4.1 reveals that the spectral slope of the high frequency scaling regime for series H_1 and H_2 is much different from the other time series. Series H_1 and H_2 were collected from an S-band radar which has a wavelength three times that used to collect the other series. The low frequency spectral slopes of H_1 and H_2 are not significantly different from the other time series.

The low frequency scaling regime is represented on all spectra of echo time series and extends from the longest timescales available with the time series to the pulse volume scale. The existence of the low frequency scaling regime in the spectra of the echo time series is consistent with the spectra of HYDRA1, HYDRA2, VPR1, and that of the sonic gauge. This is the scaling range that

will be used in further analysis. Estimates of the spectral slope β for the low frequency scaling regime are found in table 4.1. Errors quoted in table 4.1 are for the selected fitting range, but additional uncertainty results from the arbitrary decision of which range to apply the fitting. However, the range of values is not too great, thus, the selected fitting range was chosen to maximize the R^2 goodness of fit parameter. The low frequency scaling regimes of time series D_1 and D_2 were of exceptionally poor quality, probably due to the relatively short time series. Indeed, series E is also very short and resulted in a very poor fit. The exceptional quality of the spectra for series F^1 and F^2 (see figures 4.9 and 4.10) contrasts with this poor spectral behaviour. The fitting region for the high frequency scaling regimes was much less than an order of magnitude. As such, the estimates should be treated with appropriate suspicion.

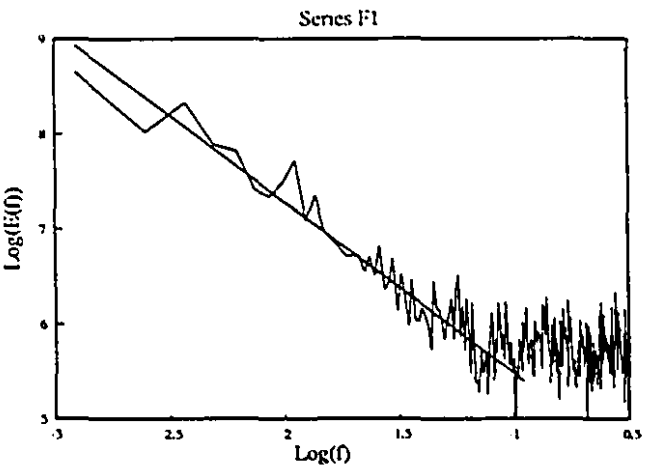

Figure 4.9: Low frequency end of the power spectrum for series F_1. The line has slope β = -1.8.

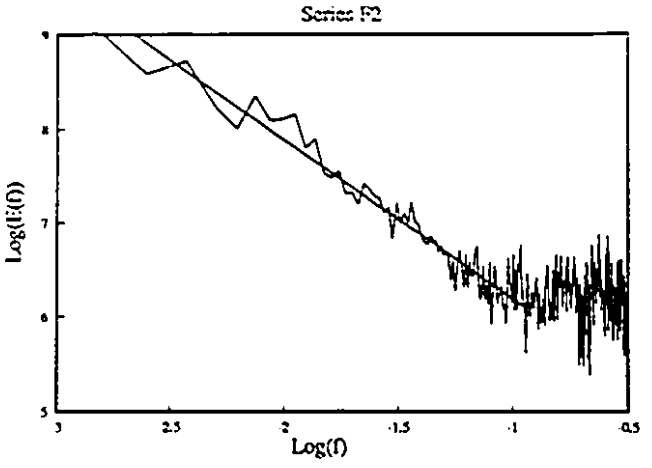

Figure 4.10: Low frequency end of the power spectrum for series F_2. The line has slope β = -1.7.

The spectral parameters estimated from series I are for the average of 16 spectra, each of which is for a time series collected from a different range gate. The averaged spectrum of series I produces an exceptionally good fit with very little error. The spectrum for VPR1 is an average of 928 4096 point spectra (see figure 4.3). 4096 points represents a scale regime of 4 seconds to 2.27 hours. The scale regime used to produce the estimate of β is between 2 seconds and 17 minutes (3 orders of magnitude). The fit is quite good and can be considered a reliable estimate of the ensemble spectral slope.

Table 4.1: Parameters derived from spectral plots of the VPR echo time series					
Series	L.F. Scale	β_{LF}	R^2	H.F. Scale	β_{HF}
A	4 s	2.01 ± 0.04	0.89	0.010 s	1.9
B_1	10 s	1.50 ± 0.10	0.78	0.016 s	0.7
B_2	8 s	1.55 ± 0.08	0.80	0.013 s	1.1
C_1	6 s	1.40 ± 0.12	0.70	0.006 s	0.7
C_2	4 s	1.35 ± 0.07	0.75	0.010 s	0.7
D_1	8 s	0.6	0.45	0.010 s	0.6
D_2	6 s	1.0	0.55	0.013 s	0.8
E	25 s	1.75 ± 0.34	0.65	0.010 s	1.1
F_1	13 s	1.82 ± 0.08	0.90	0.010 s	1.0
F_2	13 s	1.70 ± 0.05	0.95	0.010 s	0.8
G	6 s	1.45 ± 0.08	0.83	0.010 s	1.0
H_1	20 s	2.14 ± 0.09	0.87	0.020 s	4.0
H_2	20 s	1.98 ± 0.14	0.88	0.020 s	4.1
I	13 s	1.86 ± 0.05	0.98	0.032 s	1.3
VPR1	10 s	1.70 ± 0.01	0.97	N/A	N/A
VPR2	10 s	1.68 ± 0.04	0.95	N/A	N/A

The 'foot' region of the spectrum is not well represented on all spectra. The 'foot' shows a transition from the high frequency scaling regime towards white noise. The foot only appears at millisecond timescales or millimeter space scales. In the modelling section it will be shown that this regime can be artificially imposed upon the high frequency scaling behaviour by introducing white noise below the wavelength scale.

The existence of a radar measurement effect has never been displayed before and represents a simple relationship between measurement scales and rainfield variability that will be demonstrated in chapter 7. Its consequences on the statistics of $Z_{e\lambda}$ have never been examined. The sonic gauge data S1 and S2 reveal no spectral plateau, and there is no *a priori* reason that a scale break should exist in the rainfield at 40 m space scales and then at centimeter scales. The only artificial scales present in the problem are the 40 m pulse volume scale B_λ and the wavelength

scale λ_w. The presence of a plateau of limited scale range intermediate to these two artificial scales cannot be simple coincidence. The question as to how the spatial measurement scales of the radar were impressed upon the time series of the fluctuating echo is answerable in terms of drop field that exhibits temporal coherence. The simplest assumption about the nature of the coherence that explains the observations of scaling behaviour is a rainfield that is scaling over a broad range of scales extending from the inner scale of the rainfield to some scale larger than the pulse volume. The inner scale in the rainfield could be of the order of millimeters and would then correspond to turbulent viscosity scales which forms a plausible hypothesis for the 'foot'. The distributions of intensities from a random scaling rainfield have properties much different from homogeneous random fields.

4.3 The Distributions of Intensity.

A generic feature of measurements of fields that display scaling behaviour is that the distributions of intensities display 'fat' tails. However, the ability to observe the pure divergent behaviour of moments is related to whether adequate data is available (i.e. is the sampling dimension D_s high enough to allow q_D to be observed). The value of q_D for rainfall is expected to be in the range of $2 < q_D < 3$ (see the review by Lovejoy and Schertzer, 1993, and Ladoy et al. 1993). If the data set is not large enough then the moment q_s will be found as the maximum moments supported by the data, but there is no stringent reason why this moment should exhibit 'fat' behaviour. A technique that can be used to estimate q_D is the Probability Distribution/Multiple Scaling technique (Lavallee et al. 1991). This technique was used by Seed (1989) (in a very early implementation) to show multiple scaling of radar data and by Ladoy et al (1993) to estimate q_D for an 11 year sequence of daily raingauge totals from Nimes, France. The technique examines the behaviour of histograms of intensity as a function of scale ratio (i.e. outer scale to averaging scale) and tries to show the scale invariance of $c(\gamma)$ from $Pr(\mu > \lambda^{\gamma}) \sim \lambda^{-c(\gamma)}$ by showing $c(\gamma) = -logPr/\log\lambda$ is invariant to averaging scale. However, the technique can suffer greatly from difficulties related to the proper normalization of the statistics by the ensemble mean, which is a very difficult parameter to estimate. The technique is also prone to prefactor oscillations (see relation 3.7). The implementation of PDMS by Seed (1989) simply assumed the prefactors to be unity and proceeded to make estimates of $c(\gamma)$. The existence of the spectral plateau in the time series of the fluctuating echo make the use of PDMS techniques impossible. In addition, the

ensembles are not large enough to properly normalize the distributions. If D_s is small then $q_s < q_D$ and the divergence of moments will not be observed. Given these limitations estimates of q_D are simply taken as the slope of the tail of the distribution, and it should be considered that if the data set is not large enough then linearity of the tail is not expected and q_D will be underestimated.

The comparison of the results for the distributions of intensities presented here and those in the literature of the standard theory is difficult. The difficulty arises due to the very different circumstances under which the various data sets were collected. The evidence provided by Lhermitte and Kessler (1966) of the adherence of the fluctuating echo to the Rayleigh distribution was collected under very different circumstances. Comparison of the linearity of response for the radar used by Lhermitte and Kessler and the VPR (see figure 2.2) shows that the VPR is linear over a much greater range. The perspective is also different, the VPR is vertical incidence while the radar of Lhermitte and Kessler used horizontal incidence. However, the most important differences relate to the scale of the measurement volume used and the sample size. The samples were very small (~10000 points). The data analysis of Lhermitte and Kessler (1966) used pulse volumes of enormous size. Estimates of their smallest pulse volume scale place the beam at 1 km above the surface with a beamwidth of between 3 and 4 km. As pulse volume scale increases the number of data points required to distinguish the extreme events becomes greater. The results of Lhermitte and Kessler, who examine the distributions only to probability levels of 10^{-3}, could therefore be from a scaling rainfield. While this seems a convenient explanation it is in fact a physical reality when dealing with measures of scaling fields.

Fat or algebraic probability tails appear as straight lines on log-log graphs of cumulative probability. The radar intensity time series collected for this study reveal this characteristic behaviour in the range expected for q_D. Figures 4.11a-f show the tail behaviour of the cumulative distributions of intensity for a number of the time series collected. It is immediately apparent that the distributions differ significantly from the Rayleigh form predicted for independent drops. Estimates of the exponents governing the tail behaviour of the cumulative distribution are found via

$$Pr(Z > z) \propto z^{-q_D} \tag{4.2}$$

where q_D is the slope or hyperbolic exponent of the fat tail.

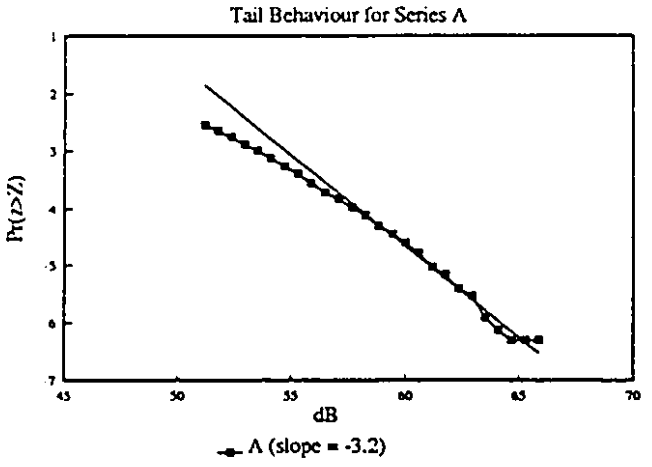

Figure 4.11-a: Asymptotic tail behaviour of the distribution of intensities for echo series A.

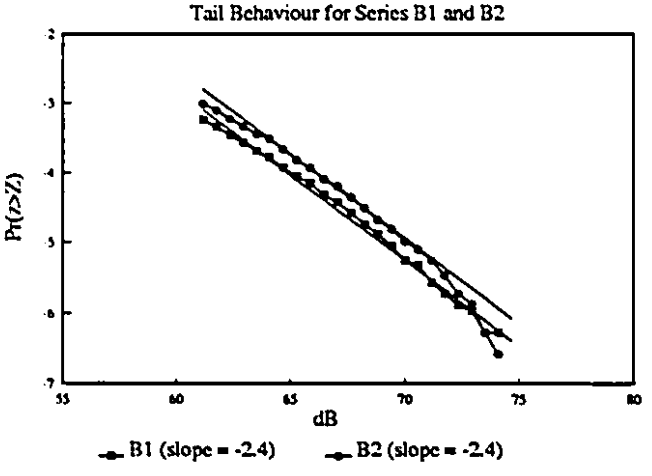

Figure 4.11-b: Asymptotic tail behaviour of the distribution of intensities for echo series B_1 and B_2.

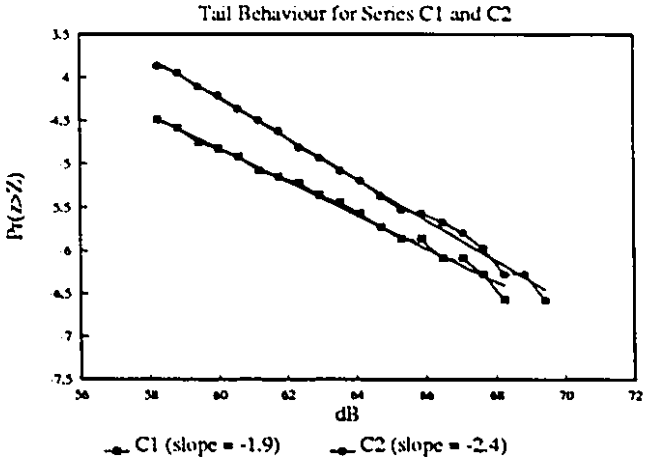

Figure 4.11-c: Asymptotic tail behaviour of the distribution of intensities for echo series C_1 and C_2.

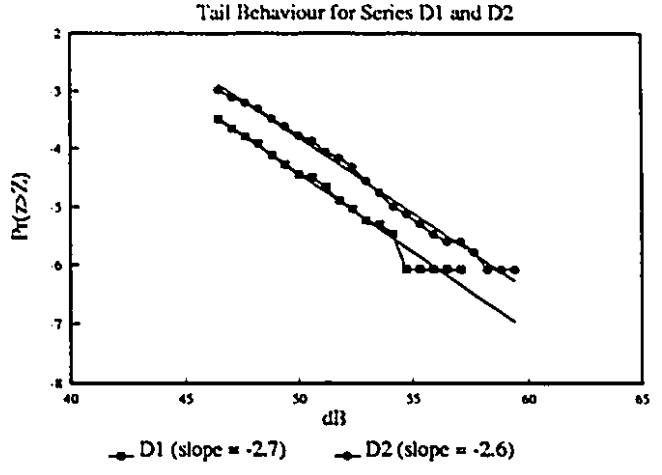

Figure 4.11-d: Asymptotic tail behaviour of the distribution of intensities for echo series D_1 and D_2.

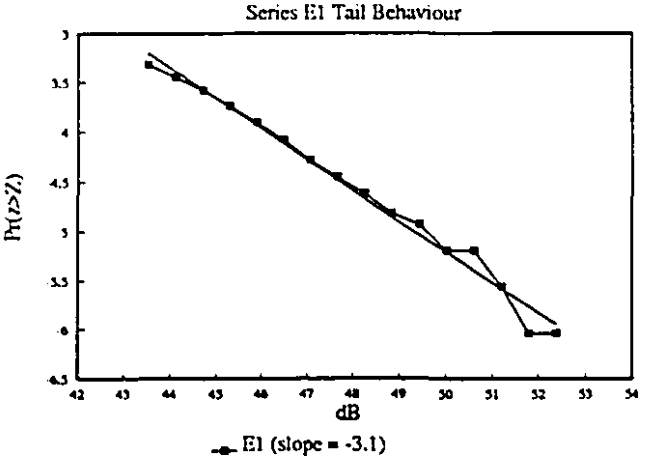

Figure 4.11-e: Asymptotic tail behaviour of the distribution of intensities for echo series E.

Table 4.2 contains estimates of q_D for the time series of the fluctuating echo estimated from figures 4.11. The values fall within the range expected for rainfall (see Ladoy et al., 1993 or Lovejoy and Schertzer, 1993).

Table 4.2: Estimates of q_D for the echo fluctuation time series.

Series	q_D
A	-3.2
B_1	-2.6
B_2	-2.4
C_1	-1.9
C_2	-2.4
D_1	-2.7
D_2	-2.6
E	-3.1

As a graphical demonstration of the scaling properties of histograms of intensities drawn from a scaling field, it will be demonstrated that histograms of the long time series of the fluctuating echo VPR1 have the same general characteristics as histograms from a scaling field. The behaviour of distributions under averaging of a multifractal is very different from that of purely random numbers. Figures 4.12 and 4.13 show histograms resulting from averages over successively large scales of averaging of a field of random numbers and of a scaling field respectively. Figure 4.12 shows how the distribution of intensities of averages of random numbers narrows as the averaging scale is increased. Figure 4.13 shows how the distributions of intensities over longer averaging lengths have a much different behaviour. This property results from the structure of the field and the non-homogeneous distributions of singularities in the field. Thus, while both fields, when averaged over the entire extent of the field, will result in a random variable with a mean of 1, the behaviour of the two with respect to averaging is very different for scales smaller than the outer scale of the field. The averaging over successively longer scales of the scaling regime of VPR1 is shown in figure 4.14. This figure has a great deal in common with the cascade field and little in common with the averaging of random numbers.

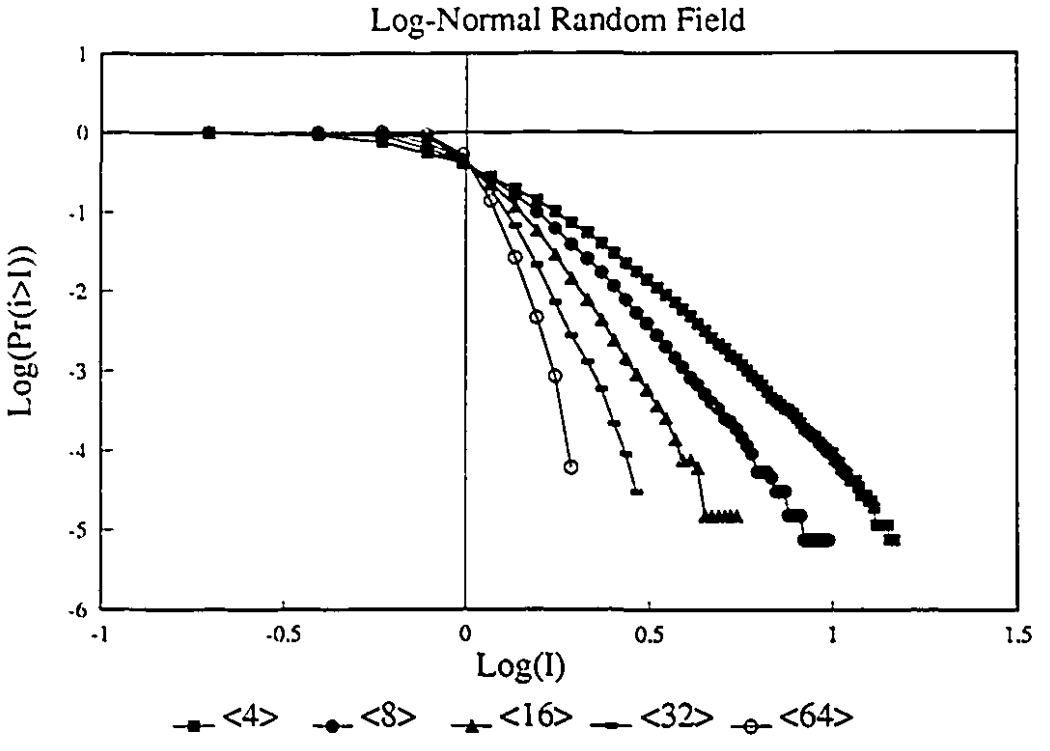

Figure 4.12: The effect of averaging scale on a log-normal random field. Construction of the field was a simple matter of filling a 2-D array with exponentiated N(0,1) numbers.

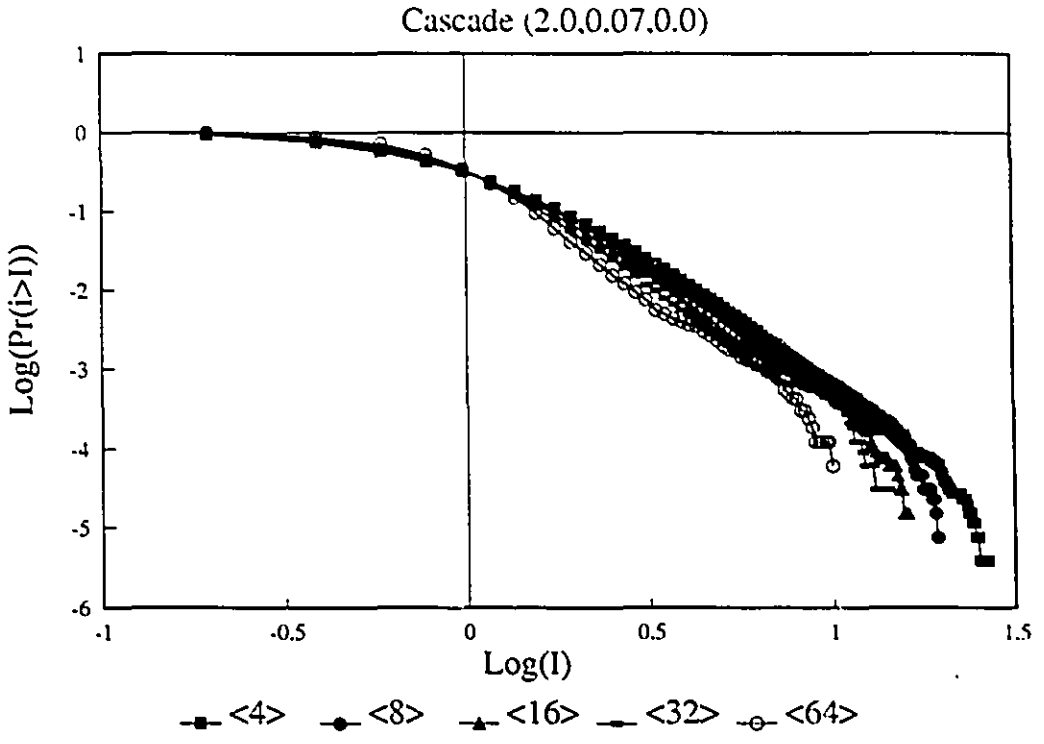

Figure 4.13: The effect of averaging scale on a cascade field. Construction of the cascade field follows the construction process outlined in Appendix B.

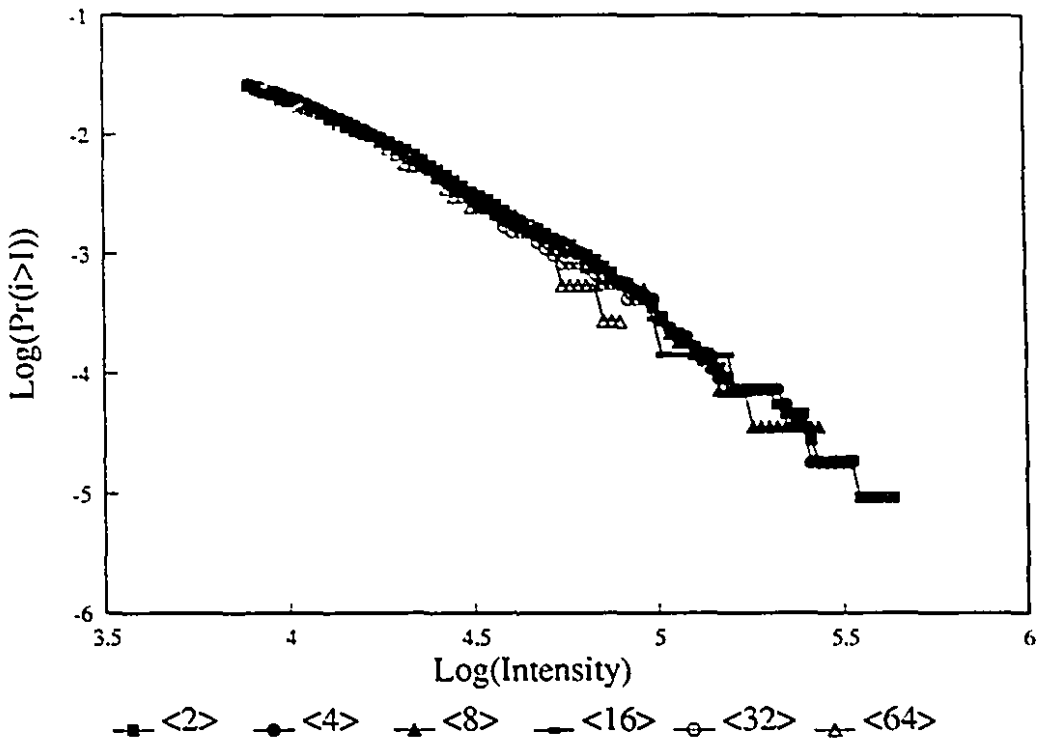

Figure 4.14: The effect of averaging scale on cumulative distributions of intensity for VPR1. Each curve is a histogram of intensities averaged over the scale indicated in the legend (the number in the legend indicates the number of points averaged. Each point represents a 2 s average of intensities).

The effect of averaging scale on the tail behaviour of distributions of intensity from the scaling regime of VPR1 was examined. The averaging scales can be taken as different scale ratios λ. Histograms are computed over the full time series. The behaviour of the curves reflect the invariance of $c(\gamma) = logPr/\log\lambda$ (relation 3.7 but ignoring prefactors) to averaging scale. According to figure 4.3 the histograms of averages of intensities plotted in figure 4.15 come from a scaling regime. The histograms of figure 4.15 suggest power law tails. Estimates of the exponents governing the tail behaviour of the intensities formed by averaging over different scales are given in table 4.3 as a function of the averaging scale. The difficulty in attempting to estimate the

exponents is that progressively larger averaging scales result in progressively fewer points on the histograms. As such, the accuracy of the estimates fall as averaging scale increases. The exponents in table 4.3 are similar to those in table 4.2.

Table 4.3: Estimates of q_D for averages of VPR1.	
Averaging Scale	q_D
4	-2.3
8	-2.3
16	-2.3
32	-2.1
64	-2.0
128	-2.3

5.0 Estimation of Multifractal Parameters.

This chapter is devoted to examining the universal multifractal behaviour of the time series of echo fluctuations. The analysis will concentrate on the low frequency scaling regime as the high frequency scaling regime is not sufficiently long to permit a meaningful analysis. The results of the spectral analysis show a scale break introduced by the pulse volume plateau. This scale break prevents the use of multifractal measurement techniques at scales below B_λ. The objective of the analysis will then be to determine whether the echo fluctuations at scales just above B_λ exhibit universal multifractal behaviour. In the rainfield there is no *a priori* reason why scaling behaviour cannot extend from the outer scale of the storm to the smallest scales of the rainfield. This chapter will first introduce a new multifractal measurement technique and will then employ it, along with the DTM technique, to examine the universal multifractal nature of the echo time series at scales just greater than the resolution scale B_λ.

This chapter consists of three sections. The first section introduces a new measurement technique which is based on the trace moments parameter estimation technique summarized in section 3. The second section investigates a problem relating to the application of multifractal parameter estimation techniques to large data sets such as VPR1. The third section presents the evidence of multiscaling in the echo fluctuation time series and concludes with a table summarizing the estimates of universal multifractal parameters.

5.1 Trace Moments and a Genetic Algorithm.

The trace moments can be used to form a realization of K(q) for a given data set. By making the assumption that the given data set is a realization of a universal multifractal process (which can be verified using DTM), K(q) can be fit to the universal form. The difficulties in optimally fitting K(q) to the universal form are varied. The most important difficulty is that expressed in section 3. K(q) (= K(q,1)) will not be universal if K(q,η) is independent of η at η = 1. If this can be shown to be the case then K(q) cannot be used to reliably estimate α and C_1. If K(q) is in the universal range then the most difficult problem is as follows: the two independent parameters α and C_1 are highly correlated. Also, the minimum, corresponding to the estimate of α, is very broad. In such a situation sophisticated optimization schemes such as gradient search techniques experience great difficulty. The range of α is between 0 and 2. The range of C_1 is between 0 and D (the dimension of the embedded space, for time series D = 1). Small changes in either parameter

results in significant changes in K(q). This sensitivity to the parameters makes the search for an optimal solution more difficult since the precision required is greater and hence the search space is larger. The fitting of K(q) is an ill-conditioned non-linear regression problem.

As an exercise a genetic algorithm was selected to try to solve the problem (see Goldberg, 1989 or Holland, 1992 for a discussion of genetic algorithms). The genetic algorithm is a very powerful heuristic algorithm which chaotically searches a function space for an optimal solution. The optimality of the solution is judged in terms of a fitness function (or goodness of fit function). The fitness function can have any shape over the domain of optimization. Given sufficient information, which is by most standards a very small subset of the search space, the genetic algorithm will find the optimal solution. The beauty of the genetic algorithm is that it is not fooled by local minima and its convergence rate is initially exceptionally fast. Since this thesis is concerned with the statistical behaviour of the fluctuating echo, and not with the development of new artificial intelligence techniques, a brief discussion of genetic algorithm specifics is relegated to appendix C. However, it should be noted that the approach and use of a genetic algorithm in this problem is original.

For a genetic algorithm to work a fitness function which measures the goodness of fit and a one to one transformation for the parameters to the genetic coding are required. The fitness function was taken as the sum of absolute differences between predicted and measured values of K(q)

$$Fitness = \frac{1}{\sum_i | K_e(q_i) - K(q_i) |} \tag{5.1}$$

where $K_e(q)$ is computed using trace moments. A mean absolute difference (MAD) approach was chosen, but a least squares approach also works well. The fitness function is used as an informal measure of the error of the fit. The higher the value of the fitness the better the match between $K_e(q)$ and K(q).

The genetic algorithm uses the fitness function to operate on sequences of 0s and 1s called chromosomes and decide which chromosome is best (see Appendix C for a detailed discussion). In order to make this scheme fit K(q), α and C_1 are coded into chromosomes. Each chromosome is composed of 41 positions or alleles which can be either 1 or 0. This means that each chromosome

can represent a number up to 2^{41}. In order to fit K(q), α is coded into the top 21 positions and C_1 is coded into the bottom 20 positions. Floating point division of α by 2_{20} gives a number between 0 and 2. Floating point division of C_1 by 2^{20} gives a number in the range 0 to 1. This simple one-to-one relation between chromosomes and α and C_1 allows the genetic algorithm to fit K(q) to $K_e(q)$.

5.2 Long Time Series and the Zero Problem.

A difficulty with the application of the multifractal analysis techniques to long rainfall data sets was noted. This difficulty likely affects the majority of results quoted in the literature (see e.g. Tessier et al., 1993). Analysis using TM/GA and DTM of intensity series A through H revealed estimates of α in the range 1.8 to 2.0 while estimates of C_1 were centered around 0.3 (see below). Estimates of these parameters for rainfall in the literature from Seed (1989), reported in Lovejoy and Schertzer (1991,1992), and Tessier et al. (1993) reported α centered on 0.5 and C_1 about 0.6. Up to the time that echo fluctuation series A through F_2 were analyzed consistency demanded that α be around 0.5 and C_1 be around 0.6. Obviously both ranges cannot be simultaneously correct.

The data sets analyzed by Tessier et al. (1993) were re-analyzed. The data used by Tessier et al. (1993) comprise long time sequences of HTI data from the VPR taken during the summer of 1990. These sets are very similar to VPR1 and VPR2. The re-analyzed data revealed the estimates of α and C_1 reported in Tessier et al. (1993) (namely $\alpha = 0.6$ and $C_1 = 0.6$). Analysis of VPR1 and VPR2 in a similar manner yielded estimates of α and C_1 consistent with those in Tessier et al. The appearance of the K(q) function estimated by Tessier et al. (1993) is as shown in figure 5.1 and is the curve noted as 'with zeros'.

The difference between intensity time series A through I and the long time series VPR1 and VPR2 is that the series A through I were recorded in continuous rainfall. Long time sequences such as VPR1 and VPR2, as well as the data used by Tessier et al. (1993), contain subsets of continual rainfall as well as subsets filled partially or entirely with zeros. The recording of intensity time series A through I representa a 'conditional sampling' of the rainfield in order to maximize the number of fluctuating echoes from precipitation. However, parameter estimation using these time series yields results that differ from those of Tessier et al. (1993).

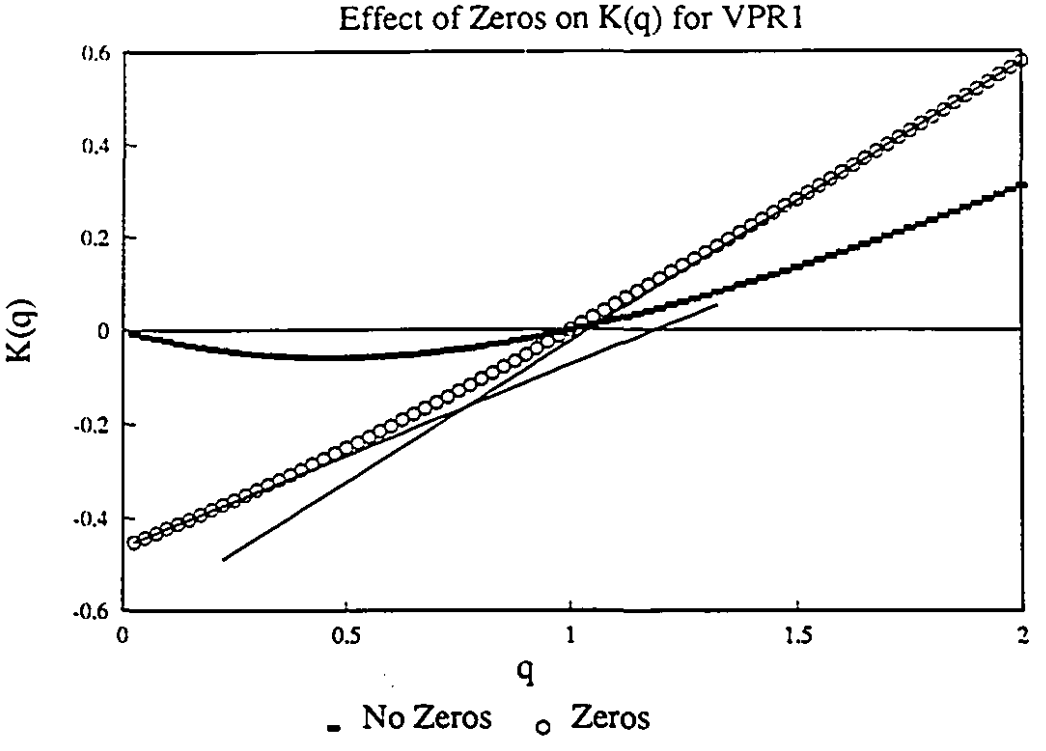

Figure 5.1: The behaviour of K(q) from analysis of VPR1 with zeros and without zeros. The K(q) function without zeros is from subsets conditionally sampled to have no zero rainfall values. The lines fit to the K(q) function with zeros give estimates of $\gamma_{min} = 0.39$ and $\gamma_s = 0.6$. q_{min} is estimated to be ~ 0.2 and $c(\gamma_{min})$ is estimated at 0.46.

Analysis of the long time series VPR1 and VPR2 using a conditional sampling strategy achieved estimates of α and C_1 consistent with those from time series A through I. The conditional sampling strategy accumulated statistics only over subsets of VPR1 and VPR2 which contained no zero rainfall rates. The appearance of the resulting K(q) function is shown in figure 5.1 and is noted as 'without zeros'. The discrepancy between the two estimates has been termed the 'zero

problem'. The conditional sampling approach to dealing with the zero problem is not very satisfactory. Conditional sampling, in this context, represents a 'quick fix' for a complicated behaviour that bears further examination.

The existence of zeros within a data set has at least two possible explanations. The first is that the rainfall rate is very small but not zero and the zero problem is due to threshold limitations of the instrumentation (i.e. a typical raingauge has a dynamical range of 3 orders of magnitude in intensity while a radar typically has 6 or 7). The other possibility is that the rainfall rate is exactly zero. The first assumption allows for the possibility that the rainfall field is finite over all space. The second assumption limits rainfall to a fractal subset. The first assumption allows a single, continuous multifractal model of rainfall. The second assumption forces a two step model, a model of the spatial distribution of non zero rain areas and then a multifractal model of the rain intensities. This question will no doubt be pursued further at a later date.

5.3 Results

In this sub-section the results of the analysis of universal multifractal behaviour of the echo fluctuation time series is examined. Echo fluctuation time series A through G, VPR_1, and VPR_2 were examined. The first section presents some examples of the scaling behaviour of the echo fluctuation time series. The following section presents a gallery of K(q) and K(q,η) functions revealing that the behaviours are consistently observed. The final section contains the tabulated estimates of α and C_1 as well as a discussion of uncertainties in the estimates.

5.3.1 Multiscaling of Moments of Z_ε.

The measurement of multiscaling behaviour to scales down to the pulse volume scale will provide adequate evidence that multiscaling models represent an adequate mode for sub-resolution variability. It must be considered that the pulse volume scale employed by the VPR is much smaller than the resolution scales used for most operational radars with operational ranges that extend up to hundreds of kilometers. Access to the scaling information in the intensity time series is obscured by the existence of the pulse volume plateau which introduces a scale break. The effect of this scaling break is evident in figure 5.2. The scale break can be avoided by averaging the data over 16 s timescales. In the case of series B_1, however, the scale break serves to decrease the available range of scales to the extent that the estimation of multifractal

parameters becomes very poor (see below). Where scale breaks were encountered at short timescales increased averaging scales were used to produce scaling moments with no scaling breaks.

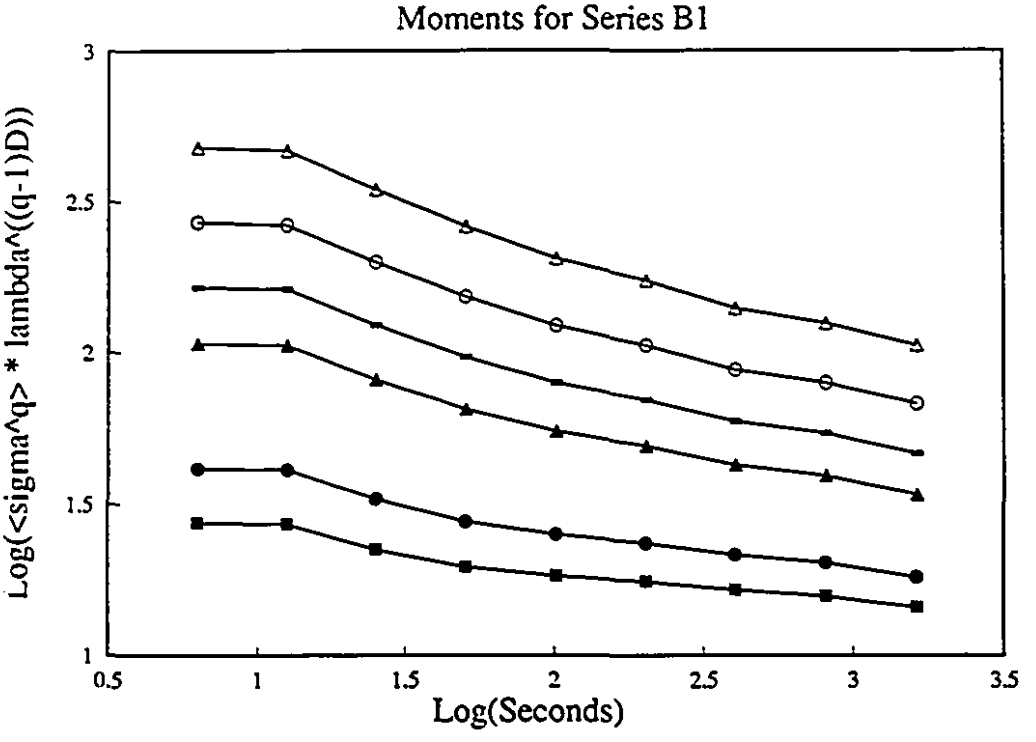

Figure 5.2: Computed moments for series B_1. The scaling break at short timescales can be removed by averaging the data over longer timescales.

Before estimates of multifractal parameters can be attempted the data must be shown to respect multiple scaling. The low frequency scaling ranges identified in section 3 were the target ranges for application of trace moments and DTM techniques. The range where scaling of moments could be expected to hold was revealed, by the spectral analysis, to be between 3000 s and 2 s (a factor of 1500).

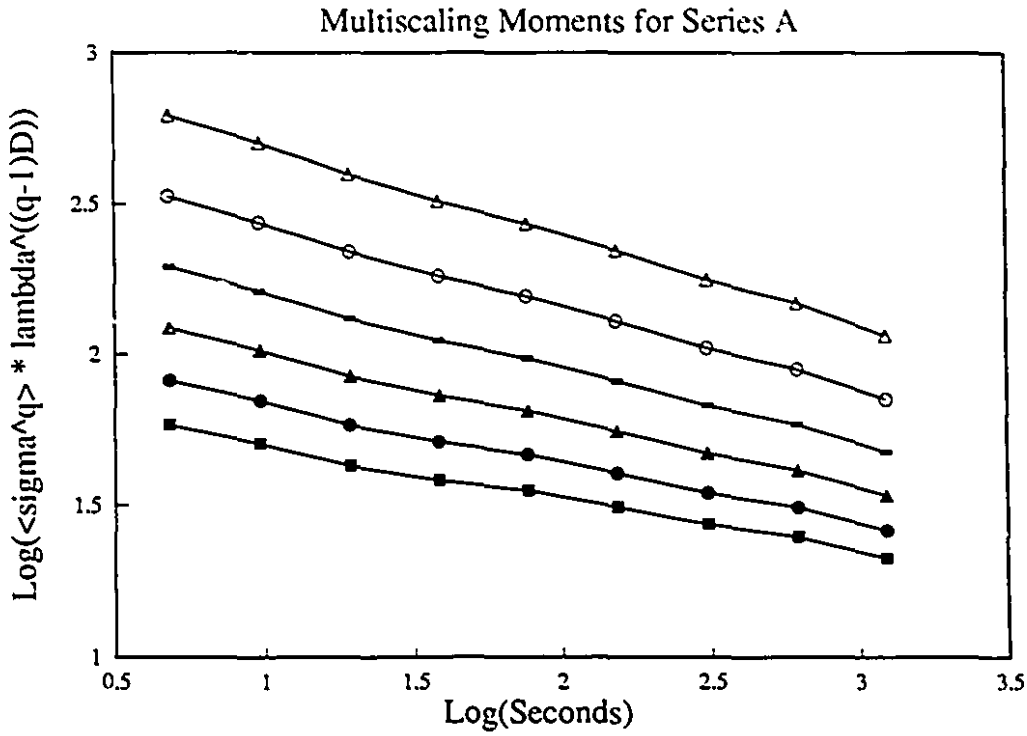

Figure 5.3: Multiscaling behaviour for series A. No break in the scaling behaviour is evident.

Figures 5.3, 5.4 and 5.5 are three examples of the multiscaling behaviour of the radar echo fluctuations. All of the time series examined displayed multiple scaling behaviour. The slopes of these lines are estimates of the function K(q) for a given q. The moment q was varied over the range 0 to 4 with an interval of 0.025 yielding 160 estimates of K(q) for each intensity time series examined.

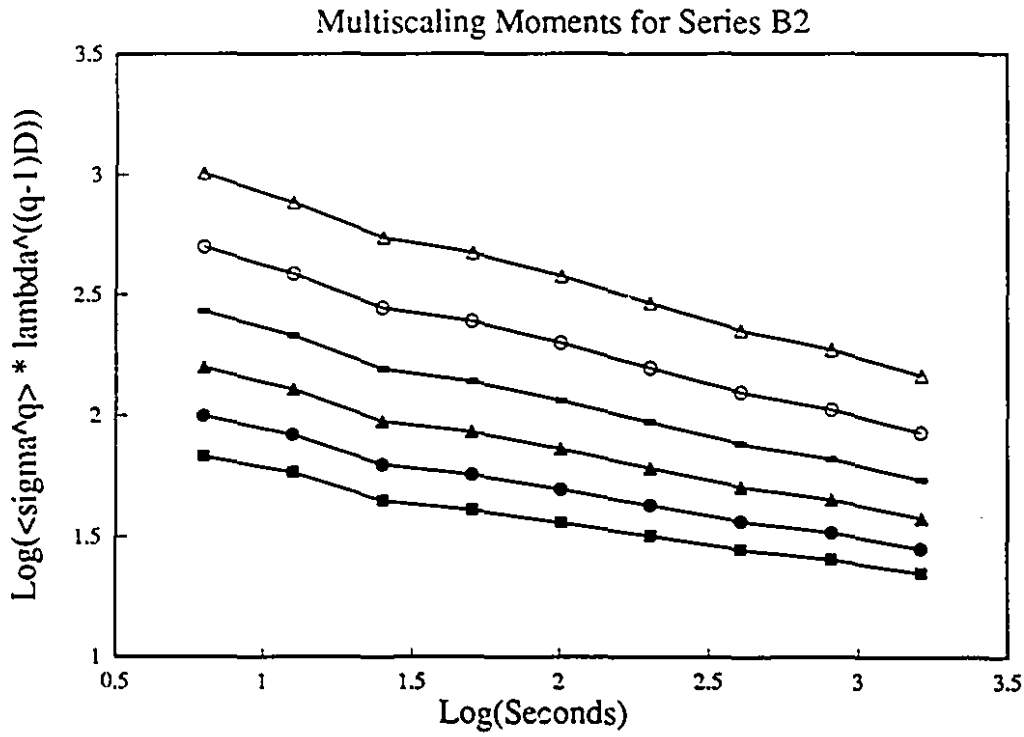

Figure 5.4: Multiscaling behaviour for series B_2.

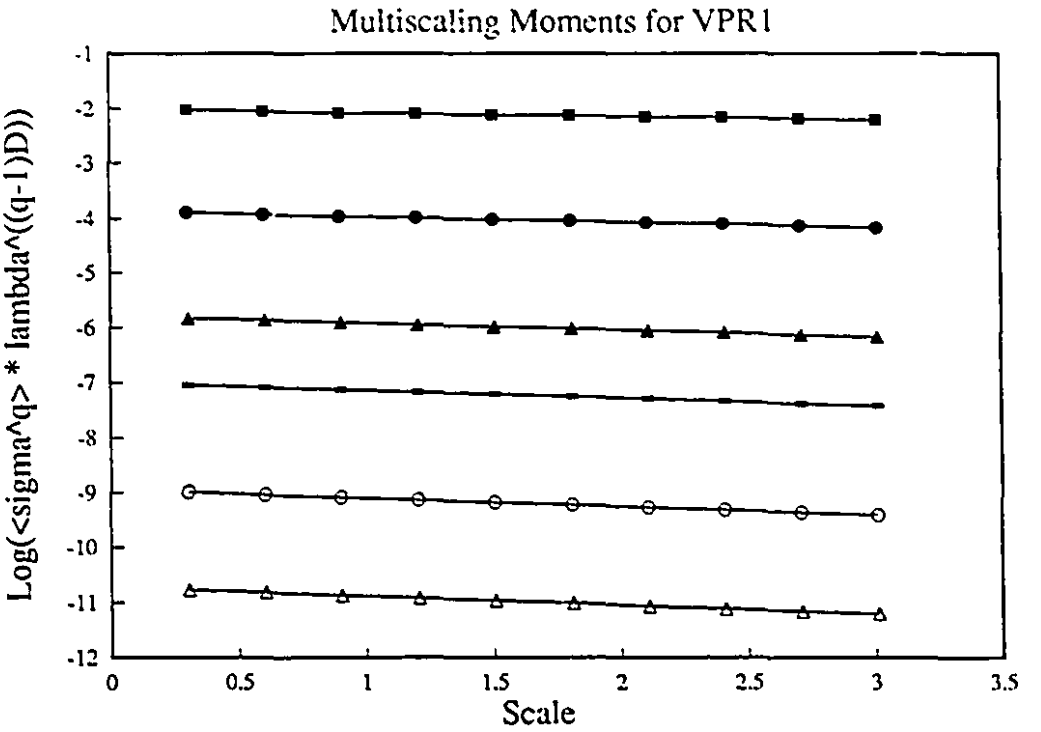

Figure 5.5: Multiscaling moments for series VPR1.

The scaling range displayed in figures 5.3, 5.4 and 5.5 is between 4 seconds and ~30 minutes. This scaling range extends down to scales just larger than the pulse volume scale. The scaling of moments of the rainfield to such small scales acts as proof that gradients are very important to small scale sin the rainfield. Further, it shows that the statistical structure of the rainfield over a large range of scales from kilometers to tens of meters is scaling. Estimation of the universal parameters α and C_1 from this multiple scaling regime in the rainfield will provide a model for this variability.

5.3.2 Graphs of K(q) and K(q,η) for Z_e.

This section provides a gallery of K(q) and K(q,η) functions used to estimate multifractal parameters. The fits to the K(q,η) functions are accomplished by simple linear regression to the linear region of the function yielding estimates of α. The linearity of the K(q,η) function is over a wide range of η. The linearity of K(q,η) to very small η values is due to the extreme sensitivity of the VPR radar system. If the radar were less sensitive the K(q,η) function would assume a sigmoid shape. The η range over which K(q,η) is universal is generally seen to end before 1.0 (log(eta) = 0). Thus, it is expected that estimates of α and C_1 by TM/GA will not be very reliable.

The figures in this section are testament to the applicability of universal multifractals to the echo fluctuation time series. Mathematical theories in general usually make poor fits to 'real' data. The figures in this section reveal a diverse set of rain cases being very well fit by the universal multifractal scale invariant function K(q,η). In part the sensitivity of the VPR is responsible. Remote sensing devices with less sensitivity, such as most raingauges (including the HYDRAs) produce much less convincing results.

Figures 5.7 and 5.8 show an examination of the statistics of time series A. Figure 5.7 shows the trace moments K(q) for a limited range of q to emphasize the fit to K(q) of the universal form in the range $0 < q < 1$, where bare and dressed cascade statistics are expected to be the same. Figure 5.8 shows a wider range of q to show how, at higher values of q, the estimates of K(q) differ from the universal form in a manner consistent with a second order phase transition (relation 3.19 and figure 3.2). Figures 5.9-a and 5.9-b show a number of computed K(q) function for the echo fluctuation time series (the curves are offset vertically to allow inter-comparison) and show the K(q) curve thought to best represent the statistics of the fluctuating echo (see Table 5.1 and the discussion in sub-section 5.3.3).

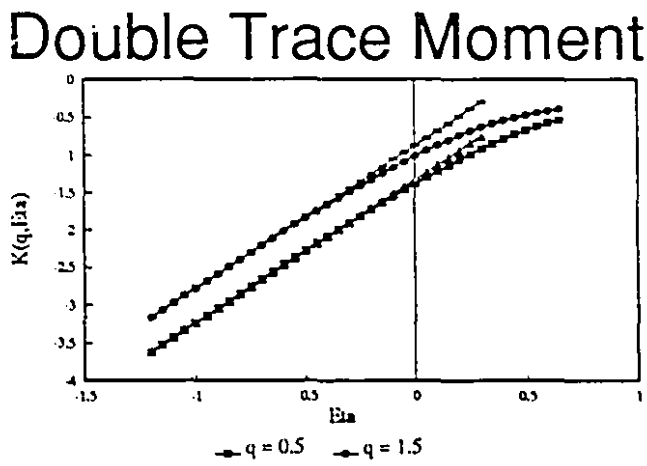

Figure 5.6-a: Log(K(q,η)) plotted against Log(η) for series A. The data were taken in three (N_s = 3) realizations of scale ratio λ = 256 (i.e. 256 averages of 8192 points). α and C_1 are drawn from the DTM columns of table 5.1. q_s for this computation is estimated at 2.45.

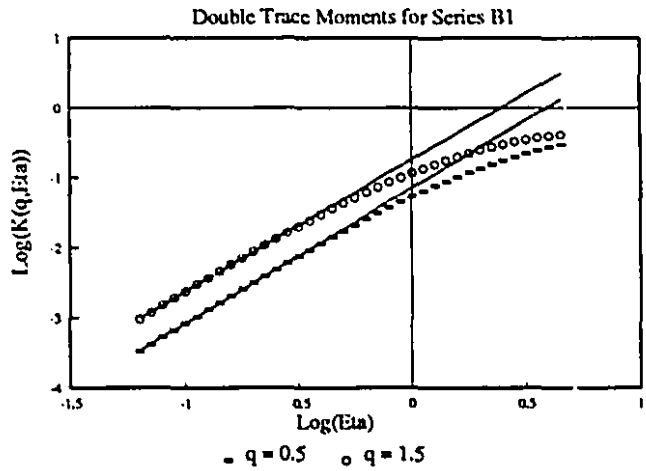

Figure 5.6-b: Log(K(q,η)) plotted against Log(η) for series B_1. q_s for this computation is estimated at 1.75 (N_s = 3, λ = 128).

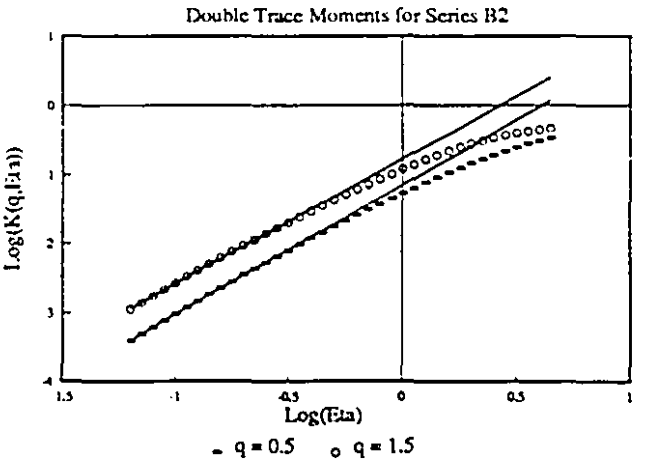

Figure 5.6-c: Log(K(q,η)) plotted against Log(η) for series B_2. q_s for this computation is estimated at 1.75 ($N_s = 3, \lambda = 128$).

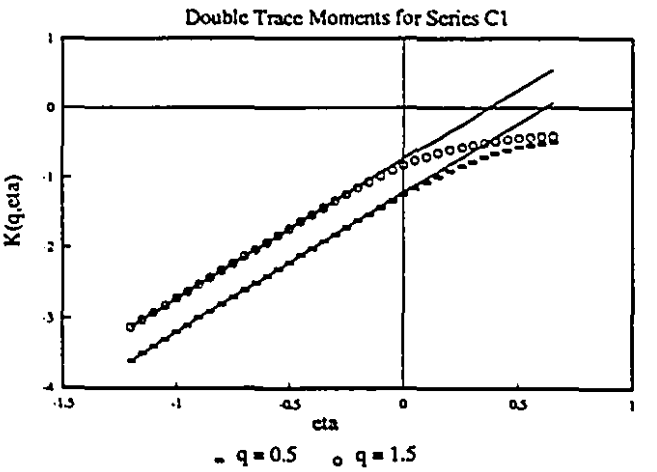

Figure 5.6-d: Log(K(q,η)) plotted against Log(η) for series C_1. q_s is estimated at 1.75 ($N_s = 1$, $\lambda = 128$).

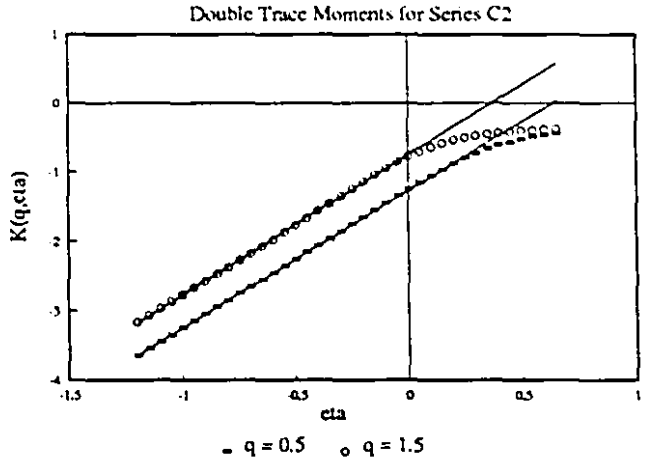

Figure 5.6-e: Log(K(q,η)) plotted against Log(η) for series C_2. q_s is estimated at 1.75 (N_s = 1, λ = 128).

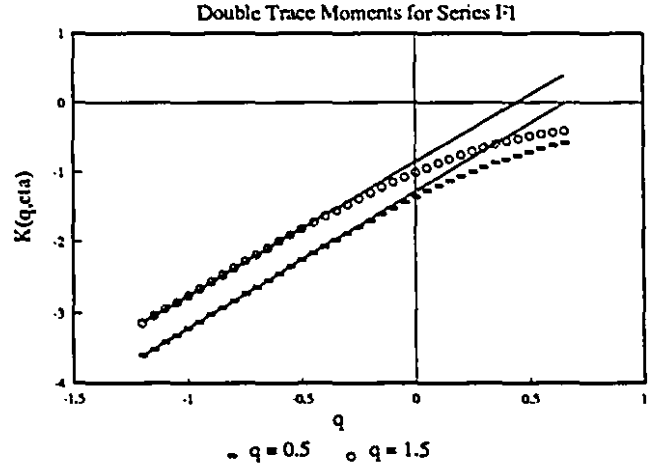

Figure 5.6-f: Log(K(q,η)) plotted against Log(η) for series F_1. q_s is estimated at 1.8 (N_s = 1, λ = 128).

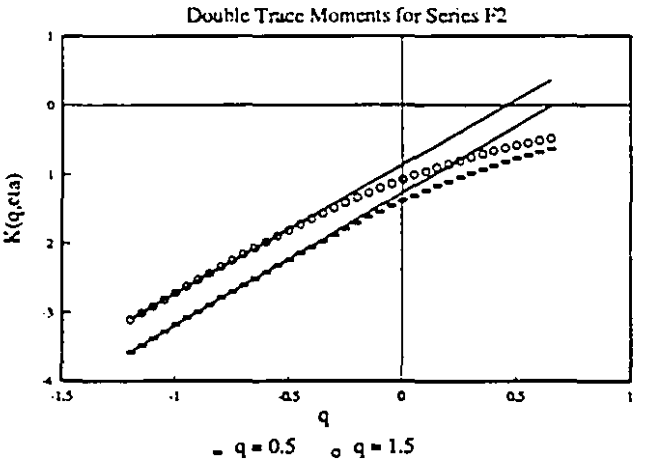

Figure 5.6-g: Log(K(q,η)) plotted against Log(η) for series F_2. q_s is estimated at 1.8 ($N_s = 1, \lambda = 128$).

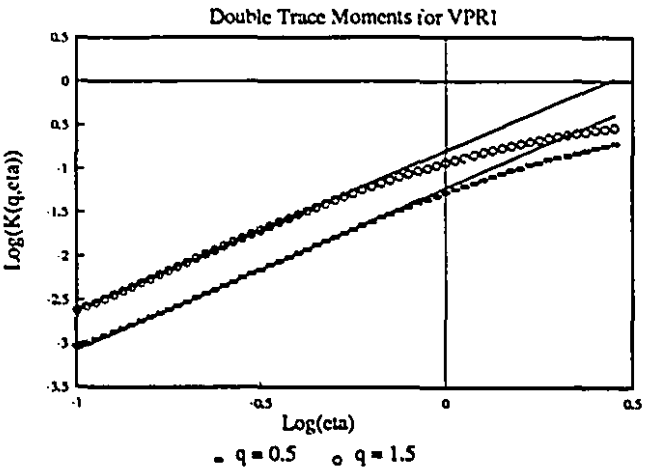

Figure 5.6-h: Log(K(q,η)) plotted against Log(η) for series VPR1. VPR1 is a long time sequence. N_s is counted as the number of subsets of scale ratio λ that contain no zeros. q_s in this case is estimated at 2.6. Note the extension to the linear region of the curve due to the substantial increase in data size.

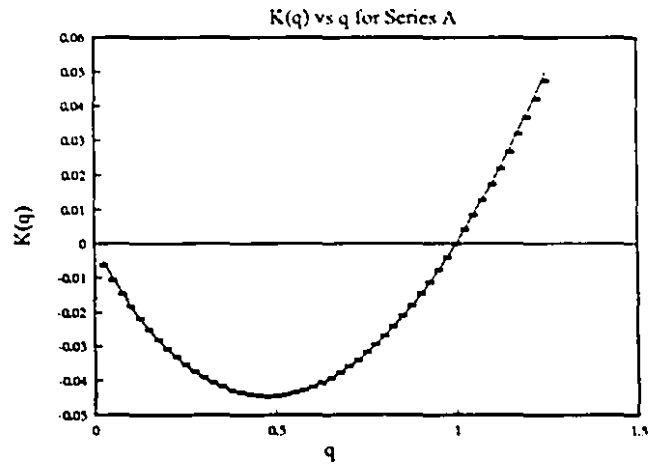

Figure 5.7: K(q) vs q computed by the trace moments algorithm and fit by the TM/GA technique for series A.

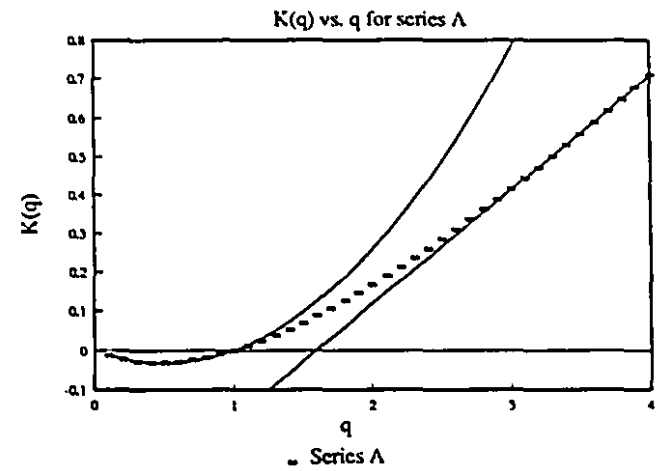

Figure 5.8: $K_s(q)$ vs q plotted for a wider range of q in order to show the effect of q_s. Beyond q_s the $K_s(q)$ has linear behaviour with slope $\gamma_s = 0.3$. The theoretical K(q) curve is also plotted for comparison with $\alpha = 1.7$ and $C_1 = 0.16$. q_s is estimated using relations 3.15 to 3.18 and gives $q_s = 2.0$ which agrees well with the behaviour of $K_s(q)$.

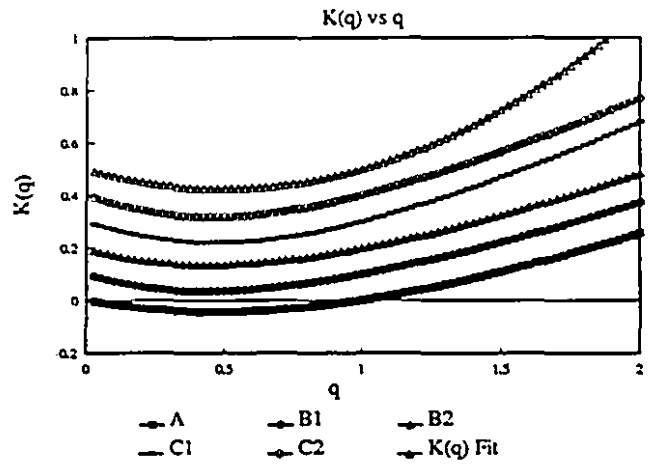

Figure 5.9-a: K(q) vs q curves for the indicated time series of the fluctuating echo. A constant is added to each curve for viewing purposes. The curves should be compared with the 'K(q) Fit' curve which has $\alpha = 2$ and $C_1 = 0.3$ (drawn from table 5.1). These estimates of α and C_1 appear to fit the bulk of the data very well.

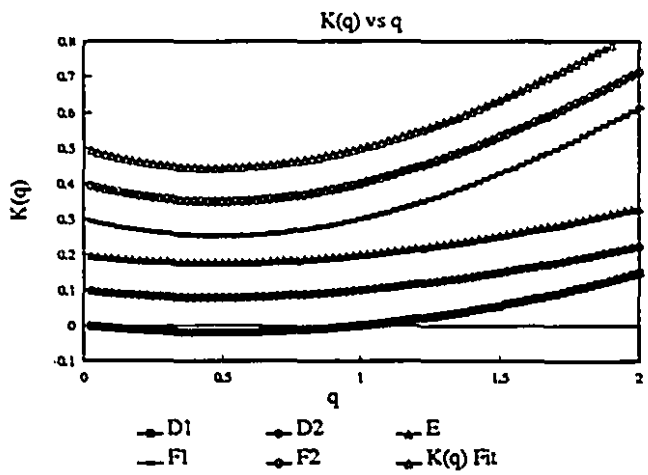

Figure 5.9-b: K(q) vs q for the indicated time series of the fluctuating echo. A constant is added to each curve for viewing purposes.

5.3.3 Estimates of Universal Multifractal Parameters.

A summary of the estimates of multifractal parameters for the intensity time series and for VPR1 and VPR2 are found in table 5.1. Table 5.1 shows that, in general, α is quite accurately estimated while C_1 is much more difficult to estimate. C_1 is an estimate of the codimension of the ensemble mean. The estimation of this quantity from such small data sets is expected to result in considerable uncertainty. The C_1 parameter generally requires an enormous amount of data to estimate accurately. The large amount of averaging of the data required to remove the scale break of the spectral plateau results in data series that are too short to provide high statistical accuracy. The shortened data sets also result in q_s values that are too small to allow TM/GA to accurately estimate α and C_1. The estimates of α for TM/GA in table 5.1 are local slopes of $\log(K(q,\eta))$ vs $\log(\eta)$ at $\log(\eta) = 0.0$. The corresponding estimates of C_1 are therefore entirely suspect. The case of series A, the longest echo time series, reveals consistent estimates of α and C_1 by both DTM and TM/GA.

In order to increase the statistical reliability of the results, the time series A through G were combined into a long series in order to approximate the ensemble statistics. The time series A through G were averaged over 4 second time scales to produce time series of the low frequency scaling regime free of the effects of the plateau. The resulting 11 short time series comprise an ensemble and represent a conditional sampling of rainfield variability during the summer of 1991. DTM and TM/GA were applied to this 'ensemble' series to produce estimates of α and C_1. The time series VPR1 represents a true ensemble of rain events over the summer rain variability. The agreement of estimates of α and C_1 between the two ensembles is quite strong. This is particularly interesting since the two estimates result from data sets collected in successive years using entirely different sampling approaches. Figures 5.9 a and b show that the α and C_1 estimated from the two ensembles fit the bulk of the data very well. The possibility that ensemble realizations of measured statistical properties from successive years could be so close suggests further research.

Table 5.1: Estimates of Multifractal Parameters using DTM and TM/GA Analysis Techniques.						
	DTM		TM/GA			
Series	α	C_1	α	C_1	FIT	H
A	1.9 ± 0.1	0.2 ± 0.1	1.74	0.16	184	0.7
B1	2.0 ± 0.4	0.4 ± 0.4	1.46	0.21	22	0.4
B2	1.9 ± 0.4	0.4 ± 0.4	1.52	0.21	36	0.5
C1	2.0 ± 0.1	0.4 ± 0.1	1.76	0.29	33	0.5
C2	2.0 ± 0.1	0.4 ± 0.1	1.74	0.30	20	0.5
D1	1.9 ± 0.4	0.1 ± 0.2	1.87	0.08	318	0.0
D2	1.8 ± 0.4	0.1 ± 0.3	1.64	0.07	394	0.0
E	1.9 ± 0.3	0.1 ± 0.2	1.80	0.08	279	0.5
F1	2.0 ± 0.1	0.2 ± 0.1	1.91	0.19	336	0.6
F2	2.0 ± 0.1	0.2 ± 0.1	1.86	0.20	168	0.5
G	1.9 ± 0.3	0.3 ± 0.2	1.75	0.20	125	0.4
Ensemble	2.0 ± 0.1	0.32 ± 0.09	1.73	0.23	52	N/A
VPR1	1.9 ± 0.2	0.3 ± 0.05	1.70	0.22	48	0.5
VPR2	1.9 ± 0.2	0.3 ± 0.07	1.76	0.22	55	0.5

The last column of table 5.1 holds estimates of the H exponent. The calculation of H combines the estimates of spectral slope β from table 4.1 with the estimates of α and C_1 from the DTM colums of table 5.1. The estimates of H are remarkably uniform and agree well with the value of H = 0.5 estimated by Lovejoy (1981). The estimates of H for series D_1 and D_2 are compromised by poor spectral behaviour (see table 4.1) due to the very short data set available after the plateau effect is removed.

The results of this section support previous studies of scaling behaviour in the rainfield, and provide the answer to the question as to the scale limit accessible to these measurement techniques using radar data. Very high temporal resolution verification of multiscaling behaviour (i.e. below the 2 s timescale associated with the pulse volume scale) in the rainfield will have to be provided by other remote sensing devices such as the sonic gauge, keeping in mind the necessity for a large dynamical range. The bulk of scaling studies in the rainfield have been of spatial data

in the form of CAPPIs etc... Thus, the results presented here support these spatial observations and show that scaling in time occurs to very small scales not accessible with most operational radar data. The observation of temporal scaling by Tessier et al. (1993) is compromised by the zero problem, but re-analyzing his data sets provided results consistent with those in table 5.1.

The radar echo fluctuation time series exhibit good scaling behaviour. The function $K(q,\eta)$ reveals that the time series respect universal multifractal behaviours for η up to $q_s \sim 2.3$. The existence of the zero problem, of course compromises the bulk of estimates of α and C_1 found in the literature, but the observation of scaling behaviour is similar. This chapter reveals that scaling behaviour can be observed in radar data to scales just above the resolution scale B_λ of the radar. The stability of the estimates of α and C_1 over two successive years presents an indication of the stationarity of the statistics over time. Indeed, estimates of the parameters from the individual echo time series, while sometimes compromised by uncertainty due to their short length, show a narrow range of results centered on the ensemble estimates.

6.0 The Statistics of $Z_{e\lambda}$ from a Spatially Scaling Rainfield.

"The fact that Euclidean geometry seems so accurately to reflect the structure of the 'space' of our world has fooled us (or our ancestors!) into thinking that this geometry is a logical necessity, or into thinking that we have an innate a priori intuitive grasp that Euclidean geometry must apply to the world in which we live."

Roger Penrose
The Emperor's New Mind

This and the next chapter describe the assumptions and steps taken to model the echo fluctuations from a multifractal rainfield with variability extending to sub-resolution scales. The ultimate objective of the modelling effort is to create artificial time series of intensities which have the same quantitative and qualitative statistical characteristics as the observed intensity time series. In this chapter a complete statistical characterization of the measured reflectivity $Z_{e\lambda}$ from multifractal sub-resolution variability is achieved. The results of this chapter constitute a general solution to the scalar multifractal radar observer's problem. The solution allows the statistical parameters of the drop field to be estimated from measured echoes. The previous data analysis section serve to justify the assumption of sub-resolution variability by showing that the only scales identifiable in time series of radar echo fluctuations are those of the radar. Given that there are no *a priori* scales in the rainfield the scaling behaviour observed at super resolution scales extends to sub-resolution scales.

6.1 Theory.

The theory developed here is for the statistics of the fluctuating echo from a multifractal field of scatterers. The development of the theory first documents that the scaling of a field that we define as the radar cross-section field scales with the same statistics as the drop field. This is necessary since we do not intend to model the positions of drops but rather the radar cross section of volumes of rain flux. The development then covers how the statistics of reflectivity factor Z_λ scale relative to the radar cross section field. The development then concentrates on the effective

reflectivity factor $Z_{\epsilon\lambda}$ which is a Fourier component of the radar cross-section field. Up until now statistics of a Fourier component of a multifractal field have been unknown. However, with the extension of scalar cascades to complex, vector and tensor cascade (Schertzer and Lovejoy, 1993a), the radar measurements can be viewed as a dressed complex cascade. The following development is supported by the numerics presented in section 6.1.2 which show that each step of the theory governing the statistics of $Z_{\epsilon\lambda}$ from a multifractal field is supported.

The relation between the radar cross section field and the drop field.

The amplitude of a radar echo is related to the volume of a drop through the cross section. The smallest scale of the rainfield will be denoted by B_Λ^{-1}. Λ^{-1} is the 'inner scale' of the rainfield and is the smallest scale to which scaling behaviour can be expected to hold. The radar measurement volume or 'pulse volume' scale (size $\lambda^{-1} > \Lambda^{-1}$) will be denoted by B_λ (B_λ should be interpreted as the set contained by ball B of scale λ, likewise for B_Λ^{-1}). B_λ is the smallest spatial scale resolvable by the radar. The radar also uses the wavelength scale λ_w which is related to the radar wavevector modulus $|\vec{k}|$ in the usual way ($= 2\pi/\lambda_w$). Given these definitions the relation between the effective cross-section σ of the smallest scale of the rainfield B_Λ and the drop field can be defined. If the position vector of the center of a small scale element $B_{\lambda i}$ is $\vec{x}_i$ then the following represents the radar echo amplitude from a cross-section field

$$\sigma_\Lambda(\vec{x}_i)e^{\vec{ik}\cdot\vec{x}_i} = \frac{1}{Vol(B_\Lambda)}\sum_{j\in B_{\Lambda_i}} V_j e^{\vec{ik}\cdot\vec{x}_j} \tag{6.1}$$

where the sum on the right hand side is over all the drops volume V_j in the small resolution element $B_{\Lambda i}$. This relation can be rewritten as

$$\sigma_\Lambda(\vec{x}_i) = \frac{1}{Vol(B_\Lambda)}\sum_{j\in B_{\Lambda i}} V_j e^{ik\Delta\vec{x}_{ij}} \tag{6.2}$$

with $\Delta\vec{x}_{ij} = \vec{x}_j - \vec{x}_i$. As long as $\Lambda \gg k$, then $\Delta\vec{x}_{ij} \ll \lambda_w$ and we have

$$\sigma_\Lambda(\vec{x}_i) \approx \frac{1}{Vol(B_\Lambda)}\sum_{j\in B_{\lambda_w}} V_j \tag{6.3}$$

This relation serves as the approximation that the cross section of an extended volume of scatterers can be represented by the total cross section at the center of the volume. This relation implies that the scaling properties of radar cross section field σ and the drop field (or rainfield), represented by V, are the same as long as Λ^{-1} is small enough:

$$<\left(\sum_{j \in B_\lambda} V_j^\eta\right)^q > (Vol(B_\lambda))^{-q} \quad = \quad \lambda^{K_V(q,\eta)} \tag{6.4}$$

and

$$K_\sigma(q,\eta) \quad = \quad K_V(q,\eta) \tag{6.5}$$

Which means that the statistics of the cross-section field are the same as the drop field.

The statistics of reflectivity in a scaling rainfield.

The reflectivity factor is defined (ignoring radar constants) as

$$Z_\lambda \quad = \quad \frac{1}{Vol(B_\lambda)} \sum_{j \in B_\lambda} V_j^2 \tag{6.6}$$

and hence

$$K_{Z_\lambda}(q,\eta) \quad = \quad K_V(q,2\eta) \tag{6.7}$$

For universal multifractals (index α) we have

$$K(q,\eta) \quad = \quad \eta^\alpha K(q,1) \quad = \quad \eta^\alpha K(q) \tag{6.8}$$

hence

$$K_{Z_\lambda}(q) \quad = \quad 2^\alpha K_V(q) \tag{6.9}$$

Thus, the statistics of the reflectivity factor Z_λ are simply related to the drop field and the radar cross section field.

The statistics of effective reflectivity $Z_{e\lambda}$ in a scaling rainfield.

Radars do not measure Z_λ directly but rather measure an effective reflectivity $Z_{e\lambda}$. We have seen that in the idealized case where the phases of the scatterers are independent random variables Marshall and Hitschfeld (1953) and Wallace (1953) elegantly showed that the resulting marginal distribution does not depend on any of the radar measurement scales. In a scaling rainfield, however, it is expected that the measured intensities are dependent upon the measurement scales. The amplitude of the scattered wave is the modulus of the Fourier component of the radar cross section field $\sigma(\vec{x})$. If the drops are no longer independent then the Fourier component is no longer that of a simple white noise but is dependent upon the scaling behaviour. Fortunately, universal multifractals can be used to quantify and model the scaling behaviours.

The amplitude A_k of the backscattered wave is the result of a Fourier component, using the pulse volume and wavelength scales, of the radar cross section field $\sigma(\vec{x})$ within the pulse volume. In considering the statistics of A_k, both the real and imaginary parts must be dealt with. Recent advances in vector cascades based on Lie algebras (as opposed to the more familiar scalar cascades) allow the definition of complex K(q) functions in the universal multifractal formalism (Schertzer and Lovejoy, 1993a). The scattering amplitude A is given by

$$A_\lambda(\vec{x}_i) = \frac{1}{Vol(B_\lambda)} \sum_{j \in B_\lambda} V_j e^{i\vec{k}\cdot\vec{x}_j} \tag{6.10}$$

The scaling statistics of the amplitude, given a scaling rainfield, are given by

$$\langle A_\lambda^q \rangle = \lambda^{K_A(q)} \tag{6.11}$$

It is necessary to introduce the real and imaginary parts of the generator Γ (recall for cascades that $\ln A_\lambda = \Gamma_\lambda$):

$$A_\lambda = e^{\Gamma_R + i\Gamma_I} \tag{6.12}$$

which gives

$$|A_\lambda| = e^{\Gamma_R} \; ; \; Arg(A_\lambda) = \Gamma_I \tag{6.13}$$

therefore it is possible to define a real and an imaginary K(q) function, one for the real part of the generator and one for the imaginary part of the generator:

$$K_A(q) = K_{A,R}(q) + iK_{A,I}(q) \tag{6.14}$$

The $K_{A,R}(q)$ characterizes the scaling of the modulus of A_k and $K_{A,I}(q)$ characterizes the scaling of the phase of A_k. The scaling of the phase will be relevant to the characterization of doppler radar data. The effective reflectivity can be defined as

$$Z_{\epsilon\lambda} = \frac{1}{Vol(B_\lambda)} \left| \sum_{j \in B_{\lambda_w}} V_j e^{ikx_j} \right|^2 \tag{6.15}$$

hence, by comparing the definitions above:

$$K_{Z_\epsilon}(q) = K_{A,R}(2q) - qD \tag{6.17}$$

where the -qD term arises due to the standard volume normalization (space dimension D) of $Z_{\epsilon\lambda}$, and the 2q arises due to the fact that the statistics are of a squared quantity.

There are two scale regimes that can be analyzed. The situation where $k << \lambda$ corresponds to the pulse length being smaller than the wavelength, and hence is unphysical. In this situation e^{ikx} is approximately constant over the pulse volume scale λ^{-1}. In this limit

$$K_{Z_\epsilon}(q) = K_V(2q) - qD \; ; \; k \ll \lambda \tag{6.18}$$

The more interesting limit $k >> \lambda$ corresponds to the situation where real measurements are made with wavelength smaller than the pulse volume scale. A_λ (and hence $Z_{\epsilon\lambda}$) can be considered to be the result of dressing the complex cascade $A_\Lambda = \sigma_\Lambda e^{ikx}$ to scale ratio λ. The difference from the normal dressing (averaging) operation is that the "inner scale" of the complex factor e^{ikx} is the wavelength λ_w. Because of the change in the inner scale (from Λ to λ_w) the variability will be lower. In this case, the results for universal complex (Lie) cascades (Schertzer and Lovejoy, 1993a) apply, and give,

$$K_{A,R}(q) - qK_{A,R}(1) = K_\sigma(q) = K_V(q) \tag{6.19}$$

(i.e. bare and dressed cascades have equivalent scaling except that for a dressed complex cascade $K_{A,R}(1)$ need not be zero, hence the additional linear term in the exponents). This relation shows that except for the normalization term $K_{A,R}(1)$, which corresponds to the multiplication by $\lambda^{K_{A,R}(1)}$, the entire statistical behaviour of the amplitude A_λ can be described in terms of that of the scaling radar cross-section field $\sigma(\vec{x})$. Applying the above formulae to relate A_λ and $Z_{e\lambda}$ we obtain:

$$K_{Z_e}(q) = K_V(2q) + q(2K_{A,R}(1) - D) \tag{6.20}$$

The implication of this relation is that

$$V_\lambda \overset{d}{=} Z_{e\lambda}^{1/2} \lambda^{K_{A,R}(1) - D/2} \tag{6.21}$$

which is the simplest deduction that can be made concerning the relation between the rainfield and the measured reflectivity. Thus, direct knowledge of the statistics of the drop field can be measured through $Z_{e\lambda}$. The scaling behaviours of Z_λ and $Z_{e\lambda}$ can be related using

$$K_{Z_e}(q) = 2^{-\alpha} K_Z(2q) + q(2K_{A,R}(1) - D) \tag{6.22}$$

In the following section a relationship between $K_{A,R}(1)$ and the C_1 of the $\sigma(\vec{x})$ field is established numerically.

In a scaling rainfield the statistics of $Z_{e\lambda}$ will preserve the scaling of the radar cross section field $\sigma(\vec{x})$ with the following results: The α-value of the $\sigma(\vec{x})$ remains invariant to the transformation. Estimates of C_1 from $Z_{e\lambda}$ are 2^α times those of the input $\sigma(\vec{x})$ field. The statistics of Z_λ and $Z_{e\lambda}$ differ only by a linear term in the exponents. The linear term is $K_{A,R}(1)$ which results from the dressing operation of the Fourier component performed on the complex cascade. $K_{A,R}(1)$ would be responsible for, for example, biases in estimates of mean $Z_{e\lambda}$. These results will hold exactly as long as the inner scale of the rainfield Λ^{-1} is smaller than the wavelength λ_w.

The formulation permits the statistics of any of the related fields to be deduced simply by measuring $Z_{e\lambda}$. Relation 6.21 presents the result that the statistics of the drop field are simply related to those of the echo fluctuations. The stablishment of $K_{A,R}(1)$ by numerical techniques in the following section will allow the relation to be used in a quantitative sense. However, the existence of this relation obviates the necessity of considering Z. The establishment of a $Z_{e\lambda}$-R_λ

(the subscript indexing the scale over which the rainfield is to be considered) relation requires the determination of R_λ in terms of V_λ. The establishement of the scaling conditional probability functions will allow errors to be estimated (see Extensions in chapter 8.2).

6.2 Numericai Results.

This section will explore the statistical behaviour of the Fourier component of a scaling radar cross section field $\sigma(\vec{x})$. The $\sigma(\vec{x})$ field will be constructed using the universal multifractal cascade generator (UMCG) described in Appendix A. The purpose of the UMCG will be to generate multifractals with specific α and C_1. The Fourier component will be computed for systematically varying pulse volume scales B_λ for a variety of wavelength λ_w scales. There are three possible regimes defined by the scales of the problem, only one of which is relevant to radar measurements. The regimes are wavelength $\lambda_w < \Lambda^{-1}$ (the inner or pixel scale of the cascade), $\lambda_w >$ outer cascade scale, and λ_w between the inner and outer scale. The case of λ_w smaller than the inner cascade scale is only relevant to millimetric wavelength radars which have other problems including severe attenuation and Mie scattering. The case of λ_w greater than the outer scale of the cascade requires that the pulse volume be shorter than the wavelength and is therefore unphysical. The third regime, where λ_w is between the inner and outer cascade scales is relevant to the radar measurement process. Figures 6.1 to 6.3 show the scaling moments for $A(\vec{k},\vec{x})$ for moments q = 0.1, 1.0 and 4.0 respectively. The legend gives the corresponding wavelengths (recall $k = \frac{2\pi}{\lambda}$) used. The outer scale of the $\sigma(\vec{x})$ field is 32768 pixels and each moment curve represents an average over 32 realizations. Estimation of the scaling moments in the scaling regime results in the moment function $K_{A,R}(q)$.

The Scaling of $A(\vec{k},\vec{x})$.

The scaling behaviours shown in figure 6.1, 6.2 and 6.3 are for five different wavevectors k (wavelength scale in pixels is given in the legend). The moments are computed from 32 realizations and reveal that the curve for the various wavevectors are exactly parallel.

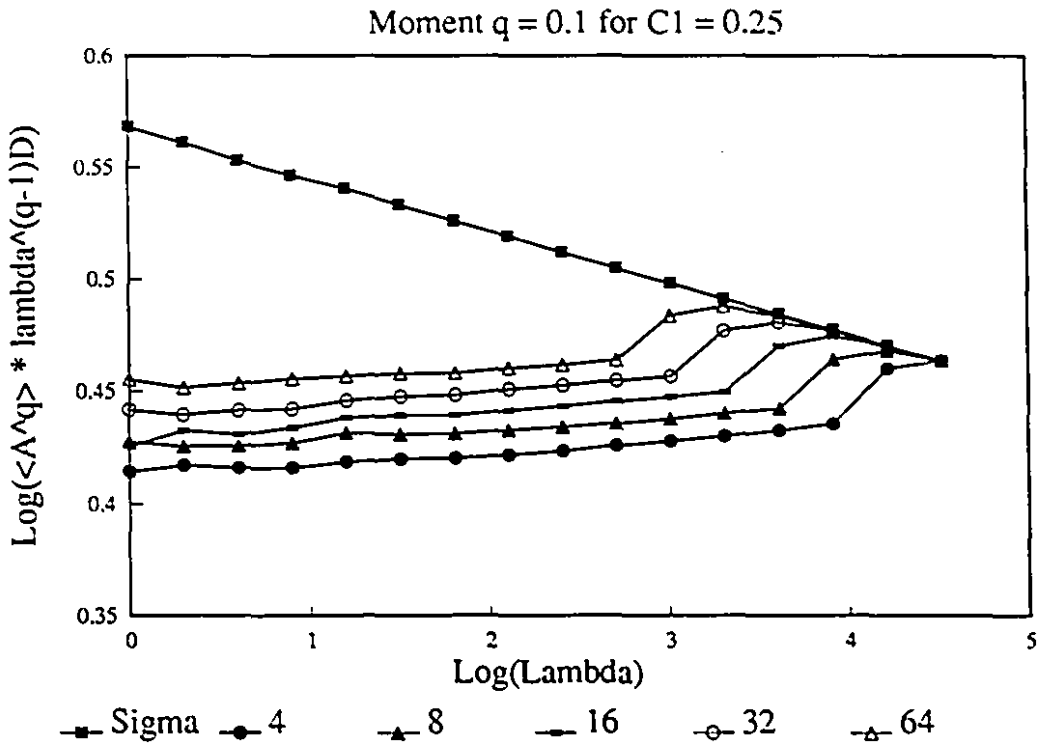

Figure 6.1: Scaling moments for q = 0.1, computed from $A(\vec{k},\vec{x})$, for $\sigma(\vec{x})$ with $C_1 = 0.25$.

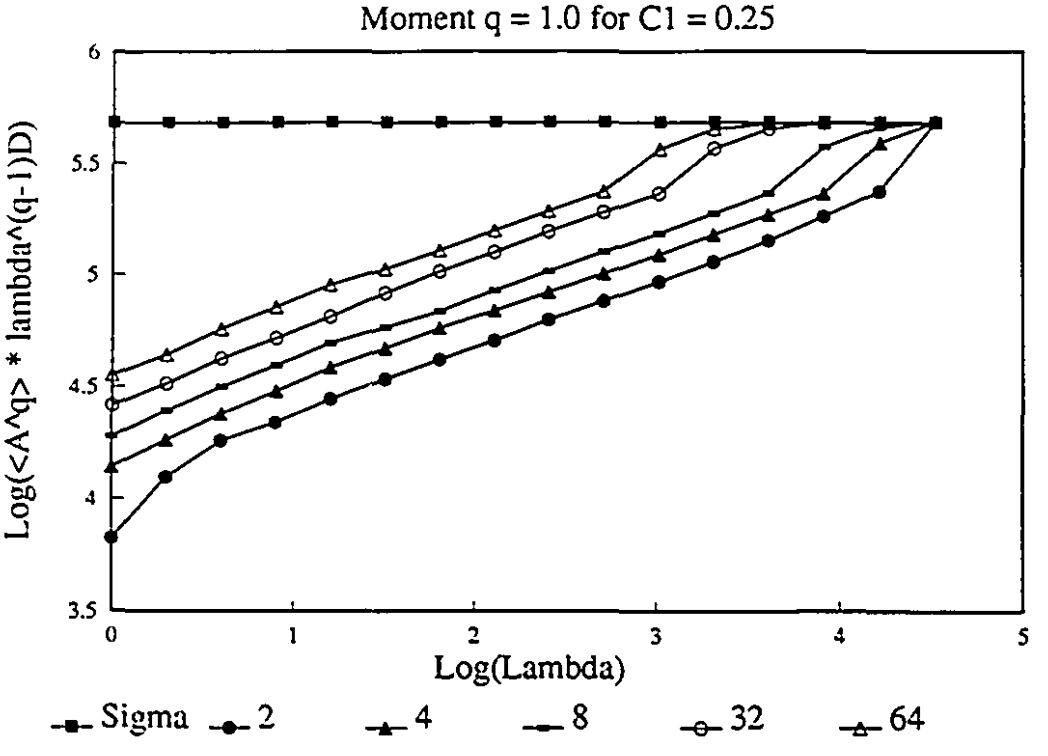

Figure 6.2: Scaling moments for q = 1.0, computed from $A(\overline{k},\overline{x})$, for $\sigma(\overline{x})$ with $C_1 = 0.25$.

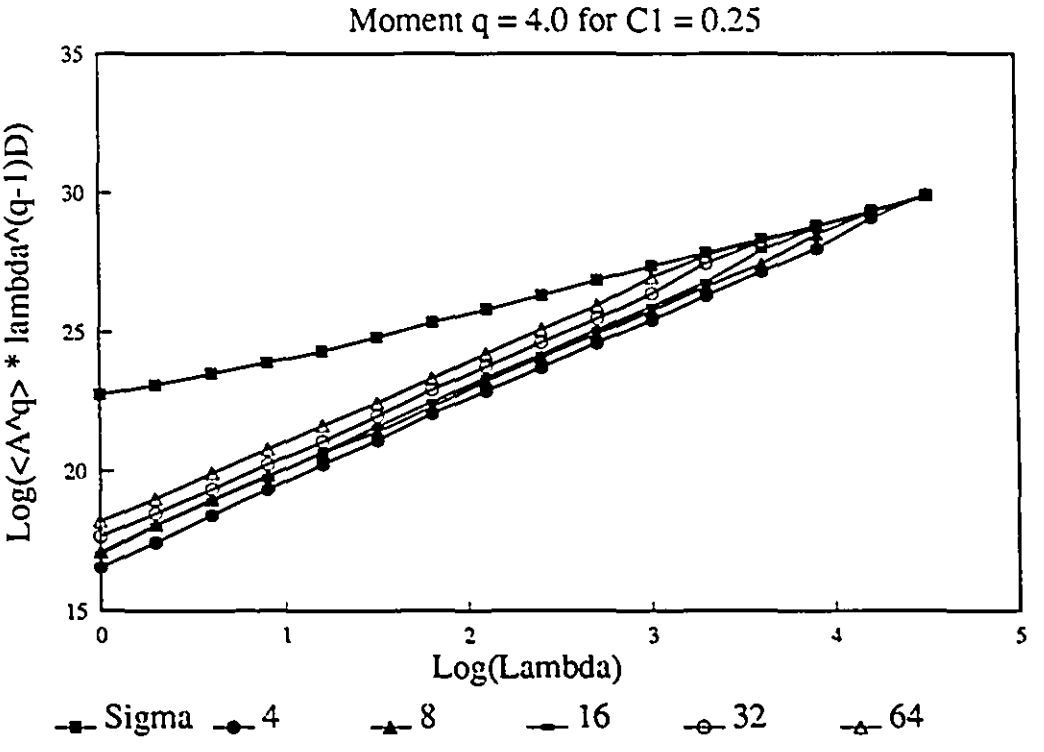

Figure 6.3: Scaling moments for q = 4.0, computed from $A(\vec{k},\vec{x})$, for $\sigma(\vec{x})$ with $C_1 = 0.25$.

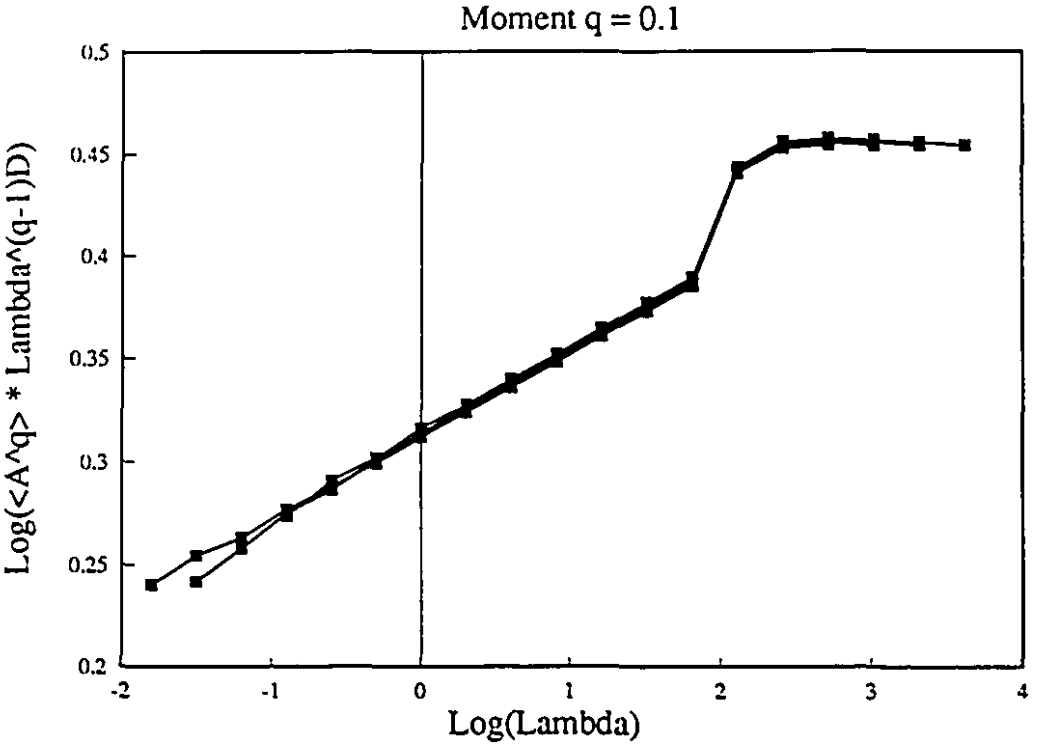

Figure 6.4: Scaling moments for q = 0.1, computed from $A(\vec{k},\vec{x})$, for $\sigma(\vec{x})$ with $C_1 = 0.05$. Each moment curve has been shifted to show the overlap of the moments and hence the invariance to λ/λ_{ss}.

$K_{A,R}(q)$ Functions.

Figure 6.5 shows the $K_{A,R}(q)$ curve for a number of wavelengths (given in pixels) computed over a $\sigma(\vec{x})$ field with $\alpha = 2.0$ and $C_1 = 0.25$. Thus, the statistics of A(k) are exactly related to those of $\sigma(\vec{x})$ by a renormalization of the moments. The renormalization of the scaling statistics by the Fourier operation does not affect the scaling behaviour but introduces the linear term $K_{A,R}(1)$ into the exponents. This set of relations represents the complete solution to the problem of the statistical behaviour of $Z_{\epsilon\lambda}$ measured from a scaling field by any wavelength/pulse volume combination.

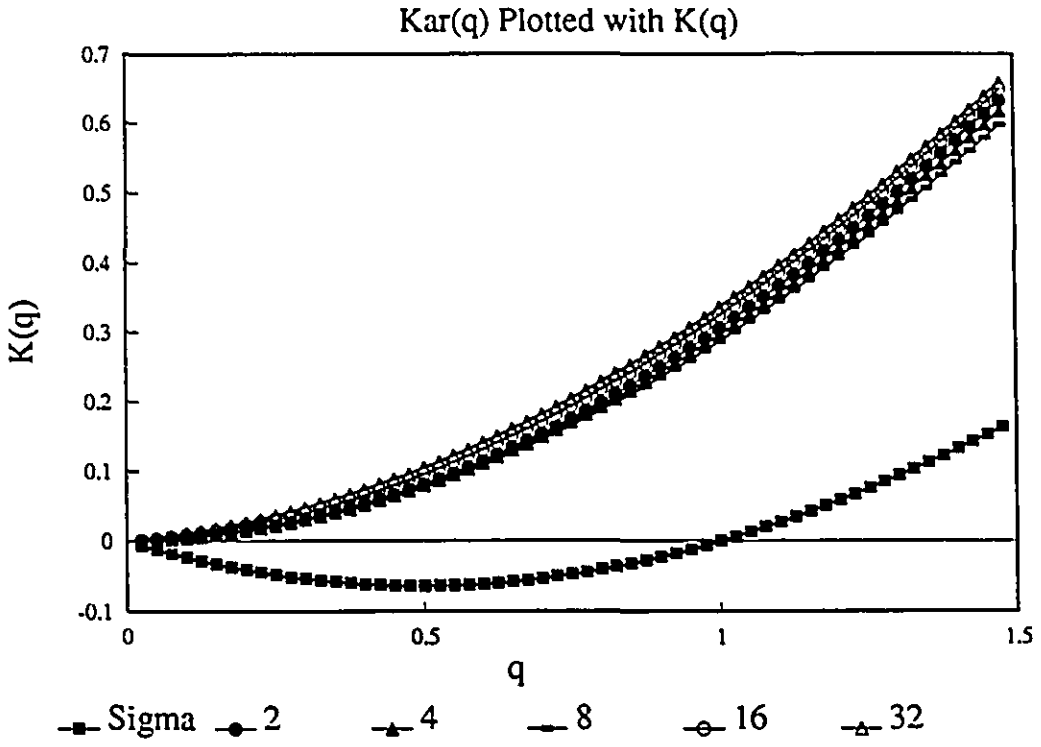

Figure 6.5: $K_{A,R}(q)$ plotted with $K_\sigma(q)$ for a number of wavelengths. The $\sigma(\vec{x})$ field has $\alpha = 2.0$ and $C_1 = 0.25$.

Figures 6.6, 6.7 and 6.8 present three cases of $K_{A,R}(q) - qK_{A,R}(1)$ curves plotted for C_1 values of 0.05, 0.15 and 0.25. The figures reveals that the curves overlap with no apparent dependence on C_1 or upon wavelength. The errors in the overlap are entirely explainable in terms of the estimation errors of the exponents for the various moments curves.

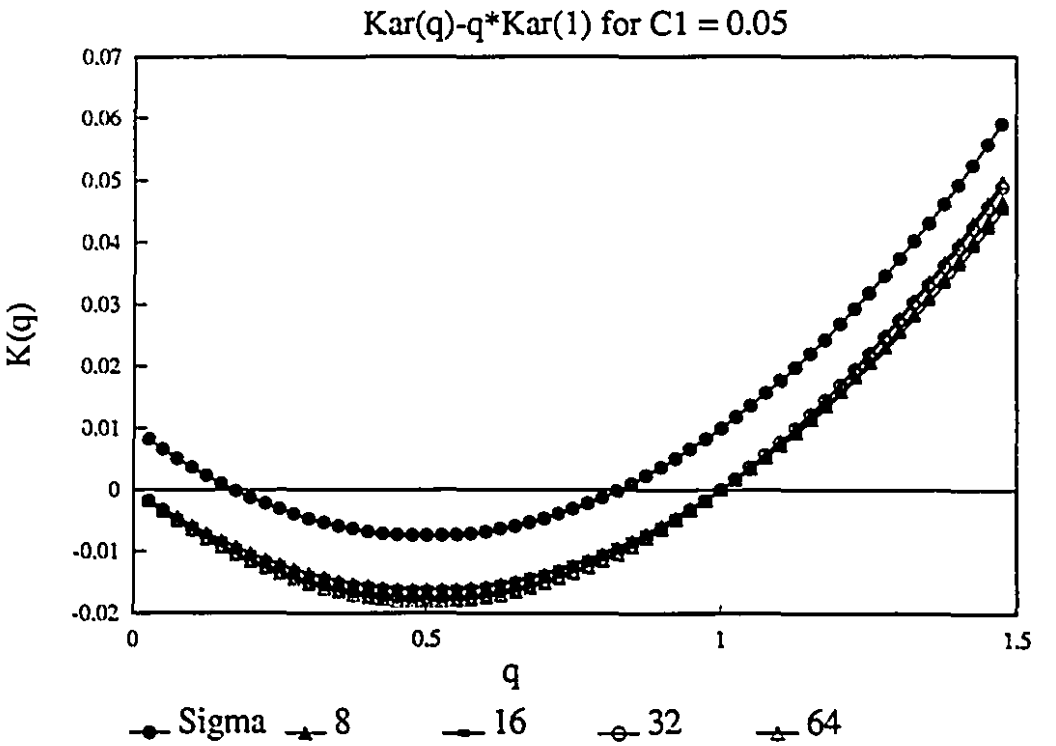

Figure 6.6: $K_{A,R}(q) - qK_{A,R}(1)$ plotted against q. The $\sigma(\vec{x})$ field has $C_1 = 0.05$. The legend gives the wavelengths in pixels. The K(q) function for the $\sigma(x)$ field is offset vertically to allow comparison.

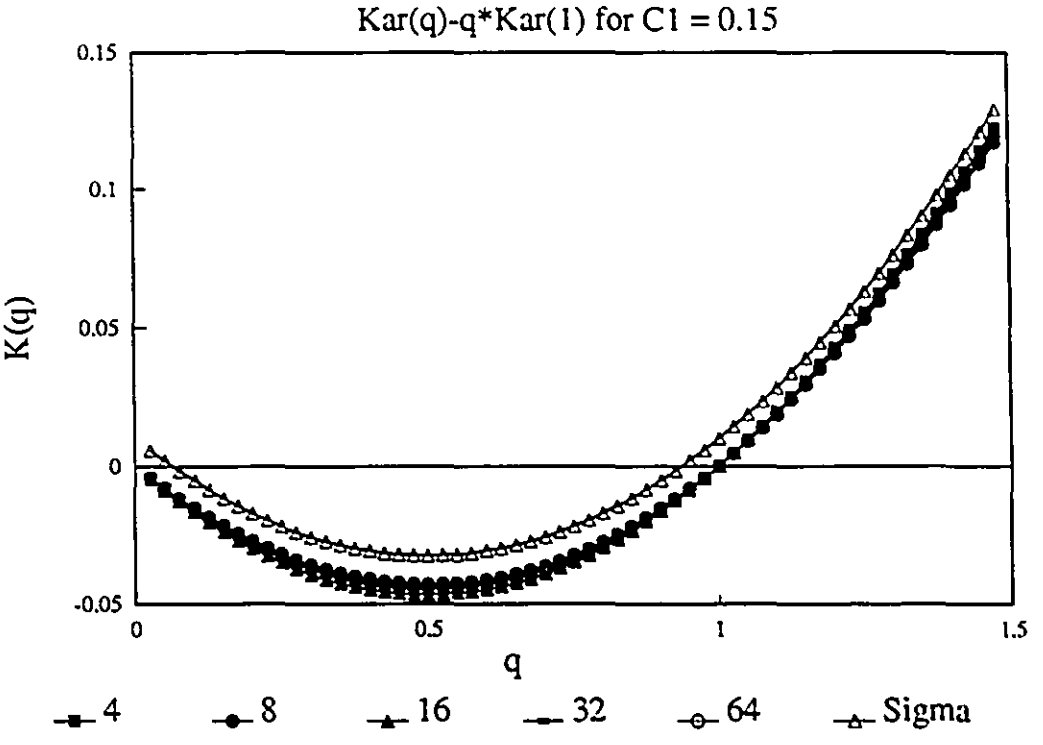

Figure 6.7: $K_{A,R}(q) - qK_{A,R}(1)$ plotted against q. The $\sigma(\vec{x})$ field has $C_1 = 0.15$. The K(q) function for the $\sigma(x)$ field is offset vertically to allow comparison.

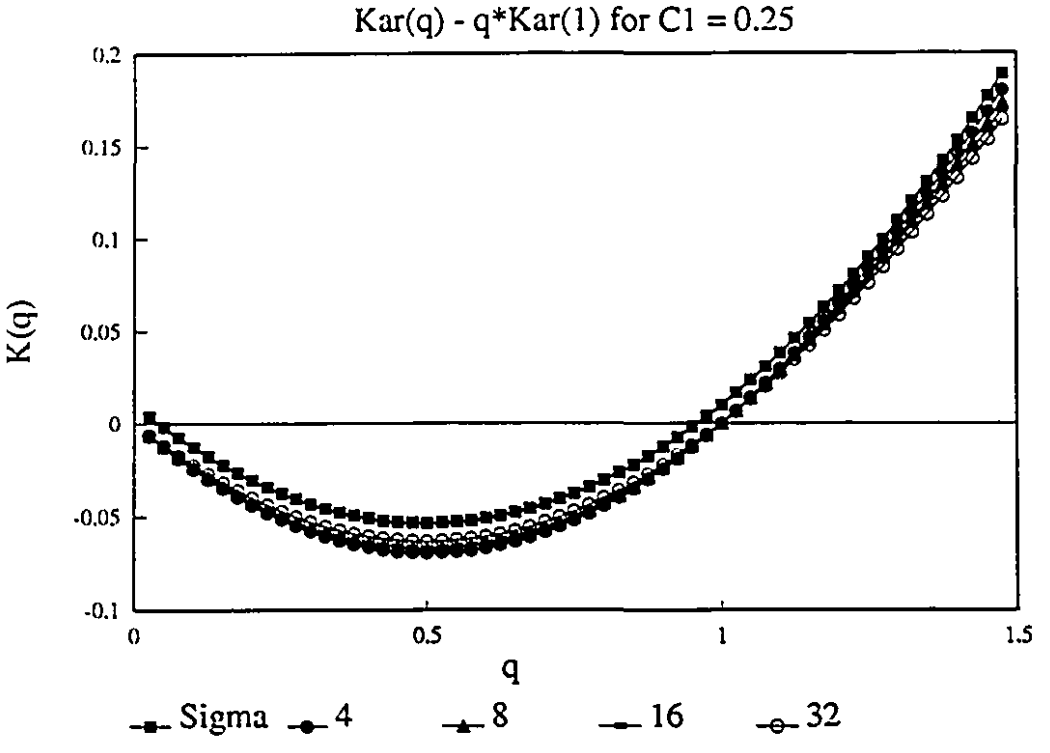

Figure 6.8: $K_{A,R}(q) - qK_{A,R}(1)$ plotted against q. The $\sigma(\vec{x})$ field has $C_1 = 0.25$. The K(q) function for the $\sigma(x)$ field is offset vertically to allow comparison.

In order to show that the results are general across all values of α the relationships for $\alpha = 1.5$ were computed and are plotted in figure 6.9 and 6.10. The values of α measured from the time series of echo fluctuations revealed α to be in the range 1.4 to 2. The results presented in the previous section suggest that $K_{A,R}(1)$ will depend upon α. Table 6.1 will reveal the dependence of $K_{A,R}(1)$ upon α.

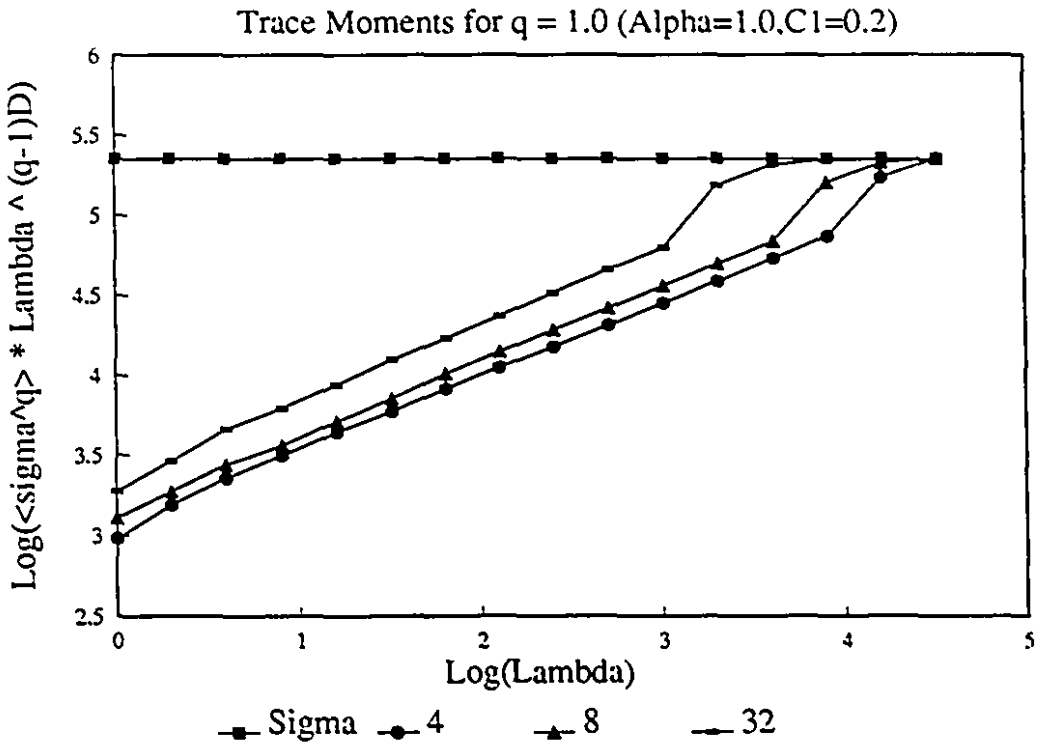

Figure 6.9: Scaling moments for q = 1.0, computed from $A(\vec{k},\vec{x})$, for $\sigma(\vec{x})$ with $\alpha = 1.5$ and $C_1 = 0.20$.

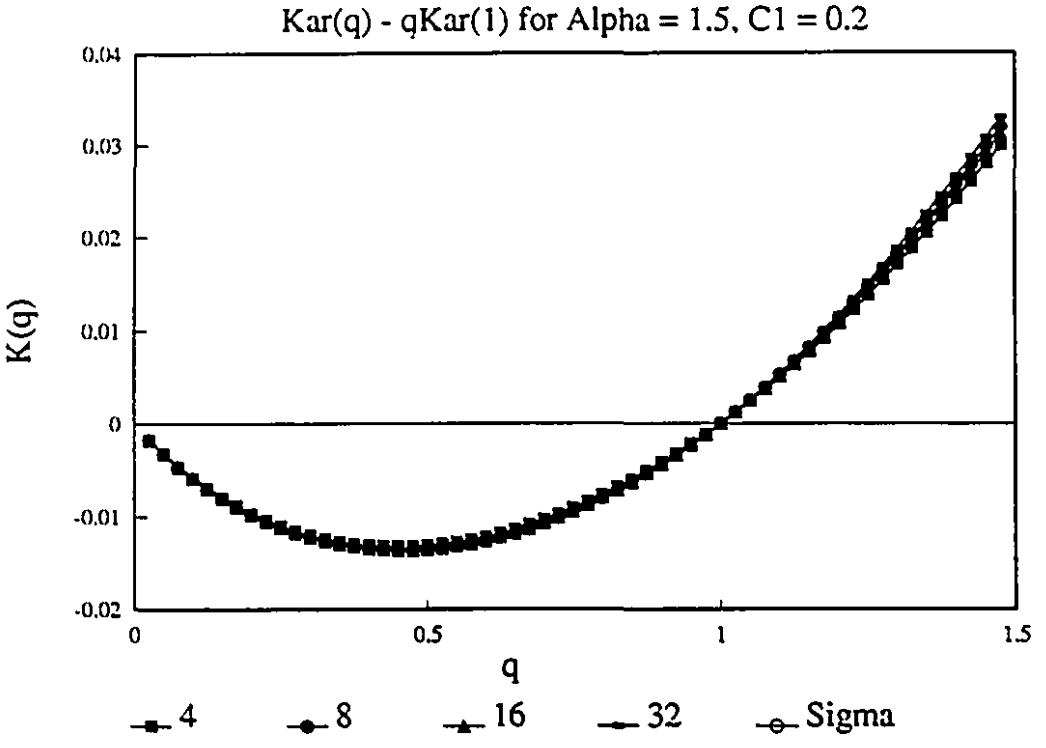

Figure 6.10: $K_{A,R}(q) - qK_{A,R}(1)$ plotted against q. The $\sigma(\vec{x})$ field has $\alpha = 1.5$ and $C_1 = 0.20$.

The Behaviour of $K_{A,R}(1)$.

$K_{A,R}(1)$ is expected to be independent of pulse volume scale or wavelength, and this is in fact observed. The dependence of $K_{A,R}(1)$ on the C_1 of the $\sigma(\vec{x})$ field is roughly linear, but the slope of the relation depends on α. Table 6.1 shows values of $K_{A,R}(1)$ for $\sigma(\vec{x})$ fields with $\alpha = 1.5$, $\alpha = 1.75$ and $\alpha = 2$ and with C_1 ranging from 0.1 to 0.55. Figure 6.11 shows the behaviour of $K_{A,R}(1)$ versus C_1 for the three values of α. The curves are computed to show that the relations appear to be general for rainfields with any α (we will take advantage of this in order to restrict the number of variable parameters in the space-time RCS model (see section 6.2)). The estimates of α and C_1 from $K_{A,R}(q) - qK_{A,R}(1)$ are consistent with those of the input $\sigma(\vec{x})$ fields.

Table 6.1: Values of $K_{A,R}(1)$.			
Input C_1	$\alpha = 2$	$\alpha = 1.75$	$\alpha = 1.5$
0.10	0.40 ± 0.02	0.45 ± 0.005	0.48 ± 0.005
0.15	0.36 ± 0.008	0.42 ± 0.005	0.48 ± 0.005
0.20	0.34 ± 0.005	0.40 ± 0.005	0.45 ± 0.005
0.25	0.30 ± 0.005	0.38 ± 0.005	0.44 ± 0.005
0.30	0.28 ± 0.005	0.36 ± 0.005	0.42 ± 0.005
0.35	0.25 ± 0.005	0.33 ± 0.005	0.40 ± 0.005
0.40	0.24 ± 0.005	0.31 ± 0.005	0.39 ± 0.005
0.45	0.22 ± 0.005	0.33 ± 0.005	0.35 ± 0.005
0.50	0.22 ± 0.005	0.31 ± 0.005	0.34 ± 0.005
0.55	0.19 ± 0.005	0.25 ± 0.005	0.33 ± 0.005

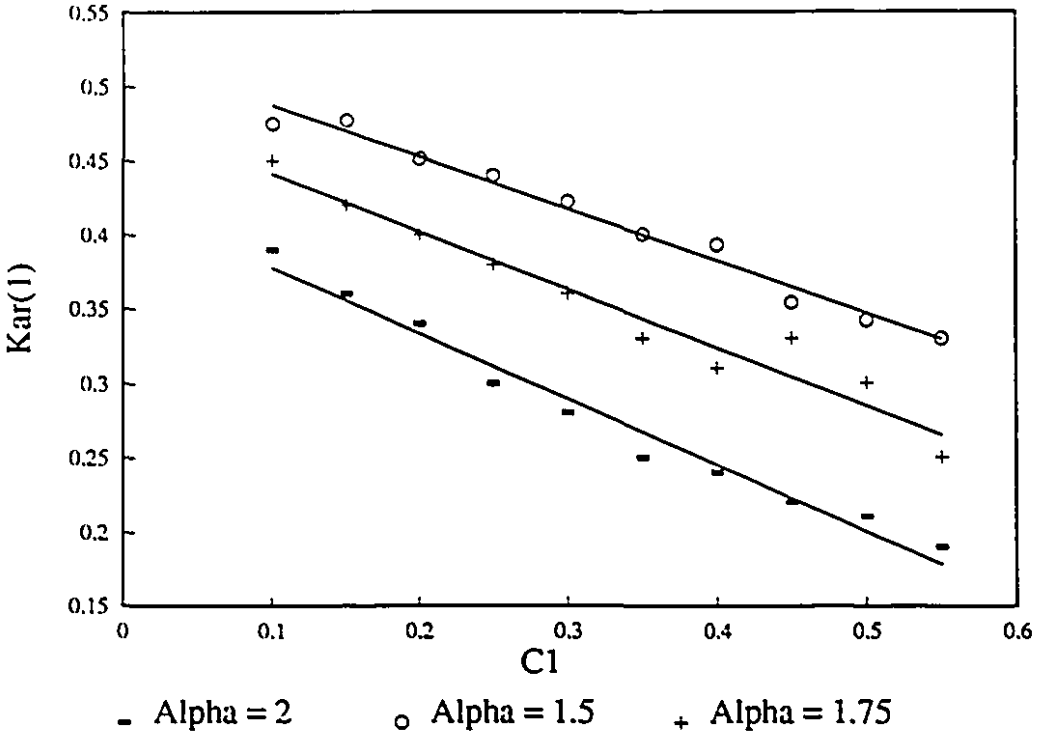

Figure 6.11: $K_{\Lambda,R}(1)$ plotted as a function of C_1 for $\alpha = 2$, $\alpha = 1.75$, and $\alpha = 1.5$.

The results of this section support the theoretical assertions as to the statistics of $Z_{\epsilon\lambda}$ presented in the previous section. The statistics of $Z_{\epsilon\lambda}$ from a scaling rainfield are therefore dependent on the measurement scales B_λ and λ_w. The standard theory of Marshall and Hitschfeld (1953) and Wallace (1953) or Lawson and Uhlenbeck (1950) have no such dependencies.

7.0 The Statistics of $Z_{e\lambda}(t)$ from a Temporally and Spatially Scaling Rainfield.

The temporal behaviours of $Z_{e\lambda}$ will be explored in this section using a simple space-time multiscaling model. The space-time model is referred to as the radar cross section (RCS) model in order to retain continuity with Duncan et al. (1992a,b). The temporal evolution of the spatial radar cross section field $\sigma(\vec{x})$ used in the last section will be simulated using 2D multifractal fields $\sigma(x,t)$. Intensities will be computed over the x-component (corresponding to columns) of the 2D $\sigma(x,t)$ fields and the evolution of the intensities in time is a function of the t-component (corresponding to rows) of the 2D $\sigma(x,t)$ fields. The 2D multiscaling model necessitates an assumption about the relation between spatial and temporal scaling. The simplest assumption concerning the temporal and spatial scaling is that they scale in the same way. The multifractals used to model the $\sigma(x,t)$ field will therefore be isotropic. However, this need not be the case as Generalized Scale Invariance (GSI) (Schertzer and Lovejoy, 1983) can be employed to change the temporal or spatial scaling exponents independently (see Pecknold et al. (1993) for a discussion).

The assumption of isotropy between temporal and spatial scaling exponents has implication to the arguments concerning the application of Taylor's hypothesis in the rainfield. Taylor's hypothesis was originally intended to allow fluctuation velocities in laboratory flows to be quantified relative to some mean motion (Taylor, 1938). In a multifractal, the variability at pregressively larger scales modulates the fluctuations at smaller scales in a scale invariant way. Thus, in a space-time representation there exists no 'mean' velocity, but rather a scale dependent 'average' velocity below which the 'fluctuations' can be defined. This relationship is of course scale inavariant in a multifractal and results in a velocity function that is an exponential function of scale. This would represent a scale invariant form of Taylor's hypothesis where the notion of a 'mean' flow velocity is replaced by a scale invariant velocity function. The consideration of scale dependent velocities and Taylor's hypothesis have been dealt with in Tessier et al. (1993).

The computations carried out in the space-time RCS model are straightforward. Two time series, one of reflectivity $Z_\lambda(t)$ and one of effective reflectivity $Z_{e\lambda}(t)$, are generated for each $\sigma(x,t)$ field. The computation for $Z_\lambda(t)$ is

Radar Cross Section Model

Construction Scales and Spectral Representation

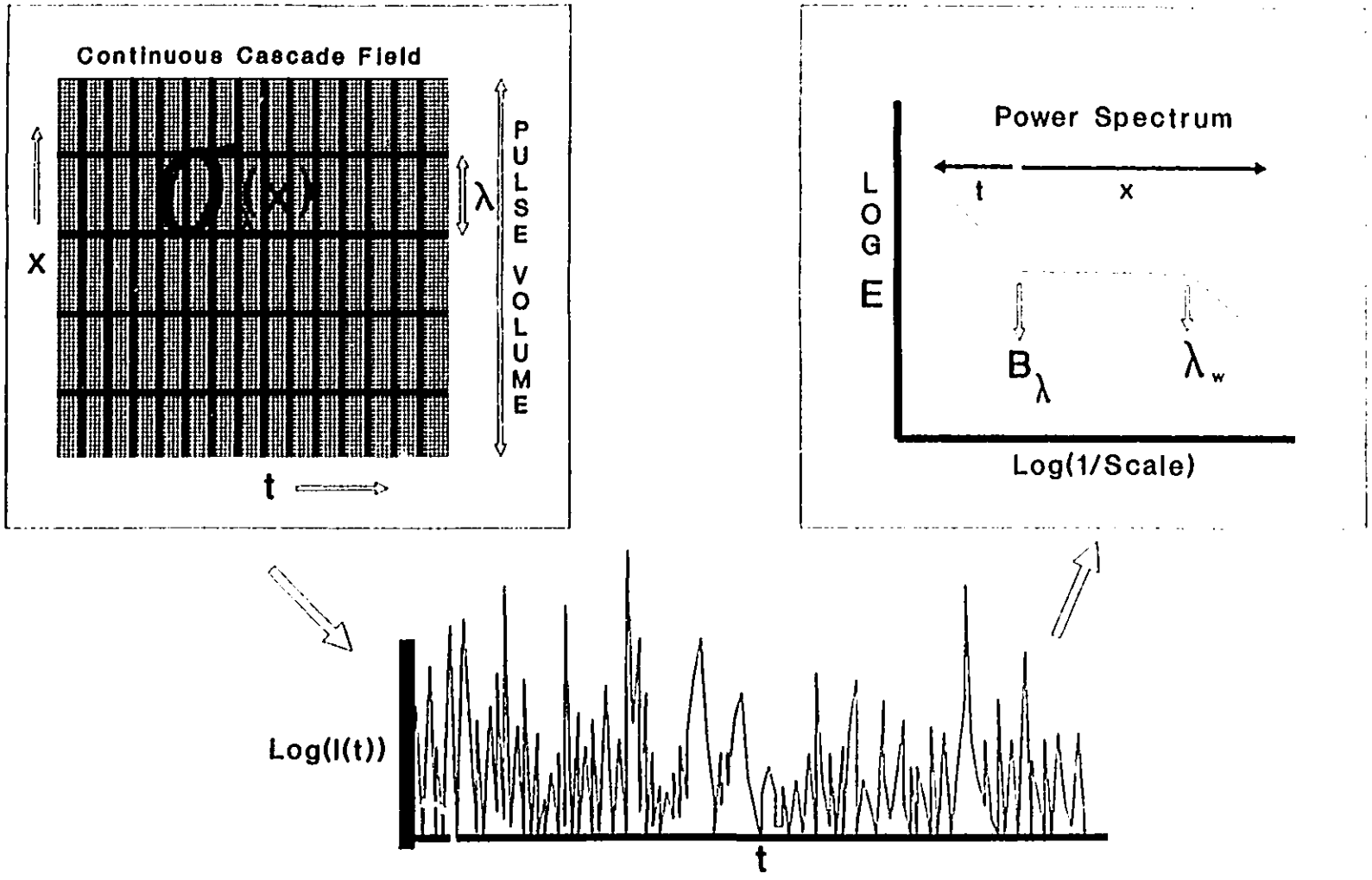

Figure 7.1: The scale relationships involved in the RCS model. The pulse volume scale B_λ and wavelength scale λ_u are translated into scaling breaks in the spectral representation of $Z_{e\lambda}(l)$

$$Z_\lambda(t) = \frac{1}{Vol(B_\lambda)} \int_{B_\lambda} \sigma(x,t)^2 dx \qquad (7.1)$$

and the computation for $Z_{\epsilon\lambda}(t)$ is

$$Z_{\epsilon\lambda}(t) = \frac{1}{Vol(B_\lambda)} \left| \int_{B_\lambda} \sigma(x,t) e^{ikx} dx \right|^2 \qquad (7.2)$$

where B_λ and λ_w will be given in units of pixels of the $\sigma(x,t)$ fields. The $\sigma(x,t)$ fields will be generated by the UMCG cascade generator described in appendix A. The range of scales available to the space-time model is limited to 2D arrays of 1024x1024 pixels. Figure 7.1 shows the relationships between the pulse volume scale B_λ and the wavelength scale λ_w on the spectral representation of the $Z_{\epsilon\lambda}(t)$ time series. The relation between the space scales B_λ and λ_w and their position on the spectrum of the time series is defined by the space time isotropy assumption. Thus, with isotropy, spatial scales of 64 pixels will appear at a frequency of f = 1/64. This relation could be changed by altering the relation between spatial and temporal scaling. Indeed, this may occur in the rainfield, but it cannot be quantified from a time series.

Due to the limited range of scales available with current computer resources the analysis of the artificial time series of $Z_\lambda(t)$ and $Z_{\epsilon\lambda}(t)$ will be restricted to two scale regimes that can be regarded as 'universal' to the radar measurement problem. The regimes of interest (see figure 7.1) are the low frequency scaling regime, given by small B_λ and small λ_w, and the high frequency scaling regime, given by large B_λ and large λ_w (with $B_\lambda > \lambda_w$). The ratio λ of scales in a realization of a time series for $Z_\lambda(t)$ or $Z_{\epsilon\lambda}(t)$ is $\lambda = 1024$ ($= L/\Gamma^{-1} = 1024/1$). Within the 1024 values of the artificial time series for $Z_{\epsilon\lambda}(t)$ the low frequency scaling, high frequency scaling, and plateau regimes coexist. The ratio of scales in the low frequency scaling regime is then $\lambda = 1024/B_\lambda$. The ratio of scales in the high frequency regime is given by the wavelength scale λ_w and can be increased by increasing λ_w.

7.1 Theory.

In this section some useful results will be drawn from chapter 6 on the spatial statistics of $Z_{\epsilon\lambda}$. The objective of the space-time model is to create time series of the fluctuating echo which

can then be analyzed in the same manner as those collected from the VPR. The results in chapter 6 reveal that α is unaltered by the transformation and that the results for specific α values are general. This allows a restriction on the parameter space of the RCS model to $\alpha = 2$. Another restriction on the parameter space of the RCS model results from the 2^{α} relation for the C_1 of the $\sigma(x,t)$ field and the C_1 of $Z_{\epsilon\lambda}$. The C_1 of the $\sigma(x,t)$ field will be restricted to values less than 0.25. This restriction is understandable by considering that if the C_1 of a time series exceeds 1 the ensemble mean of the process being considered will not be visible on any given time series. Consequently the reliability of statistical estimates made by either DTM or TM/GA will be compromised since they require a measurable ensemble mean.

Using the relations derived in chapter 6 we can anticipate the relation between the statistics of $Z_\lambda(t)$ and $Z_{\epsilon\lambda}(t)$ in the low frequency scaling regime. We examine the scaling of $Z_\lambda(t)$ and $Z_{\epsilon\lambda}(t)$ for $\lambda^{-1} > B_\lambda$ or at scales greater than the pulse volume scale. At these scales the behaviours of $Z_\lambda(t)$ and $Z_{\epsilon\lambda}(t)$ should reflect the fact that they are both squared measures of the $\sigma(x,t)$ field. Indeed, from

$$< Z_{\epsilon\lambda}^{q} > \;=\; \lambda^{K_{Z_\epsilon}(q)} \tag{7.3}$$

and

$$< Z_{\lambda}^{q} > \;=\; \lambda^{K_{Z}(q)} \tag{7.4}$$

we know, using relations 6.20 and 6.7 that

$$K_{Z_\epsilon}(q) = C_1((2q)^{\alpha} - 2q) + q(2K_{A,R}(1) - D) \tag{7.5}$$

and

$$K_{Z}(q) = 2^{\alpha} C_1 (q^{\alpha} - q) \tag{7.6}$$

which means that for the case of $\alpha = 2$,

$$K_{Z_\epsilon}(q) \;=\; 4C_1 q^2 \;+\; \text{terms...} \tag{7.7}$$

and

$$K_Z(q) = 4C_1q^2 + \text{terms...} \tag{7.8}$$

Thus, due to the construction of multifractals where large scale variability modulates the small scale, the small scale operations on the $\sigma(x,t)$ field are unimportant at large scales and the statistics of $Z_\lambda(t)$ and $Z_{\epsilon\lambda}(t)$ are similar within an approximation of terms of q of order 1. Therefore, estimates of multifractal parameters and spectral slopes from the low frequency scaling regime should be the same for both quantities.

The development of the statistical description of Z_λ and $Z_{\epsilon\lambda}$ in chapter 6 did not include the development for the distributions of singularities. The following development for the $c(\gamma)$ functions of both fields is necessary to interpret the numerical results that will follow. The distribution of singularities within the time series $Z_{\epsilon\lambda}(t)$ is governed by

$$Pr\left(Z_{\epsilon\lambda} > \lambda^{\gamma_{Z_\epsilon}}\right) = \lambda^{-c_{Z_\epsilon}\left(\gamma_{Z_\epsilon}\right)} \tag{7.9}$$

employing the Lengendre transform and using relation 6.20 we get

$$c_{Z_\epsilon} = \max_q\left(q\gamma_{Z_\epsilon} - \left(K_\nu(2q) + 2q\frac{K_{\Lambda,R}(1)}{2}\right)\right) \tag{7.10}$$

which can be rewritten

$$c_{Z_\epsilon} = \max_{2q}\left(2q\left(\frac{\gamma_{Z_\epsilon}}{2} - \frac{K_{\Lambda,R}(1)}{2}\right) - K_\nu(2q)\right) \tag{7.11}$$

which means that

$$c_{Z_\epsilon} = c_\nu\left(\frac{\gamma_{Z_\epsilon} - K_{\Lambda,R}(1)}{2}\right) \tag{7.12}$$

Thus, the operation of the Fourier component on the variability of $\sigma(x,t)$ (recall that $K_\sigma(q,\eta) \equiv K_\nu(q,\eta)$) results in a shift of the spectrum of singularities present in the $\sigma(x,t)$ field by $K_{\Lambda,R}(1)$. The shift is a reduction of the singularities by $K_{\Lambda,R}(1)$ which is a direct result of the dressing

operation (recall from section 3 that dressing (averaging) kills singularities). This is very important since the spectral and distributional behaviours of $Z_{\epsilon\lambda}(t)$ depend on the singularities present in the time series.

Relation 7.12 reveals a bias in the distributions of $Z_{\epsilon\lambda}(t)$ that differs greatly from the bias noted by Rogers (1971). The bias noted by Rogers (1971) is the result of averaging a quantity with a mean that varies in time and space. The bias in relation 7.12 results from the dressing by the radar of a complex quantity. A further bias can be introduced by averaging $Z_{\epsilon\lambda}$ values in cross range or downrange averaging schemes. The measurements made by Schaffner et al. (1980) represent the post-detection processing scenario and will reveal a bias for any type of rainfield variability. However, further analysis by Schaffner et al. (1980) might have revealed scaling behaviour. The existence of $K_{\Lambda,R}(1)$ results from sub-resolution variability and has not been dealt with previously. It affects all moments of the distribution at all averaging scales.

Further, the relation between $c_Z(\gamma)$ and $c_{Z_\epsilon}(\gamma)$ can be defined relative to $c_v(\gamma)$ and therefore to each other. Indeed, using relation 3.11 and restricting α to 2,

$$c_{Z_\epsilon}(\gamma) = c_v\left(\frac{\gamma - K_{\Lambda,R}(1)}{2}\right) = \frac{1}{4C_1}\left(\frac{\gamma}{2} + C_1 - \frac{K_{\Lambda,R}(1)}{2}\right)^2 \tag{7.13}$$

and

$$c_Z(\gamma) = \frac{1}{4C_1 2^2}(\gamma + C_1)^2 \tag{7.14}$$

which yields the relation between the singularities present in either time series,

$$c_Z(\gamma) = c_{Z_\epsilon}(\gamma - C_1 + K_{\Lambda,R}(1)) \tag{7.15}$$

when C_1 is small $K_{\Lambda,R}(1)$ is large and $Z_\lambda(t)$ has much larger singularities than $Z_{\epsilon\lambda}(t)$. The opposite is true when C_1 is large and $K_{\Lambda,R}(1)$ is small. The restriction of α to the value 2 has the deeper significance that it is the only value of α for which an identity of distributions between $Z_{\epsilon\lambda}$ and Z_λ

can be achieved (all other values of α will involve a shift and multiplication factor). This development reveals that if $C_1 = K_{A,R}(1)$ then $Pr(Z_\lambda) = Pr(Z_{\epsilon\lambda})$. This equality is found, using figure 6.11, at approximately $C_1 = 0.3$ (for the $\sigma(x,t)$ field with $\alpha = 2$).

The relations between the codimension functions of $Z_{\epsilon\lambda}(t)$ and $Z_\lambda(t)$ are necessary to interpret the spectral behaviour of the artificial time series as well as the distributional behaviour. The first thing that relation 7.15 reveals is that a relative bias between distributions of $Z_{\epsilon\lambda}(t)$ and $Z_\lambda(t)$ are dependent upon C_1 and $K_{A,R}(1)$, which is itself dependent upon C_1. Using relation 7.15 we can also speculate on the spectral energy of the time series of $Z_{\epsilon\lambda}$ and Z_λ. If $C_1 < K_{A,R}(1)$ the total spectral energy of $Z_\lambda(t)$ will be greater than that of $Z_{\epsilon\lambda}(t)$ due to the presence of increased singularities. If $C_1 < K_{A,R}(1)$ then the reverse is true. Thus, the relative spectral energies of $Z_{\epsilon\lambda}(t)$ and $Z_\lambda(t)$ are dependent upon C_1 and $K_{A,R}(1)$.

The statistics of $Z_\lambda(t)$ and $Z_{\epsilon\lambda}(t)$ would be expected to differ markedly for scales smaller than B_λ. In the case of $Z_{\epsilon\lambda}(t)$ we expect to find the spectral plateau associated with the pulse volume scale. In the case of $Z_\lambda(t)$ a corresponding scaling break at the pulse volume scale B_λ, separating the low frequency scaling regime from the high frequency scaling regime, would be expected. Statistics at scales B_λ reflect the modulation by larger scale variability. The statistics of scales smaller than B_λ are within the correlation length associated with B_λ, and hence are not easily described. The nature of the statistics in the high frequency scaling regime of both $Z_\lambda(t)$ and $Z_{\epsilon\lambda}(t)$ admit the likelihood that the statistics cannot be described in terms of universal multifractals (see section 7.3.4). The statistics will be explored in terms of a 'projection' of the spatial variability of the $\sigma(x,t)$ field onto the time axis. This 'projection' will involve the modification of available singularities due to dressing and modification of the $c(\gamma)$ function to a form different from that predicted under universality.

In summary, we expect a shift in singularity as a function of C_1. This shift will be reflected in spectral as well as distributional behaviours. Further, it is expected that the statistics of the low frequency scaling regimes of $Z_\lambda(t)$ and $Z_{\epsilon\lambda}(t)$ to be almost identical. A scaling break in the artificial time series is also expected to coincide with the pulse volume scale B_λ. The break in the time

series of $Z_{\epsilon,\lambda}(t)$ should be more obvious that that in $Z_{\lambda}(t)$ due to the prescence of the spectral plateau. The numerical explorations and results of these theoretical assertions will be presented in section 7.3.

7.2 The Parameter Space of the RCS Model.

The total parameter space of the model is potentially very large. The free parameters used to model $Z_{\epsilon,\lambda}$ include the multifractal parameters α, C_1, and H as well as the measurement scales B_{λ} and λ_w. The H parameter will generally be kept at 0 for the current study. The value of α will be kept at 2. The truly interesting parameters are B_{λ}, λ_w and C_1. However, C_1 will be restricted to values between 0 and 0.25 for reasons presented in the previous section. Table 7.1 outlines the range of these parameters investigated with the RCS model. Of the ranges of parameters shown in table 7.1 only select values will be depicted in the following analysis. Many of the combinations of the values present in table 7.1 are uninteresting and were used to isolate the interesting behaviours.

Table 7.1: Ranges of RCS model parameters explored.

Parameter	Range
Grid Scale	1024 x 1024
Pulse Volume B	8, 16, 64, 128, 256, 1024
Wavelength λ_w	4, 8, 16, 32, 64, 128, 256, 512
C_1	0.01 to 0.25 at increments of 0.02.

A shorthand notation is employed to identify the parameters used in constructing the UMCG fields as well as each artificial intensity time series. The notation for the UMCG fields is UMCG(C_1,H) indicating a multifractal field with specific C_1 and H (α is held constant at 2.0). The notation for parameters of the RCS model used to create artificial time series is RCS(Pulse Volume scale, Wavelength scale, C_1, H) or RCS(B_{λ}, λ_w, C_1, H). An example would be RCS(256,8,0.07,0.1) where B_{λ} is 256 pixels, λ_w is 8 pixels, C_1 is 0.07 and H is 0.1.

An alternative to the numerical RCS model was explored. Appendix C contains the first few lines of an early analytical formulation for the problem of reproducing the spectra of time series of the fluctuating echo assuming that the radar cross section field is scaling. The analytical expression involves the four point correlation functions of log-normal multifractals. Integration of these functions was found to be more CPU intensive than the numerical model and the approach was abandoned.

The RCS model is used to create time series of $Z_\lambda(t)$ and $Z_{\epsilon\lambda}(t)$ from realizations of 2D multifractal variability created by the UMCG. The time series comprise 1024 values. Repetition of the model create independent time series for the same set of input parameters. Generally, 256 independent runs of the RCS model were performed to create adequate quantities of data to explore the model parameter space and verify the theoretical assertions. The effect of fixed model runs can be analysed using sampling dimension (relations 3.15 through 3.18). For the analyses of the low frequency scaling regime (see below) N_s is 256, λ is 32, α is 2, and C_1 ranges from 0.04 to 1 (recall the 2^α result). Thus q_s ranges from 8 for $C_1 = 0.04$ to 1.6 for $C_1 = 1$. This effect can actually be discerned in figures 7.17 and 7.18 as the point at which the universal curves bend over at progressively lower η-values for higher C_1. The effect is not likely to be severe since it can be account for exactly, but the limitations of computer resources (and time) had to be taken into account.

7.3 Numerical Results.

This section will proceed as follows: Section 7.3.1 will present examples of the time series created by the RCS model. Section 7.3.2 will present general observations of the spectral behaviours of $Z_{\epsilon\lambda}(t)$ and $Z_\lambda(t)$ with emphasis on the dependencies of spectral appearance on B_λ and λ_w. Section 7.3.3 will examine the statistical nature of the low frequency scaling regime in depth. Section 7.3.4 will examine the statistical nature of the high frequency scaling regime.

7.3.1 The Time Series of $Z_{e\lambda}$ and Z_{λ} Created by the RCS Model.

This section provides some observations of the time series of the fluctuating echo created with the RCS model. The outer scale of the time series of $Z_{\lambda}(t)$ and $Z_{e\lambda}(t)$ is 1024 values. Statistics are computed over 256 independent realizations of each time series with the same set of input values.

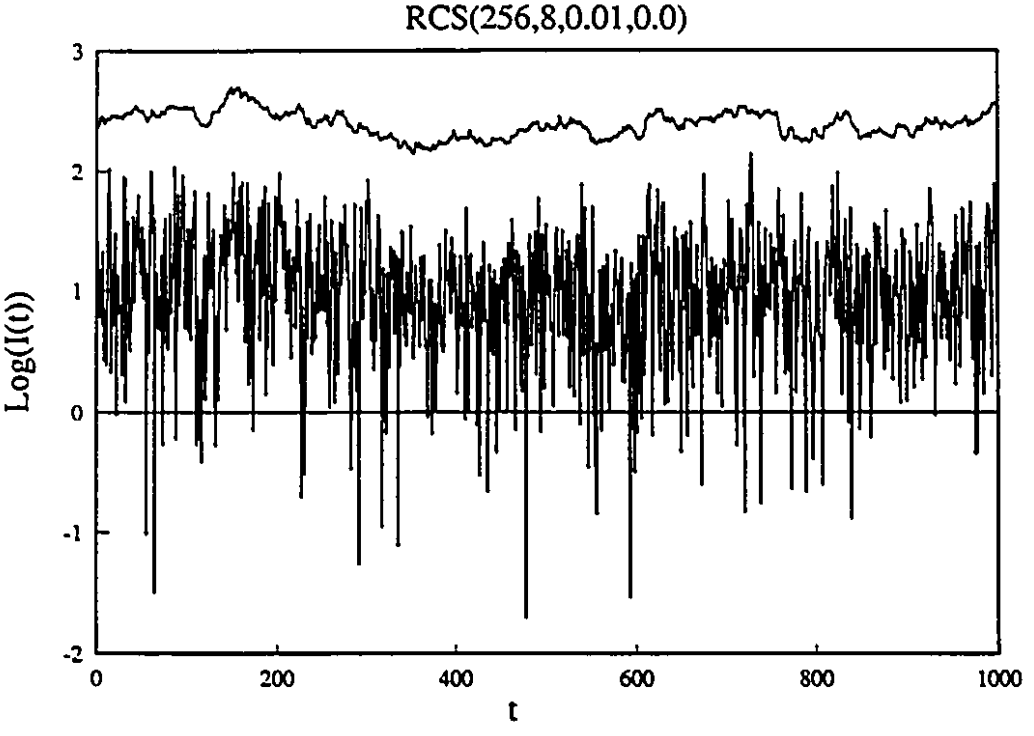

Figure 7.2: $Z_{\lambda}(t)$ and $Z_{e\lambda}(t)$ for RCS(256,8,0.01,0.0). The top curve is $\mathrm{Log}_{10}(Z_{\lambda}(t))$ and the bottom curve is $\mathrm{Log}_{10}(Z_{e\lambda}(t))$.

The effect of the complex spatial 'dressing' implied by the integral over $(\sigma(x,t)e^{i\omega_n})$ is clearly visible when $Z_{\lambda}(t)$ and $Z_{e\lambda}(t)$ are plotted together. Figure 7.2 shows 1000 elements of the

two time series plotted side by side for a C_1 of 0.01. Due to the spectral plateau (below), the high frequencies are more pronounced in $Z_{\epsilon\lambda}(t)$ than in $Z_\lambda(t)$, hence the differences in appearance. According to the data analysis sections a C_1 of 0.01 would be unrealistic, but it serves a purpose in the demonstration. Figure 7.3 shows the distribution of the values plotted in figure 7.2. 256 realizations of 1024 elements of each time series are used to compute the distributions depicted in figure 7.3. For low C_1, as in figures 7.2 and 7.3, the widening of the distribution of $Z_{\epsilon\lambda}(t)$ over $Z_\lambda(t)$ by the Fourier computation is quite pronounced. However, the order of singularity is much smaller as is predicted by relation 7.15. The shape of the distribution of $Z_{\epsilon\lambda}(t)$ is suggestive of a Rayleigh distribution, but is in fact a log-normal distribution. The Rayleigh is plotted for comparison. The similarity of the distribution of $Z_{\epsilon\lambda}$ to the Rayleigh is superficial. The $Z_{\epsilon\lambda}$ distribution is derived from a highly correlated field. None of the values of $Z_{\epsilon\lambda}$ can be considered independent. The centering, or bias, of the distribution is given by relation 7.15.

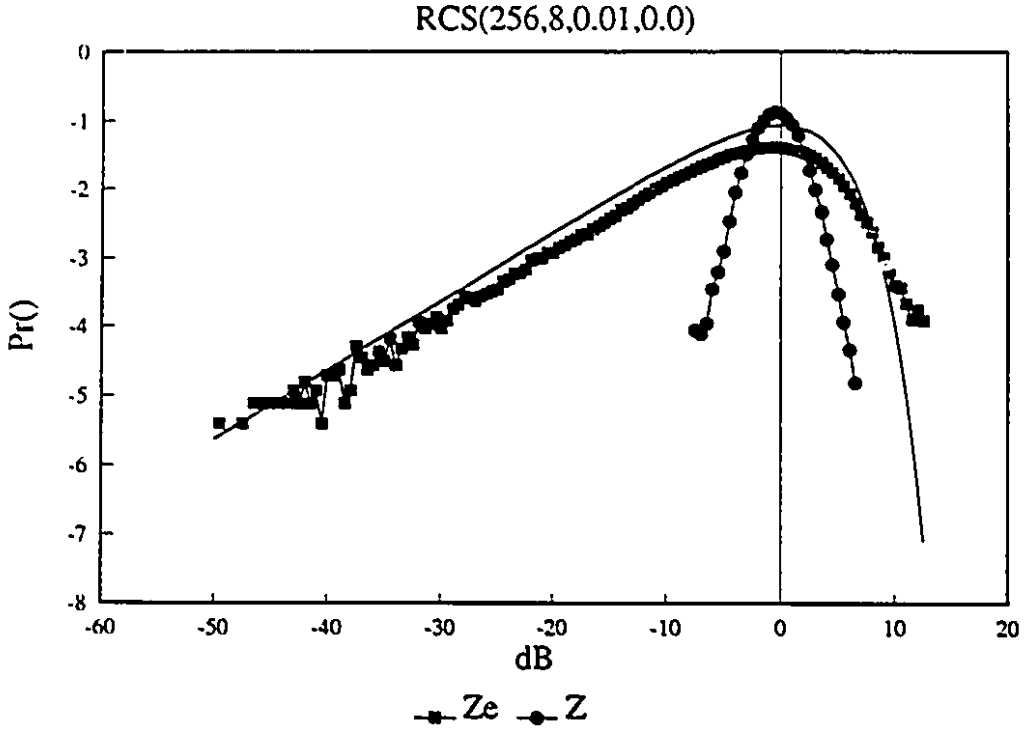

Figure 7.3: Centered distributions of Z_λ and $Z_{e\lambda}$ for RCS(256,8,0.01,0.0). The Rayleigh distribution is plotted as a line for comparison.

Comparison of figures 7.2 and 7.4 reveals the marked increase in the variability of $Z_{e\lambda}(t)$ and $Z_\lambda(t)$ as the C_l of the $\sigma(x,t)$ is increased. However, the relative increase is as qualitatively predicted by relation 7.15. Figure 7.4 reveals that $C_l = 0.05$ results in a $Z_{e\lambda}(t)$ with a dynamic range that overlaps that of $Z_\lambda(t)$. The data analysis suggests that a C_l of 0.05 for the $\sigma(x,t)$ is not too far from the measured $C_l \sim 0.1$. Comparison of the distributions plotted in figures 7.3 and 7.5 reveals that the distribution of $Z_\lambda(t)$ widens quickly as a function of increasing C_l.

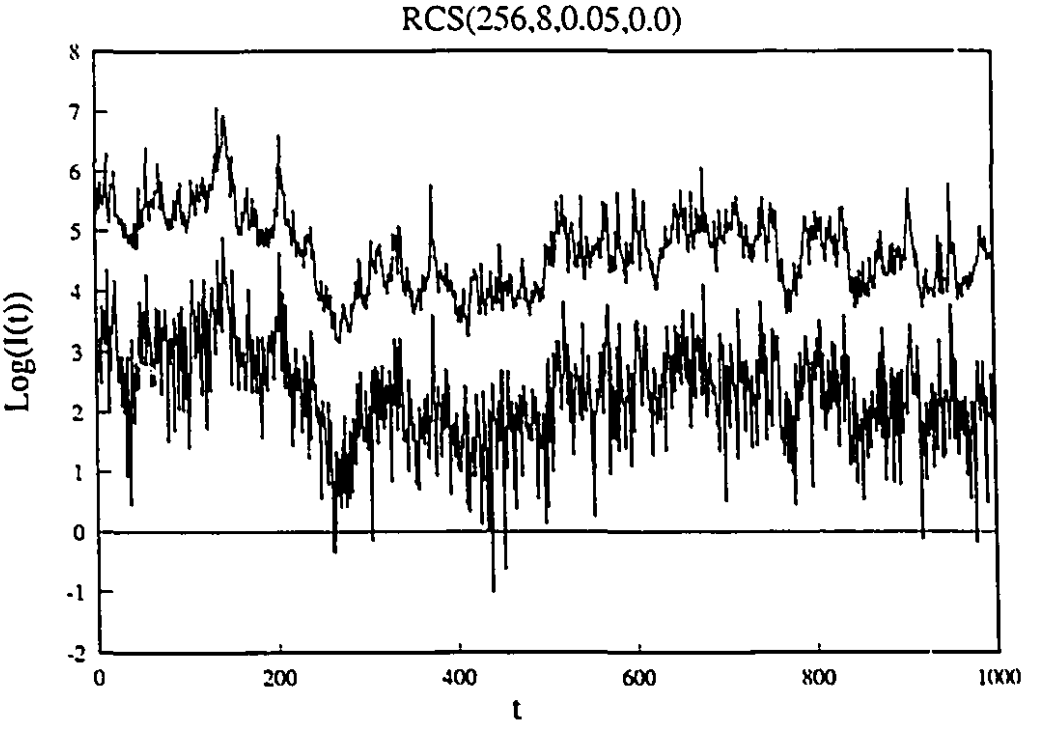

Figure 7.4: $Z_\lambda(t)$ and $Z_{\epsilon\lambda}(t)$ for RCS(256,8,0.05,0.0). The top curve is $\{\mathrm{Log}_{10}(Z_\lambda(t)) + 2\}$ and the bottom curve is $\mathrm{Log}_{10}(Z_{\epsilon\lambda}(t))$. The factor 2 is added to separate the two curves.

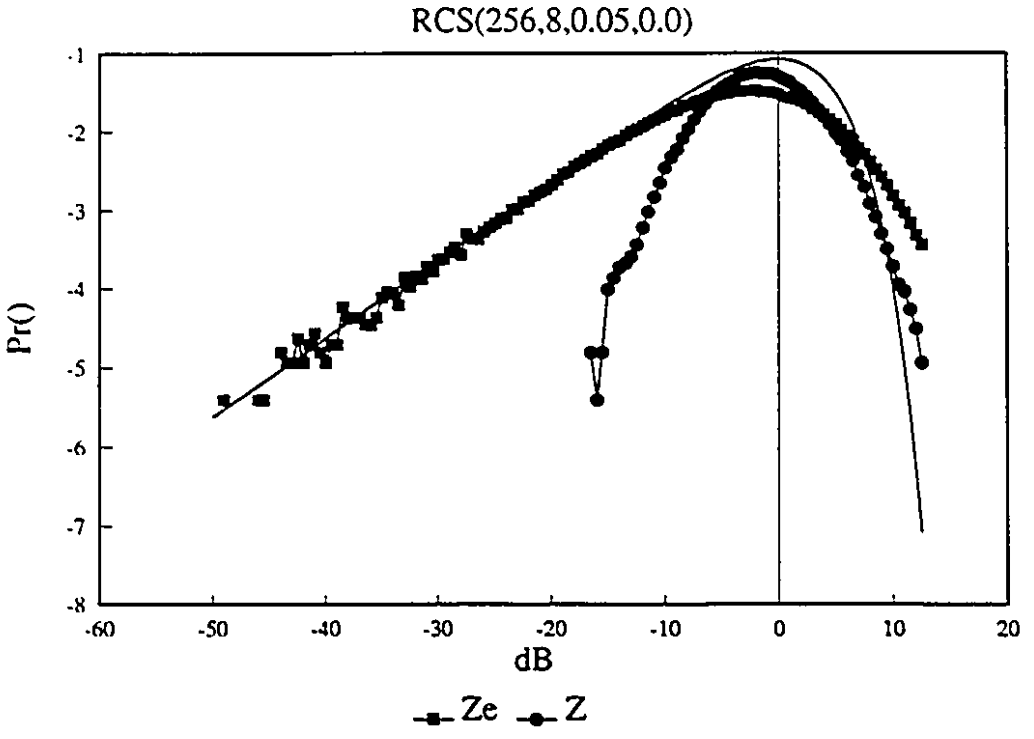

Figure 7.5: Distributions of Z_λ and $Z_{e\lambda}$ for RCS(256,8,0.05,0.0). The Rayleigh distribution is plotted for comparison.

From an experimental perspective the apparent proximity of the distribution of $Z_{e\lambda}(t)$ to the Rayleigh represents a potential problem. The shape of the distributions is a product of the Fourier component calculation, one for Poisson variability and one for scaling variability. The definition of a Poisson distribution (see Vanmarcke, 1983) requires the variability to be Poisson. The two distributions are tremendously different in the sense that the distribution of $Z_{e\lambda}(t)$ from a multiscaling field is entirely dominated by the algebraic tail. Which means that the distribution with the Rayleigh appearance actually has the description $Pr(Z_{e\lambda} > \lambda^\gamma) \approx \lambda^{-c_{Z_e}(\gamma)}$. Observation of this tail requires that adequate data is collected (i.e. D_s must be high enough). The amount of data required to distinguish this distributional behaviour from the Rayleigh behaviour is likely

prohibitive with operational radar scales and ranges considering the scale dependence of the distributions. The initial implication is that the data of Lhermitte and Kessler (1966) would be inadequate to rule out the possibility that the distribution resulted from a scaling rainfield.

7.3.2 General Observations of the Spectral Behaviours of $Z_\lambda(t)$ and $Z_{\epsilon\lambda}(t)$.

A spectral analysis of $Z_\lambda(t)$ and $Z_{\epsilon\lambda}(t)$ from the RCS model reveals the characteristic shape noted in the spectral analysis of echo fluctuation time series A through I (see figure 7.6). Figure 7.6 was produced to enhance the resolution on the scale breaks and has an outer scale of 2048 pixels. Each spectrum represents an average of 256 spectra of the 1024 intensities comprising each time series. This section will explore the general spectral characteristics of the artificial time series of $Z_\lambda(t)$ and $Z_{\epsilon\lambda}(t)$.

The Re-creation of the Pulse Volume Plateau.

The most obvious features revealed by spectral analysis of $Z_{\epsilon\lambda}(t)$ are the three spectral regions (figure 7.6). The scales on either side of the plateau correspond exactly to the pulse volume scale B_λ at the low frequency end and λ_w at the high frequency end. The extent of the scaling behaviour of the low frequency scaling regime can therefore be controlled by adjusting B_λ and the extent of the high frequency scaling regime can be adjusted by altering λ_w.

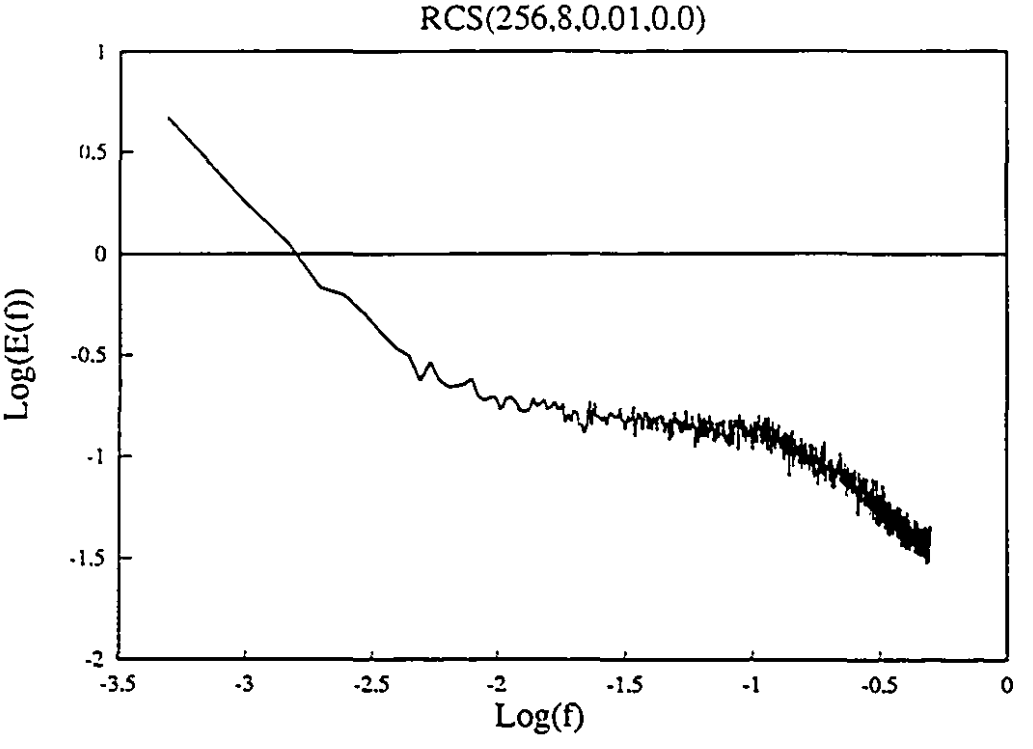

Figure 7.6: Average spectrum of $Z_{\epsilon\lambda}(t)$ resulting from the RCS model (this spectrum has an outer scale of 2048 pixels). The spectrum is an average of 256 spectra of 2048 intensities. The wavelength scale is 8 pixels (log(f) = -0.9). The pulse volume scale is 256 pixels (log(f) = -2.4).

The Dependence of Spectral Energy on C_1.

General observations about the spectral behaviour of $Z_\lambda(t)$ and $Z_{\epsilon\lambda}(t)$ that result from the RCS model are as follows: The total spectral energy is a strong function of C_1. This is a straightforward result when it is considered that $c(\gamma) = \frac{1}{\lambda C_1}(\gamma + C_1)^2$, which means that the singularities present in the time series are quadratic function of the C_1 of the $\sigma(x,t)$ (i.e. the variance increases quickly with C_1). Figure 7.7 shows the spectra of $Z_\lambda(t)$ computed at increasing values of C_1 with the corresponding spectra for $Z_{\epsilon\lambda}(t)$ in figure 7.8. Figure 7.7 shows that the spectral slope β of $Z_\lambda(t)$ is also a function of C_1 as expected from the relation $\beta = 1 - K(2,2)$. This relation is less obvious in figure 7.8 due to the strong scaling breaks.

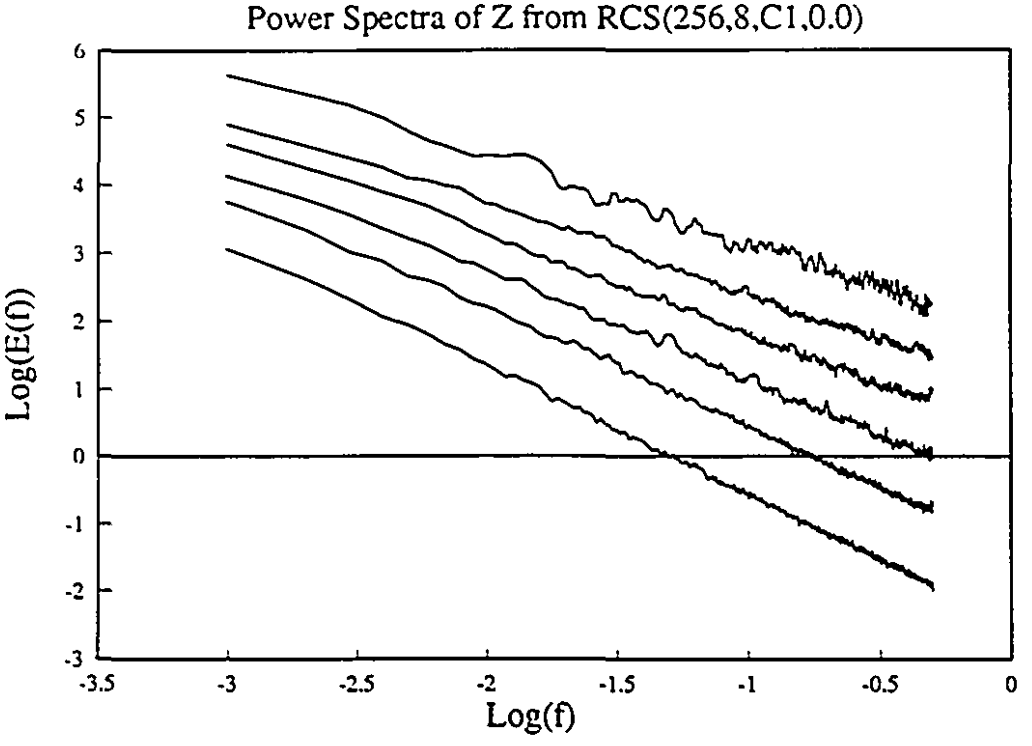

Figure 7.7: Spectra of $Z_\lambda(t)$. The bottom line is for $C_1 = 0.01$ and successively higher lines are at 0.02 increments of C_1.

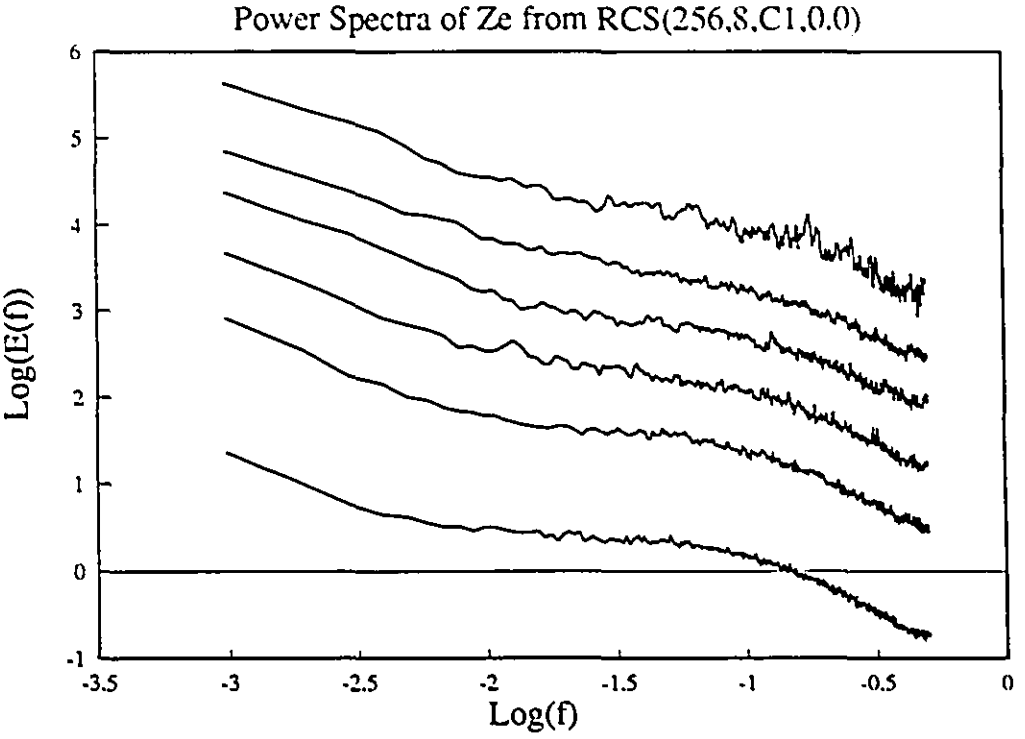

Figure 7.8: Spectra of $Z_{e\lambda}(t)$. The bottom line is for $C_1 = 0.01$ and successively higher lines are at 0.02 increments.

The relative spectral energy of $Z_\lambda(t)$ and $Z_{e\lambda}(t)$ is a function of C_1 as predicted by relation 7.15, which shows the relative ranges of singularities available to each. Increasing the value of C_1 of the $\sigma(x,t)$ field results in higher spectral energies for both curves as was shown in figures 7.7 and 7.8, but figures 7.9 and 7.10 show that the spectral energy of $Z_{e\lambda}(t)$ increases at a faster rate for increasing C_1, again as expected from relation 7.15 due to the effect of $K_{\Lambda,R}(1)$. The spectra in figure 7.10 show a great deal more noise than those in figure 7.9. The increasing variance of $\sigma_\lambda(x,t)$ as a function of C_1 as well as the limited ratio of scales available affects the quality of the spectra.

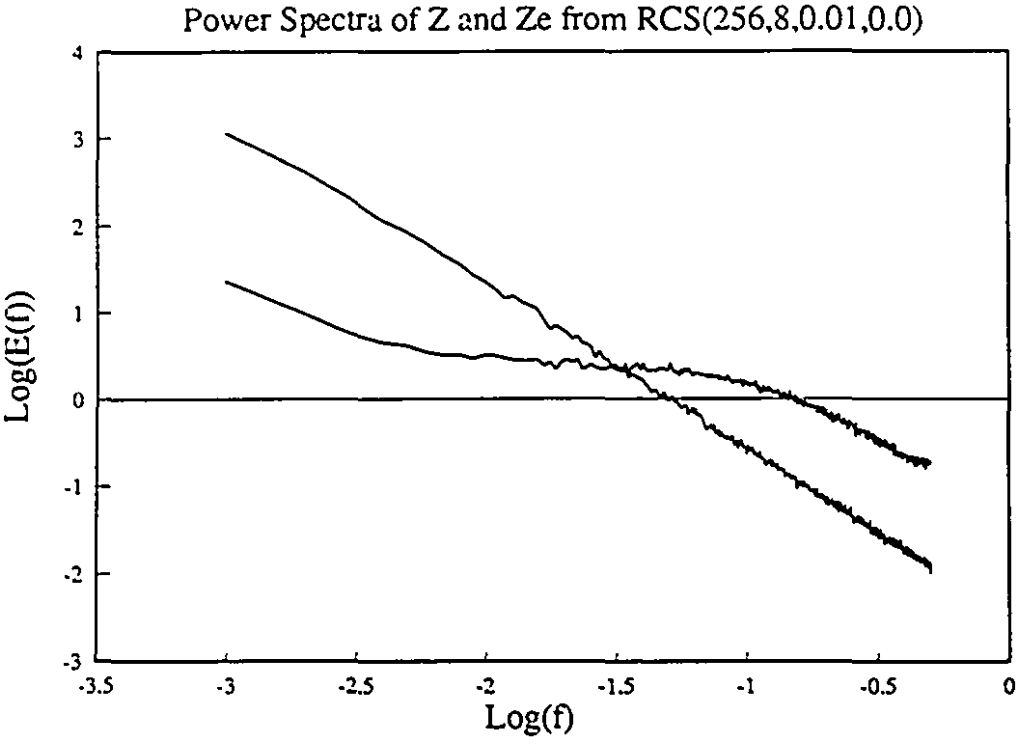

Figure 7.9: Power spectra of $Z_\lambda(t)$ and $Z_{e\lambda}(t)$ for RCS(256,8,0.01,0.0). The axes are log of frequency and log of spectral energy (or variance per unit wavelength) making the curve for $Z_\lambda(t)$ a power law (the power law has a scaling break at log(f) = -2.4 (see below)). The time series of $Z_\lambda(t)$ and $Z_{e\lambda}(t)$ resulted from exactly the same variability controlled by C_1 = 0.01. The un-obvious scaling break in $Z_\lambda(t)$ occurs at log(f) = -2.4.

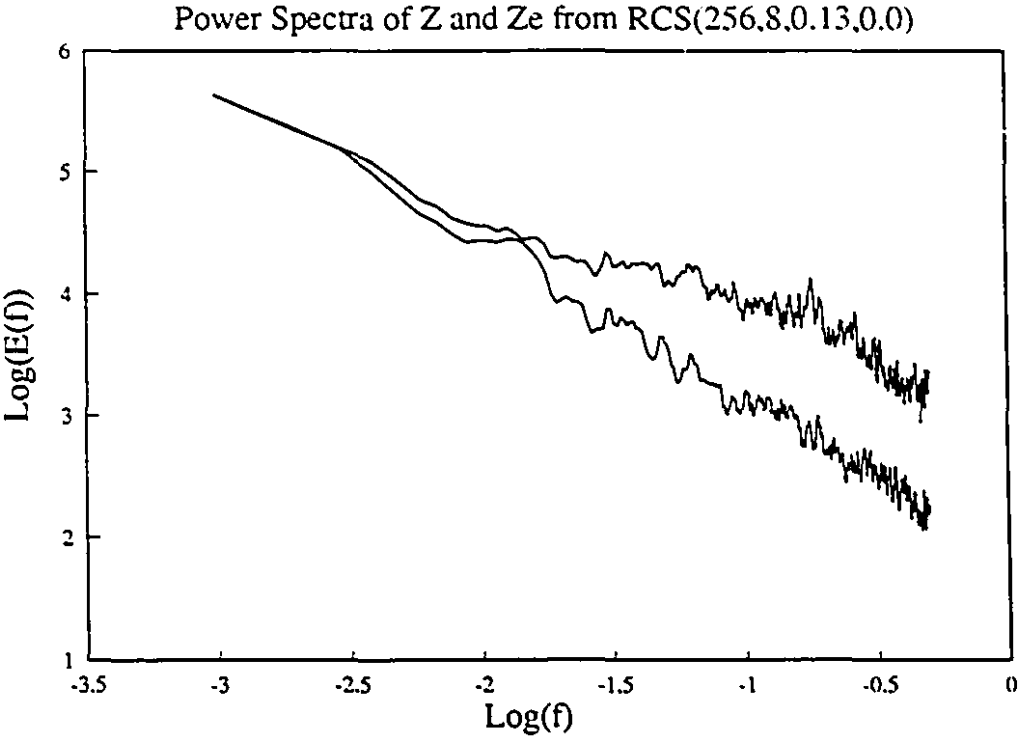

Figure 7.10: Power spectra of $Z_\lambda(t)$ (bottom curve) and $Z_{e\lambda}(t)$ (top curve) for RCS(256,8,0.13,0.0). The axes are labelled as in figure 7.9.

The Effect of Pulse Volume Scale B_λ

The pulse volume scale serves to divide the spectra into two effectively different statistical regimes. There exists a scale break on the spectra of both $Z_\lambda(t)$ and $Z_{\epsilon\lambda}(t)$ at Log(Scale = $1/B_\lambda$)). The statistics on either side of the break are distinct for the two time series. Aside from the obvious spectral plateau of $Z_{\epsilon\lambda}(t)$ the statistics of both time series at scales λ^{-1} smaller than the pulse volume scale B_λ are not universal multifractals and will be dealt with below. The statistics of the time series at scales greater than the pulse volume are the result of modulation, by the large scale temporal variability, which is a universal multifractal.

The alteration of the pulse volume scale B_λ has the straightforward effect of moving the scaling breaks in the power spectra of $Z_\lambda(t)$ and $Z_{\epsilon\lambda}(t)$. In both cases increasing B_λ causes the break to extend to progressively lower frequencies. Another general observation is that spectral energy increases with increasing pulse volume scale. The movement of the scale break with increasing B_λ for $Z_{\epsilon\lambda}(t)$ is shown in figure 7.11. Three curves appear in figure 7.11, the top curve was computed with B_λ = 256 pixels, the middle curve was computed with B_λ = 128 pixels, and the bottom curve was computed with B_λ = 64 pixels. This result reflects the fact that larger pulse volumes contain more variance and result in high spectral energies. All three curves were computed with a fixed wavelength of λ_w = 8 pixels. The plateau of the top curve extends further towards low frequencies. The bottom curve, which has the smallest pulse volume, has the shortest plateau. Note that the high frequency endpoint of the plateau, due to λ_w, is the same for all three curves.

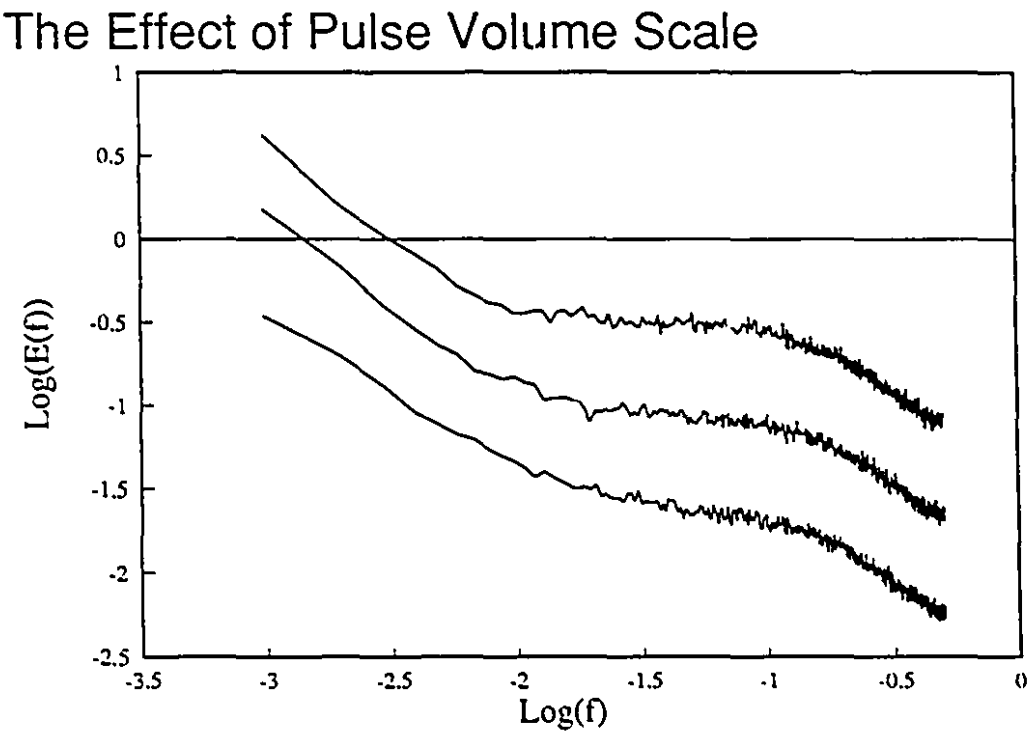

Figure 7.11: Spectra of three realizations of the RCS model with changing pulse volume scale. The top spectrum has a pulse volume scale of 256 pixels, the middle spectrum has a pulse volume scale of 128 pixels, and the bottom spectrum has a pulse volume scale of 64 pixels.

The break in the scaling of $Z_\lambda(t)$ is less pronounced as it has no spectral plateau indicating its presence. In figure 7.12 regression lines have been fit to the spectrum on either side of the scale break. The scale break occurs at the 'frequency' corresponding to the pulse volume scale B_λ which is set at 64 pixels, hence the break is at Log(1/64) = -1.8. The scale breaking operation is idealized in figure 7.13. The figure shows a transition zone around the scale break. If statistics of $Z_\lambda(t)$ or $Z_{\epsilon\lambda}(t)$ are to be compiled it must be at scales far removed from the transition zone.

Figure 7.12: A power spectrum of $Z_\lambda(t)$ showing the break in scaling due to the pulse volume scale B_λ. The scaling break is emphasized using regression lines fit to the two scaling regimes, the break is where the regression lines cross. The exponent of the low frequency regime is -1.26 and that of the high frequency regime is -1.66.

Spectral Scaling Breaks in Z(t) and Ze(t)

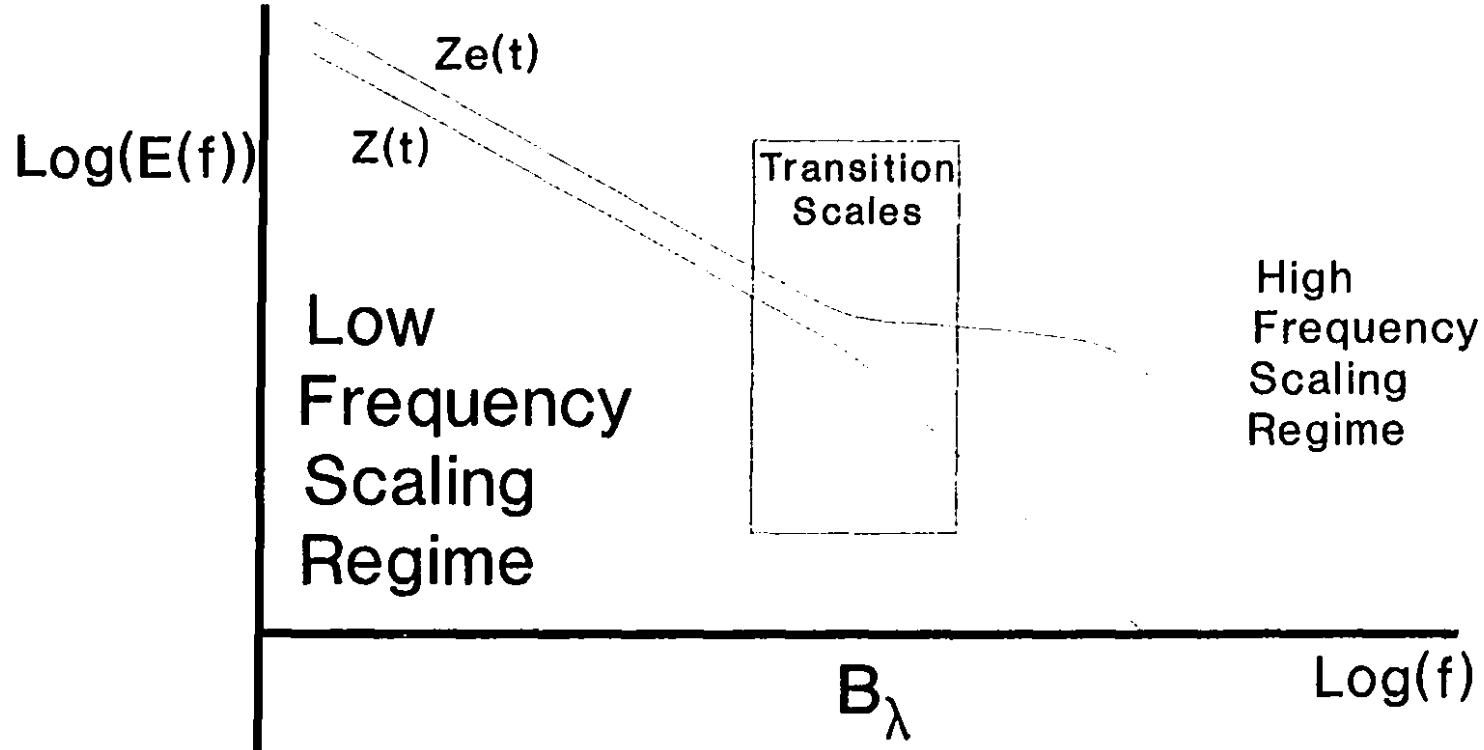

Figure 7.13: An idealization of the spectral representations of $Z_{e\lambda}(t)$ and $Z_\lambda(t)$ emphasizing the scaling break due to the pulse volume B_λ. The zone around the break is marked as a 'transition' zone where the statistics are expected to change from the relatively simple forms at low frequency to the forms at high frequency. Estimates of statistical parameters should be taken from scales much larger or much smaller than the scale break.

The Effect of Wavelength Scale λ_w.

The spectral dependence upon the wavelength scale affects only $Z_{e\lambda}(t)$ and gives a straightforward break at $f = 1/\lambda_w$. Figure 7.14 shows that as wavelength increases (by factors of 2 from bottom to top) the spectral slope appears to be a function of wavelength. It is only at wavelengths in excess of 64 pixels that the high frequency scaling regime seems uncontaminated by the transition zone about the break point. The figure also shows how the scaling break associated with λ_w moves towards lower frequencies as the wavelength increases. For $\lambda_w > 64$ pixels we can attempt to analyse the statistics of the high frequency scaling regime. The difficulties with this regime will be dealt with in section 7.3.4.

In terms of measurements made by most operational radar systems this result would imply that data taken in this scale regime is dependent upon wavelength. For radar systems with much longer wavelengths, such as profilers, the high frequency scaling regime may or may not be clearly visible.

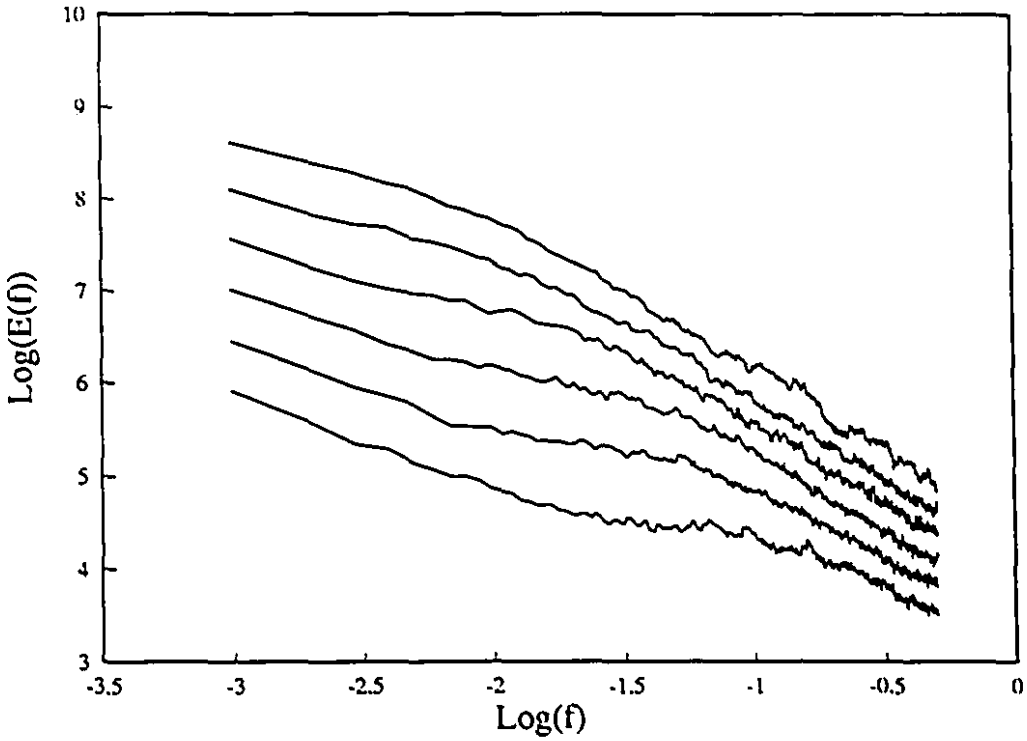

Figure 7.14: The effect of different wavelengths on the spectral representation of the $Z_{\epsilon\lambda}(t)$ time series. The figure clearly shows that the spectral slope is wavelength dependent for short wavelengths but seems to become wavelength independent for longer wavelengths. The figure also shows clearly how spectral energy increases with wavelength. The model used for these computation was RCS(1024, Wavelength, 0.1, 0.0) with wavelength scales of (from bottom to top) 16, 32, 64, 128, 256 and 512 pixels.

7.3.3 The Low Frequency Scaling Regime.

In this section we verify the approximations made in relations 7.7 and 7.8. We expect $Z_\lambda(t)$ and $Z_{\epsilon\lambda}(t)$ to have similar scaling behaviours at scales sufficiently larger than the pusle volume scale. Far from the pulse volume scale B the statistics of $Z_{\epsilon\lambda}$ and Z_λ will likely only reflect the

fact that they are both squares of the $\sigma_\lambda(x,t)$ field. The analysis of the low frequency scaling regime was conducted using a pulse volume scale B_λ of 16 pixels, and a wavelength scale λ_w of 8 pixels. The multifractal analysis was straightforward: A scale ratio λ of 32 was used (i.e. L = 1024 pixels and l = 32 pixels leaving a factor of 2 in scale between the scale break and the inner scale l of the analysis). DTM was used to establish the extent of the universal regime and estimate the universal parameters. The analysis will be presented graphically in figure 7.15 through 7.19. Each figure contains curves for 5 values of C_1. Results are tabulated in table 7.2.

Scaling Moments for $Z_\lambda(t)$.

Scaling moments of $Z_\lambda(t)$ are presented in figure 7.15 for a selection of 5 of the 13 values of C_1 attempted. In each figure the ratio of scales examined was $\lambda = 32$. The scale range corresponds to scales from 32 pixels to 1024 pixels. Computationally, this involves summing each 1024 point time series of $Z_\lambda(t)$ over 32 values and examining the scaling behaviours of the resulting 32 values. Statistics are then accumulated over the 256 independent runs of the RCS model.

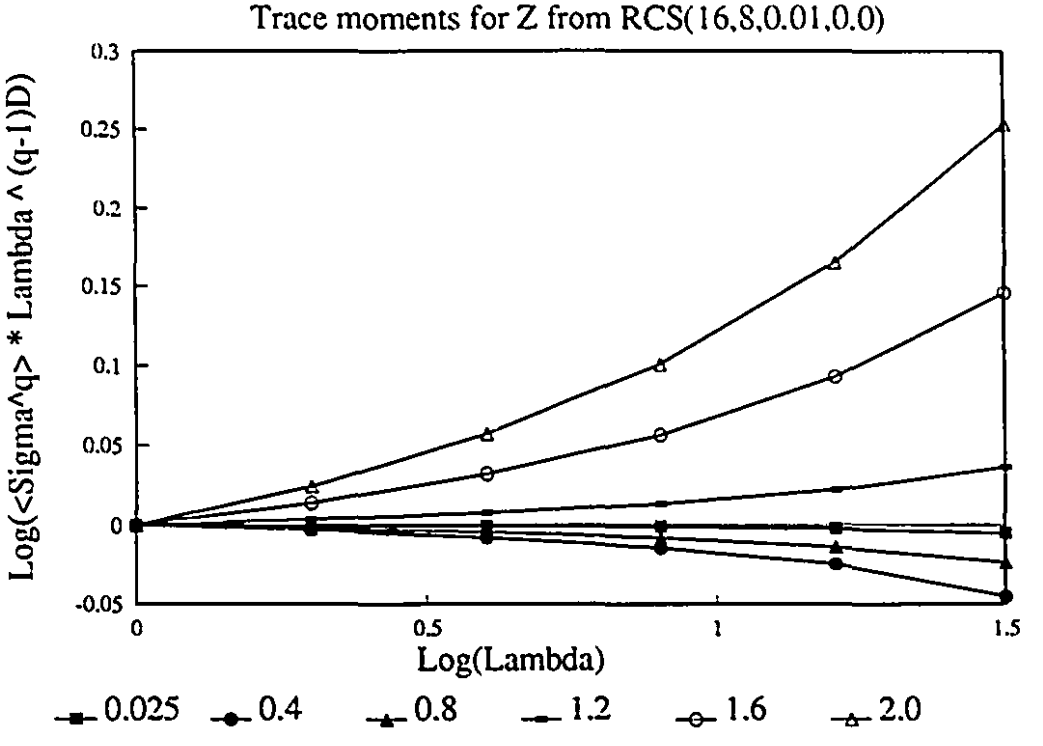

Figure 7.15-a: Scaling moments for $Z_\lambda(t)$ from RCS(16,8,0.01,0.0). The legend gives the order of moment q for the curves.

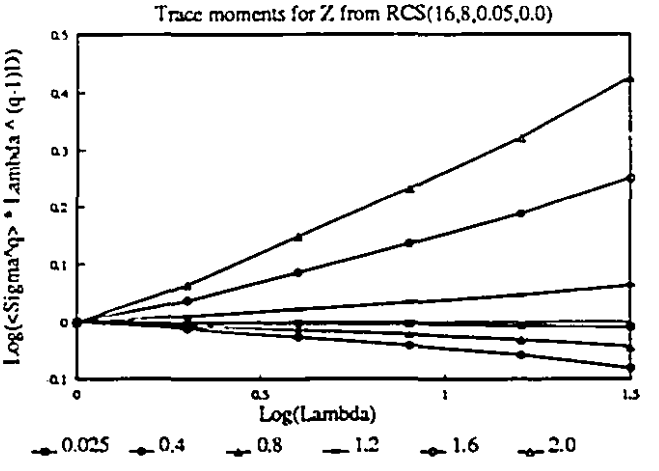

Figure 7.15-b: Scaling moments for $Z_\lambda(t)$ from RCS(16,8,0.05,0.0). The scale ratios are as in figure 7.15-a. The scaling of $Z_\lambda(t)$ at $C_1 = 0.05$ is good and is robust. The legend gives the order of moment q for the curves.

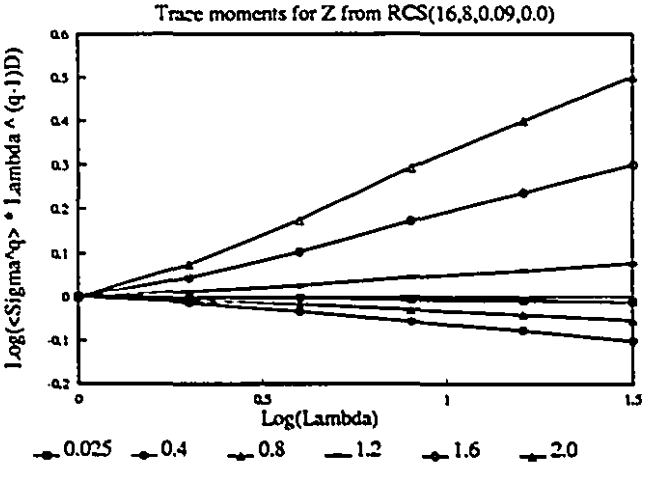

Figure 7.15-c: Scaling moments for $Z_\lambda(t)$ from RCS(16,8,0.09,0.0). The scale ratios are as in figure 7.15-a. The scaling of $Z_\lambda(t)$ at $C_1 = 0.09$ is very good and is robust. The legend gives the order of moment q for the curves.

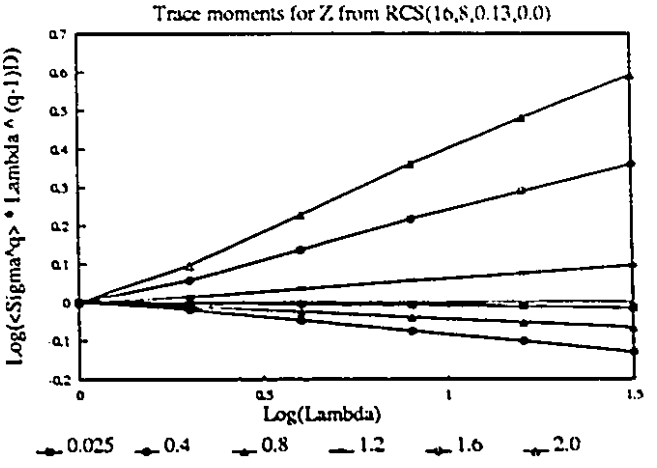

Figure 7.15-d: Scaling moments for $Z_\lambda(t)$ from RCS(16,8,0.13,0.0). The scale ratios are as in figure 7.15-a. The scaling of $Z_\lambda(t)$ at $C_1 = 0.13$ is very good and is robust. The legend gives the order of moment q for the curves.

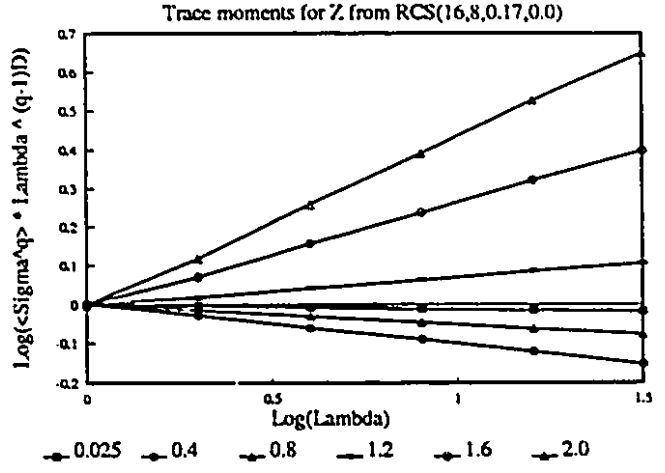

Figure 7.15-e: Scaling moments for $Z_\lambda(t)$ from RCS(16,8,0.17,0.0). The scale ratios are as in figure 7.15-a. The scaling of $Z_\lambda(t)$ at $C_1 = 0.17$ is excellent and is robust. The legend gives the order of moment q for the curves.

Scaling Moments for $Z_{e\lambda}(t)$.

Scaling moments of $Z_{e\lambda}(t)$ are presented in figure 7.16 for the same scale ranges and C_1 values presented in figure 7.16. Comparison of corresponding graphs of figures 7.15 and 7.16 reveals that the scaling behaviours are almost identical.

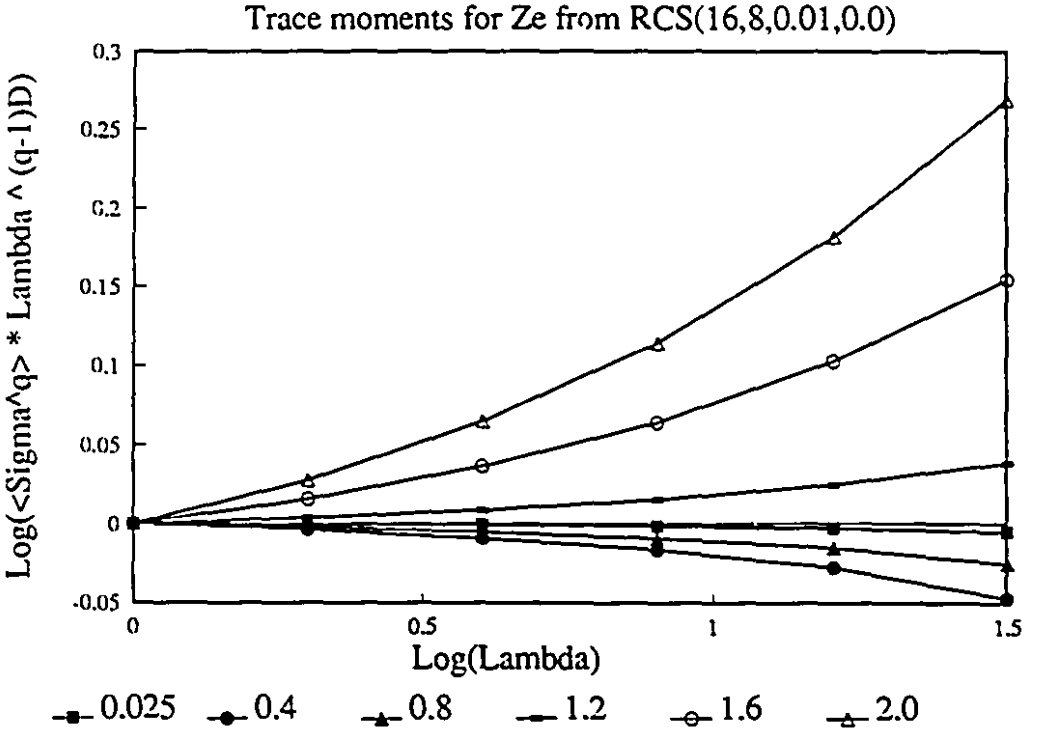

Figure 7.16-a: Scaling moments for $Z_{e\lambda}(t)$ from RCS(16,8,0.01,0.0). The scaling of $Z_{e\lambda}$ at C_1 = 0.05 is good and is robust. The legend gives the order of moment q for the curves.

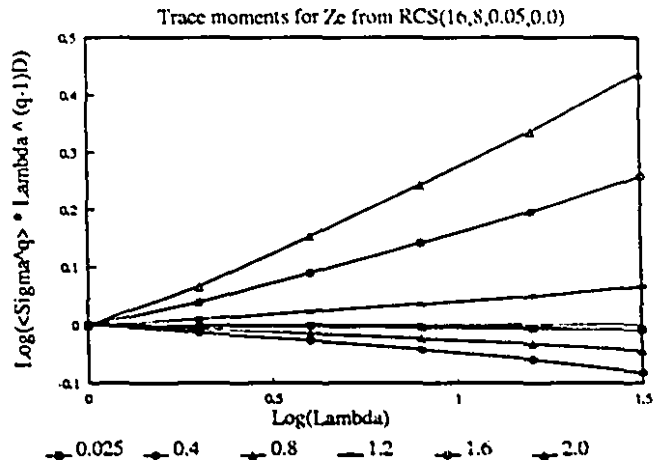

Figure 7.16-b: Scaling moments for $Z_{\epsilon\lambda}(t)$ from RCS(16,8,0.05,0.0). The scale ratios are as in figure 7.16-a. The scaling of $Z_{\epsilon\lambda}$ at $C_1 = 0.05$ is very good and is robust. The legend gives the order of moment q for the curves.

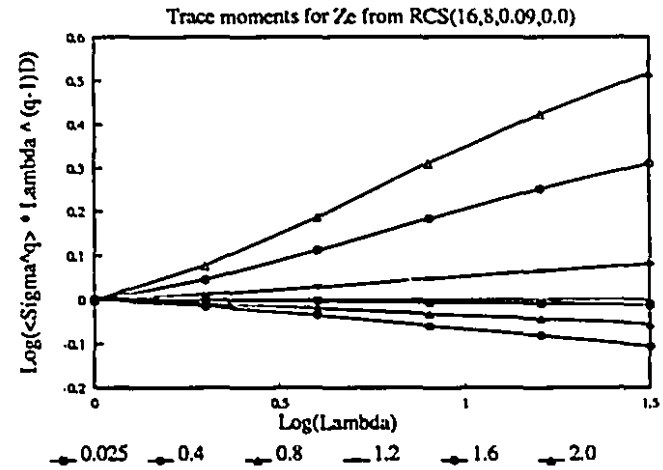

Figure 7.16-c: Scaling moments for $Z_{\epsilon\lambda}(t)$ from RCS(16,8,0.09,0.0). The scale ratios are as in figure 7.16-a. The scaling of $Z_{\epsilon\lambda}$ at $C_1 = 0.09$ is very good and is robust. The legend gives the order of moment q for the curves.

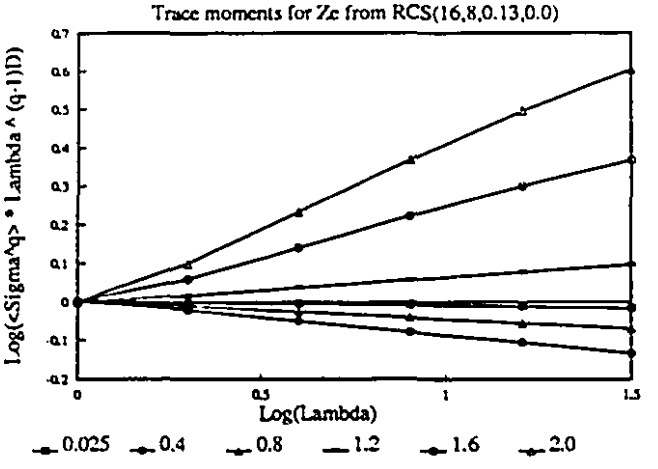

Figure 7.16-d: Scaling moments for $Z_{\epsilon\lambda}(t)$ from RCS(16,8,0.13,0.0). The scale ratios are as in figure 7.16-a. The scaling of $Z_{\epsilon\lambda}$ at $C_1 = 0.13$ is very good and is robust. The legend gives the order of moment q for the curves.

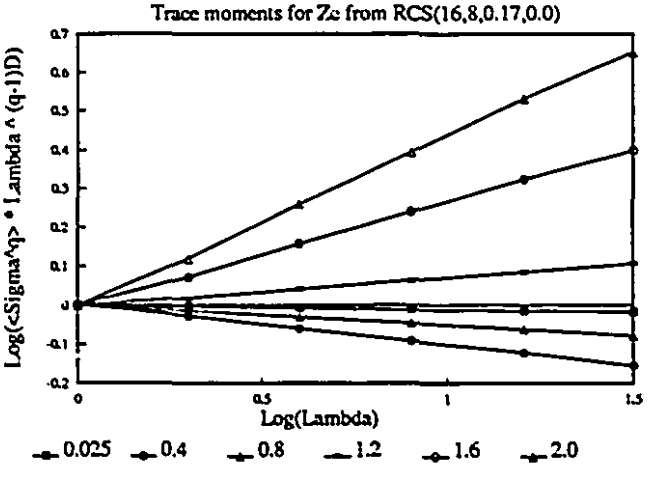

Figure 7.16-e: Scaling moments for $Z_{\epsilon\lambda}(t)$ from RCS(16,8,0.17,0.0). The scale ratios are as in figure 7.16-a. The scaling of $Z_{\epsilon\lambda}$ at $C_1 = 0.17$ is good and is robust. The legend gives the order of moment q for the curves.

Universal Function curves Log($K(q,\eta)$) vs Log(η) for $Z_\lambda(t)$.

Figures 7.17 and 7.18 present the universal functions Log($K(q,\eta)$) vs Log(η) for $Z_\lambda(t)$ and $Z_{\epsilon\lambda}(t)$ respectively. The deviation from universal behaviour at high η-values corresponds roughly to the q_s values computed from the fixed size of the time series. Estimates of the exponents of the linear regions between $-1 < \eta < -0.5$ are summarised in table 7.2. A line of slope $\alpha = 2$ is plotted on each graph for reference. The scaling regime used for the DTM analysis is the same as that presented in figures 7.15 and 7.16.

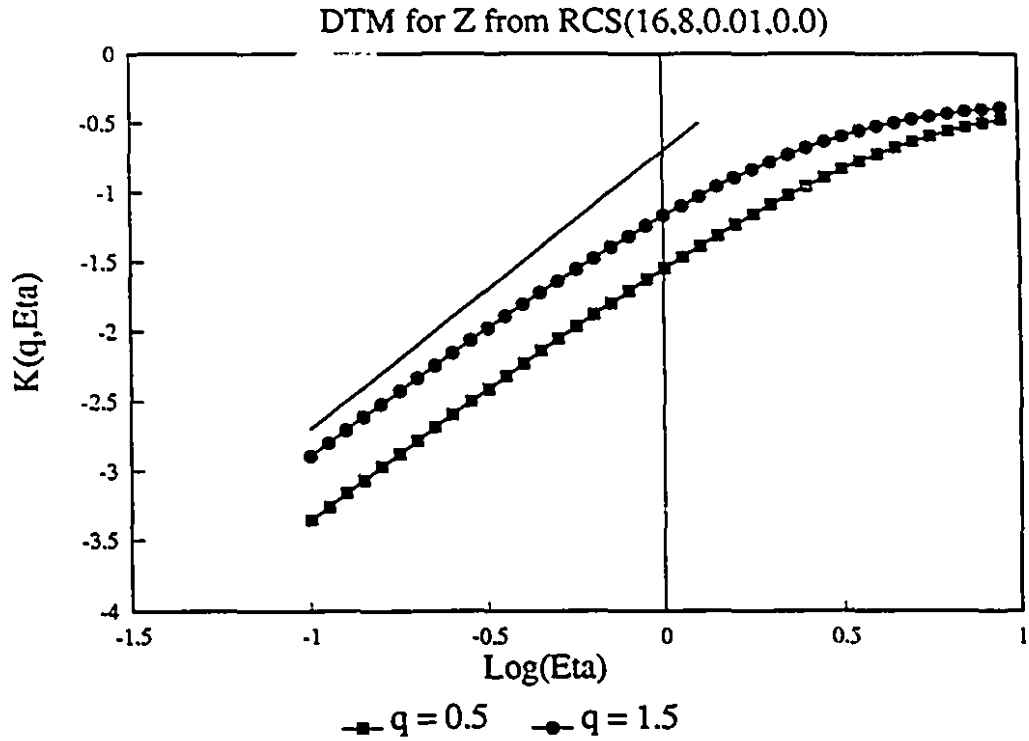

Figure 7.17-a: The universal function curves Log($K(q,\eta)$) vs Log(η) for $Z_\lambda(t)$ from RCS(16,8,0.01,0.0).

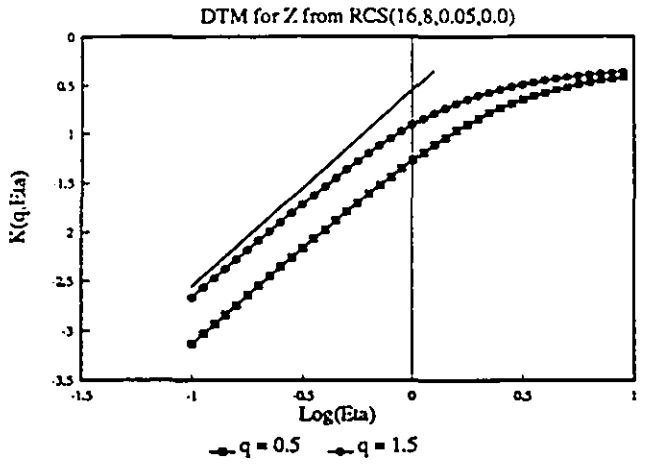

Figure 7.17-b: The universal function curves Log($K(q,\eta)$) vs Log(η) for $Z_\lambda(t)$ from RCS(16,8,0.05,0.0).

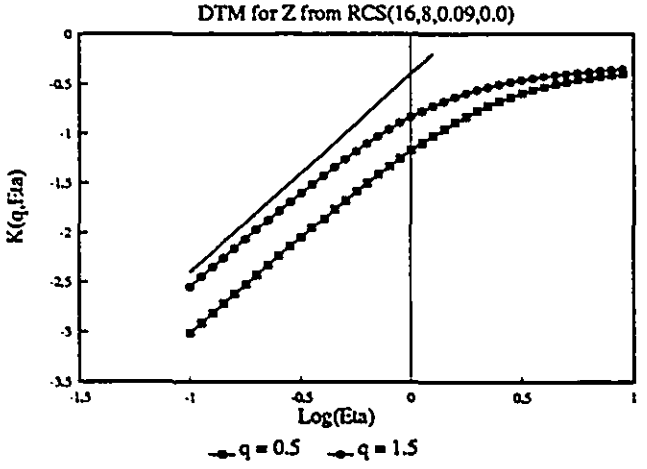

Figure 7.17-c: The universal function curves Log($K(q,\eta)$) vs Log(η) for $Z_\lambda(t)$ from RCS(16,8,0.09,0.0).

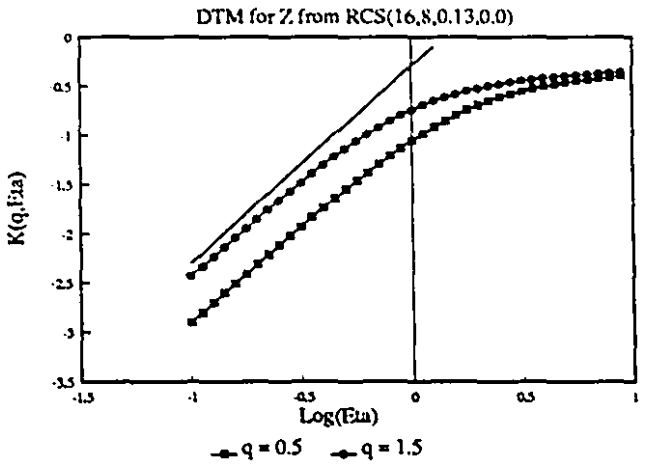

Figure 7.17-d: The universal function curves Log($K(q,\eta)$) vs Log(η) for $Z_\lambda(t)$ from RCS(16,8,0.13,0.0).

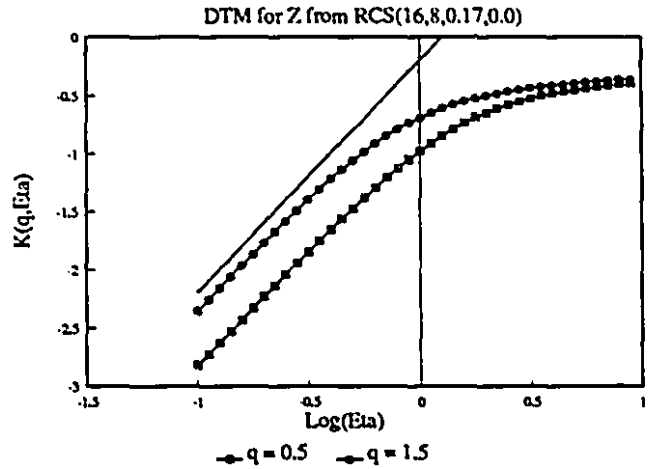

Figure 7.17-e: The universal function curves Log($K(q,\eta)$) vs Log(η) for $Z_\lambda(t)$ from RCS(16,8,0.17,0.0).

Universal Function curves Log($K(q,\eta)$) vs Log(η) for $Z_{e\lambda}(t)$.

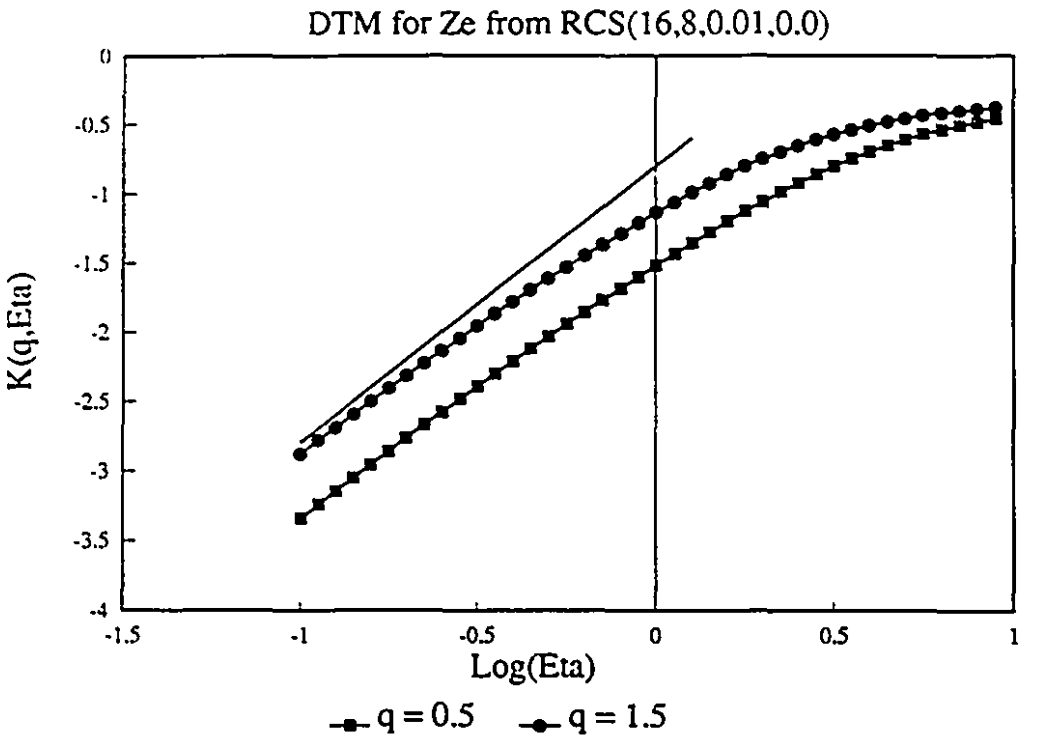

Figure 7.18-a: The universal function curves Log($K(q,\eta)$) vs Log(η) for $Z_{e\lambda}(t)$ from RCS(16,8,0.01,0.0).

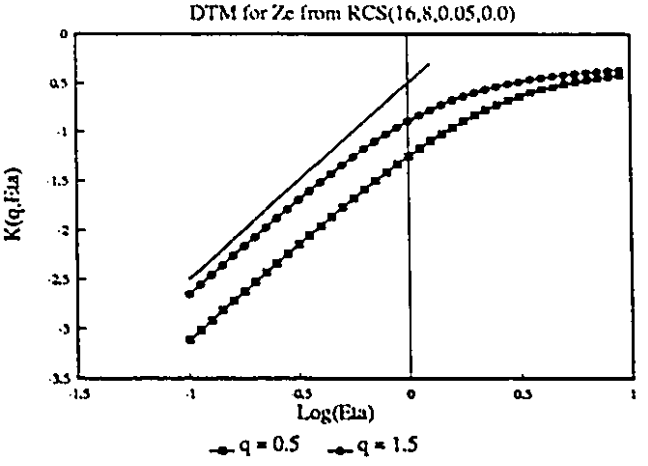

Figure 7.18-b: The universal function curves Log($K(q,\eta)$) vs Log(η) for $Z_{\epsilon\lambda}(t)$ from RCS(16,8,0.05,0.0).

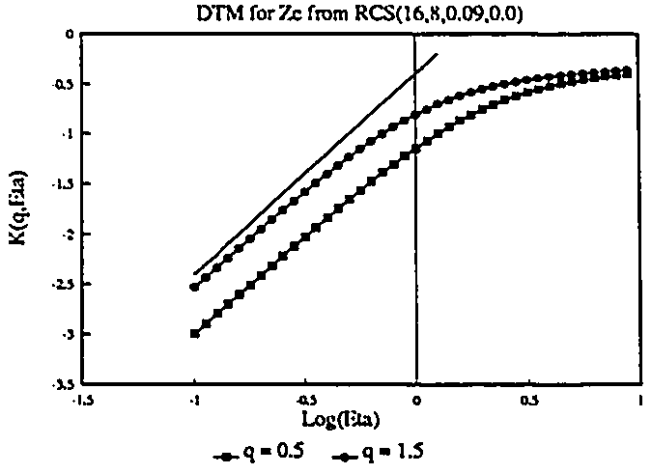

Figure 7.18-c: The universal function curves Log($K(q,\eta)$) vs Log(η) for $Z_{\epsilon\lambda}(t)$ from RCS(16,8,0.09,0.0).

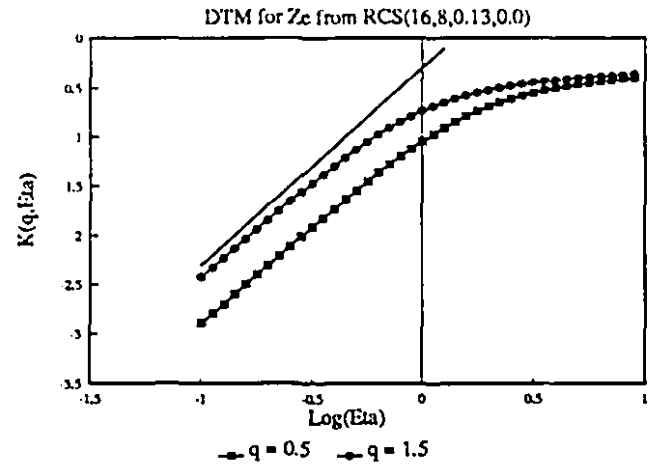

Figure 7.18-d: The universal function curves Log($K(q,\eta)$) vs Log(η) for $Z_{\epsilon\lambda}(t)$ from RCS(16,8,0.13,0.0).

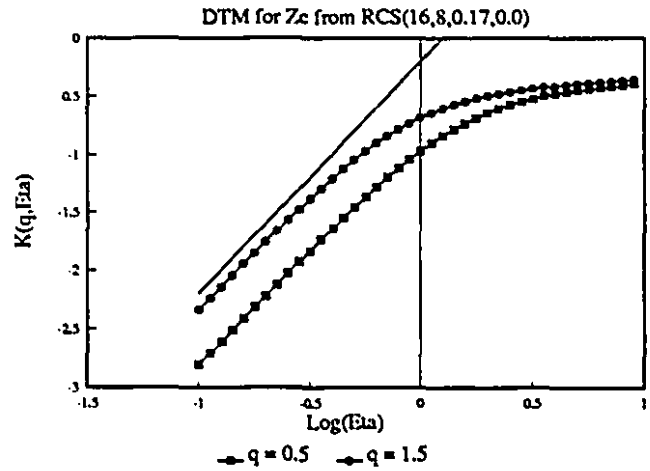

Figure 7.18-e: The universal function curves Log($K(q,\eta)$) vs Log(η) for $Z_{\epsilon\lambda}(t)$ from RCS(16,8,0.17,0.0).

Trace Moment curves $K(q)$ vs q for $Z_\lambda(t)$ and $Z_{\epsilon\lambda}(t)$.

Relations 7.7 and 7.8 show that in the low frequency scaling regime the K(q) functions for $Z_\lambda(t)$ and $Z_{\epsilon\lambda}(t)$ should be very similar. An additional effect is present in the time-space RCS model. The effect of averaging in time to examine the low frequency scaling requires additional 'dressing' which further suppresses the linear term $qK_{A,R}(1)$ that differentiates the two curves. The near coincident nature of the K(q) curves for $Z_\lambda(t)$ and $Z_{\epsilon\lambda}(t)$ that follow support this explanation.

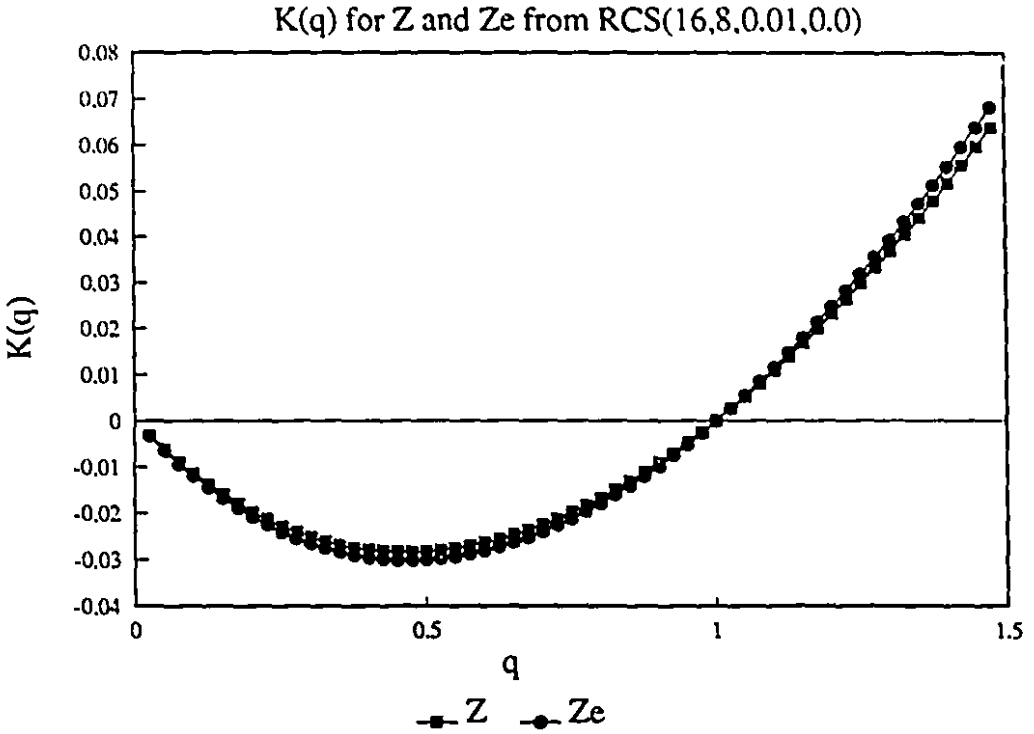

Figure 7.19-a: K(q) vs q curves for $Z_\lambda(t)$ and $Z_{\epsilon\lambda}(t)$ for RCS(16,8,0.01,0.0). These curves show that for $C_1 = 0.01$ the statistics of the low frequency scaling regime of $Z_\lambda(t)$ and $Z_{\epsilon\lambda}(t)$ are very close.

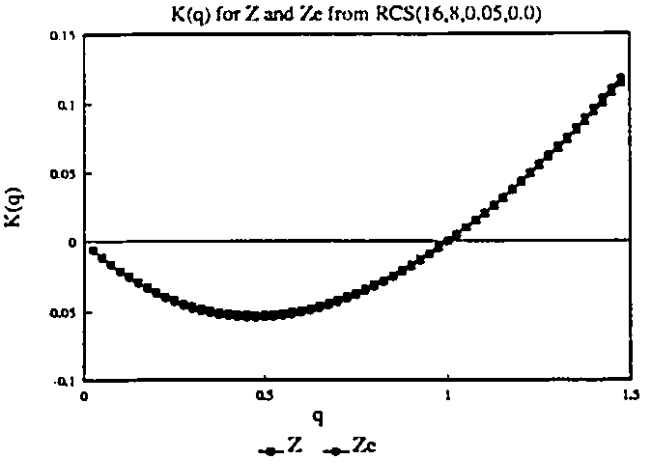

Figure 7.19-b: K(q) vs q curves for $Z_\lambda(t)$ and $Z_{\epsilon\lambda}(t)$ for RCS(16,8,0.05,0.0). The strong overlap of these curves shows that for $C_1 = 0.05$ the statistics of $Z_\lambda(t)$ and $Z_{\epsilon\lambda}(t)$ in the low frequency scaling regime are very close.

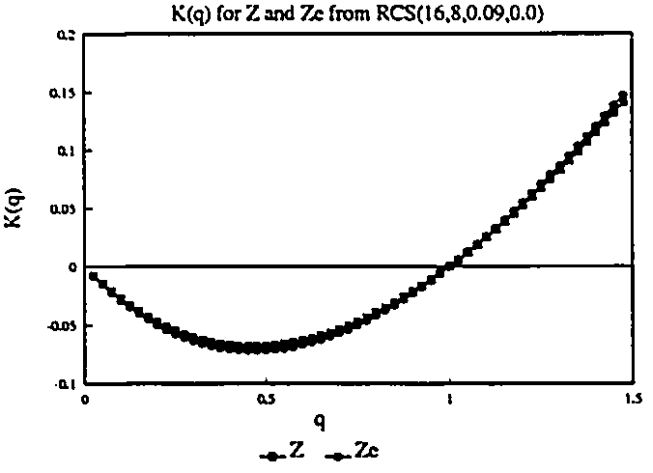

Figure 7.19-c: K(q) vs q curves for $Z_\lambda(t)$ and $Z_{\epsilon\lambda}(t)$ for RCS(16,8,0.09,0.0). The strong overlap of these curves shows that for $C_1 = 0.09$ the statistics of $Z_\lambda(t)$ and $Z_{\epsilon\lambda}(t)$ in the low frequency scaling regime are very close.

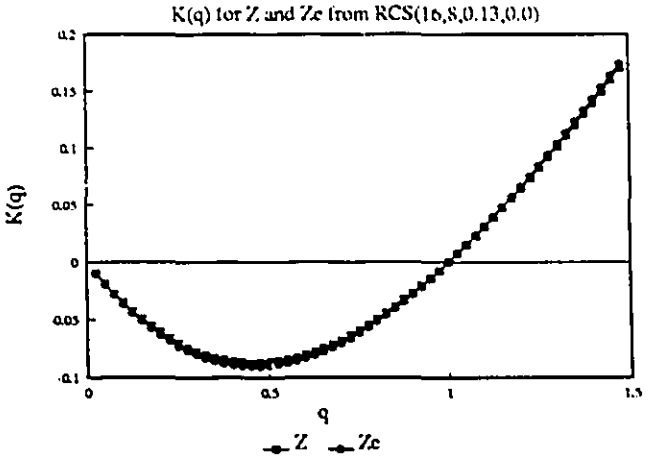

Figure 7.19-d: K(q) vs q curves for $Z_\lambda(t)$ and $Z_{\epsilon\lambda}(t)$ for RCS(16,8,0.13,0.0). The strong overlap of these curves shows that for $C_1 = 0.13$ the statistics of $Z_\lambda(t)$ and $Z_{\epsilon\lambda}(t)$ in the low frequency scaling regime are very close.

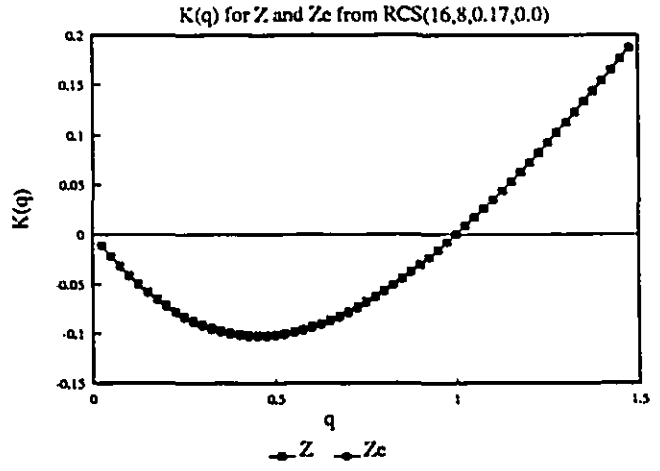

Figure 7.19-e: K(q) vs q curves for $Z_\lambda(t)$ and $Z_{\epsilon\lambda}(t)$ for RCS(16,8,0.17,0.0). The strong overlap of these curves shows that for $C_1 = 0.17$ the statistics of $Z_\lambda(t)$ and $Z_{\epsilon\lambda}(t)$ in the low frequency scaling regime are very close.

Table 7.2 shows the estimates of α and C_1 obtained from the linear regions of figures 7.17 and 7.18. computed from time series of $Z_\lambda(t)$ and $Z_{\epsilon\lambda}(t)$ resulting from RCS(16,8,C_1,0.0). The estimates of α and C_1 in the low frequency scaling regime show the behaviour expected from relations 7.7 and 7.8 within experimental error. The estimates of C_1 are very similar for the two time series and are generally four times (2^α) the input C_1 values. Numerous trials of these results were produced and the resulting behaviours are exactly similar for smaller pulse volume scales (i.e. the analyses were performed for numerous runs of RCS(8,8,C_1,0.0) with exactly similar results). The similarity of results for different small pulse volume scales suggests the transition zone about the pulse volume scale break does not extend to measures taken from scales at least a factor of two greater than the B_λ scale.

Table 7.2: Estimates of Universal Multifractal Parameters for $Z_\lambda(t)$ and $Z_{\epsilon\lambda}(t)$ from RCS(16,8,C_1,0.0)

$\sigma_\lambda(x,t)$	$Z_{\epsilon\lambda}$		Z_λ	
C_1	α	C_1	α	C_1
0.01	1.9 ± 0.4	0.1 ± 0.2	1.9 ± 0.4	0.1 ± 0.2
0.03	1.9 ± 0.3	0.2 ± 0.2	1.9 ± 0.3	0.2 ± 0.2
0.05	1.9 ± 0.2	0.2 ± 0.2	1.9 ± 0.3	0.2 ± 0.2
0.07	1.9 ± 0.2	0.3 ± 0.1	1.9 ± 0.2	0.3 ± 0.1
0.09	1.9 ± 0.1	0.4 ± 0.1	2.0 ± 0.1	0.4 ± 0.1
0.11	2.0 ± 0.1	0.4 ± 0.1	2.0 ± 0.1	0.4 ± 0.1
0.13	2.0 ± 0.1	0.4 ± 0.1	2.0 ± 0.1	0.4 ± 0.1
0.15	2.0 ± 0.1	0.5 ± 0.1	2.0 ± 0.1	0.5 ± 0.1
0.17	2.0 ± 0.1	0.6 ± 0.1	2.0 ± 0.1	0.5 ± 0.1
0.19	2.0 ± 0.1	0.6 ± 0.1	2.0 ± 0.1	0.6 ± 0.1
0.21	2.0 ± 0.1	0.74 ± 0.04	2.0 ± 0.1	0.7 ± 0.1
0.23	2.0 ± 0.1	0.7 ± 0.1	2.0 ± 0.1	0.7 ± 0.1
0.25	2.0 ± 0.1	0.8 ± 0.1	2.0 ± 0.1	0.8 ± 0.1

The Behaviour of Distributions of $Z_{\epsilon\lambda}$.

The centering of distributions of $Z_{\epsilon\lambda}(t)$ is influenced by $K_{\lambda R}(1)$ and is dependent upon the pulse volume scale B_λ, as is expected from relations 7.13 and 7.14 and their Legendre transforms 6.7 and 6.20. The centering of the distributions at fixed wavelength λ_w and C_1 of the $\sigma(x,t)$ field is then controlled by B_λ and is expected to decrease with increasing B_λ. Figure 7.20 shows that this is in fact the case. The centering of the distributions, or bias, decreases as a function of increasing B_λ. The distribution can also be seen to narrow as B_λ increases. This behaviour, if taken to the limit of very large pulse volumes (at long range for instance) would result in a distribution that would be superficially indistinguishable from a Rayleigh distribution for small data sets.

The behaviour of distributions of $Z_{\epsilon\lambda}(t)$ with increasing pulse volume scale is presented in figure 7.20. The distributions presented in figure 7.20 include the distributions for 4, 64 and 1024 pixel pulse volumes. The Rayleigh curve is presented to show how increasing pulse volume scale produces distributions which superficially approach the Rayleigh shape. Each of the distributions is an average from 256 histograms, each resulting from a realization of the RCS model for the given parameters. The wavelength λ_w is held constant at 4 pixels. The distributions are seen to narrow with increasing B_λ. This behaviour is particularly evident in the high tail of the distribution where the 1024 pixel pulse volume severely underestimates the number of extreme values found with the 4 pixel pulse volume. The bias in the distribution is inversely related to B_λ. The 4 pixel pulse volume is biased to -5.5 dB, the 64 pixel pulse volume is biased to -3.5 dB and the 1024 pixel pulse volume is biased to -1.0 dB. It is clearly evident from these results that even in a multifractal rainfield a very large pulse volume will produce only a small bias in the distribution. Indeed, the scale ratio λ of 256 for the 1024 pixel pulse volume (i.e. L = 1024 pixels and l = 4 pixels) should be compared to the scale ratio of 1500 for most operational radars (i.e. 150 m pulse of 10 cm wavelengths), which are then averaged in downrange or cross range averaging schemes.

The immediate consequence of dependence of the distribution on pulse volume scale is range dependent statistics. Figure 7.20 clearly shows that as the pulse volume scale B_λ increases the distribution narrows and a bias results. Relation 3.7 is the standard result for scale dependence

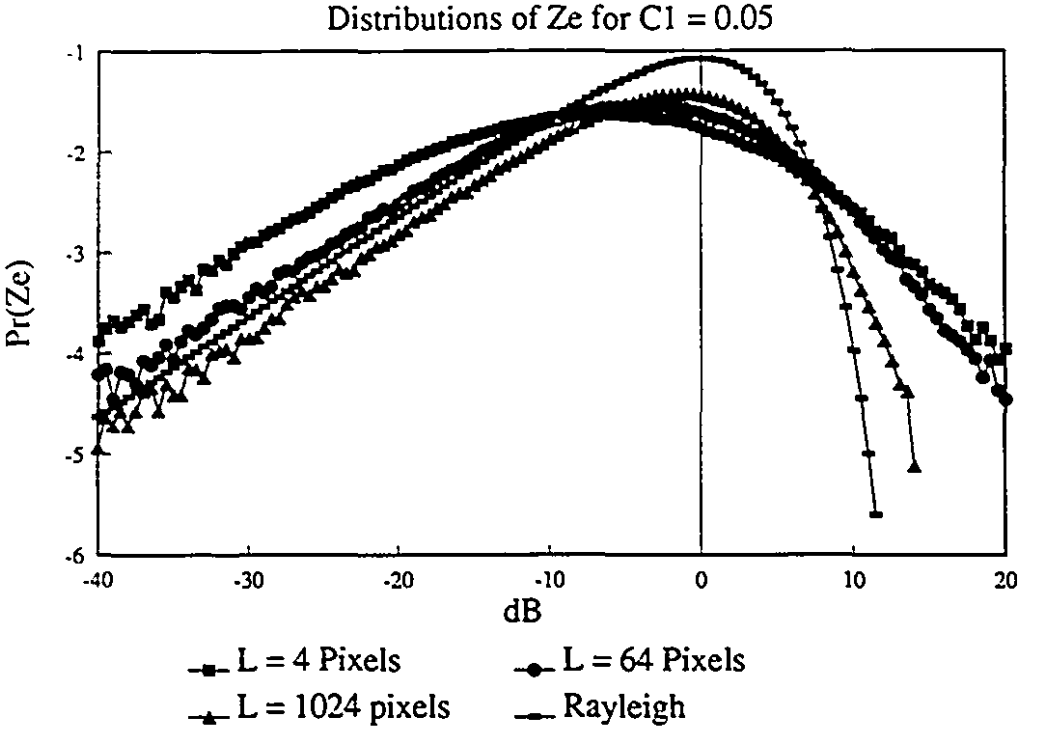

Figure 7.20: The effect of pulse volume scale on distributions of intensity for $C_1 = 0.05$. The legend gives the pulse volume scale L in pixels used to compute the distributions. Each distribution is an average of 256 distributions. The Rayleigh curve is plotted for reference to show that increasing pulse volume scale results in distributions superficially approaching the characteristic Rayleigh shape.

of staitstics. It must be kept in mind that the pulse volume scale of a radar is a function of range and hence each range gate will have a different scale. The range dependence of distributions of radar reflectivities is therefore displayed in figure 7.20 and is quantifiable in terms of relation 3.7.

$K_{A,R}(1)$ is a function of the C_1 of the $\sigma_\lambda(x,t)$ field. The bias of the distributions is therefore a function of the underlying variability. Figure 7.21 shows that as the C_1 of the $\sigma_\lambda(x,t)$ field

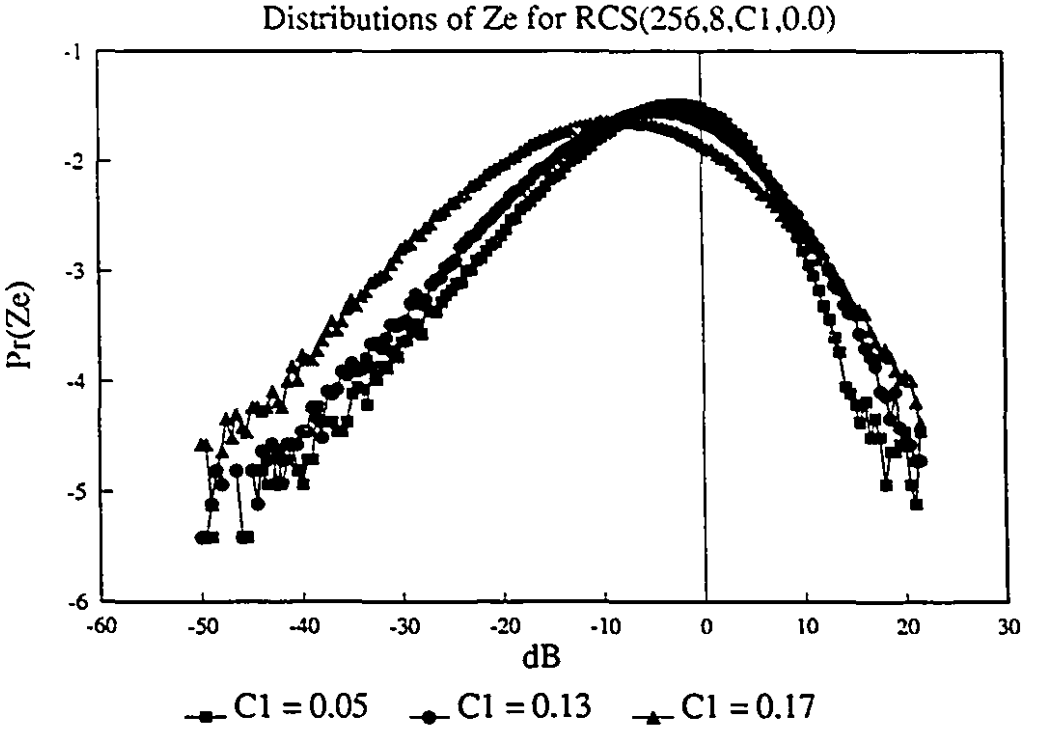

Figure 7.21: The effect of increasing C_1 on distributions of $Z_{e\lambda}(t)$. The pulse volume scale is 256 pixels and the wavelength is 8 pixels. The legend gives the value of C_1 for the computed distribution. The bias in the distribution is a function of C_1.

increases, for fixed B_λ and λ_w, the bias of the distribution also increases. This characteristic behaviour has already been established by Rogers (1971) for an ad-hoc function specifying gradients in the rainfield at super resolution scales, but we can exactly specify the variability and hence explore the bias. For example, with $B_\lambda = 256$ pixels and $\lambda_w = 8$ pixels, a C_1 of 0.05 gives a bias of -2 dB, a C_1 of 0.13 gives a bias of -8 dB and a C_1 of 0.17 gives a bias of -11 dB. The 'bias function' is a 2D function with dependences on scale as well as on the C_1 of the $\sigma(x,t)$ field.

This section shows that the behaviours of the distributions of $Z_{\epsilon\lambda}(t)$ are fully determined in terms of measurable parameters. As an alternative to the standard theory of Rogers (1971) the multiscaling arguments presented here can explain and quantify all the observables related to the distributional behaviour of $Z_{\epsilon\lambda}(t)$ resulting from sub-resolution variability. The dependence of the various effects on α and C_1 provides a solid framework from which it is possible to meaningfully compare radar data sets resulting from different resolutions and different dynamical variability.

The Spectral Behaviour of $Z_\lambda(t)$ and $Z_{\epsilon\lambda}(t)$.

The spectral behaviour of the low frequency scaling regime, with α fixed at 2, is a function of C_1. The realization that the time series of $Z_\lambda(t)$ and $Z_{\epsilon\lambda}(t)$ are squared quantities and are therefore governed statistically by $K(q,\eta)$ with $\eta = 2$ allows the prediction of the spectral slopes of $Z_\lambda(t)$ and $Z_{\epsilon\lambda}(t)$ for different C_1. The fact that $\alpha = 2$ means that the spectral slope $\beta = 1 - K(2,2) = 1 - 4C_1$. Table 7.3 shows that this relation is well respected, within error bars, for $Z_\lambda(t)$. Estimates of the spectral slope for $Z_{\epsilon\lambda}(t)$ reveals some persistent difficulties at low C_1 (persistent over all 5 trials).

Table 7.3: Estimates of β from the Low Frequency Scaling Regime for $Z_\lambda(t)$ and $Z_{e\lambda}(t)$.			
C_1	β_Z	β_{Z_e}	β 1- $K_v(2,2)$
0.01	1.0 ± 0.2	0.8 ± 0.1	0.96
0.03	0.95 ± 0.07	0.78 ± 0.05	0.88
0.05	0.85 ± 0.06	0.70 ± 0.07	0.80
0.07	0.69 ± 0.07	0.65 ± 0.02	0.72
0.09	0.70 ± 0.04	0.5 ± 0.2	0.64
0.11	0.56 ± 0.04	0.50 ± 0.07	0.56
0.13	0.54 ± 0.06	0.47 ± 0.04	0.48
0.15	0.45 ± 0.09	0.3 ± 0.1	0.40
0.17	0.35 ± 0.05	0.28 ± 0.04	0.32
0.19	0.40 ± 0.07	0.28 ± 0.07	0.24
0.21	0.26 ± 0.07	0.25 ± 0.08	0.16
0.23	0.2 ± 0.1	0.2 ± 0.1	0.08
0.25	0.2 ± 0.2	0.2 ± 0.2	0.0

The adherence of the low frequency spectral behaviour of $Z_{e\lambda}(t)$ and $Z_\lambda(t)$ is within experimental error of the expected results. Differences from the expected behaviour are attributable to the limited range of scales available to the RCS model.

7.3.4 The High Frequency Scaling Regime.

The high frequency scaling regime exists at scales smaller than the wavelength scale. Results from this regime are likely to be more pedagogical than useful since the wavelength scales of most operational radars are very close to the inner scales of the radar cross section field. Although, the evidence in section 4 suggests that operationally the high frequency scaling regime could be used to estimate the inner scale of the rainfield by estimating the scale break associated

with the 'foot'. Systematic analysis of this regime requires that the pulse volume scale be made as large as possible (1024 pixels) and the wavelength scale be left as a free variable with the proviso that it is large enough to avoid the transition zones around the scale break at λ_w. Analysis of this regime must be conducted at scales much smaller than the wavelength scale break.

It was demonstrated previously, for a constant value of C_1, that the spectral slope of the high frequency scaling regime for $Z_{\epsilon\lambda}(t)$ becomes free of the transition around the high frequency scaling break for wavelengths greater than 64 pixels. Thus, selection of a wavelength larger than 64 pixels allows the statistical nature of the high frequency scaling regime to be explored. The statistics of the high frequency scaling regime of both $Z_\lambda(t)$ and $Z_{\epsilon\lambda}(t)$ will be examined as a function of input C_1.

The statistics of $Z_\lambda(t)$ and $Z_{\epsilon\lambda}(t)$ in the high frequency scale regime are those of a 'projection' of the spatial variability of $\sigma(x,t)$ onto the time axis. The notion of a multifractal projection is relatively new (see Garrido et al., 1993), but can be understood to involve a shift in singularities $\gamma \rightarrow \gamma - 1$ and a shift in $c(\gamma)$ to $c(\gamma) \rightarrow c(\gamma) - 1$ with the provision that $c(\gamma) > 0$. This transition is likely to result in a fundamental scale breaking and hence the statistics will no longer adhere to the universal forms. Few results are available for such projections, therefore the emphasis in this section will be mostly on the cataloguing of these behaviours for consideration when an adequate theory becomes available.

Universal Multifractal Behaviour of the High Frequency Scaling Regime.

Estimates of universal multifractal parameters from the high frequency scaling regime reveal a very slow dependence upon the C_1 of the $\sigma(x,t)$ fields. Estimates of scaling moments from this regime were made using a pulse volume scale B_λ of 1024 pixels and a wavelength scale λ_w of 256 pixels. Scales up to 64 pixels were examined to avoid the transition zone around the scale break at 256 pixels in the $Z_{\epsilon\lambda}(t)$ time series. The $Z_\lambda(t)$ time series has no break at this scale. Estimates of universal parameters were made using DTM and are presented in table 7.4.

Slight curvature is noticeable in the scaling moments. This curvature is stronger for small input C_1 values and is consistent for independent runs of the model. Estimates of the universal parameters from independent model runs are very consistent. The behaviour of the universal

curves in figure 7.23 and 7.24 seems adequate for estimation of α. The K(q) curves for $Z_\lambda(t)$ and $Z_{\epsilon\lambda}(t)$ shows a marked difference in behaviour. However, there exists no theoretical results to quantify the difference.

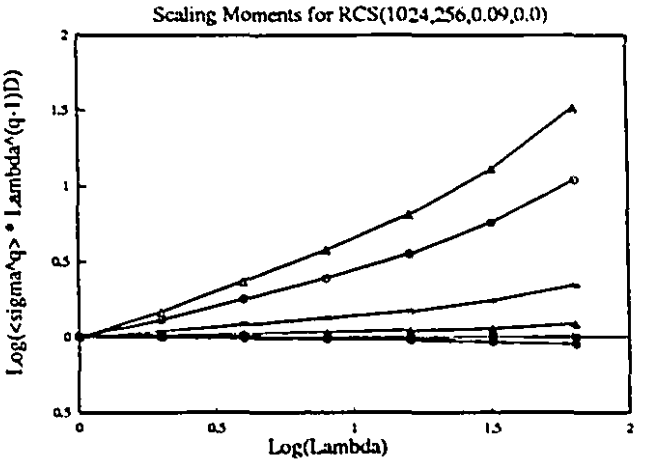

Figure 7.22-a: Scaling moments for $Z_{\epsilon\lambda}(t)$ from RCS(1024,256,0.09,0.0). The scaling moments are computed over 64 pixels in the high frequency scaling regime.

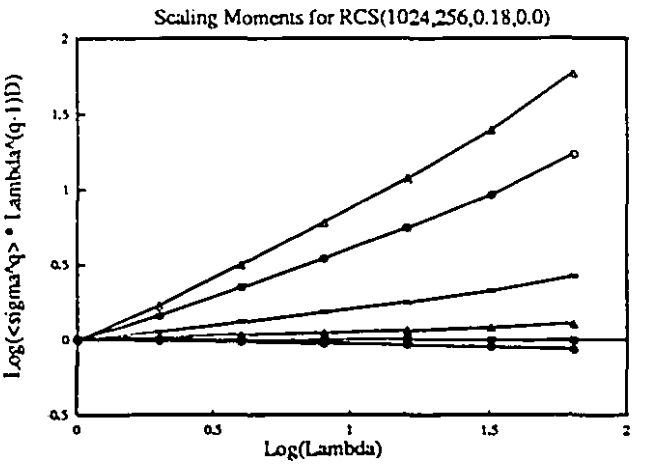

Figure 7.22-b: Scaling moments for $Z_{\epsilon\lambda}(t)$ from RCS(1024,256,0.18,0.0).

The linearity of the Log($K(q,\eta)$) Vs Log(η) curves indicates that universal multifractal behaviour is carried through to the high frequency scaling regime. The linearity is over a substantial range of η. The q_s value is around 2 ($\eta = 0.3$).

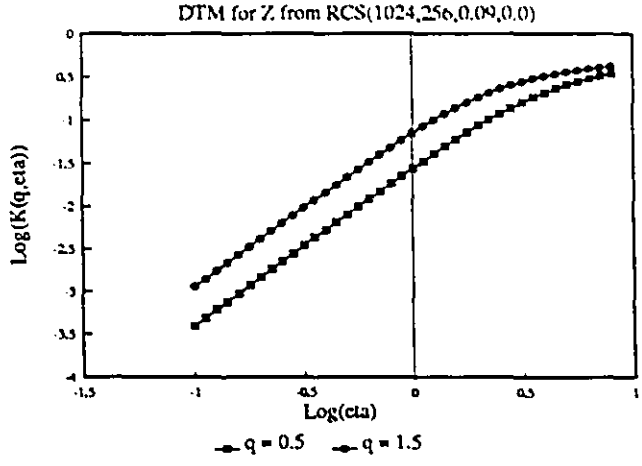

Figure 7.23-a: Log($K(q,\eta)$) Vs Log(η) for Z from RCS(1024,256,0.09,0.0).

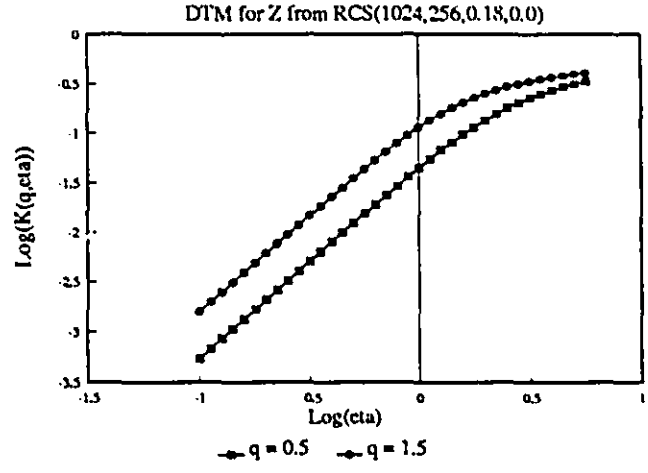

Figure 7.23-b: Log($K(q,\eta)$) Vs Log(η) for Z from RCS(1024,256,0.18,0.0).

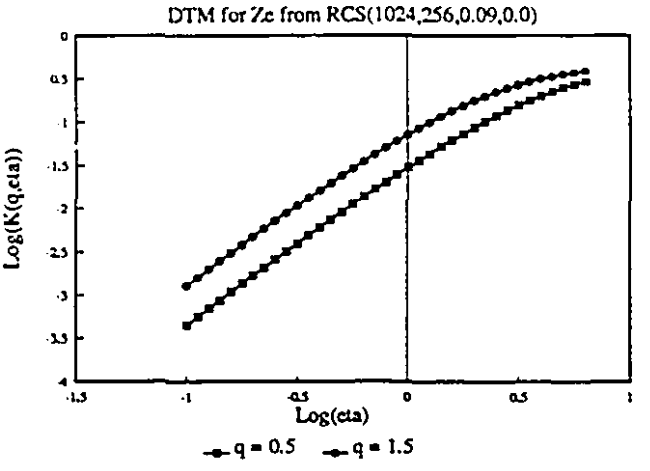

Figure 7.24-a: Log($K(q,\eta)$) Vs Log(η) for Z_e from RCS(1024,256,0.09,0.0).

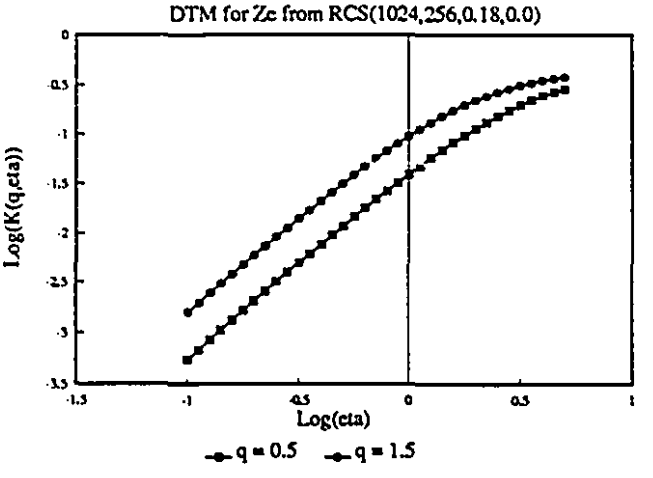

Figure 7.24-b: Log($K(q,\eta)$) Vs Log(η) for Z_e from RCS(1024,256,0.18,0.0).

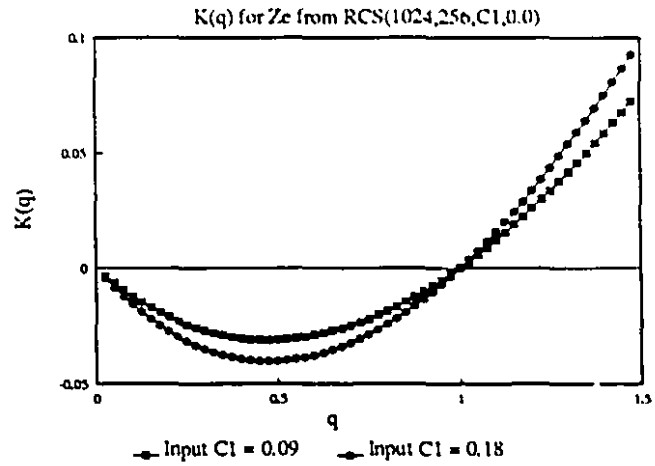

Figure 7.25: K(q) vs q for $Z_{\epsilon\lambda}(t)$ from RCS(1024,256,C_1,0.0) with C_1 = 0.09 and 0.18. The linearity of the q = 0.5 $K(q,\eta)$ curve at η = 0 suggests that the K(q) curves are accurate representations of the statistical moments. Estimates of the universal parameters from these curves coincide with those tabulated in table 6.7.

Table 7.4: Universal multifractal parameters from the high frequency scaling regime.

	Z_λ		$Z_{\epsilon\lambda}$	
C_1	α	C_1	α	C_1
0.03	1.9 ± 0.1	0.12 ± 0.02	1.9 ± 0.1	0.09 ± 0.03
0.06	1.9 ± 0.1	0.13 ± 0.02	1.9 ± 0.1	0.10 ± 0.03
0.09	1.9 ± 0.1	0.14 ± 0.02	1.9 ± 0.1	0.12 ± 0.02
0.12	1.9 ± 0.1	0.15 ± 0.01	1.9 ± 0.1	0.14 ± 0.03
0.15	1.9 ± 0.1	0.16 ± 0.01	1.9 ± 0.1	0.17 ± 0.02
0.18	1.9 ± 0.1	0.18 ± 0.02	1.9 ± 0.1	0.20 ± 0.02
0.21	1.9 ± 0.1	0.20 ± 0.01	1.9 ± 0.1	0.22 ± 0.01
0.24	1.9 ± 0.1	0.21 ± 0.01	1.9 ± 0.1	0.25 ± 0.01

Spectral Behaviour of the High Frequency Scaling Regime.

The spectral exponents β presented in table 7.5 are those of a non-conservative multifractal. Figures 7.22 to 7.25 and table 7.4 shows that the high frequency scaling regime seems to display universal multifractal behaviour. Thus the non-conservative nature of the spectrum originates with the projection, a sum of squares for $Z_\lambda(t)$ and the Fourier component for $Z_{\epsilon\lambda}(t)$.The spectrum of $Z_{\epsilon\lambda}(t)$ appears less dependent upon C_1.

Table 7.5: Estimates of β for the high frequency scaling regime of $Z_\lambda(t)$ and $Z_{\epsilon\lambda}(t)$ as a function of input C_1.

C_1	β_Z	β_{Z_ϵ}
0.03	1.80 ± 0.01	1.93 ± 0.01
0.06	1.51 ± 0.004	1.86 ± 0.01
0.09	1.38 ± 0.01	1.78 ± 0.01
0.12	1.13 ± 0.02	1.65 ± 0.02
0.15	1.06 ± 0.01	1.57 ± 0.01
0.18	0.86 ± 0.02	1.45 ± 0.02
0.21	0.77 ± 0.02	1.29 ± 0.02
0.24	0.69 ± 0.01	1.17 ± 0.01

Demonstration of Scale Dependent Means in the High Frequency Scaling Regime.

A demonstration of the effect of varying the wavelength on the computed means of $Z_{\epsilon\lambda}(t)$ is given in figure 7.26. The dependence of the mean upon wavelength, with B_λ held constant, is given by

$$\langle Z_{\epsilon\lambda} \rangle \propto \left(\frac{1}{\lambda_w}\right)^{K_{Z_\epsilon}(1)} \tag{6.25}$$

Figure 7.26 shows the behaviour of $\langle Z_{e\lambda} \rangle$ as a function of increasing λ_w for $C_1 = 0.1$, which gives $K_{Z_e}(1) = 0.80$ (from table 6.1, $K_{Z_e}(1) = 2K_{A,R}(1)$). The change of wavelength intuitively has no effect on moments of $Z_\lambda(t)$. Measurement of the slope of $\text{Log}(\langle Z_{e\lambda} \rangle)$ vs $\text{Log}(\lambda_w)$ gives a value of 0.86 which is another method to estimate $K_{A,R}(1)$.

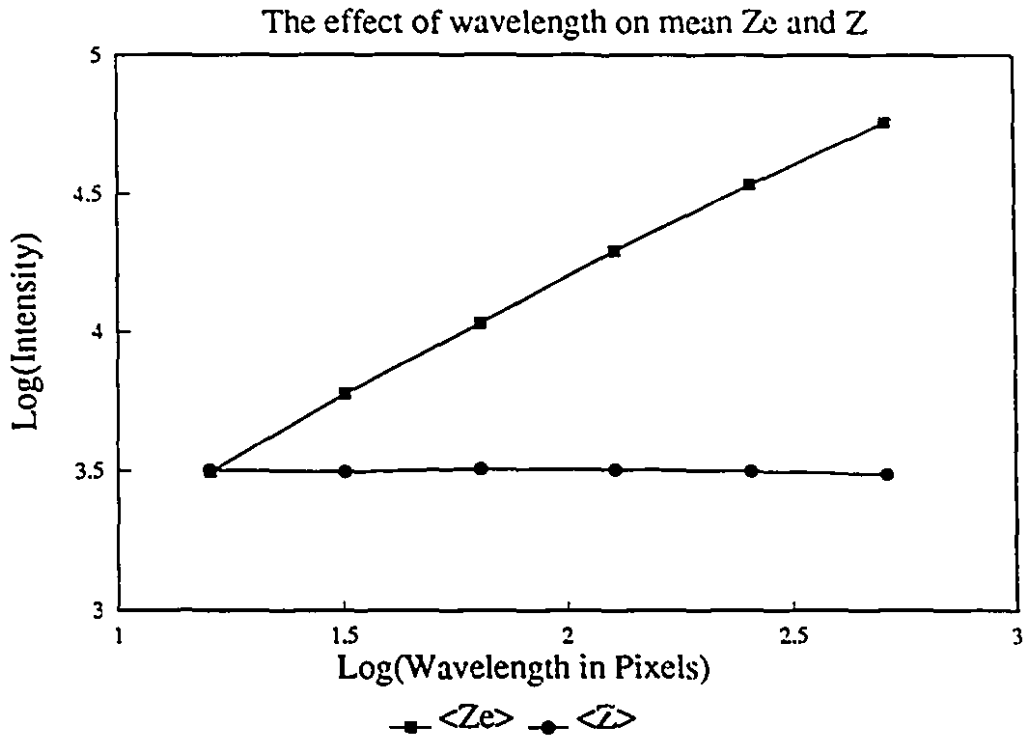

Figure 7.26: The effect of wavelength on $\langle Z_{e\lambda}(t) \rangle$ and $\langle Z_\lambda(t) \rangle$ for 6 wavelengths. The wavelengths used were 16, 32, 64, 128, 256, 512 pixels. $\langle Z_{e\lambda}(t) \rangle$ is clearly a function of wavelength.

The results of this demonstration clearly emphasize the dependence on measurement scale of intensities measured by a radar from a scaling rainfield. Simply by changing wavelength there is a shift of singularities moderated by $K_{A,R}(1)$, and the distributions are centered differently.

Simulataneous observation of the same rainfield by multiple radars of different wavelength will face difficulties such as this. The results show that even if the radars are electronically calibrated to high precision the mean intensities will differ by an amount dependent on the scales of observation B_λ and λ_w, as well as on the variability of the drop field characterized by C_1.

7.3.4.1 The 'Foot' Region.

Reproduction of the 'foot' region noticed in the spectra of the echo fluctuation time series is possible by introducing white noise below the wavelength scale. Recall that the 'foot' appears at the highest frequencies as a break in the high frequency scaling regime and results in the bending of the spectral slope towards a white noise (zero slope) character. The application of the successful modelling of this effect is to any field which exhibits scaling behaviour down to some inner scale Λ^{-1} and below this scale is independent.

The RCS model construction process was altered to allow the introduction of white noise at scales smaller than the wavelength scale. The computation of $Z_{\epsilon\lambda}(t)$ was modified such that white noise was introduced at a scale of $\lambda_w/2$. Modifying the percentage of the wavelength filled with noise affects the point at which the high frequency scaling regime is broken. Figure 7.27 shows the high frequency scaling regime when white noise is introduced. The spectrum is clearly not of the form $E(k) \propto k^{-\beta}$, as there is a scaling break at λ_w corresponding exactly to the scale at which white noise was intoduced.

The reproducibility of the foot suggests that there is a scale in the rainfield below which the drops no longer exhibit scaling behaviour. Corroborating evidence for this idea is provided by the work of Rodi et al. (1992). Rodi et al. examined the behaviour of droplet concentrations using the FFSSP probe (Brenguier, 1992). The spectral analysis of this droplet concentration data reveals the same spectral behaviour shown by the foot region. The droplet field is likely non-scaling at millimeter scales. The scale breaking of the high frequency scaling regime roughly coincides with the viscous scales of the turbulent windfield.

The lack of scaling behaviour in the high frequency scaling regime makes multifractal analysis tools inapplicable to this regime. The simplicity of the scaling assumption is shattered by the introduction of white noise.

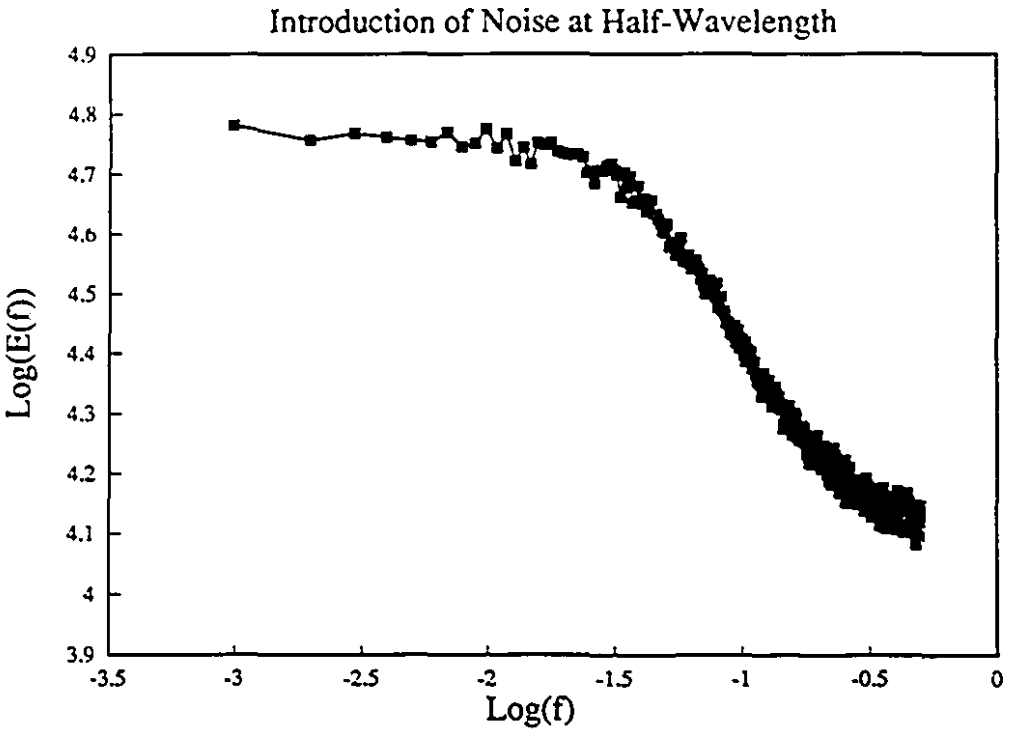

Figure 7.27: RCS model construction including a 'foot'. The foot was introduced by replacing half of the variability in each wavelength with white noise. Note that the scaling behaviour is broken at half wavelength.

8.0 Conclusions, Implications, and Extensions.

8.1 Conclusions.

The major contribution that this thesis makes is in the introduction of the simple idea that the scaling variability of rainfall observed by radars at super-resolution scales extends to sub-resolution scales. This simple idea leads immediately to the core of central results which comprise a full statistical description of the fluctuating radar echo from multiscaling rainfield variability. The qualitative and quantitative features of the statistics arising from this assumption, and the resulting models, match those of observed time series of the fluctuating echo very well. The statistical formulation provides a complete framework for the interpretation of echo fluctuations from a scale invariant rainfield and represents the general solution to the scalar multifractal radar observer's problem. What is special about the solution is that it relates the measured effective reflectivity directly to the radar cross section field and hence to the concentration of water without the necessity of invoking the standard definition of reflectivity. Specific results concerning the conditional probabilities of radar echoes and the rainfield which would allow the question of accuracy to be adressed remain as an extension to this thesis (see below). The interpretation of the fluctuating echo offered by this approach differs greatly from the approach of the standard theory, whose only objective is to measure the mean reflectivity. The theory also shows that a great deal of additional information about the statistical/dynamical nature of the rainfield can be extracted from the fluctuating echo.

The ability of a simple time-space multifractal model to reproduce the spectral behaviours found in time series of the fluctuating echo is a major achievement which cannot easily be dismissed. The spectral plateau is the most graphic evidence that the measures and statistics of the fluctuating echo are affected by the measurement scales of the radar. The assumptions used in the time-space model were kept as simple as possible to emphasize the importance of the multifractal variability. The low and high frequency scaling regimes reproduced in the time-space model correspond to those observed on spectra of time series of radar echo fluctuations. The spectral analysis performed on the fluctuating echo, as well as the modelling results which show the scale dependent nature of the distribution of intensities, reveals that a simple comparison of measured intensity of radar echoes with the Rayleigh form, as performed by Lhermitte and Kessler (1966), is not adequate to determine the statistical nature of radar echoes.

Of the specific results that this thesis introduces to the interpretation of the fluctuating echo the most important and interesting is the term $K_{\Lambda,R}(1)$. $K_{\Lambda,R}(1)$ is a linear term introduced into the multifractal exponents describing the statistics of the amplitude of a radar signal from a scaling rainfield. It is the result of the complex dressing operation performed by the Fourier component operation of a radar on rainfield variability. $K_{\Lambda,R}(1)$ can be interpreted as a shift in the singularities (γ) that can be observed within time series of the fluctuating echo. In this sense $K_{\Lambda,R}(1)$, because it is a function of the variability of the rainfield described by C_1, affects the observed distributions of intensities as well as second order statistics such as the power spectrum. If the rainfield is scaling, then $K_{\Lambda,R}(1)$ is a fundamental quantity that must be known to interpret radar data. The bias in the mean of the distribution of $Z_{e\lambda}$ relative to the distribution of Z_λ as well as the behaviour of the distribution with scale are all dependent upon $K_{\Lambda,R}(1)$. Indeed, the relation between the statistics of the drops V and the measured reflectivity of a scaling rainfield are described in terms of $K_{\Lambda,R}(1)$.

Another useful result is the 2^α relation between C_1 of the radar cross section field $\sigma(x,t)$ and the measured C_1 of the echo fluctuation time series $Z_{e\lambda}(t)$. This result shows that estimates of C_1, or sparsity of the mean rainfield, derived from radar data are actually 2^α times those of the $\sigma(x,t)$ field. In the case of the estimates of α and C_1 made by this thesis, this result would indicate that the C_1 of the V field over the VPR is around 0.1 from year to year.

The impressive ability of the multifractal models to reproduce the observables of the radar echo fluctuation problem makes the notion of multifractal sub-resolution variability the logical alternative to the sub-resolution homogeneity assumptions of the standard theory. The assumption of sub-resolution homogeneity in the interpretation of radar echo fluctuations is no longer necessary. The relatively simple forms that result from the assumption of scaling sub-resolution rainfield variability belie the comprehensive statistical knowledge of the rainfield that they represent once the necessary parameters are estimated from measurements of the fluctuating echo.

8.2 Implications and Extensions.

The implications and possible extensions of the work presented in this thesis are enormous. This is due largely to the originality of the assumption of scaling sub-resolution variability and the ensuing complete statistical characterization of $Z_{e\lambda}$. A large number of studies using radar

have attempted to draw attention to these problems, but without result. It is my hope that the simple modelling techniques presented within this thesis inspire modifications and applications to other areas. There are a very large number of research areas where extension of the methods presented here could result in practical and theoretical results that are very valuable. Only a few of these possibilities will be outlined below. Some of the following possibilities are mere extrapolations of the results presented herein and can therefore show a personal bias towards a problem, some of the possibilities have already been discussed with experts and will be appropriately credited.

The Cross Moments of $Z_{\epsilon\lambda}$ with V_λ.

The result that (relation 6.21)

$$V_\lambda \overset{d}{=} Z_{\epsilon\lambda}^{1/2}\lambda^{K_{A,R}(1)-D/2}$$

is the simplest deduction that can be made concerning the distributions of $Z_{\epsilon\lambda}$ and V_λ. Examination of the cross moments of the distribution could provide an exact form for the conditional probability of $Z_{\epsilon\lambda}$ given V_λ (i.e. $Pr\left(Z_{\epsilon\lambda} > \lambda^{\gamma_{Z_\epsilon}} ; V_\lambda > \lambda^{\gamma_V}\right) \approx \lambda^{-c\left(\gamma_{Z_\epsilon},\gamma_V\right)}$). Knowledge of this relation would permit errors on the accuracy of the statistics of V to be computed from measures of $Z_{\epsilon\lambda}$, and would suggest new data acquisition strategies to minimize those errors. The cross moments are of the form

$$\langle Z_{\epsilon\lambda_1}^{q} V_{\lambda_2}^{q} \rangle = \lambda^{K(q_1,q_2)}$$

Analysis of the resulting scaling functions represents a significant amount of work but should yield a general expression for the cross moments. From the derived expression a general form for the conditional probabilities would result, and a more specific relation between $Z_{\epsilon\lambda}$ and V_λ could be established.

Limits on the knowledge of $Z_{\epsilon\lambda}$?

The existence of a scaling rainfield requires a fundamental shift in how data is considered and processed. The first recognition of the echo fluctuation problem was interpreted as a limit on the knowledge of $\langle Z_{\epsilon\lambda} \rangle$. In the assumptions of the standard theory each data point acquired by the radar is independent, hence each carries no information. The standard theory provides an invariant prescription for the limits of knowledge on Z_ϵ. This is embodied in the joint probability distribution $Pr(Z_\epsilon/Z)$. The well known standard deviation on averages of radar echoes $5.6dB/k^{1/2}$, where k is the number of echoes averaged, is directly dependent upon the rainfield being uniform. In the universal multifractal formalism the mean is just another moment of $Z_{\epsilon\lambda}$. Determination of the universal function K(q) represents a complete characterization of the signal information. The degree of moment that can be directly verified is given by D_s. Determination of the K(q) function is not dependent upon the accurate measurement of $\langle Z_{\epsilon\lambda} \rangle$. All that is necessary is sufficient data to define a small range of $K(q,\eta)$ vs η. Thus, within the universal multifractal formalism each data point represents a contribution to the determination of all moments. The universal multifractal formalism represents a more efficient use of the information present in the signal returning to a radar from precipitation.

Information Conservation: Storage and Display Strategies.

As in Marshall and Hitschfeld (1953) the recognition of the statistics of the problem affect how the data is stored. The conservation of this information places heavy requirements on the data acquisition and storage technology. Indeed, the technology may still not exist for efficient storage and retrieval from a source such as a volume scanning radar. The preservation of scaling structure in radar data requires that the data be stored in unmodified form (this assumes the data contains no scaling breaks like the plateau). For scanning radars the data must be stored in its native radial format without any averaging. Averaging operations necessarily reduce the information content of signals. This vastly increases the storage requirements for radar data, but provides the opportunity of greater understanding of the dynamical context of rainfall measurements. Display systems would therefore be required to cope with the data in radial format which would imply a large number of computations.

Sub-Resolution Dependence of SAR Measurements.

Synthetic Aperture Radar (SAR) is probably the application for the results presented in this thesis that represents the most exciting possibility. The image construction process used for SAR radar data necessarily involves assumptions about the sub-resolution homogeneity of targets. The difficulty is that SAR radars are used to examine a very wide variety of targets of which rain is not one. The SAR problem represents the possibility of further applications of complex cascades since the SAR radar processing strategy is fully coherent. Thus, a tensorial form of the RCS model would be required. The number of free parameters to the model would therefore be enormous. Current SAR processing strategies do not deal with sub-resolution inhomogeneity (Livingston, personal communication, 1993).

Sub-Resolution Dependence of Doppler Radar Measurements.

The formulation for the marginal statistics of $Z_{e\lambda}$ involves the following expression for the complex moments of the amplitude of the signal returned from rain

$$A_\lambda = e^{\Gamma_R + i\Gamma_I}$$

which gives

$$|A_\lambda| = e^{\Gamma_R} \quad Arg(A_\lambda) = \Gamma_I$$

therefore it is possible to define two K(q) functions, one for the real part of the generator and one for the imaginary part of the generator:

$$K_A(q) = K_{A,R}(q) + iK_{A,I}(q)$$

The complex component of the $K_A(q)$ function governs the scaling of the doppler phase component of doppler measurements. Irrespective of whether this term turns out to be trivial the inclusion of sub-resolution variability with the attendant change in assumptions about the velocity dependences in the drop field, immediately yields an explanation for the width of the doppler spectrum. It is likely that doppler spectrum width will be found to depend on the dynamical quantities α and C_1.

Range Dependent $Z_{e\lambda}$-R.

The statistics of $Z_{e\lambda}$ are dependent upon the ratio of the pulse volume scale B to the wavelength scale λ_w. In the RCS model the scale of the pulse volume was kept constant in keeping with the observed data sets and the limitations of the computer model. The volume of the pulse as a function of range is given by $v = l \cdot r\theta_v \cdot r\theta_h$. For most operational weather radars the pulse will be observed out to ranges of at least 200 km. At this range the lateral scales far exceed the pulse length scale l. As a result the expanding pulse volume will have a different characteristic scale at each range gate. As such, the statistics of $Z_{e\lambda}$ will depend on this characteristic scale and will therefore be range dependent. A small correction for this effect could easily be introduced to any processing strategy.

Dynamically Determined Z-R.

The recent suggestion by Atlas and Rosenfeld (1993) that Z-R relationships be implemented in a case sensitive fashion. The work of Atlas and Rosenfeld (1993) shows that the most representative Z-R relation can be categorized according to rain type. In an automated system the appropriate Z-R relation would be used based on observation of storm type.

A possible alternative to this plan, which at this stage is very speculative, would consist of using the measured dynamical quantities α and C_1 to determine the dynamical context of the rain in order to determine the appropriate $Z_{e\lambda}$-R relation. The relations for the marginal statistics of $Z_{e\lambda}$ provide the relation between measured universal parameters and those of the $\sigma(x,t)$ field. The advantage of the dynamical quantities is that they are measured rather than being subjective descriptions of rain type. Such an ability could vastly improve rainfall raingauge comparisons by providing an exact context for comparison of the two scale dependent measures of rainfield variability. Currently there exists no such database of dynamics versus Z-R relationship. Implementation of a calibrated, or self-calibrating, form of this strategy in an automated setting would be relatively straightforward.

The Effect of Droplet Clustering on Drop Formation.

A natural question that arises from the consideration of the rain flux μ_R as a cascade quantity is the nature of drop clustering. The clustering of rain flux onto smaller volumes inevitably results in the concentration of liquid water. The range of scales over which this clustering occurs likely extend from the large outer scales observed in section 4.1 to very small scales. In this thesis it is assumed that the rain flux exhibits self-similar behaviour to scales smaller than the 3 cm wavelength scale. To date only Poisson type clustering (trivial clustering) has been considered in the solution of the formation of drops. The effect of non-trivial clustering of the type inherent to multifractals on the formation rate and distribution size of drops has never been examined. An effort by Zawadzki (1993, personal communication) is currently underway to examine this effect. In the context of a scaling theory of radar echo fluctuations the dynamics of a particular rain event can be determined and the degree of clustering, measured as C_1, could be estimated. Parameterization of a scaling drop formation model could then be implemented in real time with the correct data acquisition strategy.

$Z_{e\lambda}$-A relations.

Attenuation is a quantity that is also determined with the supposition that $Z_{e\lambda}$ is a well determined quantity. Scaling non-uniformity of the rainfield introduces an exponent into any path integrated quantity, of which attenuation is only an example. This is important to the extent that it adds another dimension to the problem of microwave communications or to short wavelength cloud radars.

9.0 References.

Allred, L., And G. Kelly, 1993. A General Solution to Optimization Problems Using a Differentially Applied Genetic Algorithm. Paper presented at Alife III, Santa Fe Institute, Santa Fe, New Mexico.

Armijo, L., 1966. Statistical properties of radar echo patterns and the radar echo process. *Journal of Atmospheric Science*, 23, 560-568.

Atlas, D. (ed.), 1990. Radar in Meteorology: Battan Memorial and 40th Anniversary Radar Meteorology Conference,. AMS, Boston.

Atlas, D., and C.W. Ulbrich, 1990. Early Foundations of the Measurement of Rainfall by Radar. In Radar in Meteorology: Battan Memorial and 40th Anniversary Radar Meteorology Conference, ed D. Atlas, AMS, Boston.

Austin, P.M., 1952. A Study of the Amplitude Distribution Function for Radar Echoes from Precipitation. Technical Report #17, M.I.T.

Austin, P.M., And R.A. Houze, 1972. Analysis of the Structure of Precipitation Patterns in New England. *Journal of Applied Meteorology*, 11, 926-935.

Austin, P.M., 1987. Relation between Measured Radar Reflectivity and Surface Rainfall, *Monthly Weather Review* 115, 1053-1070.

Bak, P., C. Tang, and K. Weissenfeld, 1987. Self-Organized Critical Phenomena. *Physical Review Letters*, 59, 381-385.

Battan, L, 1973. Radar Observation of the Atmosphere. University of Chicago Press.

Beard, K.V., D.B. Johnson and A.R. Jameson, 1983. Collisional Forcing of Raindrop Oscillations, *Journal of the Atmospheric Sciences*, 40, 455-462.

Beard, K.V., 1984. Raindrop Oscillations: Evaluations of a Potential Flow Model with Gravity, *Journal of the Atmospheric Sciences*, 41, 1765-1774.

Beard, K.V., and C. Chuang, 1987. A New Model for the Equilibrium Shape of Raindrops, *Journal of the Atmospheric Sciences*, 44, 1509-1524.

Bell, T.L., 1987. A Space-Time Stochastic Model of Rainfall for Satellite Remote Sensing Studies. *Journal of Geophysical Research*, 92, 9631-9643.

Bras, R.L., and I. Rodriguez-Iturbe, 1976. Rainfall Generation: A Nonstationary Time Varying Multidimensional Model. *Water Resources Research*, 12, 450-456.

Brax, P. and R. Pechanski, 1991. Levy-Stable law description of intermittent behaviour and quark-gluon phase transitions. *Physical Letters B*, 225-230.

Brenguier, J.L., 1992. Statistical properties of the droplet spatial distribution in stratocumulus. Preprints 11Th International Conference on Clouds and Precipitation, 125-128, AMS, Boston.

Chandrasekar, V., W.A. Cooper and V.N. Bringi, 1987. Axis Ratios and Oscillations of Raindrops, *Journal of the Atmospheric Sciences*, 45(8), 1323-1333.

Cho, H-R., 1985. Stochastic Dynamics of Precipitation: An Example. *Water Resources Research*, 21, 1225-1232.

Cole, J.W., 1964. Statistics related to the shape and scale of pattern elements. Final Report, Contract Cwb-10709, Travelers Research Center, Hartford, Conn.

Crane, R.K., 1990. Space-Time Structure of Rain Rate Fields. *Journal of Geophysical Research*, 95, 2011-2020.

Douglas, R.H., 1990. The Stormy Weather Group (Canada). In Radar in Meteorology: Battan Memorial and 40th Anniversary Radar Meteorology Conference, ed D. Atlas, AMS, Boston.

Drufuca, G., 1977. Radar-Derived Statistics on the Structure of Precipitation Patterns. *Journal of Applied Meteorology*, 16, 1029-1035.

Duncan, M.R., F. Fabry, S. Lovejoy, and D. Schertzer, 1992a. "An Examination of High PRF Time Series from a Vertical Pointing Radar: The Observer's Problem Revisited." Preprints, 2nd International Symposium on Hydrological Applications of Weather Radar, Hannover, Germany, September, 7-10, 1992.
Revised, 1993 for publication in book form of preprints. Manuscript retitled "Radar Measurement Scales and Non-Uniformity in the Rainfield".

Duncan, M.R., S. Lovejoy, F. Fabry and D. Schertzer, 1992b. "The Fluctuating Radar Cross Section (RCS) of Multifractal Scatterers". Preprints, 11Th International Conference on Clouds and Precipitation, Montreal, Canada.

Duncan, M.R., A. Bellon, A. Kilambi, and G.L. Austin, 1992. "PPS and PPSjr: A Distribution Network for Weather Radar Products, Severe Weather Warnings and Rainfall Forecasts". Preprints, Eighth International Conference on Interactive Information and Processing Systems for Meteorology, Oceanography, and Hydrology, Atlanta, Georgia, AMS, Boston.

du Toit, P.S., 1967. Doppler Radar Observations of Drop Sizes in Continuous Rain. *Journal of Applied Meteorology*, 6, 1082-1087.

Eagleson, P.S, N.M Fennessey, W. Quilang, I. Rodriguez-Iturbe, 1987. Application of spatial Poisson models to air mass thunderstorm rainfall. *Journal of Geophysical Research*, 92, 9661-9678.

Fabry, F., 1990. Precipitation Estimates by Radar: A Zenith Pointing Perspective. M.Sc. Thesis, McGill Unversity, Montreal, Canada, 83 pp.

Fabry, F., A. Bellon, and M.R. Duncan, 1993. High Resolution Rainfall Measurements by Radar for Very Small Basins: The Sampling Problem Reexamined. Submitted to Journal of Hydrology.

Falconer, K, 1989. Fractal Geometry Mathematical Foundations and Applications. Wiley and Sons, New York, 288 pp.

Feder, J., 1988. Fractals. Plenum Press, New York, 283 pp.

Feller, W., 1971. An Introduction to Probability Theory and its Applications. John Wiley and Sons, New York.

Frisch, U., P.L. Sulem, and M. Nelkin, 1978. A simple dynamical model of intermittency in fully developed turbulence. *Journal of Fluid Mechanics*, 87, 719-724.

Gabriel. P., S. Lovejoy, D. Schertzer, and G.L. Austin, 1988. Multifractal Analysis of Satellite Resolution Dependance. *Geophysical Research Letters*, 1373-1376.

Garrido, P., 1993. M.Sc. Thesis, McGill University.

Goldberg, D.E., 1989. Genetic Algorithms in Search, Optimization, and Machine Learning. Addison-Wesley, New York, 412 pp.

Grassberger, P., 1983. Generalized Dimensions of Strange Attractors. *Physics Letters A*, 97, 227.

Grosh, R.C., 1989. The Highly Non-Linear Aspects of Z-R and VT-Z Caused by Raindrop Terminal Fall Speeds, 24th Conference on Radar Meteorology, AMS, Boston.

Grosh, R.C., 1991. A Review of Rain Drop Size Distribution Measurements, 25th Conference on Radar Meteorology, AMS, Boston.

Gunn, K.L.S., and T.W.R. East, 1954. The microwave properties of precipitation particles. *Quarterly Journal of the Royal Meteorological Society*, 80, 522-544.

Gupta, V.K., and E. Waymire, 1987. On Taylor's Hypothesis and Dissipation in Rainfall. *Journal of Geophysical Research*, 92(D8), 9657-9660.

Gupta, V.K., and E. Waymire, 1990. Multiscaling Properties of Spatial Rainfall and River Flow Distributions. *Journal of Geophysical Research*, 95(D3), 1999-2009.

Gupta, V.K., and E. Waymire, 1993. A Statistical Analysis of Mesoscale Rainfall as a Random Cascade. *Journal of Applied Meteorology*, 32(2), 251-267.

Halsey, T.C., M.H. Jensen, L.P. Kadanoff, I. Procaccia, and B. Shraiman, 1986. Fractal Measures and their Singularities: The Characterization of Strange Sets. *Physical Review A 33*, 1141-1151.

Hentschel, H.G.E., I. Procaccia, 1983. The Infinite Number of Generalized Dimensions of Fractals and Strange Attractors, *Physica 8D*, 435-444.

Holland, J.H., 1992. Adaptation in Natural and Artificial Systems. MIT Press, Cambridge, Mass, 211pp.

Hosking, J.G., and C.D. Stow, 1987. Ground-Based, High-Resolution Measurements of the Spatial and Temporal Distribution of Rainfall, *Journal of Climate and Applied Meteorology*, 26, 1530-1539.

Hubert, P., Y. Tessier, P. Ladoy, S. Lovejoy, D. Schertzer, J.P. Carbonnel, S. Violette, I. Desurosne, and F. Schmitt, 1993. Multifractals and Extreme Rainfall Events. *Geophysical Research Letters*, (In Press).

Hurst, H.E., 1951. Long-term storage capacity of reservoirs. *Transactions of the American Society of Civil Engineers*, 116, 770-808.

Katz, I., and P.J. Harvey, 1990. Radar Meteorology at Radiation Laboratory, MIT, 1941 to 1947. In Radar in Meteorology: Battan Memorial and 40th Anniversary Radar Meteorology Conference, ed D. Atlas, AMS, Boston.

Kerr, D.E., 1951. Propagation of Short Radio Waves. Dover, 710pp.

Kessler, E., 1966. Computer Program for Calculating Average Lengths of Weather Radar Echoes and Pattern Bandedness. *Journal of Atmospheric Sciences*, 23(5), 569-574.

Kolmogorov, A.N., 1941. Local Structure of Turbulence in an Incompressible Fluid at Very High Reynold's Numbers. *Dokl. Akad. Nauk SSSR*, 30(4), pp 299-303.

Kolmogorov, A.N., 1962. A refinement of previous hypotheses concerning the local structure of turbulence in viscous incompressible fluids at high Reynolds number. *Journal of Fluid Mechanics*, 83, 349.

Krajewski, W.F., R. Raghavan, and V. Chandrasekhar, 1993. Physically based Simulation of Radar Rainfall Data Using a Space-Time Rainfall Model. *Journal of Applied Meteorology*, 32, 268-283.

Ladoy, P., S. Lovejoy, and D. Schertzer, 1991. Extreme fluctuations and intermittency in climatological temperatures and precipitation. Scaling, Fractals and non-linear variability geophysics, D. Schertzer and S. Lovejoy, eds., 241-250, Kluwer.

Ladoy, P., F. Schmitt, D. Schertzer, and S. Lovejoy, 1993. Analyse Multifractale de la Variabilite Temporelle des Observations Pluviometriques a Nimes. C. Roy. Acad. Science. (In Press).

Lamperti, J., 1962. Semi-stable stochastic processes. *Transactions of the American Mathematical Society*, 104, 62-78.

Lardner, C., N. Desaulniers-Soucy, S. Lovejoy, D. Schertzer, C. Braun, and D. Lavallee, 1992. Universal Multifractal Characterization and Simulation of Speech. *International Journal of Bifurcation and Chaos*, 2(3), 715-719.

Lavallé, D., 1991. Multifractal Analysis and Simulation Techniques and Turbulent Fields, PhD Thesis, McGill University, 142 pp.

Lawson, J.L, and G.E. Uhlenbeck, 1950. Threshold Signals. M.I.T. Radiation Laboratory Series, McGraw-Hill, Toronto, 388 pp.

Lhermitte, R.M., and E. Kessler, 1966. Estimation of the Average Intensity of Precipitation Targets. Preprints of the 12th Conference on Radio Meteorology, AMS, Boston.

Lovejoy, S., 1981. The Statistical Characterization of Rain Areas in Terms of Fractals. Preprints, 20th Radar Conference, AMS, Boston.

Lovejoy, S., 1982. Area-Perimeter Relation for Rain and Cloud Areas. *Science*, 216, 185-187.

Lovejoy, S., and B.B. Mandelbrot, 1985. Fractal Properties of Rain and a Fractal Model. *Tellus*, 37A, 209-232.

Lovejoy, S., And D. Schertzer, 1985. Generalized Scale Invariance in the Atmosphere and Fractal Models of Rain. *Water Resources Research*, 21, 1233-1249.

Lovejoy, S., D. Schertzer, and A.A. Tsonis, 1987. Functional Box-Counting and Multiple Elliptical Dimensions in Rain. *Science*, 235, 1036-1038.

Lovejoy, S., And D. Schertzer, 1990a. Multifractals, Universality Classes and Satellite and Radar Measurements of Cloud and Rain Fields. *Journal of Geophysical Research*, 95(D3), 2021-2034.

Lovejoy, S., And D. Schertzer, 1990b. Fractals, Raindrops and Resolution Dependance of Rain Measurements. *Journal of Applied Meteorology*, 29, 1167-1170.

Lovejoy, S., And D. Schertzer, 1991. Multifractal Analysis Techniques and the Rain and Cloud Fields form 10^{-3} to 10^{6} m. In, Scaling, Fractals and Non-Linear Variability in Geophysics, D. Schertzer and S. Lovejoy Eds., Kluwer Academic Publishers.

Lovejoy, S. And D. Schertzer, 1993. Multifractals and Rain, In New Uncertainty Concepts in Hydrology and Water Resources, UNESCO series in Water Sciences, Cambridge University Press, Z.W. Kunzewicz ed.

Low, T.B., and R. List, 1982. Collision, Coalescence and Breakup of Raindrops. Part I: Experimentally Established Coalescence Efficiencies and Fragment Size Distribution in Breakup. *Journal of the Atmospheric Sciences*, 39, 1591-1606.

Low, T.B., And R. List, 1982. Collision, Coalescence and Breakup of Raindrops. Part II: Parameterization of Fragment Size Distributions. *Journal of the Atmospheric Sciences*, 39, 1607-1618.

Mandelbrot, B.B., 1971. A Fast Fractional Gaussian Noise Generator, *Water Resources Research*, 7(3), 543-553.

Mandelbrot, B.B., 1974. Intermittent turbulence in self-similar cascades: Divergence of high moments and dimension of the carrier. *Journal of Fluid Mechanics*, 62, 331-350.

Mandelbrot, B., And J.W. Van Ness, 1968. Fractional brownian motions, fractional noises and applications. *SIAM Review*, 10, 422-450.

Mandelbrot, B., And J.R. Wallis, 1969. Some long-rum properties of geophysical records. *Water Resources Research*, 5, 228.

Marshall, J.S., And W. Hitschfeld, 1953. Interpretation of The fluctuating Echo from Random Distributed Scatterers; Part I. *Canadian Journal of Physics*, 31, 962-994.

Marshall, J.S., And W.M. Palmer, 1948. The Distribution of Raindrops with Size. *Journal of Meteorology*, 5, 165-166.

Meneveau, C. And K.R. Sreenivasan, 1987. Simple Multifractal Cascade Model for Fully Developed Turbulence. *Physical Review Letters*, 59(13), 1424-1427.

Meneveau, C and K.R. Sreenivasan, 1989. Measurement of $f(\alpha)$ from Scaling of Histograms, and Applications to Dynamical Systems and Fully Developed Turbulence. *Physics Letters A*, 137(3), 103-112.

Meneveau, C. And K.R. Sreenivasan, 1990. The Multifractal Nature of Turbulent Energy Dissipation. Journal of Fluid Mechanics, 224, 428-484.

Musgrove, C., And M. Brook, 1975. Microwave Echo Fluctuations Produced by Vibrating Water Drops. *Journal of the Atmospheric Sciences*, 32, 2001-2007.

Obukhov, A., 1962. Some specific features of atmospheric turbulence. *Journal of Geophysical Research*, 67, 3011.

Parisi, G., And U. Frisch, 1985. A multifractal model of intermittency. Turbulence and predictability in geophysical fluid dynamics and climate dynamics. Eds. M. Ghil, R. Benzi, G. Parisi, North-Holland, 84-88.

Pecknold, S., S. Lovejoy, D. Schertzer, C. Hooge, and J.F. Malouin, 1993. The Simulation of Universal Multifractals. **Cellular Automata: Prospects in Astronomy and Astrophysics**, A. Lajeune, J. Perdang eds., World Scientific, (In Press).

Press, W.H., S.A. Teukolsky, W.T. Vetterling, and B.P. Flannery. Numerical Recipes in C (2nd ed.). Cambridge University Press, 994 pp.

Priestley, M.B., 1981. Spectral Analysis and Time Series. Academic Press, Boston, 890 pp.

Pruppacher, H.R., and K.V. Beard, 1970. A wind tunnel investigation of the internal circulation and shape of water drops falling at terminal velocity in air. *Quarterly Journal of the Royal Meteorological Society*, 96, 247-256.

Richardson, L.F., 1922. Weather Prediction by Numerical Process. Republished by Dover, 1965.

Rodi, A.R., J.L. Brenguier, and J.P. Chalon, 1992. Case Study of Cumulus Microstructure with the New FFSSP. Preprints 11Th International Conference on Clouds and Precipitation, 169-172, AMS, Boston.

Rodriguez-Iturbe, I., V.K. Gupta, and E. Waymire, 1984. Scale considerations in the modelling of temporal rainfall. *Water Resources Research*, 20, 1611-1619.

Rodriguez-Iturbe, I., 1986. Scale of Fluctuation of Rainfall Models. *Water Resources Research*, 22, 15-37.

Rodriguez-Iturbe, I., B.F. de Power, and J.B Valdes, 1987. Rectangular pulses point process models for rainfall; analysis of empirical data. *Journal of Geophysical Research*, 92, 9645-9656.

Rogers, R.R., 1971. The effect of variable target reflectivity on weather radar measurements. *Quarterly Journal of the Royal Meteorological Society*, 97, 154-167.

Rogers, R.R., 1976. Statistical Rainstorm Models: Their Theoretical and Physical Foundations. *IEEE Transactions on Antennas and Propagation*, 547-566.

Schaffner, M., R. Rhinehart, and R. Leonardi, 1980. Detection of Nonuniformities within the Radar Measurement Cell. Preprints, 19th Radar Conference, AMS, Boston, 256-263.

Schertzer, D., And S. Lovejoy, 1983. Elliptical Turbulence in the Atmosphere. Proceedings of the 4th Symposium on Turbulent Shear Flows, 11.1-11.8, Karlsrhule, West Germany.

Schertzer, D., And S. Lovejoy, 1984. Turbulence and Chaotic Phenomena in Fluids, 505-508, T. Tatsumi ed, Noth-Holland.

Schertzer, D., And S. Lovejoy, 1985a. The dimension and intermittency of atmospheric dynamics. Turbulent Shear Flows 4, 7-33, B. Launder ed., Springer-Verlag.

Schertzer, D., And S. Lovejoy, 1985b. Generalized Scale Invariance in turbulent phenomena. *P. Chem. Hydrodynamics J.* 6, 623-635.

Schertzer, D., And S. Lovejoy, 1987. Physical Modelling and Analysis of Rain and Clouds by Anisotropic Scaling Multiplicative Processes. *Journal of Geophysical Research*, 92(D8), 9692-9714.

Schertzer, D., And S. Lovejoy, 1989. Generalized Scale Invariance and Multiplicative Processes in the Atmosphere. *Pageoph*, 130, 57-81.

Schertzer, D., And S. Lovejoy, 1991. Nonlinear Geodynamical Variability: Multiple Singularities, Universality, and Observables. In Scaling, Fractals and Non-Linear Variability in Geophysics, D. Schertzer and S. Lovejoy Eds., Kluwer Academic Publishers.

Schertzer, D, S. Lovejoy, and D. Lavallee, 1993. Generic First Order Phase Transitions in Multifractal Processes. Submitted to *Physical Review Letters*.

Schertzer, D., And S. Lovejoy, 1993a. From Scalar Cascades to Lie Cascades: Joint Multifractal Analysis of Rain and Cloud Processes.

Schertzer, D., And S. Lovejoy, 1993b. Nonlinear Variability in Geophysics 3; Scaling and Multifractal Processes. Lecture Notes from EGS Richardson Memorial Conference, September 7-10, 1993, Cargese, France. Published by the AGU.

Schmitt, F., D. Lavallée, D. Schertzer, and S. Lovejoy, 1991. Empirical determination of universal multifractal exponents in turbulent velocity fields. *Physical Review Letters* (in Press).

Seed, A.W., 1989. Statistical Problem in Measuring Convective Rainfall. PhD Thesis, McGill University, 141 pp.

Seed, A.W., and G.L. Austin, 1990a. Sampling Errors for Raingauge-Derived Mean Areal Daily and Monthly Rainfall, *Journal of Hydrology* 118, 163-173.

Seed, A.W., And G.L. Austin, 1990b. Variability of Summer Florida Rainfall and its Significance for the Estimation of Rainfall by Gauges, Radar and Satellite, *Journal of Geophysical Research*, 95(D3), 2207-2215.

Segal, B., 1979. High-intensity rainfall statistics for Canada. Comm. Res. Centre, Department of Communications, Canada, report CRC 1329-E, Ottawa, Canada.

Smith, P.L., 1964. Interpretation of the Fluctuating Echo from Randomly Distributed Scatterers: Part 3. Stormy Weather Group Report MW-39, McGill University, 70 pp.

Sreenivasan, K.R., 1991. Fractals and Multifractals in Fluid Turbulence. *Annual Review of Fluid Mechanics*, 23, 539-600.

Swingle, D.M., 1990. Weather Radar in the United States Army's Fort Monmouth Laboratories. In Radar in Meteorology: Battan Memorial and 40th Anniversary Radar Meteorology Conference, ed D. Atlas, AMS, Boston.

Taqqu, M.S., 1987. Random Processes with Long-Range Dependance and High Variability. *Journal of Geophysical Research*, 92, 9683-9686.

Tessier, Y., S. Lovejoy, and D. Schertzer, 1993. Universal Multifractals in Rain and Clouds; Theory and Observations. *Journal of Applied Meteorology*, (In Press).

Torlaschi, E., And R.G. Humphries, 1983. Statistics of Reflectivity Gradients. Preprints, 21st Conference on Radar Meteorology, AMS, Boston.

Vanmarcke, E., 1983. Random Fields: Analysis and Synthesis. MIT Press. Cambridge Massachusetts.

Waymire, E., 1985. Scaling Limits and Self-Similarity in Precipitation Fields. *Water Resources Research*, 21(8), 1271-1281.

Waymire, E., And V.K. Gupta, 1981a. The Mathematical Structure of Rainfall Representations 1. A Review of the Stochastic Rainfall Models. *Water Resources Research*, 17(5), 1261-1272.

Waymire, E., And V.K. Gupta, 1981b. The Mathematical Structure of Rainfall Representations 2. A Review of the Theory of Point Processes. *Water Resources Research*, 17(5), 1273-1285.

Waymire, E., And V.K. Gupta, 1981c. The Mathematical Structure of Rainfall Representations 3. Some Applications of the Point Process Theory to Rainfall Processes. *Water Resources Research*, 17(5), 1287-1294.

Wallace, P.R., 1953. Interpretation of The fluctuating Echo from Random Distributed Scatterers; Part II. *Canadian Journal of Physics*, 31, 994-1009.

Wilson, J., D. Schertzer, and S. Lovejoy, 1991. Continuous Multiplicative Cascade Models of Rain and Clouds. In, Non-Linear Variability in Geophysics, D. Schertzer and S. Lovejoy (Eds.), Kluwer Academic Publishers.

Zawadzki, I.I., 1973. Statistical Properties of Precipitation Patterns. *Journal of Applied Meteorology*, 12, 459-472.

Zawadzki, I.I., 1984. Factors Affecting the Precision of Radar Measurements of Rain. Preprints of the 22nd Conference on Radar Meteorology, Zurich, 251-256.

Zawadzki, I.I., 1987. Fractal Structure and Exponential Decorrelation in Rain. *Journal of Geophysical Research*, 92(D8), 9586-9590.

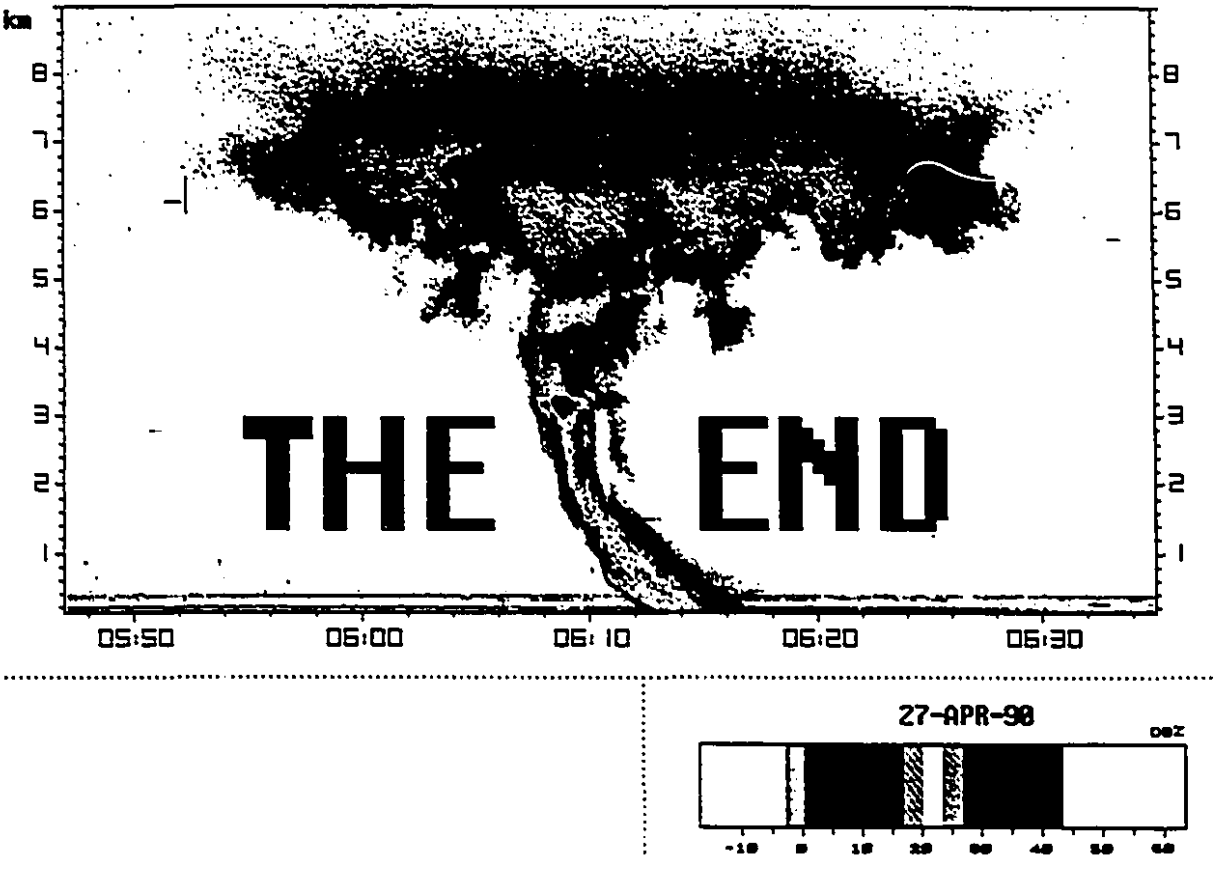

Figure END: HTI time series of the vertical structure of a small shower which passed over the VPR during the summer of 1990. Note the bright band. The startling nuclear cloud appearance of this storm should be compared to the RHI figure of a real nuclear cloud in Swingle (1990).

Appendix A: The Universal Multifractal Cascade Generator (UMCG). A Brief Explanation of the Generation of Multifractals.

In this appendix a brief, but complete, explanation of how to create universal multifractals is provided. The universal multifractal cascade generator (UMCG) is based on the work of Schertzer and Lovejoy (1987) and Wilson et al. (1991). Examples of the use of versions of the UMCG can be found in Wilson et al. (1991), Tessier et al. (1993) and Pecknold et al. (1993). The shorthand UMCG(α,C_1,H) is used to indicate a simulated multifractal field with specified α, C_1, and H.

The α-Model.

The most widely known of the cascade models is the α-model (Schertzer and Lovejoy, 1983), so named because of the divergence of moments exponent α that it introduces. The symbol q_D has already been introduced to describe the divergence of moments and will replace α in what follows. In the cascade construction process a constant field of flux, for our purposes it will be assumed that the flux quantity is rain μ_R is introduced. If the outer scale of the field is 1 then successive construction steps subdivide the field into 'boxes' of scale λ^{-1}, where λ is the ratio of the outer scale to the scale of the current construction step. The fraction of rain flux μ_R concentrated to each of the new boxes depends on the probabilities,

$$Pr\left(\mu_R = \lambda^{\gamma^+}\right) = \lambda^{-c}$$

which represents an increase or boost in flux to a box and

$$Pr\left(\mu_R = \lambda^{-\gamma^-}\right) = 1-\lambda^{-c}$$

which represents a decrease in the flux to a box. $\gamma^+ = c/\alpha$ and $\gamma^- = c/\alpha'$ with $\frac{1}{\alpha}+\frac{1}{\alpha'}=1$. In this way the initial flux is randomly distributed to finer and finer scale boxes. The parameters γ^+, γ^-, and c are usually constrained such that the ensemble average flux $<\mu_R>$ is conserved at each construction step. This relation gives

$$\lambda^{\gamma^+}\lambda^{-c}+\lambda^{-\gamma^-}(1-\lambda^{-c}) = 1$$

(there are only two free parameters among γ^+, γ^-, and c). The α-model can be further constrained such that only one free parameter exists. This results in a micro-canonical α-model or p-model. The properties of micro-canonical cascades are outlined in section 3. After n steps of the α-model the fraction of the original flux μ_R associated with a box is given by

$$(\mu_R)_n = \lambda^{\gamma_k}$$

with

$$\gamma_k = \frac{1}{n}(k\gamma^+ + (n-k)\gamma^-), \text{ with k = 1,...,n}$$

where k is the number of boosts and (n-k) is the number of decreases to the flux in the chain of multiplications that led to a given box of scale λ^{-1}. The probability of the flux intensity or singularity is given by

$$Pr(\mu_R = \lambda_k^{\gamma}) = \binom{k}{n}\lambda^{-ck}(1-\lambda^{-c})^{n-k}$$

where $\binom{k}{n}$ is the number of combinations of n objects taken k at a time. This can be rewritten as

$$Pr\left((\mu_R)_\lambda \geq (\lambda^n)_i^{\gamma}\right) = \sum_j p_{ij}(\lambda^n)^{-c_{ij}}$$

where i indexes each box, scale λ^{-1}, of the completed cascade. The p_{ij} are the scale dependant prefactors of the probability distribution and the c_{ij} are the exponents characterizing the codimension of each of the singularities γ_i. λ^n is the final scale ratio of the outer to the inner scale of the cascade. The α-model will have bounded singularities ($-\gamma^- \leq \gamma_i \leq \gamma^+$). Schertzer and Lovejoy (1987) carry the renormalization further by replacing this n step two state cascade by a single λ^n step cascade with n+1 states. This cascade process will then correspond to the random cascade described by Gupta and Waymire (1993). Making the replacement $\lambda^n \rightarrow \lambda$, and taking the limit $\lambda \rightarrow \infty$, the term in the sum with the smallest c_{ij} will dominate. Defining

$$c_i = \min\{c_{ij}\} = c(\gamma_i)$$

which yields for $\lambda \rightarrow \infty$;

$$Pr\left((\mu_R)_\lambda \geq \lambda^{\gamma_i}\right) = p_i \lambda^{-c_i}$$

where c_i is the codimension and p_i is the scale dependant prefactor. Dropping the subscript i and allowing for a continuum of states the probabilities may be written as

$$Pr\left((\mu_R)_\lambda \geq \lambda^{\gamma}\right) = p(\gamma) \cdot \lambda^{-c(\gamma)}$$

This basic multifractal relation for cascade is usually written as

$$Pr\left((\mu_R)_\lambda \geq \lambda^{\gamma}\right) = \lambda^{-c(\gamma)}$$

with the understanding that the equality takes into account the unstated logarithmic prefactors. This relation shows that each singularity or intensity of the final cascade field has a codimension given by the codimension function $c(\gamma)$. For continuous processes $c(\gamma)$ is a continuous convex function.

While adequate for the production of multifractals, the most serious deficiency of the α-model is the lack of control over C_1 and α. The next sub-section presents a process which creates universal multifractals with specific α and C_1.

The Generator Γ_λ and the Simulation of Universal Multifractals.

In the above development some quantity, such as rain flux μ_R, is concentrated by a cascade process to smaller and smaller regions. The cascade process is multiplicative. It is perhaps more intuitive to consider it as an additive process. Schertzer and Lovejoy (1991) introduced the generator $\Gamma_\lambda = \ln(\mu_R)$, and consider that the comparison of two stages of construction of a cascade, for instance at scale ratio λ and at scale ratio λ', can be considered in terms of the addition of the two generators. The importance of Γ_λ is that it represents a cascade completed to scale ratio λ. In this sense, constructing a multiplicative cascade through n steps, from λ to λ' can be accomplished by adding the generators Γ_λ and $\Gamma_{\lambda'}$. The following relation defines Γ_λ,

$$< (\mu_R)_\lambda^q > = < e^{q\Gamma_\lambda} > = e^{K_\lambda(q)} = e^{\ln(\lambda)K(q)} = \lambda^{K(q)}$$

$\lambda^{K(q)}$ is the "Laplace characteristics function" of Γ_λ. Γ_λ can be considered to be a noise source. The purpose of the generator is to describe the multiplicative cascade as an additive process, as such, there are stringent conditions on the form of the generator.

The determination of an appropriate form for the generator Γ_λ has been accomplished by Wilson et al. (1991). Pecknold et al. (1993) go through the details much more thoroughly. The basic result is that

$$\Gamma_\lambda(\vec{x}) = \int_{S_{1,\lambda}} f(\vec{k})\bar{\gamma}(\vec{k})e^{i\vec{k}\cdot\vec{x}}d\vec{k}$$

The domain of integration $S_{1,\lambda}$ is the domain of Fourier space with $1 \leq |\vec{k}| \leq \lambda$ since Γ_λ must be smooth for scales smaller than λ^{-1}. $f(\vec{k})$ is a real non-random filter that produces a 1/f or pink noise. $\bar{\gamma}(\vec{k})$ is a stationary noise source (referred to as the sub-generator) which must satisfy the following conditions:

1) $\bar{\gamma}(\vec{k}) = \bar{\gamma}^*(-\vec{k})$ since $\Gamma_\lambda(\vec{x})$ is real.

2) $\langle\bar{\gamma}(\vec{k})\bar{\gamma}(\vec{k}')\rangle = \sigma^2\delta(\vec{k}+\vec{k}')$, which follows from the fact that $\bar{\gamma}(\vec{k})$ is stationary and the Gaussian assumption which means that $\sigma^2 < \infty$.

3) $\langle\bar{\gamma}(\vec{k})\rangle = 0$. This is done for convenience.

$\bar{\gamma}(\vec{k})$ is usually chosen to be a Levy noise, but depends on the desired α (i.e. if $\alpha = 1$ is desired, a Cauchy generator is required, if $\alpha = 2$ is desired, which is the case for nearly lognormal multifractals, a Gaussian generator is used). Thus, α affects the singular nature of the multifractal. C_1 is affected by the variance of the noise source $\bar{\gamma}(\vec{k})$. As such, appropriate normalization of the variance of $\bar{\gamma}(\vec{k})$ results in multifractals with a prescribed C_1.

In order for the generator to be multiscaling it must obey the following properties:

1) The spectrum must scale as k^{-1}, in order to obtain scaling behaviour: that is , a $\log\lambda$ divergence of K(q).

2) The generator must be band-limited to wave-number between [1,λ]. This requirement ensures that for scales smaller than λ^{-1} the field will be smooth. λ^{-1} will therefore be the resolution of the field.

3) The probability distribution of the generator must fall off more than exponentially for positive fluctuations. This requirement ensures the convergence of K(q) for $q > 0$.

4) The generator must be normalized such that $K(1) = 0$. This is the condition for the conservation of the mean of the field at varying scales.

A generator, such as the UMCG that is used in this thesis, which obeys these conditions will produce universal multifractals.

The Universal Multifractal Cascade Generator.

The implementation of the multifractal generator used for this thesis is referred to as the Universal Multifractal Cascade Generator (UMCG). Figure A.1 shows the systematic construction steps necessary to build a universal multifractal. Creating multifractals in Fourier space has the advantage that the clusters that inevitably result in the field are not restricted by the (normally) ratio of 2 construction process common to multiplicative techniques. The filtering process that occurs after the creation of the universal multifractal field will be discussed below. Multifractal fields produced with the UMCG generally have the prescribed $\alpha \pm 5\%$ and $C_1 \pm 10\%$.

The UMCG construction process detailed in figure A.2 is illustrated by figures A.3, A.4 and A.5. Figure A.3 is the sub-generator field (white noise). The sub-generator field is a white noise (uncorrelated) field of random numbers distributed, in this case, as a Gaussian ($\alpha = 2$). The sub-generator field is then taken into Fourier space using a fast Fourier transform (FFT) and multiplied (filtered) as k^{-1}. Following an inverse FFT the generator field is identified as a 1/f or pink noise distributed as the sub-generator. Figure A.4 is the multifractal resulting from exponentiation of the generator field. Figure A.5 is the result of filtering (fractional integration) of the multifractal in figure A.4 by k^{-H}, with $H = 0.2$. The H-filter is intended to carry the conservative multifractal, which has spectral slope $\beta = 1 - K(2)$ to a non-conservative field with a deeper spectral slope, given by $\beta = 2H + 1 - K(2)$.

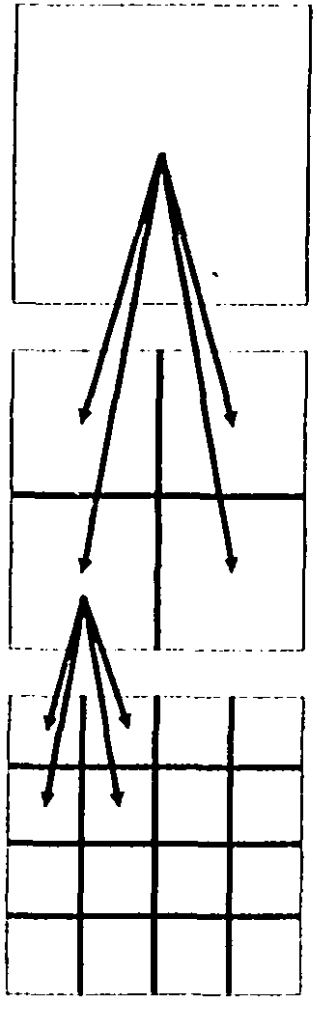

$\lambda = 1$

Construction Level 0

Initial Mass = σ_1

$\lambda = 1/2$

Construction Level 1

Mass = $\sum \sigma_1(x)$

Density = $\sigma_{1/2}(x) = \sigma_1 W_1(x)$

$\lambda = 1/4$

Construction Level 2

Mass = $\sum \sigma_{1/2}(x)$

Density = $\sigma_{1/4}(x) = \sigma_{1/2} W_2(x)$

Generation of σ_λ by Multiplicative Cascade

Figure A.1: Idealization of the multiplicative cascade construction process. An array filled with initial values is successively sub-divided into smaller volumes each of which is multiplied by a random number drawn from a distribution W.

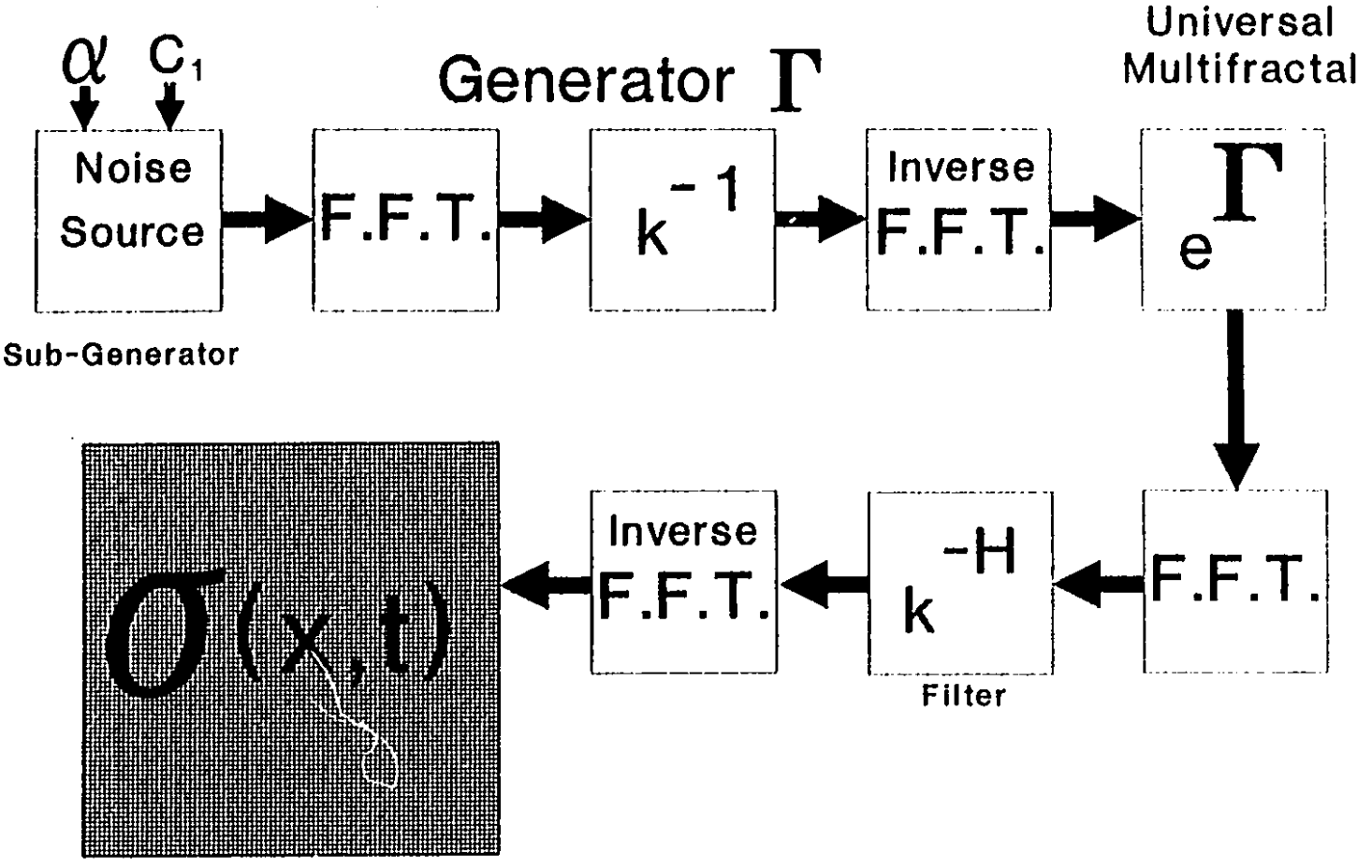

The Universal Multifractal Cascade Generator (UMCG)

Figure A.2: The Fourier space Universal Multifractal Cascade Generator. The UMCG process produces multifractals with controllable statistical properties.

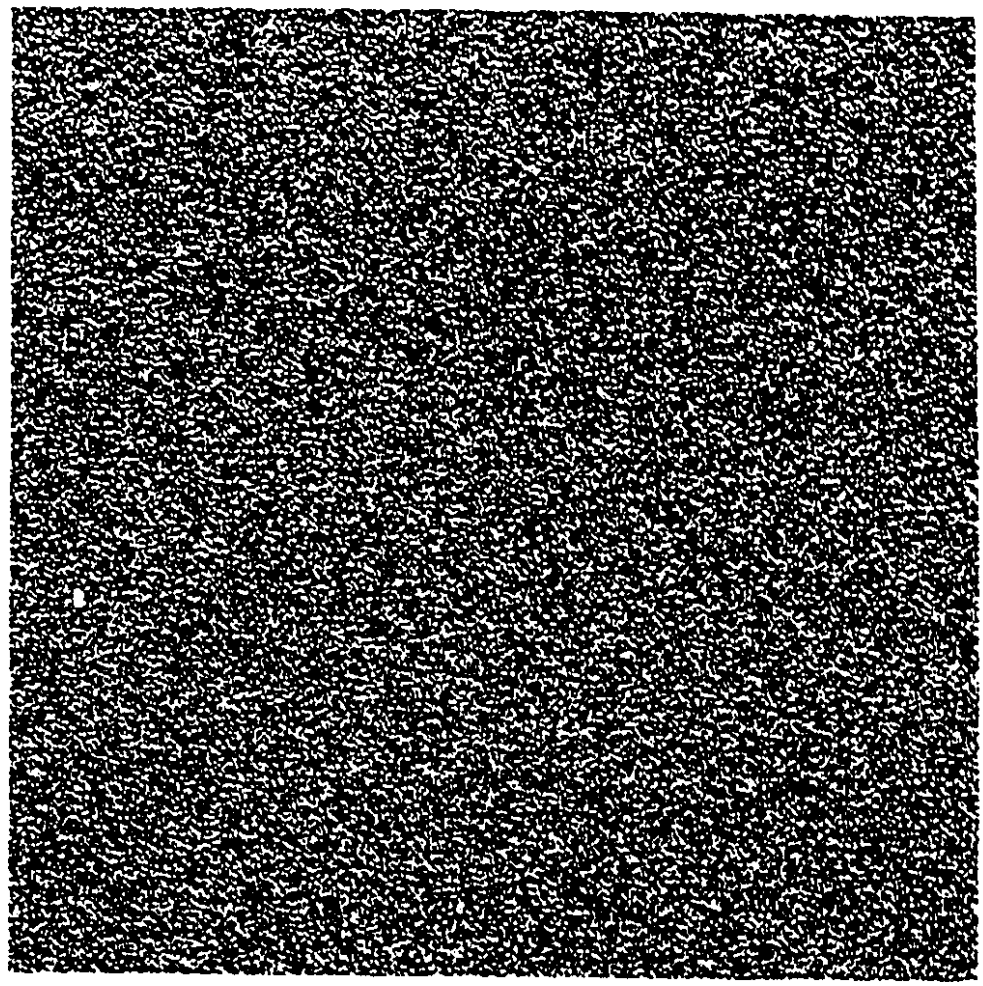

Figure A.3: The sub-generator field. An array of Gaussian deviates with variance properly normalized.

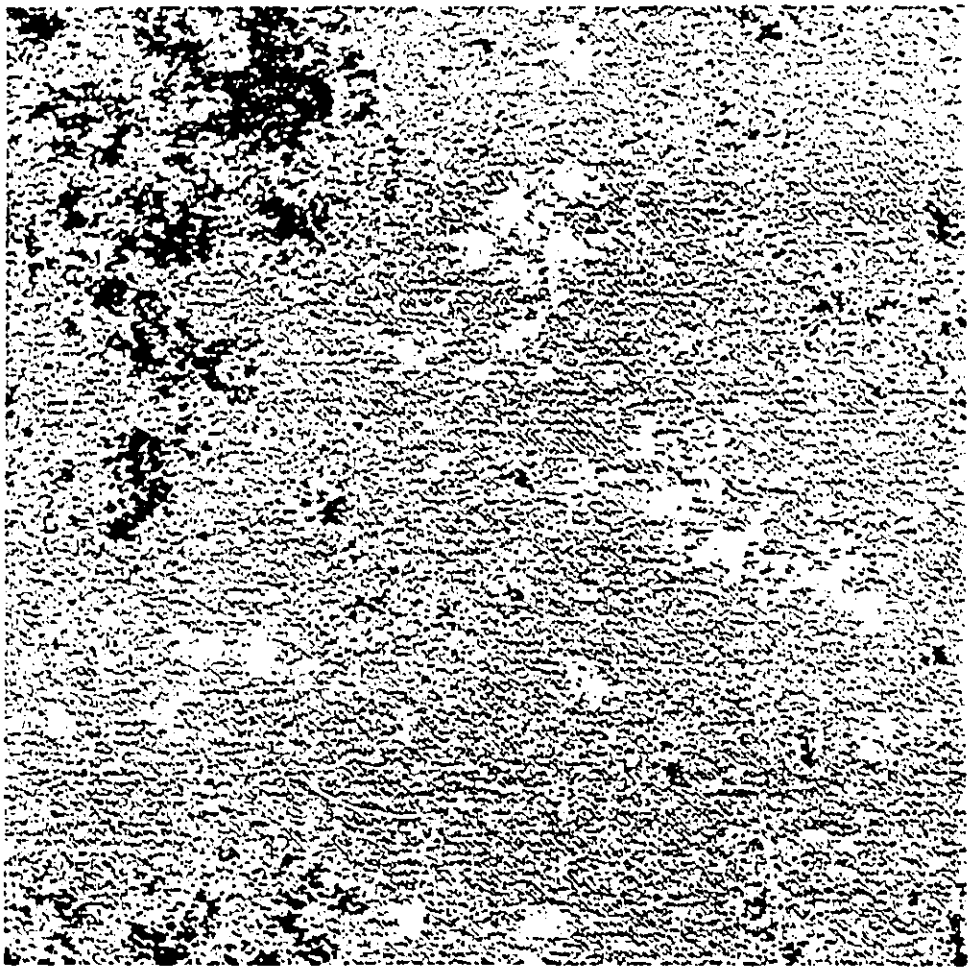

Figure A.4: The universal multifractal that results from performing an f_1 filtering operation on the sub-generator field in figure A.3 in Fourier space and then exponentiating the result.

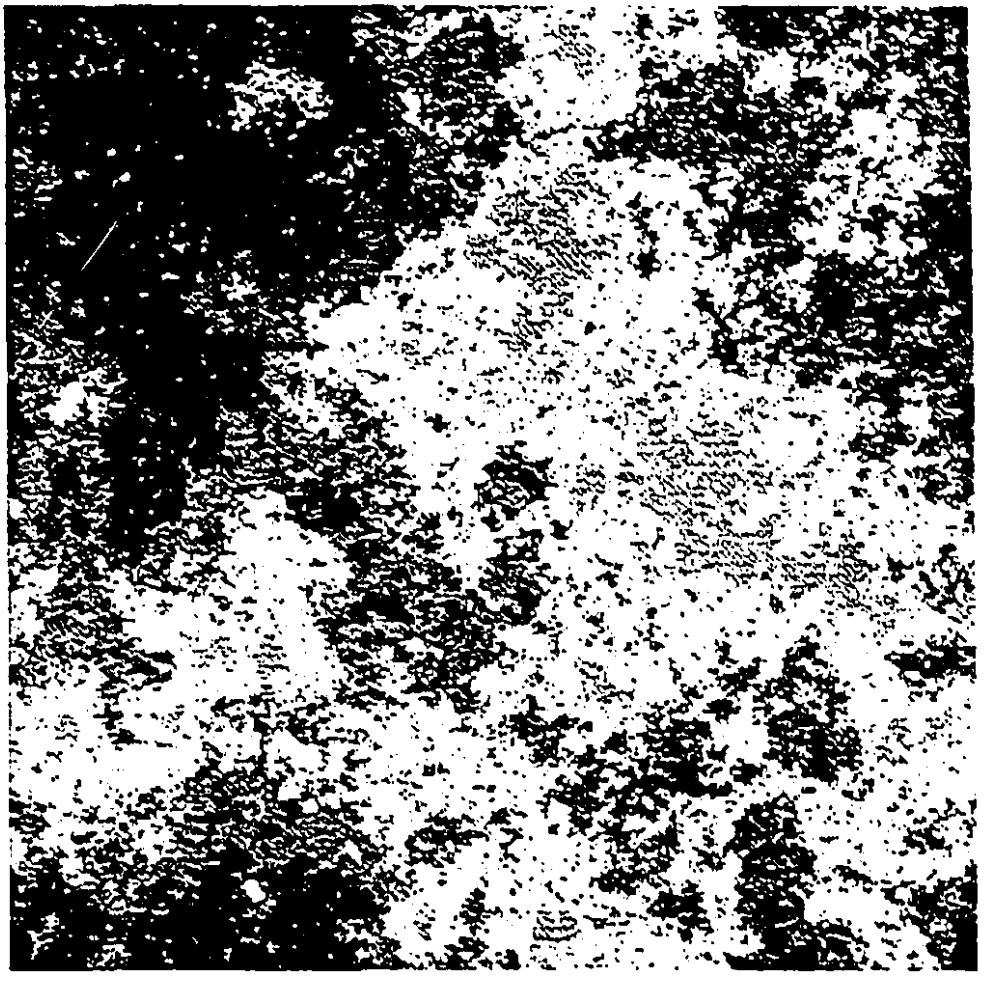

Figure A.5: The multifractal after filtering with a spectral filter with exponent H = 0.2. The smooth appearance (i.e. lacking the blocky appearance of real-space multiplicative construction processes) of the multifractal is due entirely to the Fourier space construction process.

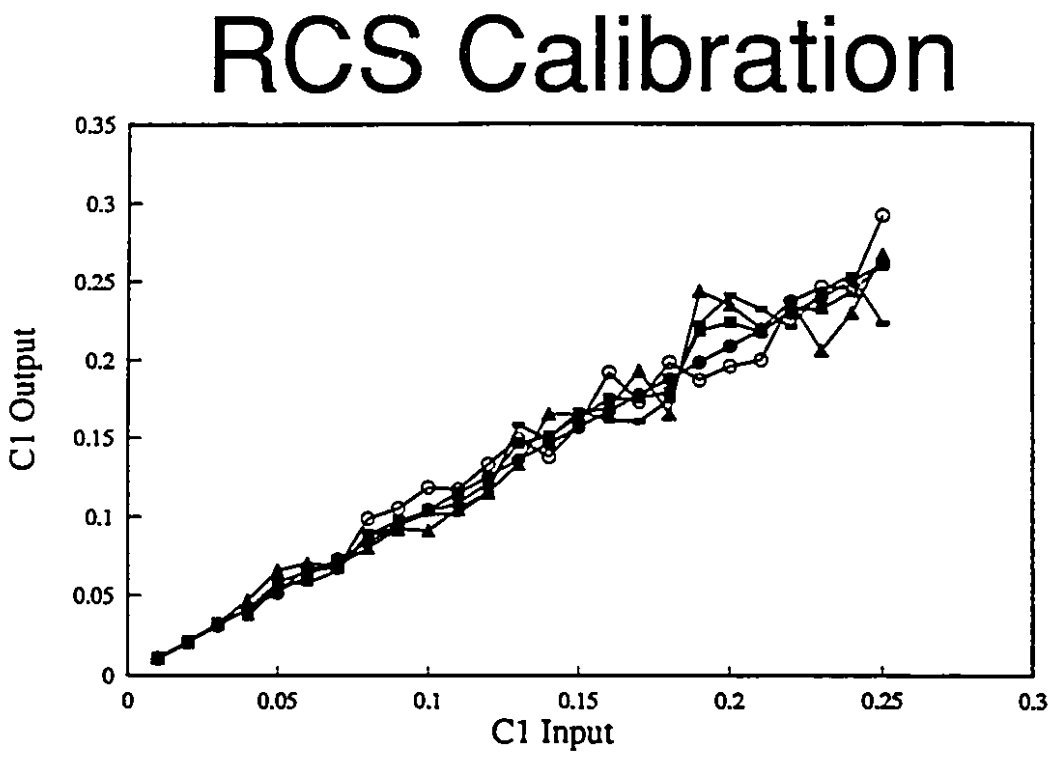

Figure A.6: Calibration of the UMCG used for the RCS model. The line of slope 1 indicates that the UMCG produces multifractals with the correct C_1. The input α is held constant at 2.0 and the output α is also 2.0.

The component sub-routines of the UMCG generator and the RCS model can be found in Numerical Recipes (Press et al., 1992). The routines used include: FOUR1, and FOURN (FFT algorithms), and RAN3, GASDEV (random number generators). Typical run times on a 16 MFlop SGI Elan were on the order of 4 minutes per 1024x1024 array. The UMCG was coded initially to run on PC machines in the memory space beyond 1 Meg in PC 'protected mode' operation. Special

assembler (machine language) routines were written to enter protected mode and then to perform floating point operations on the high memory locations. Inspiration and some know-how for these routines is due to Williams (Dr Dobbs Journal, 1990).

The 2D $\sigma_\lambda(x,t)$ fields produced by the UMCG generator for the RCS model (see Chapter 7) were tested using the TM/GA technique. For each model input C_1 the output C_1 was computed. The plot of C_1(input) against C_1(output) is shown in figure A.6. The slope of the line is 1 ± 0.05. It should be noted from figure A.6 that the variance of C_1(output) increases with C_1(input). This property is expected since the UMCG is a stochastic process. The linearity of the calibration curve in fig. A.6 is the major justification for using the UMCG to generate $\sigma_\lambda(x,t)$ fields.

Appendix B: The Genetic Algorithm and TM/GA.

The genetic algorithm (GA) is an optimization algorithm modelled on the genetic replication, crossover, and mutation processes found in biological systems. The algorithm's uses the natural optimization ability of the genetic processes of mutation and crossover to optimize functions with arbitrary criteria in non-linear search spaces. According to Holland (1992) genetics may be seen as nature's method of searching non-linear function spaces in the presence of optimizing criteria (generally referred to as fitness and presented as a fitness function). In nature, however, it is possible that the conditions for a given optimal solution may be variable in time and hence the search represents the non-ending quest of producing the best adapted population to deal with the environment.

```
*-------------------------------------------------------------*
   GENERATION 0    Average Fitness = 1.4838
Initial Population Maximum Fitness = 15.9225
Initial Population Average Fitness = 1.4838
Initial Population Minimum Fitness = 0.0858482
Initial Population Sum of Fitness  = 29.6761
*-------------------------------------------------------------*
              Chromosome                    Fit Parents X  (α)    C1
0)  10001101100111111001000000010011 0.843 ( 0, 0)  0 1.106 0.251
1)  00001000110110111101100110100101 0.086 ( 0, 0)  0 0.069 0.700
2)  11100010100000111011011100010011 0.524 ( 0, 0)  0 1.770 0.430
3)  11011111101000001001001111010111  15.9 ( 0, 0)  0 1.747 0.156
4)  00101110010110010100101010111011 0.137 ( 0, 0)  0 0.362 0.584
5)  10101101101001100101000100010011 0.239 ( 0, 0)  0 1.357 0.633
6)  01000111001110111111100101110111 0.097 ( 0, 0)  0 0.557 0.898
7)  10101100100111011101110001111101 0.202 ( 0, 0)  0 1.349 0.723
8)  01001101110011001110100001111101 0.112 ( 0, 0)  0 0.608 0.816
9)  01011110100000100110110001011101 0.117 ( 0, 0)  0 0.738 0.847
10) 00111111101000111000110110101110 2.44 ( 0, 0)  0 0.497 0.107
11) 10100011000010100001110010010100  1.3 ( 0, 0)  0 1.274 0.223
12) 11100110010110010011001111001100 0.59 ( 0, 0)  0 1.800 0.405
13) 11111101101100101000111010100100 2.33 ( 0, 0)  0 1.982 0.114
14) 01010110100110000101000111010111 0.156 ( 0, 0)  0 0.677 0.639
15) 10101010011000000100001111000011 0.299 ( 0, 0)  0 1.331 0.529
16) 10101010101001001001010110111010  3.85 ( 0, 0)  0 1.333 0.170
17) 01111000000010110111100110010101 0.116 ( 0, 0)  0 0.938 0.950
18) 01001100100001100100111001000110 0.155 ( 0, 0)  0 0.598 0.612
19) 00110011111010001100011010011111 0.151 ( 0, 0)  0 0.406 0.552
*-------------------------------------------------------------*
```

The coding of a genetic algorithm on a computer is a simple process that need be conducted only once. GA code consists largely of flexible indexing of a population of strings which represent the chromosomes or genetic information (strings of 1s and 0s). This code and that for mutation and crossover of the strings remains invariant from one problem to the next. The heart of the GA is the fitness function, and this function will differ for each problem. The function space will also differ for each problem. In the TM/GA application the function search space is limited to two variables of known range and the fitness function is easily formulated as a function of the sum of absolute differences between the estimated and theoretical K(q) function at a known set of points (see eq. 7.11).

Five generations of a TM/GA run are provided to show the progression of a genetic algorithm towards an optimal solution. For the example, only 20 individuals and 5 generations were used. In normal operation 500 individuals and 11 generations are used. Each panel gives the full information of a generation of the GA. Average fitness, total fitness, as well as a listing of each individual in the population with corresponding fitness, parents, crossover point, α and C_1. The reader is encouraged to examine the panels successively and gain reassurance that the algorithm is systematically moving the population towards maximum fitness and hence is optimizing the fitness function.

The figure 'GENERATION 0' shows the initial population of a GA algorithm for the TM/GA technique. The population of chromosomes are numbered from 0 to 19 for 20 individuals. Initially the 0's and 1's are chosen at random, which is clearly visible in the lack of pattern in GENERATION 0. The Fit number is the fitness of the corresponding chromosome. The α and C_1 are shown for each chromosome.

```
*****************************************************************
   GENERATION 1   Average Fitness = 7.84108
*****************************************************************
       Population Maximum Fitness = 16.3417
       Population Average Fitness = 7.84108
       Population Minimum Fitness = 0.523554
       Population Sum of Fitness  = 156.822
       Number of Mutations        = 1
       Number of Crossovers       = 7
*---------------------------------------------------------------*
```

	Chromosome	Fit	Parents	X	(α)	C_1
0)	11011111101000001001001111101011 1	15.9	(3, 3)	32	1.747	0.156
1)	11011111101000001001001111101011 1	15.9	(3, 3)	32	1.747	0.156
2)	10101010101001001001010111101111 1	3.68	(3,16)	8	1.333	0.171
3)	11011111101000001001001110111101 0	13.7	(3,16)	8	1.747	0.154
4)	00111111101000111001010111011110 1 0	0.941	(16,10)	14	0.497	0.170
5)	10101010101001001000110110101110 0	3.57	(16,10)	14	1.333	0.107
6)	11111101101000001001001111101011 1	6.59	(3,13)	25	1.981	0.156
7)	11011111101100101000111010100100 0	2.75	(3,13)	25	1.748	0.114
8)	10100011000010100001110010011101 0	1.3	(16,11)	5	1.274	0.224
9)	10101010101001001001010110110100 0	3.89	(16,11)	5	1.333	0.170
10)	00111111101000111000110111101011 1	2.39	(3,10)	8	0.497	0.109
11)	11011111101000001001001110101110 0	13.1	(3,10)	8	1.747	0.154
12)	11011111001000001001001111101011 1	16.3	(3, 3)	15	1.743	0.156
13)	11011111101000001001001111101011 1	15.9	(3, 3)	15	1.747	0.156
14)	10101010101001001001010110111111 1	3.84	(3,16)	3	1.333	0.170
15)	11011111101000001001001111101001 0	15.8	(3,16)	3	1.747	0.156
16)	00111111101000111000110110101110 0	2.44	(10, 2)	32	0.497	0.107
17)	11100010100000111011011110001001 1 1	0.524	(10, 2)	32	1.770	0.430
18)	11011111101000001001001111101011 1	15.9	(3,13)	32	1.747	0.156
19)	11111101101100101000111010100100 0	2.33	(3,13)	32	1.982	0.114

```
*---------------------------------------------------------------*
```

The population of chromosomes in GENERATION 1 shows the surprising power of the GA. Individuals are selected on the basis of their fitness. The probability that a particular individual will be selected is given by its fitness divided by the population sum of fitness. This weighted probability favours the more fit individuals but does not exclusively select them, the reasoning for this is subtle but is related to the necessity of retaining a good mix of information across generations. Once two individuals are selected there is a 60% probability (a variable) that a crossover will take place. If a crossover does take place a crossover point is randomly selected and the transfer of information executed. The Parents column gives the index of the two parents of the previous

generation and the column marked X gives the position along the chromosome that crossover took place. For example, individuals 14 and 15 share parents 3 and 16 in the previous generation. Examination of the fitnesses for individuals 3 and 16 of GENERATION 0 reveals fitnesses of 15.9 and 3.85. Individuals 14 and 15 of GENERATION 1 have fitnesses of 3.84 and 15.8, which reveals that the crossover actually decreased the fitness of both individuals. However, the average population fitness increased 500% due largely to the high probability of selecting individual 3 of GENERATION 0. It should also be noted that individual 12 of GENERATION 1 is a product of a crossover of individual 3 of GENERATION 0 with itself. Given this fact its fitness should not be different, however, the fitness of individual 12 of GENERATION 1 increased due to a mutation. Mutations occur with a probability of 0.5% for each 1 or 0 carried to another individual. The mutation process introduces new information randomly into a population. Too high a mutation rate (> 1%) tends to destroy a population by randomizing the individuals.

```
*****************************************************************
   GENERATION 2   Average Fitness = 11.7211
*****************************************************************
       Population Maximum Fitness = 16.3121
       Population Average Fitness = 11.7211
       Population Minimum Fitness = 2.3342
       Population Sum of Fitness  = 234.421
       Number of Mutations        = 6
       Number of Crossovers       = 11
*---------------------------------------------------------------*
```

	Chromosome	Fit	Parents	X	(α)	C_1
0)	11011111101000001001001111101011 1	15.9	(1, 3)	32	1.747	0.156
1)	11011111101000001001001110111101 0	13.7	(1, 3)	32	1.747	0.154
2)	00111111101000111000110110101110 0	2.44	(16, 0)	32	0.497	0.107
3)	11011111101001001001001111101011 1	15.9	(16, 0)	32	1.747	0.156
4)	11011111101000001000111010100100 0	2.76	(7,11)	14	1.747	0.114
5)	11011111101100101001001110101110 0	13	(7,11)	14	1.748	0.154
6)	11011111101000001001001111101011 1	15.9	(1,15)	32	1.747	0.156
7)	11011111101000001001001111101001 0	15.8	(1,15)	32	1.747	0.156
8)	11011111101000001001001110111101 0	13.7	(3,19)	32	1.747	0.154
9)	11111101101100101000111010100100 0	2.33	(3,19)	32	1.982	0.114
10)	11011111101000001001001111101011 1	15.9	(1,13)	3	1.747	0.156
11)	11011111101000001001001111101011 1	15.9	(1,13)	3	1.747	0.156
12)	11011111101000101001001110101110 0	13.1	(11, 1)	32	1.747	0.154
13)	10011111101000001001001111101011 1	5.24	(11, 1)	32	1.247	0.156
14)	11011111101000001001001110111101 1	13.7	(12, 3)	1	1.747	0.154
15)	11011111001000001001001111101011 0	16.3	(12, 3)	1	1.743	0.156
16)	10011111101000001001001111101011 1	5.24	(0,13)	32	1.247	0.156
17)	11011111101000001001001111101011 1	15.9	(0,13)	32	1.747	0.156
18)	11011111001000001001000111101011 1	5.71	(13,12)	4	1.743	0.140
19)	11011111101000001001001111101011 1	15.9	(13,12)	4	1.747	0.156

GENERATION 2 reveals that the chromosomes are almost completely organized. It should be noted that the average population fitness has increased greatly over that of GENERATION 1. It should also be noted that much of the randomness of GENERATIONS 0 and 1 is now gone. The ability of GAs to quickly search spaces and center on the pattern of 1s and 0s (known as schemata or schemas) that gives the most fit population makes them potentially very valuable in pattern recognition problems.

```
**********************************************************************
   GENERATION 3   Average Fitness = 13.1995
**********************************************************************
       Population Maximum Fitness = 16.3417
       Population Average Fitness = 13.1995
       Population Minimum Fitness = 2.34259
       Population Sum of Fitness  = 263.989
       Number of Mutations        = 8
       Number of Crossovers       = 16
*---------------------------------------------------------------------*

              Chromosome                        Fit Parents X  (α)    C1

0)  11011111101000001001001111101011l  15.9 ( 0, 7) 32 1.747 0.156
1)  11011111101000001001001111101001O  15.8 ( 0, 7) 32 1.747 0.156
2)  11011111101000001001001111101011l  15.9 (19,17) 32 1.747 0.156
3)  11011111101000001001001111101011l  15.9 (19,17) 32 1.747 0.156
4)  11011111101100001001001111101011l  15.9 (16, 4) 20 1.748 0.156
5)  10011111101000001000111010100l000  5.14 (16, 4) 20 1.247 0.114
6)  11011111001000001001000111101011l  5.71 (17,18)  9 1.743 0.140
7)  11011111101000001001001111101011l  15.9 (17,18)  9 1.747 0.156
8)  11011111101000001001001110101llOO  13.1 (12, 1) 11 1.747 0.154
9)  11011111101000101001001110111lOlO  13.7 (12, 1) 11 1.747 0.154
10) 11011111101000001001001111101011l  15.9 (19, 7) 32 1.747 0.156
11) 11011111101000001001011111101001O  6.06 (19, 7) 32 1.747 0.187
12) 11011111101000001001001111100l000  15.5 ( 9,10)  5 1.747 0.155
13) 11111101101100101000111010lOlOlll  2.34 ( 9,10)  5 1.982 0.115
14) 11011111001000001001001111101011O  16.3 (15, 6) 32 1.743 0.156
15) 11011111101000001001001111101011l  15.9 (15, 6) 32 1.747 0.156
16) 11011111101100101001001110101llOO    13 ( 5,14) 32 1.748 0.154
17) 11011111101000001001001110111lOll  13.7 ( 5,14) 32 1.747 0.154
18) 11011111101000001001001111101011O  15.9 (15,19) 20 1.747 0.156
19) 11011111001000001001001111101011l  16.3 (15,19) 20 1.743 0.156
*---------------------------------------------------------------------*
```

```
**********************************************************************
   GENERATION 4   Average Fitness = 13.1729
**********************************************************************
       Population Maximum Fitness = 16.3283
       Population Average Fitness = 13.1729
       Population Minimum Fitness = 2.75571
       Population Sum of Fitness  = 263.457
       Number of Mutations        = 13
       Number of Crossovers       = 22
*---------------------------------------------------------------------*
```

	Chromosome	Fit	Parents	X	(α)	C_1
0)	11011111101100101001001110101110 0	13	(16, 8)	25	1.748	0.154
1)	11011111101000001001001110101110 0	13.1	(16, 8)	25	1.747	0.154
2)	11011111101100101001001110101110 0	13	(16, 6)	32	1.748	0.154
3)	11011111001000001001000111101011 1	5.71	(16, 6)	32	1.743	0.140
4)	11011111101000001000111010100100 0	2.76	(5, 8)	15	1.747	0.114
5)	10011111101000001001001110101110 0	5.66	(5, 8)	15	1.247	0.154
6)	11011111101000001001001111101011 1	15.9	(4,10)	0	1.747	0.156
7)	11011111101100001001001111101011 1	15.9	(4,10)	0	1.748	0.156
8)	11011111101100101001001110101110 0	13	(16,16)	32	1.748	0.154
9)	11011111101100101001001110101110 0	13	(16,16)	32	1.748	0.154
10)	11011111101100101001001110100100 0	12.7	(16, 7)	32	1.748	0.154
11)	11011111101000001001001110101011 1	13	(16, 7)	32	1.747	0.154
12)	11011111101100001001001111101011 1	15.9	(4, 4)	1	1.748	0.156
13)	11011111101100001001001111101011 1	15.9	(4, 4)	1	1.748	0.156
14)	11011111101000001001001111101011 1	15.9	(0, 1)	20	1.747	0.156
15)	11011111101000001001001111000010 0	15.4	(0, 1)	20	1.747	0.155
16)	11011111101000001001001111101001 0	15.8	(1, 7)	30	1.747	0.156
17)	11011111101000001001001111101011 1	15.9	(1, 7)	30	1.747	0.156
18)	11011111101000001001001111001000 0	15.5	(12,19)	32	1.747	0.155
19)	11011111001001001001001111101011 1	16.3	(12,19)	32	1.743	0.156

```
*---------------------------------------------------------------------*
```

The operational implementation of TM/GA uses a large number of individuals and a larger number of generations. The TM/GA uses 500 individuals and 11 generations. Convergence to the optimal answer is similar to that presented in this section. The process is repeated a number of times for confidence. Correlations within the random number generators can play havoc with the GA and cause it to produce poor optimal fits. Repetitions of the TM/GA process over the same data set a number of times provides a number of optimal solutions. The solution with the highest fitness is then selected from among the repetitions.

The convergence of a genetic population to a particular answer is a theoretically infinite process. Given an infinite amount of time the GA will find the answer. For the purposes of TM/GA where other estimation errors, such as the estimates of the slopes of the various scaling moments in TM place a limit on the ultimate accuracy it is only necessary for the GA to get the answer within a neighborhood. This may be viewed as a flexibility rather than a limitation since deterministic algorithms work very hard to find the answer, but GAs can be limited to provide an estimate. The precision of the estimate will be at the discretion of the user.

```
*****************************************************************
   GENERATION 5   Average = 14.9278
*****************************************************************
       Population Maximum Fitness = 31.4956
       Population Average Fitness = 14.9278
       Population Minimum Fitness = 5.24125
       Population Sum of Fitness  = 298.557
       Number of Mutations        = 17
       Number of Crossovers       = 28
*---------------------------------------------------------------*
```

	Chromosome	Fit	Parents	X	(α)	C_1
0)	11011111101100101001001110101110 0	13	(2,13)	32	1.748	0.154
1)	11011011101100001001001111101011 1	20	(2,13)	32	1.716	0.156
2)	10011111101000001001001111101011 1	5.24	(14, 0)	32	1.247	0.156
3)	11011111101100101001001110101110 0	13	(14, 0)	32	1.748	0.154
4)	11011111101100001001001110101110 0	13	(8,12)	8	1.748	0.154
5)	11011111101100101001001111101011 1	15.9	(8,12)	8	1.748	0.156
6)	11011111101000001001001111101011 1	15.9	(17, 2)	24	1.747	0.156
7)	11001111101100101001001110101110 0	31.5	(17, 2)	24	1.623	0.154
8)	11011111101000001001001111101011 1	15.9	(12,16)	8	1.747	0.156
9)	11011111101100001001001111101001 0	15.7	(12,16)	8	1.748	0.156
10)	11011111101100101001001110101110 0	13	(1, 0)	9	1.748	0.154
11)	11011111101000001001001110101110 0	13.1	(1, 0)	9	1.747	0.154
12)	11011111101100101001001110101110 0	13	(8, 1)	32	1.748	0.154
13)	11011111101000001001001110101110 0	13.1	(8, 1)	32	1.747	0.154
14)	11011111101000001001001111101001 0	15.8	(16, 7)	32	1.747	0.156
15)	11011111101100001001001111101011 1	15.9	(16, 7)	32	1.748	0.156
16)	11011111101000001001001110110100 0	13.3	(18,11)	5	1.747	0.154
17)	11011111101000001001001111101011 1	15.9	(18,11)	5	1.747	0.156
18)	11011111101100101001001110101110 0	13	(1, 8)	1	1.748	0.154
19)	11011111101000001001001110101110 0	13.1	(1, 8)	1	1.747	0.154

In a GA spontaneous improvements in individual fitness are common, but the main concern is that the population fitness increase from generation to generation. Individual 7 of GENERATION 5 has the parents 17 and 2 from GENERATION 4 and represents an obvious improvement. If the sequence of generations were continued it is likely that individual 7 would be carried over and the improvements distributed among the population. It is important to note the well ordered structure of the chromosome pattern after only 5 generations. All the individuals look similar and the algorithm has largely exhausted the initial information and is making improvements slowly by mutation.

The mutation/crossover heuristic represents an extremely powerful optimizing capability. As discussed in Goldberg (1989), theoretically there is only one condition under which a GA will fail to find an optimal answer, and that situation is very hard to reproduce. Operationally there are some considerations that relate to the initial amount of information that a GA is fed about a problem prior to search. Allred and Kelly (1993) show that a GA rapidly uses the initial information and grinds to a halt (as seen by GENERATION 2). The speed at which a GA searches through a function space is simply amazing, but this also means that a great deal of information must initially be supplied if the GA is to find an answer in a complex space. Allred and Kelly (1993) proposed the Differentially Applied Genetic Algorithm (DAGA) to help with this problem. DAGA involves the process of reintroducing variability into the search space during successive generations of the GA.

Appendix C: An Analytical Framework for Modelling the Fluctuating Echo.

It was originally thought that the direct analytical and numerical modelling of the power spectrum represented the best course of action for understanding the spectral behaviour of time series of the fluctuating echo. However, the analytical forms were quickly bogged down by the number of assumptions necessary to realize the functional forms of lognormal multifractals. The successes of the numerical model far outweighed the numerical cumberances of the analytical forms which eventually had to be integrated numerically. Thus, the numerical modelling approach was pursued in 1 and 2 dimensions and led to the results in chapter 6 and 7.

As was mentioned in section 7 the analytical form of the power spectrum is based on the behaviour of the four point correlation function of $\sigma_\lambda(x,t)$. From the evidence presented it is now assumed that $\sigma_\lambda(x,t)$ is a multifractal field. The following development terminates with the definition of the power spectrum as the four-point correlation function of $\sigma(x,t)$.

Consider a one dimensional distribution of radar scatterers $\sigma_\lambda(x,t)$ varying in time with an inner dissipation scale λ^{-1}. The radar wavenumber is k/2 (the factor 2 is for convenience as it takes into account the round trip distance). The pulse volume length is L. We will take the outer scale of the process to be 1 hence L will be restricted to the region L<1. We will use units such that the velocity is unity. The amplitude of the reflected wave is:

$$A(k,t) = \int_{-L}^{L} e^{ikx}\sigma_\lambda(x,t)dx \qquad (C.1)$$

The measured intensity normalized for pulse length is:

$$I(k,t) = \frac{1}{L}AA^* \qquad (C.2)$$

We seek an expression for the (ensemble averaged) spectrum of I(k,t), for signals of duration T. T is expected to be long duration. The power spectrum is expressed as :

$$E_k(\omega) = \frac{1}{2T}\int_{-T}^{T} e^{i\omega\tau} < I(k,0)I(k,\tau) > d\tau \qquad (C.3)$$

The power spectrum is the forward Fourier transform of the correlation function of intensities. This follows from the Wiener-Khintchin theorem (using the assumption that I(k,t) is stationary in time). The limits of integration are determined by the size of the pulse volume. The power spectrum expressed in terms of the signal amplitudes is a function of the four point correlation function of the amplitudes:

$$E_k(\omega) = \frac{1}{8TL^2}\int_{-T}^{T} e^{i\omega\tau}\int_{-L^4}^{L^4} e^{ikx_1}e^{ikx_2}e^{ikx_3}e^{ikx_4} < \sigma(x_1,0)\sigma(x_2,\tilde{U})\sigma(x_3,\tau)\sigma(x_4,\tau) > dx_1dx_2dx_3dx_4d\tau \quad (C.4)$$